

Non-Aqueous Single-Metal Redox Flow Batteries

by

Aaron A. Shinkle

A dissertation submitted in partial fulfillment  
of the requirements for the degree of  
Doctor of Philosophy  
(Chemical Engineering)  
in the University of Michigan  
2013

Doctoral Committee:

Assistant Professor Charles W. Monroe, Co-Chair  
Professor Levi T. Thompson Jr., Co-Chair  
Professor John W. Halloran  
Associate Professor Suljo Linic

## Acknowledgements

I would like to acknowledge the support of the dissertation committee, Monroe research group, Thompson research group, Prof. Rasmussen, and Dr. Sleightholme. I would like to thank the University of Michigan-Fraunhofer Alternative Energy Technologies for Transportation program for funding my research. The Electron Microbeam Analysis Laboratory and Horace Rackham Graduate School were also instrumental in the completion of research for my degree.

## Table of Contents

Acknowledgements .....	ii
List of Figures .....	vi
List of Tables .....	xvii
List of Abbreviations .....	xviii
Abstract .....	xx
Chapter 1 Introduction .....	1
1.1 Introduction to Redox Flow Batteries .....	1
1.2 Aqueous Redox Flow Battery Systems .....	4
1.3 Non-aqueous Systems .....	10
Chapter 2 Effects of the Liquid Electrolyte .....	18
2.1 Experimental Techniques .....	18
2.1.1 Cyclic Voltammetry .....	18
2.1.2 Charge/Discharge .....	24
2.2 Active-Species Metal Center .....	37
2.2.1 Background and Approach .....	37
2.2.2 Results: Manganese Acetylacetonate .....	38
2.2.3 Results: Chromium Acetylacetonate .....	44
2.2.4 Results: Vanadium Acetylacetonate .....	50
2.2.5 Discussion .....	58
2.3 Ligand Modification .....	60
2.3.1 Background .....	60
2.3.2 Approach .....	62
2.3.3 Results .....	64
2.3.4 Discussion & Future Ligand Work .....	78
2.4 Solvent and Support Selection .....	79

2.4.1	Background.....	79
2.4.2	Experimental Design.....	81
2.4.3	Results: Physical Properties .....	85
2.4.4	Results: Electrochemical Properties .....	90
2.4.5	Discussion: Desired Solution Properties .....	97
2.4.6	Conclusion .....	106
Chapter 3 Effects of the Cell Components .....		108
3.1	Membrane .....	108
3.1.1	Background.....	108
3.1.2	Results: Pretreatment .....	112
3.1.3	Results: Impedance .....	118
3.1.4	Discussion & Future Membrane Work .....	122
3.2	Electrodes .....	124
3.2.1	Background.....	124
3.2.2	Approach .....	126
3.2.3	Results: Experimental .....	127
3.2.4	Results: Mechanistically-Based Kinetic Model .....	130
3.2.5	Discussion .....	144
Chapter 4 Redox Flow Battery Performance .....		146
4.1	Degradation Mechanisms.....	146
4.1.1	Approach .....	146
4.1.2	Results: Cyclic Voltammetry .....	147
4.1.3	Results: Charge/Discharge – Modest Oxygen Content Glovebox	154
4.1.4	Results: Charge/Discharge – Minimal Oxygen Content Glovebox	159
4.1.5	Discussion .....	161
4.1.6	Summary .....	163
4.2	Concentration tests.....	164
4.2.1	Background and Approach .....	164
4.2.2	Results .....	167
4.2.3	Discussion .....	175
4.3	Capacity .....	177

4.3.1	Background and Approach .....	177
4.3.2	Results: Electrochemistry .....	177
4.3.3	Results: Scanning Electron Microscopy .....	188
4.3.4	Discussion .....	197
Chapter 5 Conclusion and Future Work .....		201
5.1	Conclusion.....	201
5.2	Future Work.....	206
Bibliography.....		210

## List of Figures

Figure 1.1.1-1 General schematic of a redox flow battery .....	3
Figure 1.2.1-1 Cyclic voltammogram with a glassy carbon disk electrode in (aqueous) 0.01 M $\text{VO}_2\text{SO}_4$ and 2 M $\text{H}_2\text{SO}_4$ in ultrapure $\text{H}_2\text{O}$ . Scan rate 10 mV/s; measurements performed at room temperature. ....	9
Figure 1.3.1-1 Charging profile for 0.1 M ruthenium acetylacetonate and 1 M $\text{TEABF}_4$ in acetonitrile at a current of 1 mA. (Reprinted from Chakrabarti <i>et al.</i> [52]) .....	12
Figure 2.1.1-1 Cyclic voltammetry cell.....	20
Figure 2.1.1-2 Cyclic voltammogram of 0.1 M tetraethylammonium tetrafluoroborate in acetonitrile. Glassy carbon working electrode. Scan rate 25 mV/s. ....	23
Figure 2.1.1-3 Cyclic voltammogram of 0.01 M $\text{V}(\text{acac})_3$ and 0.1 M tetraethylammonium tetrafluoroborate in acetonitrile. Glassy carbon working electrode. Scan rate 25 mV/s. ....	24
Figure 2.1.2-1 Photograph of an H-type charge/discharge cell. The blue liquid represents the volume filled with liquid electrolyte.....	26
Figure 2.1.2-2 Photograph of the 1-D type charge/discharge cell. The brown liquid is a typical $\text{V}(\text{acac})_3$ electrolyte. ....	26
Figure 2.1.2-3 Chronoamperometry of 0.5 M $\text{TEABF}_4$ in acetonitrile. Aluminum electrodes in an H-cell with Neosepta AHA membrane. [Blue (upper line)] Potential input to the cell, [Red (lower line)] Current response. ....	28
Figure 2.1.2-4 Cyclic voltammogram of 0.01 M $\text{V}(\text{acac})_3$ and 0.05 M $\text{TEABF}_4$ in acetonitrile. Scan rate 100 mV/s. Working electrode: aluminum foil, counter electrode: graphite plate, reference electrode: $\text{Ag}/\text{Ag}^+$ . ....	29

Figure 2.1.2-5 Chronoamperometry of graphite electrodes in 0.5 M TEABF <sub>4</sub> in acetonitrile. H-cell with Neosepta AHA membrane was used. [Blue (upper line)] Potential input to the cell, [Red (lower line)] Current response. ....	30
Figure 2.1.2-6 Schematic of a 4-electrode 1-D charge/discharge cell. ....	30
Figure 2.1.2-7 Cyclic voltammogram of 0.01 M V(acac) <sub>3</sub> , 0.05 M TEABF <sub>4</sub> in acetonitrile. Scan rate 100 mV/s with glassy carbon working electrode. ....	33
Figure 2.1.2-8 Plot of the Nernst equation for a single-electron disproportionation reaction with a 2.18 V formal potential. ....	33
Figure 2.1.2-9 Common input parameters for charge/discharge experiments ....	34
Figure 2.1.2-10 Theoretical charge/discharge curve for a cell with [Solid red line] 300 Ohms of ohmic resistance and [Dashed blue line] no resistances. Based on the charge/discharge input described above. ....	35
Figure 2.2.2-1 Cyclic voltammograms measured at a glassy carbon electrode in 0.05 M Mn(acac) <sub>3</sub> and 0.5 M TEABF <sub>4</sub> in ACN; scan rate 100 mV/s; room temperature. ....	38
Figure 2.2.2-2 Cyclic voltammograms measured at a glassy carbon electrode in 0.05 M Mn(acac) <sub>3</sub> and 0.5 M TEABF <sub>4</sub> in ACN at scan rates of 10, 50, 100, and 200 mV/s, arrows show direction of increasing scan rate; room temperature. ...	40
Figure 2.2.2-3 Charge–discharge curves for 0.05 M Mn(acac) <sub>3</sub> and 0.5 M TEABF <sub>4</sub> in ACN; charge current 1 mA and discharge current 0.1 mA; room temperature. ....	42
Figure 2.2.3-1 Cyclic voltammograms measured at a glassy carbon electrode in 0.05 M Cr(acac) <sub>3</sub> and 0.5 M TEABF <sub>4</sub> in ACN; scan rate 50 mV/s; room temperature. ....	44
Figure 2.2.3-2 Cyclic voltammograms measured at a glassy carbon electrode in 0.05 M Cr(acac) <sub>3</sub> and 0.5 M TEABF <sub>4</sub> in ACN at scan rates of 50, 200, and 500 mV/s. Arrows show direction of increasing scan rate; room temperature. ....	46
Figure 2.2.3-3 Charge–discharge curves for 0.05 M Cr(acac) <sub>3</sub> and 0.5 M TEABF <sub>4</sub> in ACN; charge current 1 mA and discharge current 0.1 mA; room temperature. ....	49

Figure 2.2.4-1 Cyclic voltammogram measured at a glassy carbon electrode in 0.01 M V(acac) <sub>3</sub> and 0.05 M TEABF <sub>4</sub> in ACN; scan rate 100 mV/s; room temperature. ....	50
Figure 2.2.4-2 Cyclic voltammogram of 0.01 M V(acac) <sub>3</sub> , 0.05 M TEABF <sub>4</sub> solution with vanadyl acetylacetonate added at [blue] 0 M, [red] 0.0028 M, and [green] 0.0076 M. Scan rate 500 mV/s at room temperature on a glassy carbon electrode. ....	52
Figure 2.2.4-3 Infrared spectra of vanadium acetylacetonate from jars of varying age and a vanadyl acetylacetonate. Samples run under nitrogen and preheated for 2 hours at 150°C. ....	54
Figure 2.2.4-4 Cyclic voltammogram of O <sub>2</sub> electroreduction at Pt taken at multiple scan rates. Reprinted from [79]. ....	54
Figure 2.2.4-5 Cyclic voltammograms measured at a glassy carbon electrode in 0.01 M V(acac) <sub>3</sub> and 0.05 M TEABF <sub>4</sub> in ACN at scan rates of 5, 10, 20, 30, and 50 mV/s, arrows show direction of increasing scan rate; room temperature. ....	55
Figure 2.2.4-6 Plot of V(III) / V(IV) peak height vs. scan rate <sup>1/2</sup> based on cyclic voltammograms measured at a glassy carbon electrode in 0.01 M V(acac) <sub>3</sub> and 0.05 M TEABF <sub>4</sub> in ACN at scan rates of 5, 10, 20, 30, and 50 mV/s; room temperature. ....	56
Figure 2.2.4-7 [Blue] Charge–discharge curves for 0.05 M V(acac) <sub>3</sub> and 0.5 M TEABF <sub>4</sub> in ACN; [Thin red line] constant charge current 1 mA and constant discharge current 0.5 mA; room temperature. ....	57
Figure 2.3.2-1 Base ligand structure for modifications.....	63
Figure 2.3.2-2 Structures of ligands created by Sanford group in the University of Michigan Chemistry Department. ....	63
Figure 2.3.3-1 Cyclic voltammogram of 0.1 M TEABF <sub>4</sub> in acetonitrile at 100 mV/s with a glassy carbon working electrode. Sequential additions of 1 equivalent of ~2.6 mM Hacac and ~2.3 mM TEOH. ....	65
Figure 2.3.3-2 Cyclic voltammograms: (a) 0.5 mM Fe(acac) <sub>3</sub> ; (b) 0.5 mM Fe(acac) + 2 equiv of OH <sup>-</sup> [(Bu <sub>4</sub> N)OH], initial scan; (c) solution from (b), 1.5 min later; (d) solution from (b), 3 min later; (e) solution from (b), 5 min later. Cold acetonitrile [0.1 M (Et <sub>4</sub> Cl)ClO <sub>4</sub> ] (dry ice/acetonitrile bath) solutions were used.	



Conditions: scan rate 0.1 V /s; glassy-carbon working electrode (0.09 cm<sup>2</sup>); SCE vs NHE, +0.242 V. Figure reproduced from [85]..... 66

Figure 2.3.3-3 Cyclic voltammogram of 0.01 M V(acac)<sub>3</sub>, 0.01 M TEAOH, and 0.1 M TEABF<sub>4</sub> in acetonitrile. Solution cycled at 100 mV/s; displaying voltammograms from [pink] 0 min, [green] 1 min, [blue] 3 min, [red] 5 min, [black] 10 min after the addition of the TEAOH..... 67

Figure 2.3.3-4 Cyclic voltammograms of 0.01 M V(tmhd)<sub>3</sub>, 0.5 M TEABF<sub>4</sub> in acetonitrile with a glassy carbon electrode. Multiple voltammograms were taken at varying scan rates. .... 69

Figure 2.3.3-5 Cyclic voltammograms of 0.01 M V(tmhd)<sub>3</sub>, 0.5 M TEABF<sub>4</sub> in acetonitrile with a glassy carbon electrode at a scan rate of 500 mV/s. Multiple voltammograms were taken at varying amounts of TEAOH added. .... 70

Figure 2.3.3-6 Cyclic voltammograms of [Htmhd] 0.01 M Htmhd and 0.5 M TEABF<sub>4</sub> in acetonitrile, [Htmhd + TEAOH] 0.01 M Htmhd, 0.01 M TEAOH, and 0.5 M TEABF<sub>4</sub> in acetonitrile, [Blank] 0.5 M TEABF<sub>4</sub> in acetonitrile with a glassy carbon electrode at a scan rate of 100 mV/s. .... 71

Figure 2.3.3-7 Cyclic voltammograms of 0.01 M V(dppd)<sub>3</sub>, 0.5 M TEABF<sub>4</sub> in acetonitrile with a glassy carbon electrode. Multiple voltammograms were taken at varying scan rates. .... 72

Figure 2.3.3-8 Cyclic voltammograms of 0.01 M V(dppd)<sub>3</sub>, 0.5 M TEABF<sub>4</sub> in acetonitrile with a glassy carbon electrode at 100 mV/s. Voltage window -2.9 V to 1.4 V. .... 73

Figure 2.3.3-9 Cyclic voltammograms of [Hdppd] 0.01 M Hdppd and 0.5 M TEABF<sub>4</sub> in acetonitrile, [Hdppd + TEAOH] 0.01 M Hdppd, 0.01 M TEAOH, and 0.5 M TEABF<sub>4</sub> in acetonitrile, [Blank] 0.5 M TEABF<sub>4</sub> in acetonitrile with a glassy carbon electrode at a scan rate of 100 mV/s. .... 74

Figure 2.3.3-10 Cyclic voltammograms of 0.01 M V(dppd)<sub>3</sub>, 0.5 M TEABF<sub>4</sub> in acetonitrile with a glassy carbon electrode at a scan rate of 500 mV/s. Multiple voltammograms were taken at varying amounts of TEAOH added. .... 75

Figure 2.3.3-11 Cyclic voltammograms of 0.01 M V(mpd)<sub>3</sub>, 0.5 M TEABF<sub>4</sub> in acetonitrile with a glassy carbon electrode. Multiple voltammograms were taken at varying scan rates. .... 76

Figure 2.3.3-12 Cyclic voltammograms of 0.01 M V(mpd) <sub>3</sub> , 0.5 M TEABF <sub>4</sub> in acetonitrile with a glassy carbon electrode at a scan rate of 500 mV/s. Multiple voltammograms were taken at varying amounts of TEAOH added. ....	77
Figure 2.3.3-13 Cyclic voltammograms of [Hmpd] 0.01 M Hmpd and 0.5 M TEABF <sub>4</sub> in acetonitrile, [Hmpd + TEAOH] 0.01 M Hmpd, 0.01 M TEAOH, and 0.5 M TEABF <sub>4</sub> in acetonitrile, [Blank] 0.5 M TEABF <sub>4</sub> in acetonitrile with a glassy carbon electrode at a scan rate of 100 mV/s. ....	78
Figure 2.4.2-1 Experimental screening plan for solvent/supports. ....	85
Figure 2.4.3-1 Indication of solubility at 0.1 M for all solvent/solute combinations. ....	86
Figure 2.4.3-2 Conductivity of each 0.1 M supporting electrolyte in solvent combination. ....	87
Figure 2.4.3-3 Densities of binary solutions of vanadium acetylacetonate in acetonitrile as a function of solute concentration. The points represent experimental measurements and the line is a linear fit ( $R^2 = 0.97$ ) forced through the density of pure ACN at room temperature. ....	89
Figure 2.4.3-4 Plot of density vs. support concentration for TEABF <sub>4</sub> in ACN. ....	90
Figure 2.4.3-5 Maximum solubility of each solute/solvent combination. Data labeled (1) are values taken from [90]. ....	90
Figure 2.4.4-1 Cyclic voltammogram of 0.01 M V(acac) <sub>3</sub> and 0.05 M TEABF <sub>4</sub> in DMF or ACN. Scan rate 100 mV/s with glassy carbon working electrode and Ag/Ag <sup>+</sup> reference electrode. ....	93
Figure 2.4.4-2 Cyclic voltammogram of 0.01 M V(acac) <sub>3</sub> and 0.05 M TBABF <sub>4</sub> in DMF or ACN. Scan rate 100 mV/s with glassy carbon working electrode and Ag/Ag <sup>+</sup> reference electrode. ....	93
Figure 2.4.4-3 Cyclic voltammogram of 0.01 M V(acac) <sub>3</sub> and 0.05 M TBAPF <sub>6</sub> in DMF or ACN. Scan rate 100 mV/s with glassy carbon working electrode and Ag/Ag <sup>+</sup> reference electrode. ....	94
Figure 2.4.4-4 Cyclic voltammogram of 0.01 M V(acac) <sub>3</sub> and 0.05 M BmimTFSI in DMF or ACN. Scan rate 100 mV/s with glassy carbon working electrode and Ag/Ag <sup>+</sup> reference electrode. ....	94

Figure 2.4.4-5 Charge/Discharge plot for 0.1 M V(acac)<sub>3</sub> and 0.5 M TEABF<sub>4</sub> in acetonitrile in a 4-electrode 1-D cell with graphite electrodes and Neosepta AHA membrane. 1mA charge current added until 40 % of the theoretical maximum energy has been added, rest for 2 hours, then discharge at 1 mA until 0.5 V. ... 96

Figure 2.4.4-6 Charge/Discharge plot for 0.1 M V(acac)<sub>3</sub> and 0.5 M TEABF<sub>4</sub> in dimethylformamide in a 4-electrode 1-D cell with graphite electrodes and Neosepta AHA membrane. 1mA charge current added until 40 % of the theoretical maximum energy has been added, rest for 2 hours, then discharge at 1 mA until 0.5 V. .... 97

Figure 2.4.5-1 Plot of p-values for the correlation between each solvent property and the V(acac)<sub>3</sub> solubility. .... 101

Figure 2.4.5-2 Regression of V(acac)<sub>3</sub> solubility with solvent molar volume..... 101

Figure 2.4.5-3 Plot of p-values for the correlation between each solvent property and the solution conductivity..... 103

Figure 2.4.5-4 Regression of solution conductivity with Hansen polarity..... 103

Figure 2.4.5-5 Plot of Hansen Polarity Parameter vs. Hansen Hydrogen Bonding Parameter for several classifications of solvents. [N] is Nitromethane and [S] is Dimethylsulfoxide. Taken from [92]. .... 105

Figure 3.1.2-1 Cyclic voltammogram of 0.06 M TEABF<sub>4</sub> and 0.06 M TEACl in acetonitrile. Gold microelectrode working electrode at 100 mV/s. .... 115

Figure 3.1.2-2 Calibration curve for the peak height of the oxidation at ~0.2 V as a function of the concentration of TEACl in a 0.12 M TEA<sup>+</sup> solution (Balance is TEABF<sub>4</sub>). Gold microelectrode working electrode with scan rate 100 mV/s. .... 115

Figure 3.1.2-3 Cyclic voltammogram of [Standard (Red)] 0.0029 M TEACl and 0.1171 M TEABF<sub>4</sub> in acetonitrile, [Neosepta AHA (Blue)] Solution after soaking a Neosepta AHA membrane for 10 hours..... 117

Figure 3.1.2-4 Plot of percentage chloride removed by a single soaking of Neosepta AHA in a 0.4 M solution of TEABF<sub>4</sub> with time..... 117

Figure 3.1.3-1 Picture of impedance cell. .... 119

Figure 3.1.3-2 Impedance plot for Selemion DSV anion exchange membrane zoomed in to the high frequency region..... 120

Figure 3.1.3-3 Impedance plot for Neosepta AHA anion exchange membrane zoomed in to the high frequency region..... 120

Figure 3.1.3-4 Screen capture of the fitting program used to determine the circle fit to the data for Selemion DSV shown in Figure 3.1.3-2. .... 120

Figure 3.2.3-1 Cyclic voltammograms ( $\omega=500$ ) for glassy carbon, gold, and platinum microelectrodes in 0.01M V(III)(acac)<sub>3</sub>, 0.05 M TEABF<sub>4</sub> in ACN. Measurements performed at 23°C..... 128

Figure 3.2.3-2 Cyclic voltammograms ( $\omega=500-1490$ ) for (A) gold, (B) platinum, and (C) glassy carbon microelectrodes in 0.01M V(III)(acac)<sub>3</sub>, 0.05 M TEABF<sub>4</sub> in ACN. Measurements performed at 23 °C. .... 129

Figure 3.2.4-1 LSV for the V(III) / V(IV) redox couple at (A) glassy carbon [squares] (B) gold [triangles] (C) platinum [circles], and (D) all microelectrodes in 0.01 M V(III)(acac)<sub>3</sub> and 0.05 M TEABF<sub>4</sub> in ACN. Scan rate 0.3 mV/s ( $\omega=7.4$ ) on glassy carbon and 1 mV/s ( $\omega=0.25$ ) on gold and platinum; measurements performed at 23 °C; arrow indicates direction of change in potential..... 132

Figure 3.2.4-2 LSV for the V(II) / V(III) redox couple at (A) glassy carbon [squares] (B) gold [triangles] (C) platinum [circles], and (D) all microelectrodes in 0.01 M V(III)(acac)<sub>3</sub> and 0.05 M TEABF<sub>4</sub> in ACN. Scan rate 0.3 mV/s ( $\omega=7.4$ ) on glassy carbon and 1 mV/s ( $\omega=0.25$ ) on gold and platinum; measurements performed at 23 °C; arrow indicates direction of change in potential..... 133

Figure 4.1.2-1 Comparison of cyclic voltammograms with a glassy carbon electrode in deoxygenated (dotted line) and oxygenated (solid line) solutions of 0.01 M V(acac)<sub>3</sub> and 0.05 M TEABF<sub>4</sub> in ACN. Scan rate 100 mV/s; measurements performed at room temperature. Inset: cyclic voltammograms at 200 mV/s of a similar system without active species present. .... 148

Figure 4.1.2-2 Comparison of cyclic voltammograms with a glassy carbon electrode for water-free (dotted line) and hydrated (solid line) solutions of 0.01 M V(acac)<sub>3</sub> and 0.05 M TEABF<sub>4</sub> in ACN. Scan rate 100 mV/s; measurements performed at room temperature. The hydrated experiment contains 4 vol% water. .... 150

Figure 4.1.2-3 Comparison of cyclic voltammograms with a glassy carbon electrode for 0.01 M V(acac)<sub>3</sub> and 0.05 M TEABF<sub>4</sub> in ACN (dotted line), 'aged' 0.01 M V(acac)<sub>3</sub> and 0.05 M TEABF<sub>4</sub> in ACN (black line), and 0.01 M VO(acac)<sub>2</sub>

and 0.05 M TEABF <sub>4</sub> in ACN (grey line). Scan rate 100 mV/s; measurements performed at room temperature.....	152
Figure 4.1.3-1 Coulombic and energy efficiency plot associated with the charge / discharge experiment shown in Figure 4.2.2-5.....	155
Figure 4.1.3-2 Cyclic voltammograms of the positive electrolyte before (thin gray line) and after (thick blue line) performing the charge/discharge experiment presented in Figure 4.2.2-5. Glassy carbon electrode; scan rate 100 mV/s; room temperature. Pure acetonitrile was used to dilute the V(acac) <sub>3</sub> concentration down to 0.0125 M before voltammetry was performed.....	157
Figure 4.1.3-3 Cyclic voltammograms of the negative electrolyte before (thin gray line) and after (thick blue line) performing the charge/discharge experiment presented in Figure 4.2.2-5. Glassy carbon electrode; scan rate 100 mV/s; room temperature. Pure acetonitrile was used to dilute the V(acac) <sub>3</sub> concentration down to 0.0125 M before voltammetry was performed.....	157
Figure 4.1.3-4 Plot of open circuit potential vs. % theoretical SOC for the charge/discharge experiment shown in Figure 4.2.2-5.....	158
Figure 4.1.4-1 Charge/discharge response for the first 7 cycles of 0.1 M V(acac) <sub>3</sub> and 0.5 M TEABF <sub>4</sub> in ACN in a 1-D cell with graphite electrodes and a Neosepta AHA separator. Measurements performed at room temperature in an Ar-atmosphere glove box. ....	159
Figure 4.1.4-2 Coulombic and energy efficiency plot associated with the charge/discharge experiment shown in Figure 4.1.4-1.....	160
Figure 4.1.4-3 Plot of open circuit potential vs. % theoretical SOC for the charge/discharge experiment shown in Figure 4.1.4-1.....	161
Figure 4.1.5-1 Cyclic voltammogram of [blue] 0.01 M V(acac) <sub>3</sub> , 0.05 M TEABF <sub>4</sub> in acetonitrile and [red] 0.01 M VO(acac) <sub>2</sub> , 0.05 M TEABF <sub>4</sub> in acetonitrile. Glassy carbon working electrode; 100 mV/s scan rate; Ag/Ag <sup>+</sup> reference electrode....	162
Figure 4.2.1-1 Plot of active species concentration remaining in solution after waiting 18 days for precipitation to occur as a function of solution temperature. Numbers on the right side are the fraction of V(V) in a V(IV) solution. Figure taken from [121].....	166
Figure 4.2.2-1 Solubility plot for V(acac) <sub>3</sub> and TEABF <sub>4</sub> in ACN. [Blue dots] Miscible solutions [Red line] Predicted solubility limit. ....	168

Figure 4.2.2-2 Solubility plot for $\text{Cr}(\text{acac})_3$ and $\text{TEABF}_4$ in ACN. [Blue dots] Miscible solutions [Red line] Predicted solubility limit. ....	169
Figure 4.2.2-3 Charge/discharge response for the first 10 cycles of 0.05 M $\text{V}(\text{acac})_3$ and 0.5 M $\text{TEABF}_4$ in ACN in an 1-D cell with graphite electrodes and a Neosepta AHA separator. Measurements performed at room temperature in a $\text{N}_2$ -atmosphere glove box. ....	170
Figure 4.2.2-4 Charge/discharge response for the first 10 cycles of 0.075 M $\text{V}(\text{acac})_3$ and 0.5 M $\text{TEABF}_4$ in ACN in an 1-D cell with graphite electrodes and a Neosepta AHA separator. Measurements performed at room temperature in a $\text{N}_2$ -atmosphere glove box. ....	171
Figure 4.2.2-5 Charge/discharge response for the first 10 cycles of 0.1 M $\text{V}(\text{acac})_3$ and 0.5 M $\text{TEABF}_4$ in ACN in an 1-D cell with graphite electrodes and a Neosepta AHA separator. Measurements performed at room temperature in a $\text{N}_2$ -atmosphere glove box. ....	171
Figure 4.2.2-6 Charge/discharge response for the first 10 cycles of 0.25 M $\text{V}(\text{acac})_3$ and 0.5 M $\text{TEABF}_4$ in ACN in an 1-D cell with graphite electrodes and a Neosepta AHA separator. Measurements performed at room temperature in a $\text{N}_2$ -atmosphere glove box. ....	173
Figure 4.2.2-7 Charge/discharge response for the first 10 cycles of 0.4 M $\text{V}(\text{acac})_3$ and 0.5 M $\text{TEABF}_4$ in ACN in an 1-D cell with graphite electrodes and a Neosepta AHA separator. Measurements performed at room temperature in a $\text{N}_2$ -atmosphere glove box. ....	173
Figure 4.2.2-8 Plot of efficiency as a function of active species concentration based on the C/D shown in Figure 4.2.2-3 through Figure 4.2.2-7. ....	174
Figure 4.2.3-1 Plot of energy density as a function of active-species concentration based on the C/D shown in Figure 4.2.2-3 through Figure 4.2.2-7. ....	176
Figure 4.2.3-2 Plot of active species concentration as a function of support concentration, based on the C/D shown in Figure 4.2.2-3 through Figure 4.2.2-7, showing the regions of precipitation. ....	176
Figure 4.3.2-1 Charge/discharge response for the first 9 cycles of 0.1 M $\text{V}(\text{acac})_3$ and 0.5 M $\text{TEABF}_4$ in ACN in an 1-D cell with graphite electrodes and a Neosepta AHA separator. Measurements performed at room temperature in an Ar-atmosphere glove box. ....	178

Figure 4.3.2-2 Plot of capacity vs. cycle number associated with Figure 4.3.2-1. .....	179
Figure 4.3.2-3 Charge/discharge response for a 0.1 M $V(acac)_3$ and 0.5 M TEABF <sub>4</sub> in ACN 1-D cell with graphite electrodes and a Neosepta AHA separator. Measurements performed at room temperature in an Ar-atmosphere glove box. .....	180
Figure 4.3.2-4 Plot of discharge overpotential as a function of cycle number for the data shown in Figure 4.3.2-3. ....	182
Figure 4.3.2-5 Charge/discharge response for a 0.1 M $V(acac)_3$ and 0.5 M TEABF <sub>4</sub> in DMF 1-D cell with graphite electrodes and a Neosepta AHA separator. Measurements performed at room temperature in an Ar-atmosphere glove box. ....	185
Figure 4.3.2-6 Plot of discharge overpotential as a function of cycle number for the data shown in Figure 4.3.2-5. ....	186
Figure 4.3.3-1 SEM of the as-received electrode. ....	189
Figure 4.3.3-2 SEM images of the negative electrode in 0.1 M $V(acac)_3$ and 0.5 M TEABF <sub>4</sub> in solvent. [Top] After cycling for 300 hours with graphite electrodes, [Bottom] After soaking for 300 hours, [Left] Solvent: acetonitrile, [Right] Solvent: dimethylformamide. ....	190
Figure 4.3.3-3 Zoom in of the SEM in the top right of Figure 4.3.3-2 (an electrode cycled in DMF electrolyte). ....	192
Figure 4.3.3-4 SEM images of the positive electrode in 0.1 M $V(acac)_3$ and 0.5 M TEABF <sub>4</sub> in solvent. [Top] After cycling for 300 hours with graphite electrodes, [Bottom] After soaking for 300 hours, [Left] Solvent: acetonitrile, [Right] Solvent: dimethylformamide. ....	193
Figure 4.3.3-5 Zoom in of the SEM in the top of Figure 4.3.3-4. [Left] Solvent: ACN, [Right] Solvent: DMF. ....	193
Figure 4.3.3-6 SEM of the as-received Neosepta AHA membrane. ....	194
Figure 4.3.3-7 SEM images of the membrane after soaking for 300 hours in 0.1 M $V(acac)_3$ and 0.5 M TEABF <sub>4</sub> in solvent. [Left] Solvent: ACN, [Right] Solvent: DMF. ....	195

Figure 4.3.3-8 SEM images of the membrane after cycling for 300 hours in 0.1 M  $V(acac)_3$  and 0.5 M  $TEABF_4$  in ACN..... 197

Figure 4.3.3-9 SEM images of the membrane after cycling for 300 hours in 0.1 M  $V(acac)_3$  and 0.5 M  $TEABF_4$  in DMF..... 197



## List of Tables

Table 2.2.5-1 Summary of all active-metal performance characteristics. ....	59
Table 2.4.2-1 List of supporting electrolytes examined and their chemical structure. ....	82
Table 2.4.2-2 List of solvents examined and their chemical structure. ....	83
Table 2.4.5-1 Table of solvent properties for ACN, DMF, THF, DMC, and HEX. The asterisk denotes that the value is calculated by dividing the molar mass by the solvent density found in [95]. ....	99
Table 2.4.5-2 Table of aprotic solvents with the corresponding Hansen Polarity Parameter and Solvent molar volume. ....	106
Table 3.1.3-1 Table of results detailing the resistance and resistivity of several commercial anion exchange membranes. ....	121
Table 3.2.4-1 Symmetry factor and exchange-current density for the V(II) / V(III) redox couple at glassy carbon, gold, and platinum electrodes in 0.01M V(III)(acac) <sub>3</sub> , 0.05M TEABF <sub>4</sub> in ACN. Measurements performed at 23°C.....	142

## List of Abbreviations

acac <sup>-</sup>	Acetylacetonate
ACN	Acetonitrile
BF <sub>4</sub> <sup>-</sup>	Tetrafluoroborate
bmim <sup>+</sup>	(1-butyl,3-methyl)imidazoleum
bpy	2,2'-bipyridine
ClO <sub>4</sub> <sup>-</sup>	Perchlorate
Cr(acac) <sub>3</sub>	Chromium acetylacetonate
C/D	Charge/discharge
CV	Cyclic voltammetry
DMC	Dimethylcarbonate
DMF	Dimethylformamide
DMSO	Dimethylsulfoxide
dpm <sup>-</sup>	Dipivaloymethane
ESR	Electrical series resistance
EPDM	Ethylene propylene diene monomer
Fe(acac) <sub>3</sub>	Iron acetylacetonate
Hacac	Acetylacetone
Hdppd	1,5-diphenyl-2,4-pentanedione
HEX	Hexane
hfacac <sup>-</sup>	Hexafluoroacetylacetonate
Hmpd	3-methyl-2,4-pentanedione
Htmhd	2,2,6,6-tetramethyl-3,5-heptanedione
ICP	Inductively coupled plasma
LSV	Linear-sweep voltammetry
Mn(acac) <sub>3</sub>	Manganese acetylacetonate
Na <sup>+</sup>	Sodium
PF <sub>6</sub> <sup>-</sup>	Hexafluorophosphate
PTFE	Polytetrafluoroethylene
RFB	Redox flow battery
Rh(acac) <sub>3</sub>	Rhodium acetylacetonate
SEM	Scanning electron microscopy
SOC	State of charge
TBA <sup>+</sup>	Tetrabutylammonium

TEA <sup>+</sup>	Tetraethylammonium
TEABF <sub>4</sub>	Tetraethylammonium tetrafluoroborate
TEACl	Tetraethylammonium chloride
TEAOH	Tetraethylammonium hydroxide
TFSI	Bis(trifluoromethanesulfonyl)imide
THF	Tetrahydrofuran
triflate	Trifluoromethanesulfonate
V(acac) <sub>3</sub>	Vanadium acetylacetonate
V(dppd) <sub>3</sub>	Vanadium tris(1,5-diphenyl-2,4-pentanedionate)
V(mpd) <sub>3</sub>	Vanadium tris(3-methyl-2,4-pentanedionate)
V(tmhd) <sub>3</sub>	Vanadium tris(2,2,6,6-tetramethyl-3,5-heptanedionate)
VO(acac) <sub>2</sub>	Vanadyl acetylacetonate

## Abstract

Redox flow batteries (RFBs) are being developed for large-scale energy storage and load-leveling systems for solar or wind power. Aqueous chemistries are used for current commercial RFBs, in which energy and power density are limited by the stability range of water. Non-aqueous solvents offer stability windows up to four times greater than those for aqueous solvents. The goal of my research was to examine all components of a non-aqueous-vanadium-single-metal RFB and determine their effects on key performance characteristics.

First, relationships between the structure, composition, and function of acetylacetonate metal complex based electrolytes were examined in an effort to determine strategies for their further development and provide initial guidelines for their use. Vanadium, chromium, and manganese acetylacetonate complexes had maximum energy densities of 18, 18, and 9 Wh/L respectively with reversible electrochemistry for V and Mn; therefore vanadium was selected for more extensive testing. Substitution of the ligands demonstrated the ability to change solubility by two orders of magnitude. Results from examination of a variety of solvent/supporting electrolyte combinations indicated that solvents with low solvent molar volumes and high polarities possessed desirable properties (acetonitrile is optimal).

Effects of the cell components (membrane resistance and electrode kinetics) on the cell performance were also examined. The lowest resistance

membranes, Selemion DSV or Neosepta AHA, were chosen to reduce energy losses. The kinetics of the desired reaction on gold, platinum, and glassy carbon electrodes showed minimal kinetic limitations suggesting outer-shell-electron-transfer reactions occur.

Finally, the stability was examined. When exposed to water or oxygen, the V(II)/V(III) redox couple becomes irreversible and vanadyl acetylacetonate is formed. Even in the absence of oxygen or water impurities, the capacity of the RFB fades dramatically. This fade could be a consequence of precipitation stemming from a reaction between the charged active species and the acetonitrile solvent. Overpotentials on the electrode and membrane increased with cycling – likely due to precipitation and mechanical degradation and could contribute to capacity fade (based on results from scanning electron microscopy).

Overall I found that the non-aqueous all-vanadium RFB could be a promising candidate for future batteries after stability of the cell components is addressed.

## Chapter 1 Introduction

### 1.1 Introduction to Redox Flow Batteries

The worldwide average power demand in 2009 was 16 TW [1]. According to Tester *et al.*, solar and wind power, which have maximum possible supply capacities of 86,000 TW and 870 TW, respectively, could satisfy this demand [2]. Lewis suggests that practical numbers for solar and wind are 600 TW and 2 TW, respectively, which are still sufficient to meet a significant portion of the worldwide energy demand [3]. Since wind and solar power create energy stochastically, they also require storage systems, so that excess energy can be stored to deliver energy during wind and solar deficient times. The development of storage technologies is one of the key challenges facing the large-scale implementation of solar and wind power.

RFBs offer robust, reversible, high-capacity energy storage, and promise the load-leveling capability necessary to facilitate the grid penetration of stochastic renewable energy sources. RFBs can be used in any location, regardless of terrain. Aqueous vanadium RFBs achieve coulombic efficiencies of up to 75 %, and are currently being used in wind farms worldwide, including those at Sorne Hill in Ireland and Huxley Hill in Tasmania [4]. Recently, several installations have occurred in the USA, including the largest installation (currently) of 8MWh at the Painesville Municipal Electric Plant in Ohio [5]. Although their primary commercial use is for load leveling [6-8], there is some

interest in these systems for uninterruptible power supplies, storage devices for future electric car charging stations in remote areas, and even for electric vehicles themselves.

RFBs differ from most other rechargeable batteries because the energy is stored in liquid electrolytes, rather than in solid electrodes. For example, in a lithium-ion cell, lithium ions from the liquid electrolyte are intercalated into the electrodes; the capacity of the lithium-ion battery is dictated by both the lithium content in the electrolyte and electrode size. The power of a lithium-ion battery is increased by increasing the electrode size, thus coupling the power and energy. The RFB concept, in contrast, decouples power capacity from energy capacity. The electrodes in the reactors are theoretically inert, providing sources or sinks for electrons, and the number of cell reactors stacked together and the electrode size in each cell determines the overall power; the total mass of electrolytic solution flowed through the reactor stack determines the energy-storage capacity [4]. This decoupling of power and energy makes RFBs scalable and flexible to meet customer needs. Since energy densities in liquid electrolytes are relatively low, RFBs are most commonly used for stationary applications – particularly, large power plants.

Another advantage of RFBs is that electrochemical reactions at the liquid/solid interfaces tend to be fast [4]. While the electrodes of a Li-ion battery show mechanical fatigue over time due to the insertion reactions, the electrodes in a RFB should not. Consequently, the lifetimes of RFBs are much longer than those of other battery systems [4].

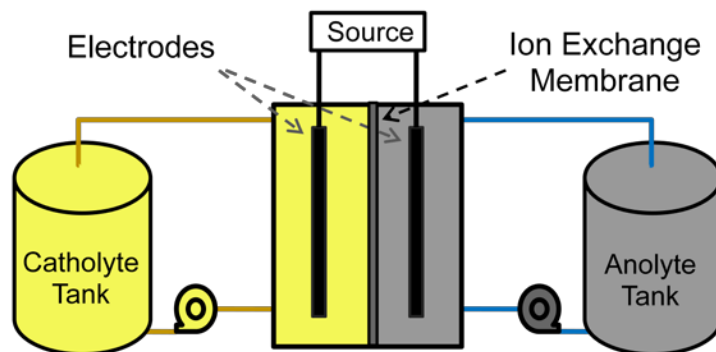


Figure 1.1.1-1 General schematic of a redox flow battery

A RFB consists principally of the following components: a main cell, electrolyte tanks, and a flow system, depicted schematically in Figure 1.1.1-1. An electrical power source such as solar cells is used to charge the RFB. During operation of the battery, the electrolyte is continuously pumped from the storage tanks through two separate chambers in the main cell. The storage tanks are usually much larger than the main reactor in which redox reactions occur. The cell comprises two current collectors, an anode, a cathode, and an ion-exchange membrane that separates the anode chamber from the cathode chamber.

If a voltage difference is imposed between the electrodes, electrons flow through the electrode/solution interfaces, driving redox reactions involving active materials dissolved in the liquids. To enhance their area, the electrodes tend to be made of high-surface-area porous materials, most commonly carbon [4]. The membrane that separates the positive and negative electrolytes is chosen to keep the solutions electronically isolated, while allowing interchange of ions between the chambers (ion-selective membranes tend to be used to minimize self-discharge reactions in the cell interior [9]). As electrons flow through the electrodes and charge is transferred across the electrode/liquid interfaces, ions



pass through the membrane to maintain overall charge neutrality. The separator can be a main source of transport limitations in an RFB (high resistance to ion flow), and can significantly affect the power and energy efficiency of the battery [10].

The liquid electrolytes in a RFB have three principal components: redox active species, supporting electrolyte, and solvent. The active species oxidizes or reduces to convert electricity to chemical energy; its composition and structure dictates characteristics of the battery such as cell potential, reversibility, and kinetics. The supporting electrolyte is designed to be a spectator in the reaction and is present only to provide conductivity to the solution. The solvent dictates the solubilities of the active species and supporting electrolyte, which affect energy and power density; it also determines most of the physical properties of the solution. In combination, the solvent and supporting electrolyte specify the stability window of the solution as a whole, which can place limits on the possible active-species reactions that can be used to store energy.

## 1.2 Aqueous Redox Flow Battery Systems

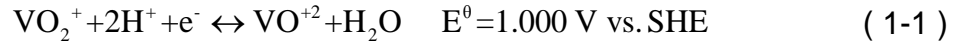
Literature on RFBs dates back to 1974, when Thaller *et al.* at NASA tested many different active species [11]. One notable chemistry was the zinc/bromine RFB system, which plates zinc metal on one electrode and converts bromide ions to bromine or tribromide on the other [12, 13]. The greatest challenge facing development of this system is crossover through the membrane. The bromine gas formed at the bromine electrode can cross the membrane fairly easily, where it reacts with the zinc electrode directly, causing a parasitic loss of energy. To

alleviate crossover, the bromine liquid electrolyte contained organic complexing agents to retain the bromine and limit crossover while charging. The resulting dense oil phase mixes with the aqueous electrolyte on discharge.

A similar chemistry to Zn/Br was formulated based on a bromine/polysulfide RFB [14, 15] (replacing the zinc electrode with sulfur). The active species in this system are sodium bromide on the positive side and sodium polysulfide on the negative. During charging the bromide ions oxidize, then form a tribromide complex, while the polysulfide ion is reduced to sulfide. This results in an open-circuit potential of approximately 1.5 V depending on the concentration of the active species. This cell chemistry faces several challenges: a large amount of cross-contamination through the membrane, deposition of sulfur species in the membrane, and formation of H<sub>2</sub>S and Br<sub>2</sub> gas. Furthermore, this chemistry retains all of the most significant problems of its predecessor.

All of these early RFBs used multiple redox-active species in the liquid electrolytes, a configuration referred to as a “dual-active-species”. Examples of dual-active-species RFB chemistries include iron/chromium [16], iron/titanium [17], as well as the previously mentioned sodium-polysulfide/bromine [14, 15, 18], and commercial zinc/bromine [12, 19] hybrid systems. The presence of distinct active species is significant because all RFBs are susceptible to active-species crossover. Dual-active-species RFBs often require periodic electrolyte reactivation after long-term operation [10, 20, 21], because they can degrade irreversibly when constituents of the anolyte and catholyte mix or reach the electrode surfaces.

In 1985, the first single-active-species RFB, based on vanadium, was suggested by Pelligri and Spaziante [22], and was soon realized in practice by Skyllas-Kazacos *et al.* [23]. The aqueous all-vanadium chemistry, patented in 1986, is currently the most commonly studied RFB system [23]. In sulfuric acid at pH near zero, the all-vanadium RFB half-reactions are [24-28]



Thus the overall cell reaction is



It is important to note that the support acid in an all-vanadium RFB provides protons for the overall cell reaction, making the equilibrium cell potential pH-dependent. At the negative electrode, V(II) oxidizes on the electrode surface, forming V(III) and freeing an electron during discharge. The electron traverses the external circuit to the cathode and, to maintain charge neutrality, hydrogen ions pass through the membrane from the anode chamber to the cathode chamber. At the positive electrode, V(V) is reduced to V(IV), consuming two hydrogen ions and an electron while producing water. During charging, energetic electrons are supplied by an external source, and the reactions at the positive and negative electrodes reverse.

The aqueous vanadium RFB can achieve coulombic efficiencies of 95 %, meaning that most of the current input to the battery can be removed [23]. Skyllas-Kazacos *et al.* suggest that the coulombic efficiency was less than 100 % primarily because of crossover through the membrane. However, a second

potential reason for reduced efficiency could be water electrolysis, which occurs near the potential for V(II)/V(III) redox couple. Overall energy efficiencies of 80-85 %, calculated from the ratio of energy input to the energy output, were achieved [29].

Much research has focused on modifications to the original all-vanadium RFB. Many recent adjustments of the cell chemistry replace the V(IV) / V(V) couple, because it is not stable in the presence of many popular membranes. Vanadium/bromide was tested by Skyllas-Kazacos *et al.*[30] but resulted in lower cell potential, current density, and efficiency than the all-vanadium chemistry. Xue *et al.* [31] reported that a vanadium/manganese system (using manganese on the positive electrode) had an efficiency of 63 % – probably due to crossover through the membrane. Several researchers reported a vanadium/cerium [32-34] flow cell using a cylindrical geometry. This system was able to reach 90 % coulombic efficiency when using a porous Vycor frit instead of an expensive proton exchange membrane.

State-of-the-art RFB systems use active-species concentrations up to 3 M [35]. These RFB systems reach 75-85 % coulombic efficiencies, 60-70 % energy efficiencies, and near 1.5 V discharge potentials in an H-cell configuration [36, 37]. Complex reactor designs have been successfully used to increase the coulombic efficiencies to up to 97 % with 86 % energy efficiency [29] using microporous [10] or ion-exchange membrane [38] separators.

There are several limitations associated with aqueous RFB systems: membrane crossover, membrane cost/stability, electrolysis of water, and low energy density.

To mitigate crossover, membranes with small pore sizes and/or functionalization to enhance ion selectivity are used [9]. As the pore size decreases, the resistance of the membrane will increase, which results in an energy loss within the battery system. Therefore, the selected membrane must balance resistance of the membrane with crossover – and the balance depends on the electrolyte used. For example, the zinc/bromine system discussed previously requires the use of a flocculent to stop crossover [12, 13], or a constant separation process; the all-vanadium system begins with the same complexes in both electrolytes and thus is crossover resistant.

Many recent reports focus on membrane stability because the V(V) species oxidizes many commercial membranes [9]. Most early research on all-vanadium RFBs involved Nafion membranes (sulfonic-acid ionomer membranes with perfluorinated backbones), which have excellent selectivity and low ionic resistance. However, to cut costs, a host of commercially available membranes were examined. It was found that Nafion and the “New Selemion anion exchange membrane” could provide sufficient stability. Both membranes have similar cost [9]. Membranes based on crosslinked, sulfonated polyethylene (called “Daramic”) separator materials have been produced [39-41]. Researchers have also examined a membrane-less RFB cell [42].

A key issue with aqueous RFBs is their relatively narrow stability window (1.23 V, not accounting for the overpotential associated with water-splitting), which is limited by the electrolysis of water. This issue can be seen when examining the cyclic voltammetry (CV) for the all-vanadium system electrolyte, shown in Figure 1.2.1-1. At -0.5 V vs. SHE, a peak associated with the reduction of V(III) to V(II) is observed; at the same time, formation of hydrogen gas occurs, as seen by the dramatic increase in reduction current density (peaks identified by Sum *et al.* [24, 25]). Thus it is difficult to achieve long term cycling of aqueous all-vanadium RFBs without the loss of some water to hydrogen evolution.

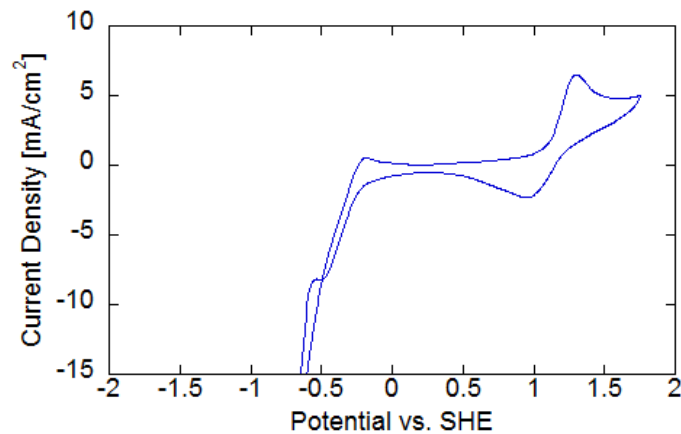
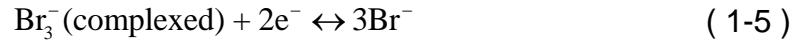


Figure 1.2.1-1 Cyclic voltammogram with a glassy carbon disk electrode in (aqueous) 0.01 M  $\text{VOSO}_4$  and 2 M  $\text{H}_2\text{SO}_4$  in ultrapure  $\text{H}_2\text{O}$ . Scan rate 10 mV/s; measurements performed at room temperature.

Another limitation of aqueous RFBs is the energy density. The energy density generally scales with the number of electrons transferred ( $n$ ), solution concentration ( $c_{\text{active}}$ ), and potential window ( $V_{\text{Cell}}$ ), as

$$\hat{E} \propto \frac{1}{2} n F V_{\text{Cell}} c_{\text{active}} \quad (1-4)$$

The recent advances by Skyllas-Kazacos et al. have pushed aqueous RFB systems to the performance limits that are thermodynamically possible in the presence of water. Their latest battery chemistry uses vanadium bromide [30] active species to achieve a two-electron transfer reaction in one electrolyte, which follows the reaction scheme



This system was cycled with 3-4 M vanadium bromide and 8-10 M hydrogen bromide [43]. An energy density of 50 Wh/kg was achieved [44]. Since this system already uses multiple electrons at high concentration, increasing cell potential is the last possible strategy by which energy density can be increased. Thus the presence of water creates a hard ceiling on the maximum energy density possible in existing RFB systems.

### 1.3 Non-aqueous Systems

Non-aqueous systems can support cell reactions with potentials up to 5 V, depending on the solvent used [45] – a factor of four greater than the thermodynamic potential window allowed by water. Since energy density scales linearly with cell potential, a move to non-aqueous solvents is an attractive next step for transformational RFB research. Water is not only limiting in terms of its potential window but also the temperature range within which it is liquid.

Changing the solvent could enable the use of RFBs in extreme climates where they currently are not viable. For example, acetonitrile, an attractive non-

aqueous solvent, is a liquid at temperatures between  $-45$  and  $82$  °C and is suitable for colder climates, while dimethylformamide is a liquid between  $-61$  and  $153$  °C. Non-aqueous solvents allow the use of many high-energy RFB reactions and thus will be the focus of this dissertation. There are several reports of non-aqueous RFBs using chemistries based on ruthenium, uranium, chromium, manganese, and vanadium [46-51].

Matsuda *et al.* reported on ruthenium complexes (ruthenium acetylacetonate and tris(2,2'-bipyridine)ruthenium (II) tetrafluoroborate) in non-aqueous electrolytes for RFB applications [46]. They used tetraethylammonium tetrafluoroborate ( $\text{TEABF}_4$ ) as the supporting electrolyte and acetonitrile ( $\text{CH}_3\text{CN}$ , also abbreviated as ACN) as the solvent. CV experiments showed a cell voltage of  $2.6$  V for the system. The conductivity was optimized, and charge/discharge experiments were performed to determine efficiency. Matsuda *et al.* observed an optimum efficiency as a function of active-species concentration [46]. This optimum occurred in the range of  $0.02$ - $0.05$  M, tris(2,2'-bipyridine)ruthenium (II) tetrafluoroborate ( $\text{Ru}(\text{bpy})_3$ ) while very low efficiencies were observed for concentrations greater than  $0.1$  M or less than  $0.01$  M. Crossover of active species was expected to be the cause for the low efficiencies at high concentrations due to the increased diffusion driving force.

A paper published in 2007 by Chakrabarti *et al.* reported charge/discharge curves from an investigation of the feasibility for RFBs of ruthenium and iron complexes (ruthenium acetylacetonate, tris(2,2'-bipyridine)ruthenium (II) tetrafluoroborate, tris(2,2'-bipyridine)iron (II) perchlorate, and rubrene) in ACN



with TEABF<sub>4</sub> support [52]. Results from these non-aqueous systems were compared to those for aqueous all-vanadium system. CV experiments were used to determine the equilibrium cell potential for ruthenium acetylacetonate (acac) and tris(2,2'-bipyridine) iron (II) perchlorate. Open-circuit voltages of 1.77 V and 2.41 V were measured for the ruthenium and iron complexes, respectively. Charge/discharge experiments on the ruthenium system revealed the behavior shown in Figure 1.3.1-1. Chakrabarti *et al.* attributed the unexpected increase in potential at 1000 minutes to a side reaction and stopped charging at 12% of theoretical capacity. The discharge voltage corresponding to this charge cycle was low as well (1.3 V). This result likely owes to contamination since Matsuda *et al.* did not notice this behavior in a similar system.

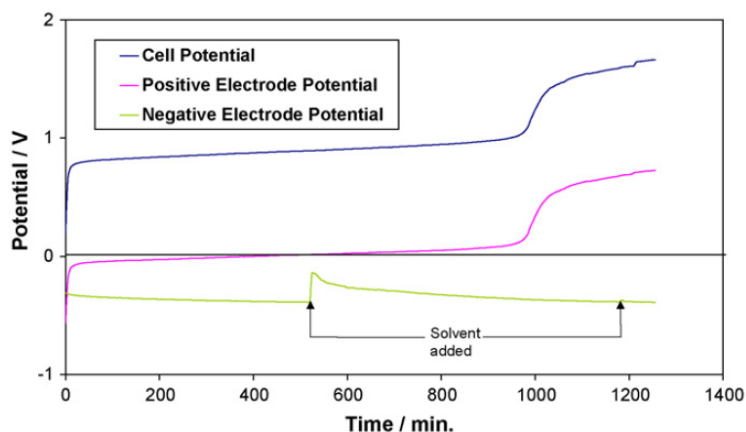


Figure 1.3.1-1 Charging profile for 0.1 M ruthenium acetylacetonate and 1 M TEABF<sub>4</sub> in acetonitrile at a current of 1 mA. (Reprinted from Chakrabarti *et al.* [52])

Chakrabarti *et al.* also recently reported the use of a ruthenium active species (ruthenium acetylacetonate), but within a novel cell design [53]. These experiments were performed using a membrane-less flow cell based on two

countercurrent laminar flow streams, with the same electrolyte on each side of the battery. In order to keep the flow laminar, very low flow rates are used to reduce the propensity for crossover, however, despite the control of the flow, the voltage efficiency was 55 %. To test the feasibility of the flow-cell design, Chakrabarti *et al.* also reported the performance of several other RFB chemistries in the laminar flow-cell configurations. The aqueous all-vanadium system had the highest energy efficiency, at 13.4 %, using 0.02 M vanadium solutions.

Yamamura *et al.* reported work on a uranium RFB in 2002 as a creative way to utilize depleted uranium [48]. The reactions involved were stated to be:



and



The work examined nine uranium  $\beta$ -diketonates in four polar, aprotic solvents (ACN, propylene carbonate, dimethylsulfoxide, and dimethylformamide) using solubility measurements and CV. They observed the highest solubilities using hexafluoroacetylacetonate ligands – greater than 0.8 M in all solvents tested, except propylene carbonate. They observed that uranium (IV) complexes with hydrophilic ligands were more soluble in solvents with smaller donor numbers. Perhaps more importantly, they succeeded in changing the solubility by three orders of magnitude by changing the structure of the ligand in the metal complex. Unfortunately, the electrochemistry resulted in cell potentials of only 1.0 to 1.2 V and significant amounts of ligand shedding (with corresponding irreversible loss of active material) occurred with cycling.

There is substantial industrial interest in RFBs. For example, researchers at Samsung are investigating non-aqueous systems. Mun *et al.* reported the use of tris(2,2'-bipyridine)nickel(II) tetrafluoroborate ( $\text{Ni}(\text{Bpy})_3(\text{BF}_4)_2$ ) and tris(2,2'-bipyridine)iron(II) tetrafluoroborate ( $\text{Fe}(\text{Bpy})_3(\text{BF}_4)_2$ ) in propylene carbonate electrolyte [54]. With these two active species, the nickel was reduced from Ni(II) to Ni(0) and the iron was oxidized from Fe(II) to Fe(III). The overall cell potential for this reaction is 2.2 V. This chemistry exploits multi-electron transfer, as well as the wider stability windows expected of non-aqueous solvents. Charge/discharge curves indicated 90 % coulombic efficiency and 82 % energy efficiency in a flow cell. However, the capacity fades by 37 % over the first five cycles, a fact that the authors attribute to membrane crossover and polarization of the cell.

There are several limitations associated with non-aqueous RFB technologies. Historically these RFBs have been found to have low internal conductivity, resulting in high overpotentials; low solubility limits of active species and supporting electrolytes, resulting in low energy densities; and additional safety concerns relative to aqueous systems. It is also worth noting that the extra cost incurred by using a non-aqueous solvent instead of water must be recuperated in other components or the solvent recycled. The cost of  $\text{VOSO}_4$  used in the aqueous systems is higher than the cost of  $\text{V}(\text{acac})_3$  used in non-aqueous systems and offsets the cost of the solvent. The bases for these observations will be elaborated upon in the remainder of this section.

RFB energy efficiency is impacted by kinetic, ohmic, and diffusional overpotentials in the cell interior. Ohmic overpotentials scale linearly with current; they arise from any series impedance, either electronic or ionic, in the electrodes, solutions, or membrane. The conductivity of the solution dictates the resistance of the solution and follows the formula

$$\text{Resistance} = \frac{\text{length}}{\text{conductivity} * \text{area}_{\text{cross-section}}} \quad (1-9)$$

Thus as the conductivity increases, the resistance decreases, which, in turn, improves the energy efficiency by reducing the power dissipated to heat as the RFB is cycled. The conductivity of the non-aqueous electrolytes reported in the literature depends on the solvent used. For example a 0.1 M TEABF<sub>4</sub> solution in ACN has a conductivity of 11.2 mS/cm, while the conductivity of the TEABF<sub>4</sub> in dimethylcarbonate is 2.5x10<sup>-5</sup> mS/cm. The aqueous all-vanadium system uses a sulfuric acid supporting electrolyte, which has a conductivity of 48.5 mS/cm at 0.1 M, but at concentrations near 2 M (where the system operates) it is around 700 mS/cm. This is not representative of all aqueous solutions, however. Using potassium chloride instead of sulfuric acid would yield a conductivity of 12.9 mS/cm at 0.1 M. It is possible for a properly selected non-aqueous electrolyte to have a higher conductivity than an aqueous one at comparable concentration.

The solubility limits of the active species and supporting electrolyte are critical to the achievement of serviceable energy densities in an RFB. Aqueous RFBs can have active-species concentrations of 3-4 M, although the all-vanadium RFB is typically operated at or below 2 M. Given that water (the solvent) has a maximum concentration of 55 M, 2 M is comparably small. Non-

aqueous systems have lower pure-solvent concentrations, which affect the maximum support concentrations they can sustain. For example, pure ACN has a concentration of 19 M at room temperature, dimethylcarbonate (a common lithium-ion-battery electrolyte) is 11.9 M, and hexane is 7.6 M. On this basis the maximum active-species concentrations are expected to be lower, a challenge that must be overcome by selecting reactions with very high cell potentials and/or multiple electrons transferred.

Finally the safety of a non-aqueous RFB is a concern – as it always is when water is replaced with an organic solvent. Most non-aqueous solvents have a 1 or 2 health hazard rating, indicating that they are ‘slightly to moderately hazardous’ (the latter requiring the use of a breathing apparatus). The biggest concern is the increase in solvent flammability – often, viable non-aqueous solvents have a flammability hazard rating of 3 (ignites at normal temperatures). Mitigation of these hazards involves much more care during assembly than an aqueous RFB, as well as more robust / costly packaging. Procedures for cell fabrication can be benchmarked based on lithium ion batteries and will not prohibit non-aqueous RFB commercialization.

Despite these limitations, non-aqueous RFBs are promising because progress on the aqueous system is stifled by limits imposed by water. Non-aqueous RFB performance has been plagued by low conductivity, low solubility, and safety concerns, all of which are motivations for ongoing research. My research aims to elucidate a path toward resolving these issues, along with many others. This dissertation will examine each of the components of a non-aqueous

single-metal RFB cell, discuss how these components affect RFB performance, and suggest how they can be altered to improve the energy density of the device. First I will examine the liquid electrolyte, starting with the active-species metal center and ligand structure; then I will examine supporting electrolytes and solvents. Next performance associated with the individual cell components (membrane and electrode) will be discussed. Finally, the performance of the battery in charge/discharge experiments will be examined, with a focus on the evolution of overpotentials and degradation during long-term non-aqueous RFB cycling.

## Chapter 2 Effects of the Liquid Electrolyte

### 2.1 Experimental Techniques

#### 2.1.1 Cyclic Voltammetry

CV is one of the principal experimental techniques used in my research. It is commonly used as a screening tool to learn about the electrochemical response of a system within a given potential range. A potentiostat is used to apply a potential, which is varied at a constant rate between two user-specified potential limits while the current response is measured. In my research the potentiostat used was an Autolab PGSTAT302N Potentiostat/Galvanostat (Ecochemie, Netherlands). When an oxidation or reduction reaction occurs, the balance between kinetic current and mass-transfer limitations causes a peak to appear in the cyclic voltammogram. By our chosen convention for the sign of voltage, peaks that appear when the voltage is sweeping upward correspond to oxidation reactions; when the voltage is sweeping downward, peaks correspond to reductions [45].

CV experiments are three-electrode tests involving a working electrode, a counter electrode, and a reference electrode. This configuration differs from that of a battery cell, which typically only has two electrodes (working and counter). The reference electrode is typically connected to a large series resistance; while the potentiostat drives current flow from the working to the counter electrode, it

only allows a negligible amount of charge to pass through the reference electrode, which establishes a baseline for voltage.

There are several common practices when performing a CV experiment to produce reproducible results [55]. The counter electrode should be much larger (at least ten times larger) than the working electrode surface area. This increases the current at the counter electrode relative to the reference electrode, reducing measurement error due to electrical series resistance (ESR). When possible, the concentration of the conductivity-enhancing supporting electrolyte used should be five to ten times larger than the concentration of the species performing the electrochemistry to reduce mass-transfer limitations arising from migration. Finally, the counter electrode should be far enough away from the other electrodes that the reaction products produced at the working electrode do not reach it by diffusion within the time of the experiment; reaction products produced at the counter should also not be allowed to reach the working electrode. The reference electrode should be as close as possible to the working electrode, however, to minimize ESR from the solution that separates the working from the reference. Therefore, a Luggin capillary is typically included in a CV cell to sample the solution directly adjacent to the electrode. Last, the counter electrode should be placed far away from both working and reference electrodes, to keep the products of reactions occurring on its surface from reaching the working electrode and changing its chemical environment.

CV results can be used to obtain: half-reaction potentials, effective reaction rates, information about reversibility, and estimates of active-species



diffusivity [45]. The most precise measurements yielded by CV are reaction potentials, which can be found by locating the midpoint between the maximum peak potentials for oxidation and reduction.



Figure 2.1.1-1 Cyclic voltammetry cell

Figure 2.1.1-1 shows the glass cell used for the CV experiments presented here based on the common practices illustrated above. This cell was based on a design by Alice Sleightholme and fabricated by the glassblower at the University of Michigan. The center compartment contains the working electrode and has inlet/outlet ports that allow a blanket of gas to be flowed above the liquid. These gas ports also allow gas to be injected into the solution. Occasionally, the gas ports were used to saturate the liquid with oxygen; more typically, residual dissolved oxygen was purged from the liquid using an inert gas such as Ar or N<sub>2</sub>. The chamber vents could also be sealed with Ace Glass o-ring seals to exclude ambient air. The metal complexes used for this work are very oxygen sensitive [56]. The cell depicted in Figure 2.1.1-1 allows for CV experiments to be performed on the bench top (instead of a glove box) if done carefully. In my

typical experimental procedure, nitrogen was bubbled into the liquid for 10 minutes. Thereafter a blanket of flowing nitrogen was maintained above the liquid to prevent the intrusion of ambient oxygen, moisture, carbon dioxide, or other gaseous contaminants.

For all the CV experiments reported here, a  $\text{Ag}/\text{Ag}^+$  reference electrode (Basi, US) was used, which contained acetonitrile-solvated 0.01 M silver nitrate (Basi, US, 99%) and 0.1 M tetraethylammonium perchlorate (Alfa Aesar, US, 98%). This reference electrode was chosen because the  $\text{Ag}/\text{Ag}^+$  half-reaction is one of the few metal oxidations that can be reliably equilibrated in non-aqueous electrolytes. The working electrode used in most cases was a glassy carbon disk electrode (Basi, US). The counter electrode used in all my experiments was a graphite plate (The Graphite Store, US) partially submerged to 5  $\text{cm}^2$ , which can be seen on the right side of Figure 2.1.1-1. The left chamber of the cell contained the reference electrode.

To obtain a thermodynamically meaningful potential, the electrochemical potential of an electron at the working electrode must be able to be related to the electrochemical potential of an electron at the reference. Ultimately this means adjacent solutions must always share a common ion. The reference chamber shown on the left of Figure 2.1.1-1 contains an auxiliary chamber, which stores a bridging electrolytic solution. In the experiments reported here a bridging reference solution of 0.05 M tetraethylammonium nitrate (Fluka, US, 98%) was used in the auxiliary reference chamber to establish a thermodynamically meaningful working-electrode potential.

The effective reaction rate for an elementary redox half-reaction can be determined from the separation between the peak potentials for oxidation and reduction species, using the theory of Nicholson and Shain [57, 58].

$$\psi(\text{peak separation}) = \frac{k_0}{(\pi Df\nu)^{1/2}} \quad (2-1)$$

Use of equation ( 2-1 ) requires knowledge of the diffusion coefficient of the electrochemically active reactant, which can be estimated by repeating CV measurements at varying scan rates (described in the next sections).

The reversibility of a half-reaction can be evaluated using CV. “Reversibility” in this context refers to the ability to oxidize a molecule and return it to its original state, rather than to the relative values of the rate constants associated with anodic and cathodic directions of a half-reaction. The peak-height ratio from the CV is used in this work to make a qualitative assessment of reversibility. The ideal peak height ratio is unity for a reversible reaction, but anything in between 0.85 and 1.15 is typical from my experience. This is because peak heights are measured relative to a baseline which has uncertainty in its determination. Deviation from typical values suggests either slow kinetics in the oxidative or reductive direction, or that multi-step reactions (involving a chemical step) are occurring on the electrode [59]. Multi-step reactions can be difficult to deconvolute in CV when one of the reaction steps is chemical, rather than electrochemical, because no current is observed for a chemical reaction. For example, if an electrochemical oxidation occurred to create a species, which then quickly reacted chemically with oxygen from the air, the cyclic voltammogram would show an oxidation peak with no corresponding reduction

peak. A similar CV pattern will occur if the reduction reaction rate is slow compared to the scan rate.

If reactions do not occur within the potential window being swept in a CV experiment, then no peaks are observed and a box-like plot with relatively low currents result, similar to the representative example shown in Figure 2.1.1-2. The shape of the cyclic voltammogram is associated with double-layer charging at the electrode surfaces. The slope of the curve can be used to calculate the resistance in between the working and counter electrodes and is very small at these low currents. Close inspection of the figure reveals a small oxidation peak at  $\sim 0.4$  V, which indicates that an electrochemical reaction has occurred. However, this peak is small and likely represents a side reaction of a low concentration species and is negligible with respect to the dominant electrochemistry.

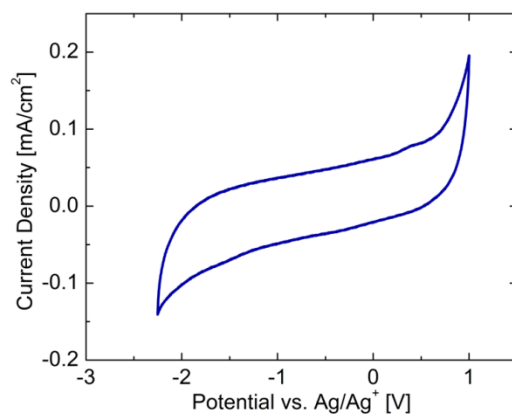


Figure 2.1.1-2 Cyclic voltammogram of 0.1 M tetraethylammonium tetrafluoroborate in acetonitrile. Glassy carbon working electrode. Scan rate 25 mV/s.

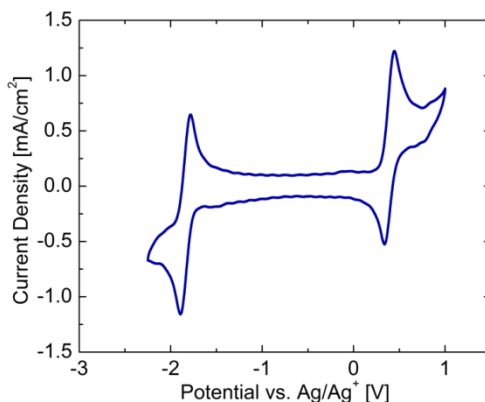


Figure 2.1.1-3 Cyclic voltammogram of 0.01 M  $V(acac)_3$  and 0.1 M tetraethylammonium tetrafluoroborate in acetonitrile. Glassy carbon working electrode. Scan rate 25 mV/s.

If an electrochemically active species,  $V(acac)_3$ , is added to the inactive solution shown in Figure 2.1.1-2, then peaks are observed. Figure 2.1.1-3 shows an example of this, where the electroactive species reacts at  $\sim -1.75$  V and  $\sim 0.4$  V. Notice that the region at  $\sim -0.5$  V has no additional reactions and matches well with the inactive system. For most of my experiments, electrolytic solutions were prepared by dissolving vanadium (III) acetylacetonate,  $V(acac)_3$ , (99.8%, Strem, US) and  $TEABF_4$  (99%, Aldrich, US) in anhydrous ACN (99.8%, Aldrich, US). Solutions were prepared and experiments performed in an argon-filled dry box to ensure the chemicals and solutions were not exposed to environmental oxygen and water.

### 2.1.2 Charge/Discharge

Charge/discharge testing is another experimental technique used frequently in my research. These tests will be employed to illustrate how active species perform in a practical RFB cell over time. Charge/discharge tests are

designed to mimic the conditions a battery would experience under long-term operation. The 'charge' step involves the addition of energy to the system, while the 'discharge' step involves energy extraction. The charge and discharge steps can be performed at constant applied potential, current, or resistive load – or a sequence of any or all of these conditions.

My experiments were performed under the commonly used constant-current condition (potential response is measured), because the resulting data are more readily analyzed. Figure 2.1.2-1 and Figure 2.1.2-2 respectively show H-type and 1-D type cell designs for performing charge/discharge experiments. Both cells were made in-house by the department glass blower.

The H-type cell is commonly used to screen electrolytes [23]. It is used because it is very easy to set up and versatile (electrodes, membranes, and liquids are easily changed). The 1-D cell has a similar purpose, but has a simpler geometry with regard to modeling. The H-cell has indirect current paths, which are difficult to model in comparison to the 1-D cell. Therefore, the H-cell was used only for the work presented in section 2.2 of this thesis. Both cells have similar primary dimensions: five-inch length and 5/8-inch inner tube diameter. These dimensions result in approximately 12.5mL of solution on each side of the membrane (25mL of liquid total in the cell). There are two differences between H- or 1-D cells and practical flow cells: first, there is no electrolyte flow in H- and 1-D cells, and second, there is a large solution resistance in H- and 1-D cells. Although H- and 1-D cells both cells have stagnant electrodes, their anolyte and catholyte compartments both contain stir bars to minimize mass-

transfer limitations near the electrodes; but these flow patterns still differ from those that would occur in a flow system. The solution resistance in the static cells is relatively large because the electrodes are approximately five inches apart, in contrast to the very small separation in practical flow cells.

Nevertheless, the solution resistance can be quantified, and the charge/discharge results can be compensated for, to extrapolate efficiencies to those that would be achieved in practical flow systems.



Figure 2.1.2-1 Photograph of an H-type charge/discharge cell. The blue liquid represents the volume filled with liquid electrolyte.

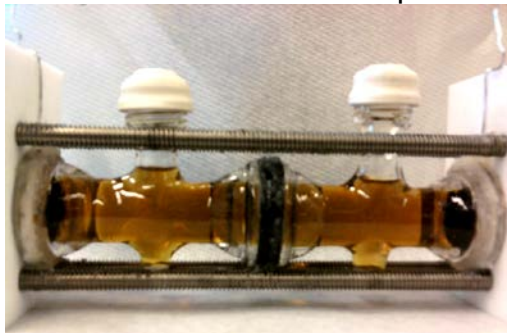


Figure 2.1.2-2 Photograph of the 1-D type charge/discharge cell. The brown liquid is a typical  $V(acac)_3$  electrolyte.

The components used in charge/discharge cells must be resistant to chemical attack by the solvent and supporting electrolyte. The 1-D cell is held together with a clamp consisting of a polytetrafluoroethylene (PTFE) plate with

four holes containing threaded aluminum rods. Ethylene propylene diene monomer (EPDM) rubber was used for the rubber septa on top of the cell, the gaskets around the membrane, and the gaskets around the electrodes. The cell body was glass (constructed from Ace Glass fittings), which was chosen for its inertness and ease of cleaning. Anion-exchange membranes were typically used to separate the chambers of the charge/discharge cell. The electrodes were typically graphite plates (Graphite store, US) and the current collectors behind them were aluminum foils (Alfa Aesar, US, 99.9999%). Prior to carrying out experiments, both the positive and negative electrodes were polished with 15  $\mu\text{m}$  silicon carbide paper, sonicated in water for 2 min, and dried for 24 hr.

A corrosion test was performed to assess the stability of the current-collector and electrode materials in the presence of the supporting electrolyte. Figure 2.1.2-3 shows the results of a chronoamperometry test with no active species present, with aluminum current collectors serving as both working and counter electrodes. The potential was increased stepwise from 3 V to 4.5 V as the current was monitored. The response current was expected to remain at zero until the potential became high enough to induce a corrosion reaction. Since no active species is present, any current observed in these experiments would correspond to undesirable electrochemical side reactions – likely corrosion. No current is noticeable in Figure 2.1.2-3; the aluminum current collector was found to be passive over the range of potentials tested (up to 4.5 V). But the current collector needs to be more than corrosion-resistant; it must also not react with the redox-active species, and it must be conductive. Figure



2.1.2-4 shows the cyclic voltammogram for the aluminum current collector in a solution of  $V(\text{acac})_3 / \text{TEABF}_4 / \text{ACN}$ . The response appears to owe predominately to double-layer charging, since the voltammogram shows no observable peaks. The double-layer current is very small ( $0.02 \text{ mA/cm}^2$ ) in comparison to the peak heights associated with a glassy carbon working electrode in a similar electrolyte ( $3.5 \text{ mA/cm}^2$ ). Also, the cyclic voltammogram has no discernible overall slope, indicating that the uncompensated ESR is low.

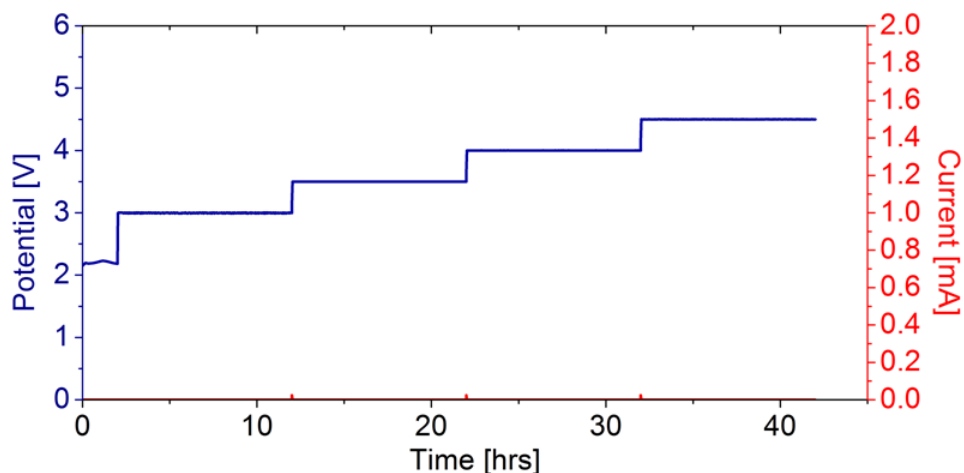


Figure 2.1.2-3 Chronoamperometry of 0.5 M  $\text{TEABF}_4$  in acetonitrile. Aluminum electrodes in an H-cell with Neosepta AHA membrane. [Blue (upper line)] Potential input to the cell, [Red (lower line)] Current response.

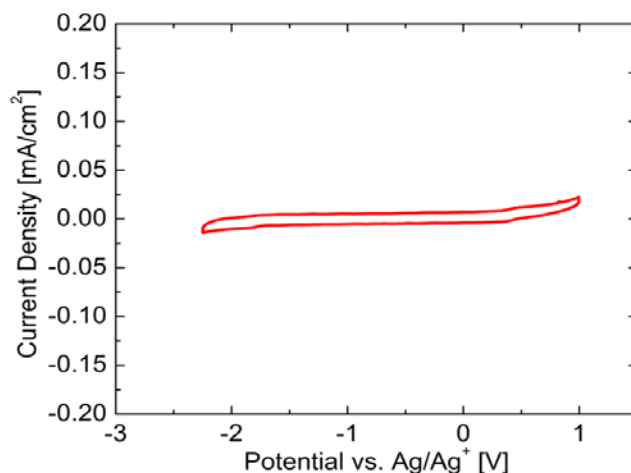


Figure 2.1.2-4 Cyclic voltammogram of 0.01 M  $V(acac)_3$  and 0.05 M  $TEABF_4$  in acetonitrile. Scan rate 100 mV/s. Working electrode: aluminum foil, counter electrode: graphite plate, reference electrode:  $Ag/Ag^+$ .

A corrosion test was also performed on graphite plate electrodes; the results are shown in Figure 2.1.2-5. This time a non-negligible current is observed, which increases as the applied potential increased, suggesting the occurrence of a redox reaction whose equilibrium potential is below 3 V. The current associated with this reaction was as high as 1 mA when 4.5 V was applied across the cell – a substantial current, given that the charge/discharge tests with  $V(acac)_3$  active species were performed at 1 mA. This issue is something to consider when carrying out charge/discharge experiments, because a large portion of the current may go toward driving electrode corrosion.

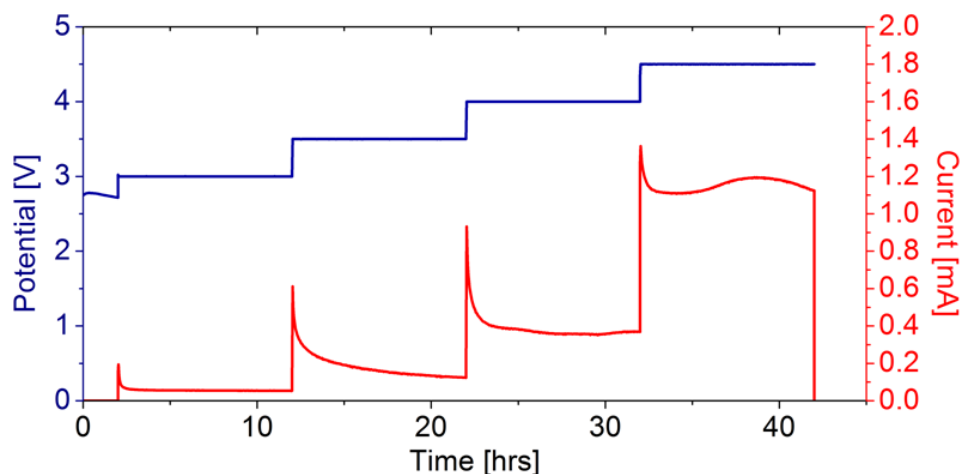


Figure 2.1.2-5 Chronoamperometry of graphite electrodes in 0.5 M TEABF<sub>4</sub> in acetonitrile. H-cell with Neosepta AHA membrane was used. [Blue (upper line)] Potential input to the cell, [Red (lower line)] Current response.

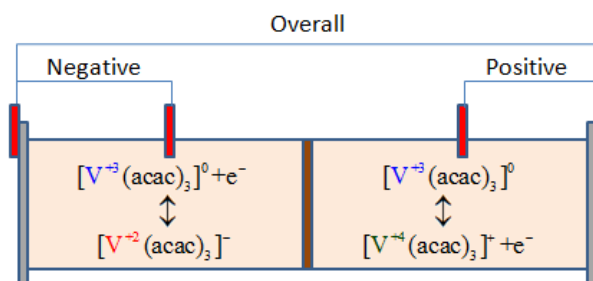


Figure 2.1.2-6 Schematic of a 4-electrode 1-D charge/discharge cell.

Figure 2.1.2-6 provides a schematic diagram of the 1-D cell from Figure 2.1.2-2, which aims to establish how electrodes can be configured within it. The positive and negative electrodes are represented by gray boxes on either end of the cell, and the membrane by a brown strip in the middle. The liquid electrolytes are shown in pink between the main electrodes and the membrane, along with the active-species reactions expected to occur. The blue brackets across the top of the cell indicate the circuitry for potential measurement across the cell. In practice the main potential measurement of interest is the one between the two

electrodes whose circuit is labeled “Overall”. This is the input or output voltage of the battery cell as a whole, and includes contributions from the cell equilibrium potential, reaction (kinetic) overpotentials, solution (diffusional and ohmic) overpotentials, and ohmic losses in the membrane. Charge/discharge experiments that only track the overall potential will be referred to as “2-electrode charge/discharge”.

The cell also has the capability to run a 4-electrode charge/discharge, where two reference electrodes are inserted into the positive and negative solutions through the fill ports in the 1-D cell. Aluminum wire was used for these electrodes; experiments with a variety of electrode materials showed that aluminum was passive and electrochemically stable in the acetonitrile-solvated vanadium RFB with TEABF<sub>4</sub> electrolyte. The extra electrodes used in the 4-electrode charge/discharge experiment allow measurement of the potential difference across the two circuits labeled “Negative” and “Positive” in the schematic. Each of these potential drops includes one surface overpotential and one-quarter of the solution overpotential, allowing the specific sources of overpotentials in the 1-D cell to be more precisely determined.

To illustrate what an expected charge/discharge curve looks like, we consider a theoretical analysis based on the CV measurement for TEABF<sub>4</sub>-supported V(acac)<sub>3</sub> in ACN. Figure 2.1.2-7 shows the CV data for this system; the anticipated formal cell potential is 2.18 V. This formal potential can be used to determine the potential the system will have when no current is flowing through the system via the Nernst equation (assuming the reactants and

products of redox reactions behave relatively ideally, so that activity coefficients are unity),

$$E = E^{\circ} - \frac{RT}{nF} \ln \left( \frac{[\text{Products}]}{[\text{Reactants}]} \right) \quad (2-2)$$

where  $E$  is the measured potential,  $E^{\circ}$  is the formal potential measured from CV,  $R$  is the universal gas constant,  $T$  is the absolute temperature,  $n$  is the number of electrons, and  $F$  is Faraday's constant (96485 C/mol).

For a single-electron disproportionation of a neutral intermediate active species, the product and reactant concentrations can be related to the total concentration of vanadium,  $[c]_{\text{total}}$ , and the fractional state of charge (SOC),  $x$ , through

$$[\text{Products}] = [c]_{\text{total}} x \quad [\text{Reactants}] = [c]_{\text{total}} (1 - x) \quad (2-3)$$

Figure 2.1.2-8 shows a plot of the formal potential as a function of the percent state of charge (%SOC=100x), using the formal potential from Figure 2.1.2-7 along with the condition that  $V(\text{acac})_3$  undergoes a single-electron disproportionation between  $V(\text{acac})_3^{+}$  and  $V(\text{acac})_3^{-}$ . The cell potential increases dramatically while the first 5 % of the vanadium(III) is converted to vanadium (IV) and (II). Then it increases slowly and passes through the equilibrium potential when half of the vanadium(III) is converted. When the solution is almost completely converted, the potential again increases dramatically towards infinity at 100 % conversion. This dramatic increase is indicative of overcharging if it is observed in the charge/discharge curves.

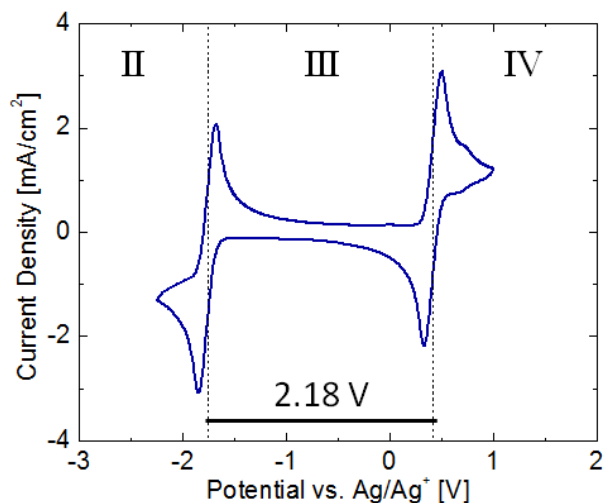


Figure 2.1.2-7 Cyclic voltammogram of 0.01 M V(acac)<sub>3</sub>, 0.05 M TEABF<sub>4</sub> in acetonitrile. Scan rate 100 mV/s with glassy carbon working electrode.

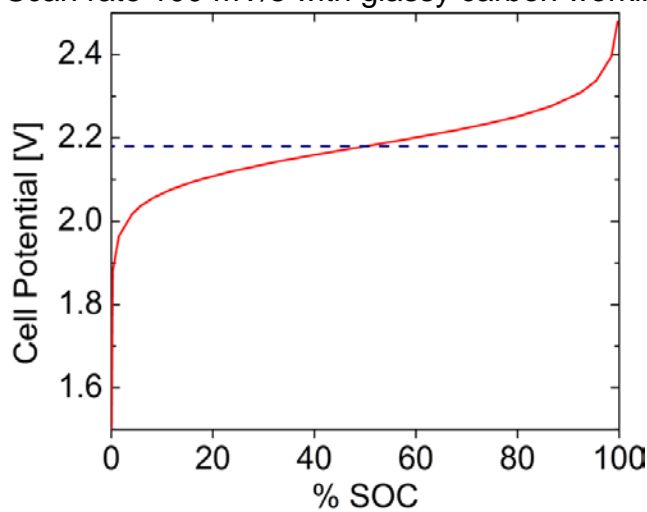


Figure 2.1.2-8 Plot of the Nernst equation for a single-electron disproportionation reaction with a 2.18 V formal potential.

For charge/discharge experiments, the currents were controlled using a Maccor Series 4000 48-channel battery tester (Maccor, U.S.). Most of the charge/discharge experiments presented here will follow a common control procedure, detailed in Figure 2.1.2-9, which is repeated a number of times until the test is stopped. Hours 0 to 9 (in the example figure) are charging steps,

followed by a 1-hour rest and subsequent discharge. A constant current is applied until 40 % of the theoretical maximum state of charge is transferred into the cell. That is, the duration of the applied current is computed such that 40 % of the vanadium(III) would disproportionate to vanadium (II) and (IV) if the desired reaction occurred with 100 % charge efficiency. For a 0.1 M  $V(acac)_3$  solution in the test cell shown (~25 mL total volume), this corresponds to a 1mA current applied for 14 hrs. The one-hour hold between charge and discharge steps allows for a relaxation to the equilibrium (open-circuit) potential, at which the Nernst equation can be used to compute the actual %SOC. The difference between the theoretical and actual %SOC is a measure of losses in the RFB. After the hold, the current is reversed and the potential is measured until the total cell voltage decreases to 0.5 V.

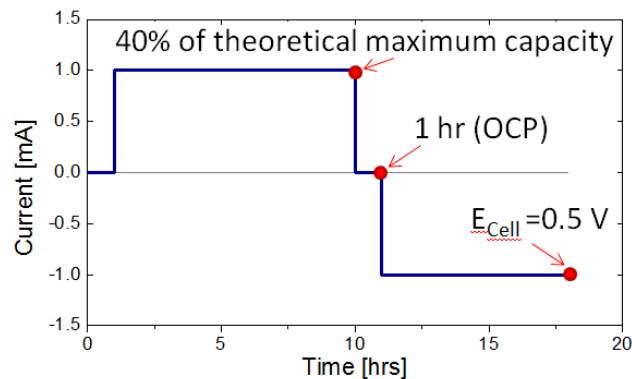


Figure 2.1.2-9 Common input parameters for charge/discharge experiments

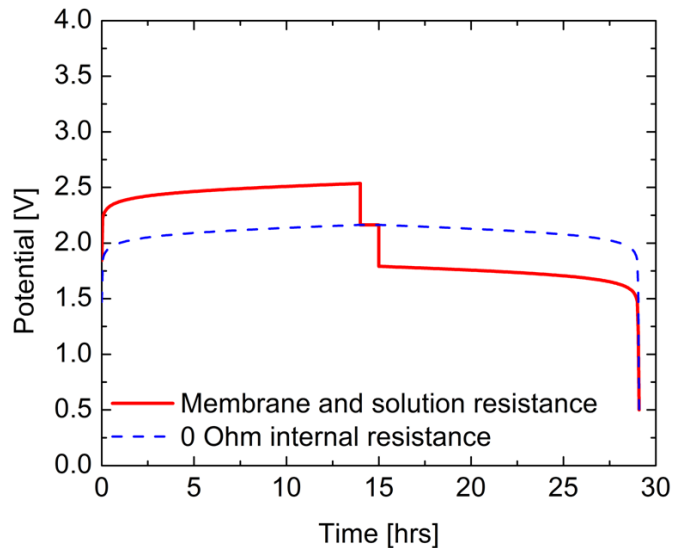


Figure 2.1.2-10 Theoretical charge/discharge curve for a cell with [Solid red line] 300 Ohms of ohmic resistance and [Dashed blue line] no resistances. Based on the charge/discharge input described above.

Using the control scheme described in Figure 2.1.2-9 and the predicted cell potential from the Nernst equation ( 2-2 ), a theoretical charge/discharge curve can be created, as shown in Figure 2.1.2-10. Two curves are illustrated; the blue curve shows how the open-circuit potential varies with %SOC, a result that would be expected if there were no overpotentials in the system. In general, overpotentials are necessary to drive dynamic processes, such as current flow through the solutions or membrane (ohmic overpotentials arising from ionic resistance), current flow across electrode surfaces (kinetic overpotential required for reaction activation, i.e., charge-transfer resistance), or variations in the concentrations of solutes within the cell due to mass-transfer limitations (concentration overpotential that arises when reactant diffusion is slow compared to the rate of charge transfer) [45]. Experiments that will be discussed later suggest that the ideal qualitative charge-discharge response can be modeled



fairly well by assuming  $\sim 300 \Omega$  of ohmic resistance and no other overpotentials in the cell. In that case, a charge/discharge experiment would yield results shown by the red curve in Figure 2.1.2-10. The internal resistance causes an increase in the potential observed during charging and a decrease in the potential on discharge which is proportional to the current. If concentration overpotentials or kinetic overpotentials are significant, then the increase or decrease of charge/discharge potential will be non-linear with respect to current. The region between the two curves shown in Figure 2.1.2-10 represents the energy lost due to overpotential. The theoretical maximum capacity of a battery determines the discharge time at a given current and is calculated by

$$\text{Discharge Time} = \frac{\text{Volume} * \text{Active Species Concentration} * F}{\text{Current}} \quad (2-4)$$

It is important to point out that Figure 2.1.2-10 depicts idealized results because it assumes that a single half-reaction occurs on each electrode during the charge-discharge process. If two half-reactions occur on an electrode, then two voltage plateaus can be expected during charge and/or discharge – a phenomenon sometimes called a “mixed potential”. In this scenario, the reaction with the lower charge voltage will occur preferentially, and the next reaction will begin to dominate after the first reactant is sufficiently exhausted. On discharge, the reaction with the higher discharge voltage will occur first. It is possible to reverse which reaction occurs first if the reaction has a low equilibrium potential but high overpotential, while the other reaction has a high equilibrium potential but low overpotential.

## 2.2 Active-Species Metal Center

### 2.2.1 Background and Approach

The metal center of the active species can affect the equilibrium cell potential [46]. This section discusses my investigation of how the metal center affects the disproportionation electrochemistry for transition-metal  $\beta$ -diketonates solvated in TEABF<sub>4</sub>/ACN. For a single metal RFB, the active metal must have at least three accessible stable oxidation states, and these must lie within the stability window of the solvent. Four first-row transition metals – V, Cr, Mn, and Co – meet this criterion, but the highest oxidation state of Co is not stable [60]. Thus testing focused on V, Cr, and Mn centers. The same ligand was used for the complexes, so that the effect of the metal center could be isolated. The  $\beta$ -diketonate ligand used was acetylacetonate (acac), which has been used for non-aqueous RFB systems in the past because complexes formed with it tend to show good electrochemical properties, and are commercially available [46, 61]. The electrochemistry of metal acac complexes has been studied in the past [62], however, most of the publications are from the chemistry literature and focus on electrochemical reduction (neglecting oxidation reactions which are important for our research). The following section focuses on determining the reduction and oxidation chemistries, as well as examining reaction properties relevant to RFB applications using charge/discharge experiments.

## 2.2.2 Results: Manganese Acetylacetonate

### 2.2.2.1 Voltammetric behavior of $\text{Mn}(\text{acac})_3$ in acetonitrile

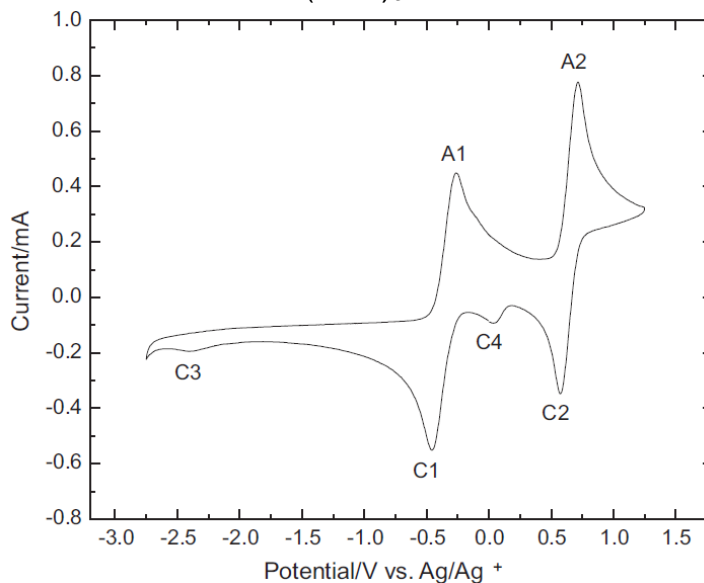
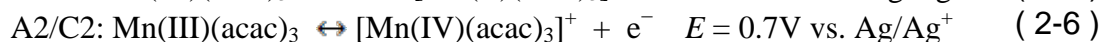


Figure 2.2.2-1 Cyclic voltammograms measured at a glassy carbon electrode in 0.05 M  $\text{Mn}(\text{acac})_3$  and 0.5 M TEABF<sub>4</sub> in ACN; scan rate 100 mV/s; room temperature.

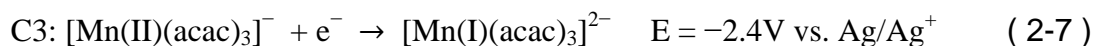
Figure 2.2.2-1 shows the CV response of a solution containing 0.05 M  $\text{Mn}(\text{acac})_3$  (Strem, US, 90%) and 0.5 M TEABF<sub>4</sub> in ACN cycled at a scan rate of 100 mV/s. The CV displays two redox couples within the solvent stability window, at -0.4 and 0.7 V vs. Ag/Ag<sup>+</sup>. The electrochemistry of  $\text{Mn}(\text{acac})_3$  has been evaluated in a range of electrolytes and with different electrode materials [63-66]. Gritzner *et al.* defined the  $\text{Mn}(\text{acac})_3$  redox potentials at Pt and Hg using solvents including ACN with tetrabutylammonium perchlorate supporting electrolyte [64]. Peak potentials and kinetics were observed to be highly dependent on solvent, supporting electrolyte, and electrode material. They reported redox couples at 0.64 and 1.70 V vs. a bis(biphenyl)chromium tetrphenylborate/bis(biphenyl)chromium reference electrode. Although

differences in the reference electrodes make it difficult to compare the absolute values of these redox potentials to those reported here, the voltage differences between the redox couples (~1.1 V) are consistent. Given the similarities, we assign the redox couples observed here to the reactions:



Features associated with half-reactions ( 2-5 ) and ( 2-6 ) are labeled on Figure 2.2.2-1. The formal potentials indicated that an RFB system based on one-electron disproportionation of Mn(acac)<sub>3</sub> would yield a 1.1 V equilibrium cell potential. This is comparable to the aqueous vanadium RFB system (1.26 V under standard conditions [67]) but much smaller than the 2.2 and 3.4V reported for the non-aqueous V(acac)<sub>3</sub> [68] and chromium acetylacetonate (Cr(acac)<sub>3</sub>) [69] systems, respectively.

Two additional reduction peaks, labeled C3 and C4, can be seen on Figure 2.2.2-1. In ACN solvent, Gritzner *et al.* reported a peak corresponding to a second reduction of Mn(acac)<sub>3</sub> at -1.49 V vs. bis(biphenyl)chromium tetraphenylborate/bis(biphenyl)chromium [64]. Although reference electrodes differed in our work, one still expects the second reduction at ~2.1 V negative of the first one. Figure 2.2.2-1 shows that the formal potential of the peak labeled C3 is -2.4 V vs. Ag/Ag<sup>+</sup>, or ~2 V more negative than the A1/C1 redox couple. This reduction peak, C3, has consequently been attributed to the reaction:



The lack of an observable corresponding oxidation peak suggested that reaction

( 2-7 ) was coulombically irreversible and would not be useful for a rechargeable RFB.

The peak in Figure 2.2.2-1 labeled C4 at 0 V vs. Ag/Ag<sup>+</sup> was not observed in the Mn(acac)<sub>3</sub> voltammetry reported by Gritzner *et al* [64]. Although the origin of peak C4 has not been determined unambiguously, one possibility is that it stems from the presence of H<sub>2</sub>O in the system. The Mn(acac)<sub>3</sub> complex used in this research contained ~10 % H<sub>2</sub>O. The peak does not appear to owe to ligand shedding, because the addition of acetylacetone to a 0.5 M TEABF<sub>4</sub> in ACN solution does not lead to peaks in the CVs near 0 V vs. Ag/Ag<sup>+</sup>.

#### 2.2.2.2 Active-species diffusivity and kinetics

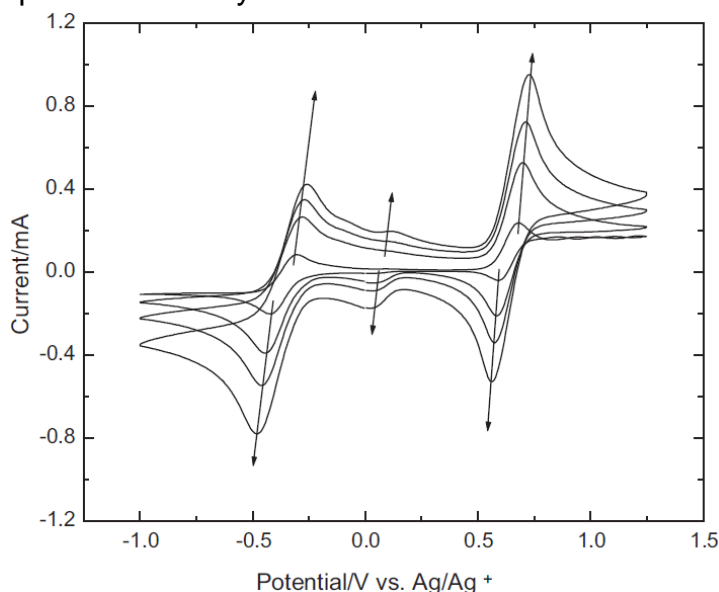


Figure 2.2.2-2 Cyclic voltammograms measured at a glassy carbon electrode in 0.05 M Mn(acac)<sub>3</sub> and 0.5 M TEABF<sub>4</sub> in ACN at scan rates of 10, 50, 100, and 200 mV/s, arrows show direction of increasing scan rate; room temperature.

Figure 2.2.2-2 shows a series of cyclic voltammograms at various scan rates for 0.05 M Mn(acac)<sub>3</sub> and 0.5 M TEABF<sub>4</sub> in ACN. For the Mn(II)/Mn(III)

redox couple, the peak separation,  $\Delta E_p$ , increased from 120 to 290 mV as the scan rate increased from 10 to 200 mV/s. Similarly, for the Mn(III)/Mn(IV) redox couple,  $\Delta E_p$  increased from 90 to 210 mV with increasing scan rate. For both redox couples, ratios of the anodic to cathodic peak currents were near unity. These observations indicate quasi-reversible electrode kinetics [45]. An oxidation peak associated with anomalous peak C4 (at ~0V) can also be observed on Figure 2.2.2-2. The peak heights for this redox couple increased with increasing scan rate.

To determine the diffusion coefficient for Mn(acac)<sub>3</sub> in the electrolytic solution, the peak heights were measured as scan rates were varied from 10 to 200 mV/s. For a reversible redox couple, the peak current  $i_p$  is given by the Randles-Sevcik equation [59]:

$$i_p = 2.69 \times 10^5 n^{3/2} A C D_o^{1/2} \nu^{1/2} \quad (2-8)$$

where  $A$  is the electrode area (0.07 cm<sup>2</sup>),  $C$  the bulk active-species concentration,  $D_o$  the active-species diffusion coefficient, and  $\nu$  the scan rate (it is assumed that  $n=1$ ). A plot of  $i_p$  vs.  $\nu^{1/2}$  yields a straight line with a slope proportional to  $D_o$  [45]. The diffusion coefficient for Mn(acac)<sub>3</sub> in a supporting electrolyte of 0.5 M TEABF<sub>4</sub> in ACN is estimated to be  $3.0 \times 10^{-6}$  cm<sup>2</sup>/s based on the cathodic peak current for the Mn(II)/Mn(III) redox couple.

For an irreversible redox couple, the peak current is governed by [59]:

$$i_p = 2.99 \times 10^5 n^{3/2} \alpha^{1/2} A C D_o^{1/2} \nu^{1/2} \quad (2-9)$$

Using this relationship, the Mn(acac)<sub>3</sub> diffusion coefficient is estimated to be  $4.8 \times 10^{-6}$  cm<sup>2</sup>/s. As the Mn(II)/Mn(III) redox couple appears to show quasi-

reversible kinetics, one would expect the value for the diffusion coefficient of the neutral complex to be in the range of  $3.0 \times 10^{-6}$ - $4.8 \times 10^{-6}$  cm<sup>2</sup>/s. This diffusivity is comparable to that for V(acac)<sub>3</sub> in the same supporting electrolyte and solvent and approximately an order of magnitude higher than that for Cr(acac)<sub>3</sub>.

### 2.2.2.3 Charge-discharge performance

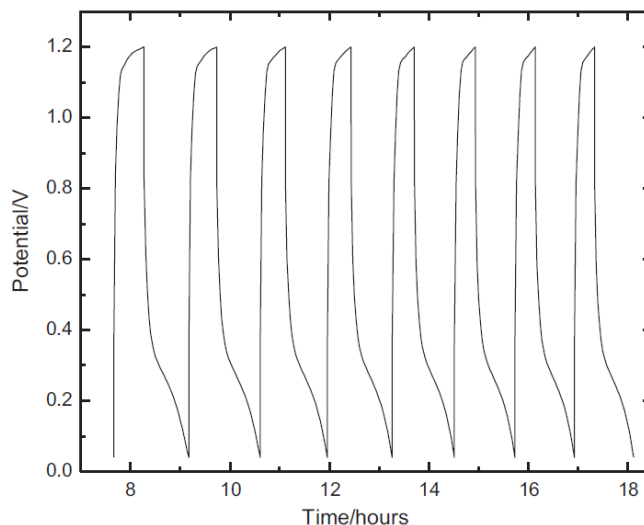


Figure 2.2.2-3 Charge-discharge curves for 0.05 M Mn(acac)<sub>3</sub> and 0.5 M TEABF<sub>4</sub> in ACN; charge current 1 mA and discharge current 0.1 mA; room temperature.

Charge-discharge characteristics for a cell containing 0.05 M Mn(acac)<sub>3</sub> and 0.5 M TEABF<sub>4</sub> in ACN were evaluated. Galvanostatic conditions were used with potential cutoffs for both charge and discharge. The charge cutoff was 1.2 V, slightly higher than the 1.1 V cell potential observed in the voltammetry for the one-electron disproportionation of Mn(acac)<sub>3</sub>. This potential should prevent the irreversible reduction of Mn(II) to Mn(0), which was observed in the voltammetry at  $\sim -2.4$  V. The discharge cutoff was set at 0.04 V to allow the system to fully

discharge without introducing side reactions. Figure 2.2.2-3 illustrates cycles 3-10. The first cycles are not shown as they correspond to the stabilization of the electrodes and electrolyte. One discharge plateau is observed at ~0.3 V for all ten cycles. This likely corresponds to the one-electron disproportionation of the  $\text{Mn}(\text{acac})_3$  species, which has a cell potential of 1.1 V. The charge and discharge voltages were respectively higher and lower than the cell voltages determined by CV. In the H-cell configuration, the electrodes were separated by a significant distance (~10 cm). Given this, the 0.5 M concentration of the support and the presence of the anion-exchange membrane separator, ohmic overpotentials were probably significant.

Coulombic efficiencies increased steadily from ~74 % for cycle 3 to ~97 % for cycle 10. This increase with cycle number owes to an unknown side reaction, with one possibility being corrosion of the electrode material. Energy efficiencies were reasonably constant at ~21 % over the cycles suggesting that the use of the voltage cutoffs prevented the irreversible reduction of Mn(III) to Mn(0).

#### 2.2.2.4 $\text{Mn}(\text{acac})_3$ Summary

A manganese acetylacetonate,  $\text{Mn}(\text{acac})_3$ , active species was evaluated for application in non-aqueous RFBs, using a  $\text{TEABF}_4/\text{ACN}$  supporting electrolyte. Results from CV indicated that the  $\text{Mn}(\text{acac})_3$  complex can be oxidized to  $[\text{Mn}(\text{acac})_3]^+$  and reduced to  $[\text{Mn}(\text{acac})_3]^-$  at a glassy carbon electrode. The anodic and cathodic half-cell reactions appeared to be electrochemically quasi-reversible and the cell potential was 1.1 V, comparable



to aqueous vanadium RFB systems, but much smaller than cell potentials reported for other non-aqueous RFB chemistries. A second, irreversible, reduction to  $[\text{Mn}(\text{acac})_3]^{2-}$  occurred at very negative potential.

The charge-discharge characteristics for an electrolyte containing 0.05 M  $\text{Mn}(\text{acac})_3$  and 0.5 M  $\text{TEABF}_4$  in ACN were evaluated in an H-type cell. One discharge plateau was observed at  $\sim 0.3$  V, which is thought to correspond to the one-electron disproportionation of the  $\text{Mn}(\text{acac})_3$  complex. Coulombic efficiencies were observed to increase with cycle number, suggesting a side reaction. Energy efficiency was reasonably constant at  $\sim 21$  %.

## 2.2.3 Results: Chromium Acetylacetonate

### 2.2.3.1 Voltammetric behavior of $\text{Cr}(\text{acac})_3$ in acetonitrile

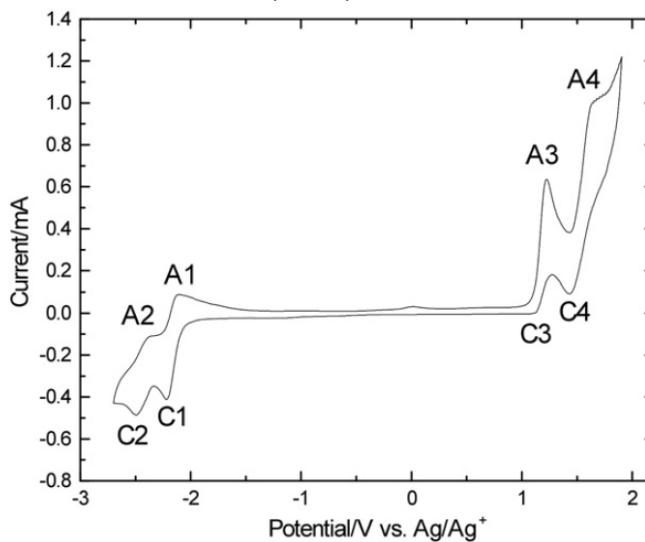
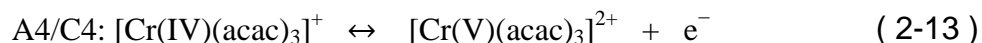
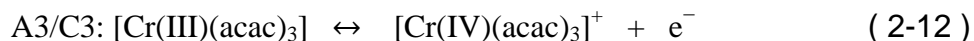


Figure 2.2.3-1 Cyclic voltammograms measured at a glassy carbon electrode in 0.05 M  $\text{Cr}(\text{acac})_3$  and 0.5 M  $\text{TEABF}_4$  in ACN; scan rate 50 mV/s; room temperature.

Figure 2.2.3-1 shows the CV at 50 mV/s for a 0.05 M Cr(acac)<sub>3</sub> (Strem, US, 97.5%) in ACN solution with 0.5 M TEABF<sub>4</sub> as the supporting electrolyte. Four redox couples were observed within the solvent stability window. Chromium acetylacetonate electrochemistry has been reported previously [63, 70-73]. Landsberg *et al.* defined the Cr(acac)<sub>3</sub> reduction potentials in dimethyl sulfoxide (DMSO) [72]. They observed two redox couples at reductive potentials and attributed them to one-electron reductions of the Cr(acac)<sub>3</sub> complex. Although the absolute values of these reduction potentials are difficult to compare with potentials reported here (due to differences in the reference electrodes used and different solvents), the voltage difference between A1/C1 and A2/C2 appears similar to that observed in our work (300-400 mV). We therefore attributed the redox couples observed at reductive potentials to the following reactions:



The redox couples observed at oxidative potentials are consequently attributed to:



Features on the cyclic voltammogram associated with redox half-reactions (2-10) – (2-13) are labeled on Figure 2.2.3-1.

The formal potentials for the half-reactions indicate that an RFB system based on one-electron disproportionation of Cr(acac)<sub>3</sub> would yield a 3.4 V

equilibrium cell potential. This is approximately 2.5 times higher than the potential reported for aqueous vanadium RFBs (1.26V under standard conditions [67]). The reversible two-electron disproportionation of  $\text{Cr}(\text{acac})_3$  could lead to a cell potential as high as 4.1 V if harnessed.

### 2.2.3.2 Active-species diffusivity and kinetics

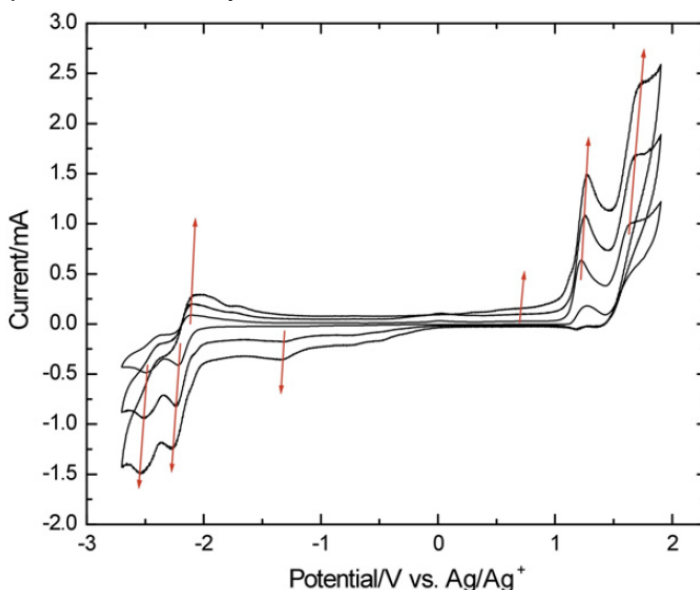


Figure 2.2.3-2 Cyclic voltammograms measured at a glassy carbon electrode in 0.05 M  $\text{Cr}(\text{acac})_3$  and 0.5 M  $\text{TEABF}_4$  in ACN at scan rates of 50, 200, and 500 mV/s. Arrows show direction of increasing scan rate; room temperature.

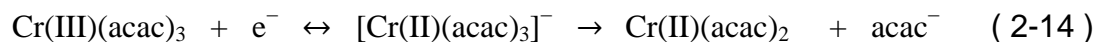
Figure 2.2.3-2 shows a series of CVs at various scan rates for electrolytic solutions containing 0.05 M  $\text{Cr}(\text{acac})_3$  and 0.5 M  $\text{TEABF}_4$  in ACN. For the  $\text{Cr}(\text{II})/\text{Cr}(\text{III})$  and  $\text{Cr}(\text{I})/\text{Cr}(\text{II})$  couples, associated with reduction of the neutral complex, the peak separation  $\Delta E_p$  increases slightly with increasing scan rate. The ratios of anodic to cathodic peak currents are near unity for both reduction couples, suggesting quasi-reversible electrode kinetics for reactions ( 2-10 ) and ( 2-11 ). No peaks for the  $\text{Cr}(\text{III})/\text{Cr}(\text{IV})$  and  $\text{Cr}(\text{IV})/\text{Cr}(\text{V})$  couples were observed

in the reduction waves of the voltammograms when scanned faster than 50 mV/s. This suggests that  $[\text{Cr(IV)(acac)}_3]^+$  and  $[\text{Cr(V)(acac)}_3]^{2+}$  reductions are either kinetically very slow or the product being created reacts before it can be reduced. If the kinetics are slow, it is possible that a catalytic electrode can be used to improve the reaction rates. Where reactions ( 2-10 ) and ( 2-11 ) show quasi-reversible kinetics, reactions ( 2-12 ) and ( 2-13 ) show near irreversible kinetics.

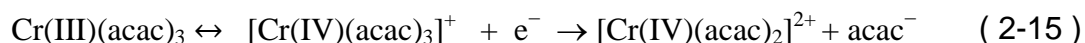
The cyclic voltammograms in Figure 2.2.3-2 also show small reduction and oxidation peaks near  $-1.25\text{ V}$  and  $0.5\text{ V}$  vs.  $\text{Ag/Ag}^+$ , respectively, which become more prominent with increasing scan rate. The origin of these features has not been determined unambiguously; by shifting the potential window examined, it is suggested that they stem from redox reactions involving a by-product of  $\text{Cr(acac)}_3$  oxidation. These anomalous redox peaks appeared only after the voltage was scanned above  $\sim 1\text{ V}$  vs.  $\text{Ag/Ag}^+$ , i.e., above the couples associated with reaction ( 2-12 ). Similar features were observed by Carano *et al.* [74] when performing CV of rhodium acetylacetonate ( $\text{Rh(acac)}_3$ ) in tetrahydrofuran (THF); they associated the anomalous redox peaks with ligand-shedding by the complex. Our experiments corroborate this observation: in the absence of active species, peaks near  $-1.25\text{ V}$  and  $0.5\text{ V}$  vs.  $\text{Ag/Ag}^+$  appear when acetylacetone is added to the support solution.

The reversibility of  $\text{Cr(acac)}_3$  electrochemistry in various solvents has been reported before [71, 72, 75]. Landsberg *et al.* concluded that the  $[\text{Cr(acac)}_3]^-$  ion was stable in DMSO because no ligand elimination was detected upon  $\text{Cr(acac)}_3$

reduction [71]. In ACN, however, Anderson *et al.* proposed the reduction mechanism of Cr(acac)<sub>3</sub> to be [70]:



Although the anomalous peaks in my research appear to be associated with Cr(acac)<sub>3</sub> oxidation instead of reduction, a similar reaction involving ligand loss might also occur. One possibility is:



Thus the anomalous reduction and oxidation peaks could arise from reactions involving the acac<sup>-</sup> ligand. Further investigation is needed to elucidate the origin of these peaks, particularly because it may represent a source of efficiency loss in the RFB charge-discharge cell.

To determine the diffusion coefficient of Cr(acac)<sub>3</sub> in the electrolytic solutions, changes in peak height were measured as scan rate was varied from 10-500 mV/s, as was done for Mn(acac)<sub>3</sub>. Based on reactions ( 2-8 ) and ( 2-9 ), the diffusion coefficient of the neutral complex was estimated to be 5.0-6.2x10<sup>-7</sup> cm<sup>2</sup>/s.

### 2.2.3.3 Charge-discharge performance

Charge-discharge characteristics for an H-type cell containing 0.05 M Cr(acac)<sub>3</sub> and 0.5 M TEABF<sub>4</sub> in ACN were evaluated. The charge voltage at 50 % SOC increases gradually and the discharge characteristics changed during the first few cycles. Coulombic and energy efficiencies reach relatively constant values after 5 cycles, when stable, qualitatively similar charge-discharge curves

are obtained. Figure 2.2.3-3 illustrates cycles 1 through 10. An issue occurred during cycle 7 which caused the discharge to stop early, so subsequent discussion will be regarding cycles 9 and 10 where results are consistent.

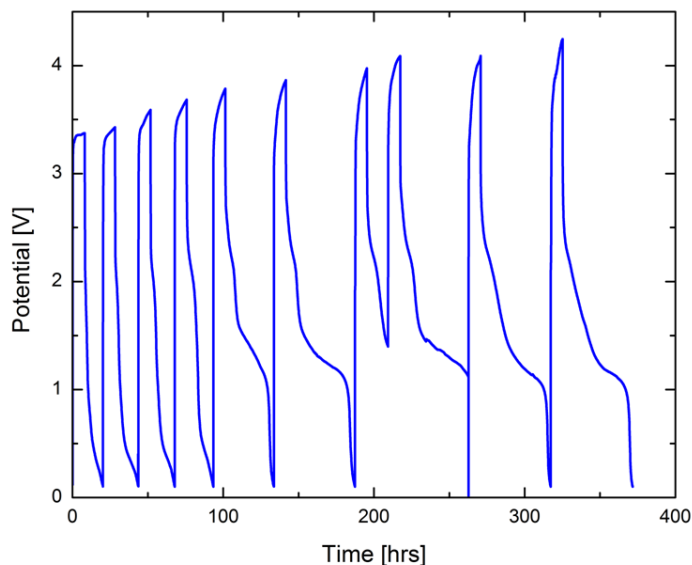


Figure 2.2.3-3 Charge–discharge curves for 0.05 M Cr(acac)<sub>3</sub> and 0.5 M TEABF<sub>4</sub> in ACN; charge current 1 mA and discharge current 0.1 mA; room temperature.

The charge and discharge voltages are respectively higher and lower than the cell voltages established by CV. Ohmic overpotentials are high for similar reasons to those provided in the discussion of the manganese system. Sluggish kinetics associated with the cathodic steps of reactions ( 2-12 ) and ( 2-13 ) may also lead to kinetic overpotentials. The charge voltages ranged from 4.0 to 4.3 V over the two cycles; two discharge plateaus appeared at ~2.2 V and ~1.2 V. Coulombic efficiencies for cycles 9 and 10 ranged from 53-58 % at 50 % SOC. These low values may owe to crossover of the active species through the separator. Energy efficiencies of approximately 21-22 % were achieved.

#### 2.2.3.4 Cr(acac)<sub>3</sub> Summary

A chromium acetylacetonate, Cr(acac)<sub>3</sub>, active species was evaluated for application in redox flow batteries, using a non-aqueous TEABF<sub>4</sub>/ACN supporting electrolyte. Results from CV indicated that the Cr(acac)<sub>3</sub> complex can be oxidized to [Cr(acac)<sub>3</sub>]<sup>+</sup> and [Cr(acac)<sub>3</sub>]<sup>2+</sup> and reduced to [Cr(acac)<sub>3</sub>]<sup>-</sup> and [Cr(acac)<sub>3</sub>]<sup>2-</sup> at a glassy carbon electrode. The rates of [Cr<sup>IV</sup>(acac)<sub>3</sub>]<sup>+</sup> and [Cr<sup>V</sup>(acac)<sub>3</sub>]<sup>2+</sup> reduction are slow. The cell potential for the one-electron disproportionation is 3.4 V.

Coulombic and energy efficiencies of 53-58 % and 21-22 %, respectively, were obtained at 50 % SOC for an electrolyte containing 0.05 M Cr(acac)<sub>3</sub> and 0.5 M TEABF<sub>4</sub>.

#### 2.2.4 Results: Vanadium Acetylacetonate

##### 2.2.4.1 Voltammetric behavior of V(acac)<sub>3</sub> in acetonitrile

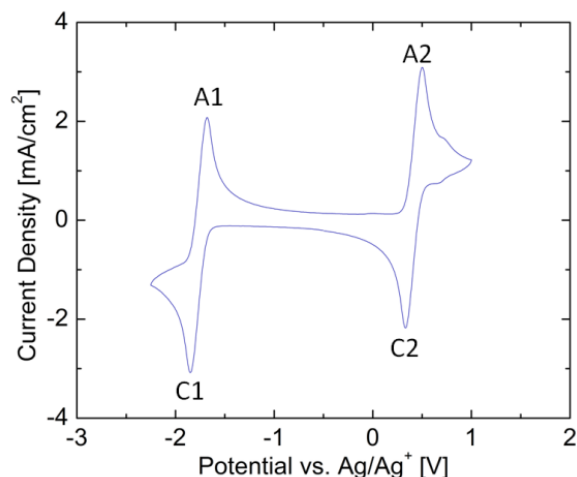
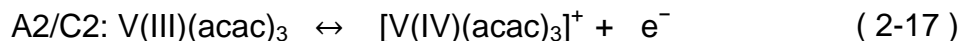
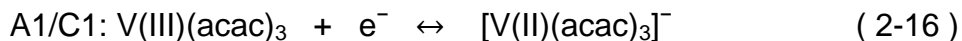


Figure 2.2.4-1 Cyclic voltammogram measured at a glassy carbon electrode in 0.01 M V(acac)<sub>3</sub> and 0.05 M TEABF<sub>4</sub> in ACN; scan rate 100 mV/s; room temperature.

Figure 2.2.4-1 shows the cyclic voltammogram for a 0.01 M V(acac)<sub>3</sub> solution with 0.05 M TEABF<sub>4</sub> in ACN cycled at 100 mV/s. Two redox couples were present within the solvent stability window (-2.5 V to 1.5 V vs. Ag/Ag<sup>+</sup>). V(acac)<sub>3</sub> electrochemistry has been reported previously [76]. Although a direct comparison between the absolute values of reduction potentials reported earlier and those in this work is difficult (due to the different solvents used), the voltage difference between the first and second reductions appears similar between the previous report and ours. We therefore attribute the redox couples observed in Figure 2.2.4-1 to the following reactions:



The overall reaction is



These formal potentials indicated by the reactions in Figure 2.2.4-1 suggests that a RFB system based on one-electron disproportionation of V(acac)<sub>3</sub> should yield a 2.18 V equilibrium cell potential. This is approximately 1.7 times higher than the potential reported for aqueous vanadium RFBs (1.26 V under standard conditions [67]).

Additionally, a small redox couple at ~0.75 V indicates the formation of a vanadyl acetylacetonate, VO(acac)<sub>2</sub>, species. This peak is proposed to correspond to redox of VO(acac)<sub>2</sub>, according to the earlier suggestion of Nawi *et*



a/. [77] that  $V(acac)_3$  readily incorporates oxygen into its structure to form  $VO(acac)_2$  with the loss of a ligand via



In order to identify the peak at  $\sim 0.75$  V, solutions of constant  $V(acac)_3$  concentration and increasing concentrations of  $VO(acac)_3$  were created. Figure 2.2.4-2 shows cyclic voltammograms of these solutions. The region of interest is at  $+0.75$  V where the major peak for  $VO(acac)_2$  oxidation occurs. The cyclic voltammograms show increasing currents as the concentration of  $VO(acac)_2$  increases, which suggests that this peak likely arises from  $VO(acac)_2$  electrochemistry.

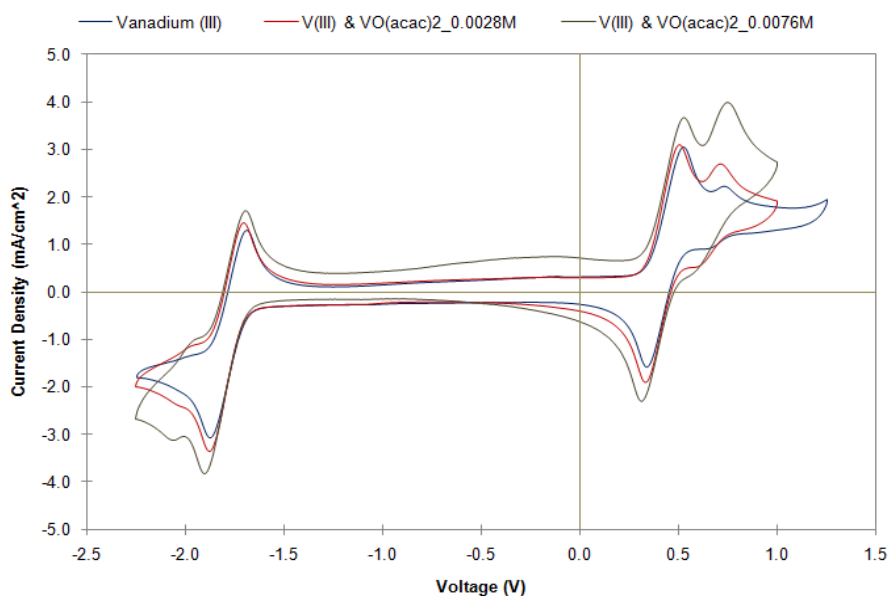


Figure 2.2.4-2 Cyclic voltammogram of 0.01 M  $V(acac)_3$ , 0.05 M  $TEABF_4$  solution with vanadyl acetylacetonate added at [blue] 0 M, [red] 0.0028 M, and [green] 0.0076 M. Scan rate 500 mV/s at room temperature on a glassy carbon electrode.

Although the presence of  $VO(acac)_2$  is confirmed, it is unknown whether  $VO(acac)_2$  forms in the dry vanadium precursor material or in solution while it

cycles. Infrared spectroscopy on the reactant powder was performed to determine if  $\text{VO}(\text{acac})_2$  forms spontaneously in  $\text{V}(\text{acac})_3$  powder as it ages. Figure 2.2.4-3 shows the resulting spectra for three different samples. The “Aged sample” line in blue is a sample taken from a reactant bottle stored with no special treatment for approximately 1 year. The “Fresh sample” line in red shows the results from a bottle received and tested within a week. A line representing a sample of pure  $\text{VO}(\text{acac})_2$  (Sigma Aldrich, US, 98 %) is also shown, for comparison. The peak identification for  $\text{V}(\text{acac})_3$  and  $\text{VO}(\text{acac})_2$  systems has been reported previously by Vlckova *et al.* [78]. In Figure 2.2.4-3, most of the peaks are related to the acetylacetonate bonds; the major peaks associated with the  $\text{V}=\text{O}$  bond occur at  $996\text{ cm}^{-1}$ . All three samples show strong vanadyl peaks, illustrating that vanadyl is likely to form in the reactant jar. Furthermore, since the fresh sample contains some vanadyl, it might not be immediately possible to guarantee vanadyl-free precursors.

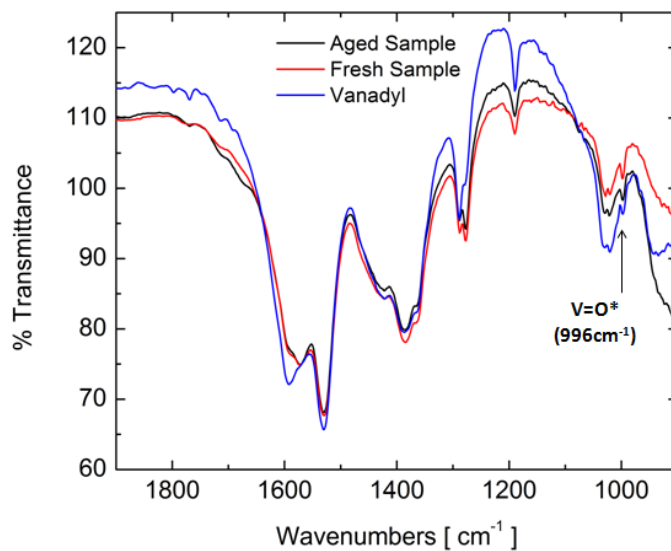


Figure 2.2.4-3 Infrared spectra of vanadium acetylacetonate from jars of varying age and a vanadyl acetylacetonate. Samples run under nitrogen and preheated for 2 hours at 150°C.

A second extraneous peak, which appeared in the CV of any non-aqueous solvent, arises from the electrochemistry of superoxide. In an ACN solvated system with a glassy carbon electrode, the reduction of oxygen to superoxide via

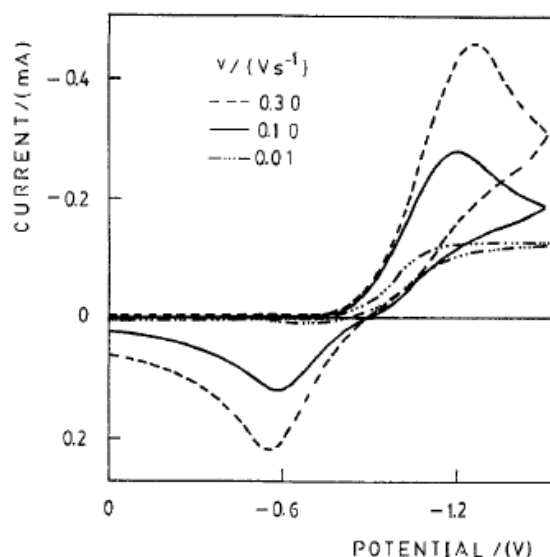


Figure 2.2.4-4 Cyclic voltammogram of  $\text{O}_2$  electroreduction at Pt taken at multiple scan rates. Reprinted from [79].

occurs at  $\sim -1.25$  V. Several researchers have observed this reaction [79, 80].

Lorenzola *et al.* performed rotating-disk electrode, CV, and spectroscopic analyses of the resulting solutions to determine the cause of the peak in Figure 2.2.4-4. Although this work was not performed in ACN, the reaction observed will likely occur in any non-aqueous solvent [80]. The spectroscopy only conclusively indicated the presence of peroxide, but it is proposed that the intermediate to peroxide formation is superoxide. This suggests that all voltammetric

experiments for non-aqueous RFBs should be run in an oxygen-free environment  
– either a glove box or a cell bubbled and blanketed with an inert gas.

#### 2.2.4.2 Active species diffusion coefficient and kinetics

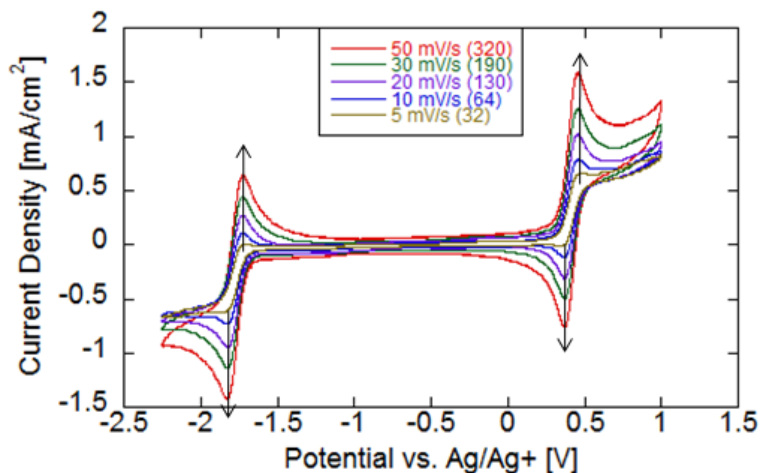


Figure 2.2.4-5 Cyclic voltammograms measured at a glassy carbon electrode in 0.01 M V(acac)<sub>3</sub> and 0.05 M TEABF<sub>4</sub> in ACN at scan rates of 5, 10, 20, 30, and 50 mV/s, arrows show direction of increasing scan rate; room temperature.

Figure 2.2.4-5 shows a series of cyclic voltammograms at various scan rates for electrolytic solutions containing 0.01 M V(acac)<sub>3</sub> and 0.05 M TEABF<sub>4</sub> in ACN. For the V(II)/V(III) couples, the peak separation  $\Delta E_p$  increased slightly with increasing scan rate from 70 to 90 mV. For the V(III)/V(IV) couples, the peak separation  $\Delta E_p$  remained constant at 70 mV. The ratios of anodic to cathodic peak currents were near unity for both reduction couples, suggesting quasi-reversible kinetics for reactions ( 2-16 ) and ( 2-17 ).

To determine the diffusion coefficient of V(acac)<sub>3</sub> in the electrolytic solutions, changes in peak height were measured as scan rates varied stepwise from 5-50 mV/s, as was done for the other active species discussed in sections

2.2.2 and 2.2.3. Based on equations ( 2-8 ) and ( 2-9 ), the diffusion coefficient of the neutral complex is calculated to be  $3.9 \times 10^{-6} \pm 1.3 \times 10^{-6} \text{ cm}^2/\text{s}$  and is shown in Figure 2.2.4-6.

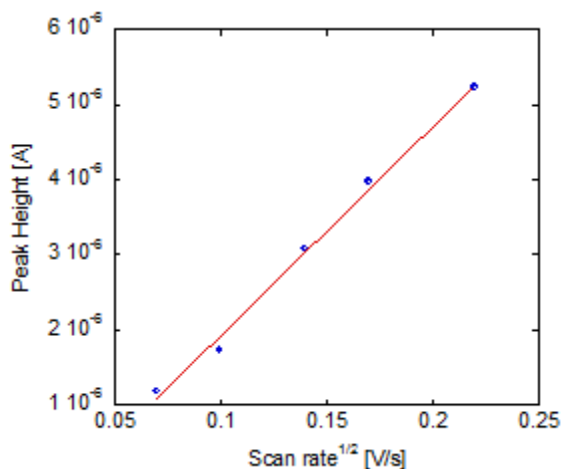


Figure 2.2.4-6 Plot of V(III) / V(IV) peak height vs. scan rate<sup>1/2</sup> based on cyclic voltammograms measured at a glassy carbon electrode in 0.01 M V(acac)<sub>3</sub> and 0.05 M TEABF<sub>4</sub> in ACN at scan rates of 5, 10, 20, 30, and 50 mV/s; room temperature.

#### 2.2.4.3 Charge-discharge performance

Charge-discharge characteristics for an H-type cell containing 0.05 M V(acac)<sub>3</sub> and 0.5 M TEABF<sub>4</sub> in ACN were evaluated. Figure 2.2.4-7 presents data from the first 10 cycles of this system.

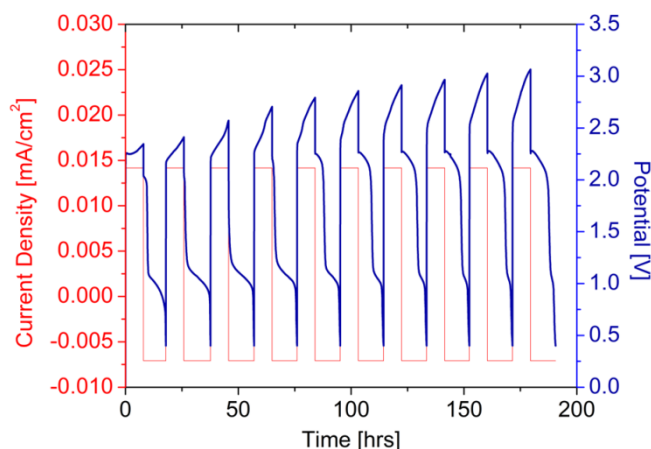


Figure 2.2.4-7 [Blue] Charge–discharge curves for 0.05 M  $V(acac)_3$  and 0.5 M  $TEABF_4$  in ACN; [Thin red line] constant charge current 1 mA and constant discharge current 0.5 mA; room temperature.

The charge/discharge curve shows a charge voltage of approximately 2.25 V during cycle 1, which is lower than expected for a redox couple with a formal potential of 2.18 V in light of the internal cell resistances. The discharge curves show two distinct plateaus, suggesting a mixed potential due to a side reaction. In cycle 1 a small plateau appears at ~2 V followed by another at ~1 V. The 2 V plateau disappears in cycle 2; another plateau appears at ~2.25 V as the system is cycled further. This new plateau did not correspond to the desired reaction because its average voltage was well above the formal potential for  $V(acac)_3$  disproportionation. It is worth noting that the coulombic efficiency is stable at ~70% for all cycles, suggesting that all the plateaus involve some form of the  $V(acac)_3$  as a reactant. As one plateau fades away, another grows in. It is believed that the 2.25 V plateau is associated with an electrochemical reaction based on a  $VO(acac)_2$  species. The reactions occurring during charge/discharge

will be discussed in more detail in later chapters, which will help to clarify these preliminary observations.

The low coulombic efficiency may owe to crossover of the active species through the separator, or to the loss of active vanadium to a parasitic reaction (precipitation, irreversible oxidation to vanadyl species, *etc*). Energy efficiencies were initially 30 %, but gradually increased with cycling, reaching 45 % by cycle 10. Ohmic overpotentials were probably significant because of the low conductivity of the electrolyte [81], the relatively large distance between the two electrodes in the H-type cell, and the relatively low ionic conductivity of the membrane separator. These large ohmic overpotentials reduced the energy efficiency.

#### 2.2.5 Discussion

The cell potential, number of electrons transferred, and concentration of active species determine the energy density of an RFB. To estimate the maximum energy densities for a particular chemistry, the active-species solubility limits can be used in place of its concentration. Solubilities of V, Cr, and Mn acetylacetonate complexes were measured using a densiometric method described in section 4.2, and are reported in Table 2.2.5-1.

	Cell Potential	Rate Constant $\times 10^3$ [cm/s]		Peak Height Ratio		Solubility (in acetonitrile)	Max. Energy Density
		M(II)/(III)	M(III)/(IV)	M(II)/(III)	M(III)/(IV)		
<b>V(acac)<sub>3</sub></b>	2.2 V	1 ± 0.4	1 ± 0.4	0.94	0.99	0.6 ± 0.05 M	18 Wh/L
<b>Mn(acac)<sub>3</sub></b>	1.1 V	0.8 ± 0.2	2 ± 0.1	0.92	1.13	0.6 ± 0.05 M	9 Wh/L
<b>Cr(acac)<sub>3</sub></b>	3.4 V	4 ± 2	7 ± 5	1.27	>>1	0.4 ± 0.05 M	18 Wh/L

Table 2.2.5-1 Summary of all active-metal performance characteristics.

The solubilities of V and Mn complexes in ACN were near 0.6 M, whereas the Cr complex was only soluble up to 0.4M. The cell potential of Cr was the highest, however, followed by V and Mn. Thus the maximum energy density was the same for V and Cr, and significantly lower for Mn.

To choose the more promising metal center between V and Cr, the reversibility of the disproportionation reaction and its kinetics should be taken into account. The effective rate constant was estimated using equation ( 2-1 ). The rate constants of the reactions for V and Mn were comparable, while those for Cr were approximately four times larger. This is likely not a fair comparison since this equation assumes reversible peak height ratios, which is not true for Cr for which irreversible models should be used. The peak height ratio for Cr was significantly larger than unity for both couples, while those for Mn and V were near unity for both couples. In conclusion, vanadium was selected as the active metal for the experiments moving forward because of its high maximum energy density and good reversibility.



## 2.3 Ligand Modification

### 2.3.1 Background

The active metal is not the only factor affecting the reaction potential, reversibility, and thermodynamics of RFB active species. The ligand surrounding the metal plays a significant role in active-species performance. Often the ligand will cause redox potentials to shift, change kinetic rates, or affect the reversibility of the half-reactions. Ligand choice is also a critical determinant of active-species solubility, since specific interactions between the solvent and active species occur predominantly with atoms in the ligand. This will be discussed further in this section, and will also be addressed in the study of solvents and supports in section 2.4. Much previous research has investigated the effect of ligands on coordination-complex electrochemistry.

Gritzner *et al.* examined several different active metals and how they were affected by modifying the ligands attached to them [82]. In particular, Gritzner focused on the reduction of Fe, Cr, and Cu centers with  $\text{acac}^-$  and hexafluoroacetylacetonate ( $\text{hfacac}^-$ ) ligand using platinum and hanging mercury drop electrodes. Very different voltammetric responses were observed depending on the ligand being studied. In the region of interest, two redox couples were observed for  $\text{Cr}(\text{acac})_3$  and three couples were observed for  $\text{Cr}(\text{hfacac})_3$ . This observation is due to a large positive shift of the redox couple (1.7 V for Cr), observed in all systems, when moving from an  $\text{acac}^-$  to  $\text{hfacac}^-$  ligand. Gritzner *et al.* proposes that the electron-withdrawing fluorine atoms facilitate the acceptance of an electron to the redox center. The amount of shift

observed depends strongly on the active-species metal center and is near zero for iron complexes. These observations were also seen by Patterson *et al.* when using Ru active metal [83], supporting the observations by Gritzner *et al.*

Yamamura *et al.* examined the effect of ligands in the context of a non-aqueous RFB system [48]. The active metal used was uranium, a choice motivated by the availability of spent nuclear waste, which presumably can be obtained at very low cost. Several different  $\beta$ -diketonate ligands were used, including  $\text{acac}^-$ , dipivaloylmethane ( $\text{dpm}^-$ ), and  $\text{hfacac}^-$ . The reaction of U(IV) / U(V) was examined using CV for the different ligands; two redox couples were observed in the range between  $-1$  V and  $-2$  V vs.  $\text{Fc}/\text{Fc}^+$ . One of the peaks is associated with the free ligand, suggesting that the complex decomposed. This was confirmed by the addition of free ligand to the system. The remaining couple corresponded to a change in oxidation state of the complex, and had a formal potential of  $-0.97$  V,  $-1.46$  V, and  $-1.52$  V for  $\text{hfacac}^-$ ,  $\text{acac}^-$ , and  $\text{dpm}^-$  respectively. This  $0.55$  V shift is associated only with the ligand and appears consistent with the hypothesis of Gritzner *et al.* Using these observations, it is possible to use electron-withdrawing characteristics of functional groups to predict how ligand structure will shift equilibrium potentials.

The solubility of complexes using different ligands in ACN, dimethylsulfoxide, dimethylformamide, and propylene carbonate was also examined by Yamamura *et al.* [48]. Solubilities over  $0.8$  M were achieved with the  $\text{hfacac}^-$  ligand complexes in all solvents except propylene carbonate. The solubility of the  $\text{acac}^-$  ligand complexes were lower (solubility  $\sim 0.4$  M) than the

hfacac<sup>-</sup> counterpart. The dpm<sup>-</sup> ligand complexes showed very low solubility in all solvents except dimethylformamide.

The electrochemical properties and solubilities of several functionalized  $\beta$ -diketonate vanadium complexes are investigated in this section. The ligand modification project was directed by Dr. Alice Sleightholme. The complexes were created by the Sanford group in the University of Michigan Chemistry Department. I performed electrochemical studies and solubility measurements.

### 2.3.2 Approach

V(acac)<sub>3</sub> has very reversible electrochemistry in acetonitrile, but a much higher solubility is needed to compete with aqueous systems. Also it would be desirable to have a vanadium complex that better resists oxidation to a vanadyl center. It is worth noting that solvent choice for RFBs is dictated primarily by electrochemical stability and the ability to provide high ionic conductivity. It is desirable for solvents to be very polar, because high polarity makes ionic species more likely to dissociate, providing larger ionic conductivity to electrolytic solutions [84]. Thus one of the more logical choices for a solvent is ACN, which is one of the most polar non-aqueous solvents available (its dielectric constant is 36.6; its dipole moment is 3.92 D).

But to enhance solubility, the ligands surrounding the active species must be chemically similar to the solvent. In V(acac)<sub>3</sub>, the oxygen atoms in acac<sup>-</sup> are coordinated to V in an octahedral configuration; the three acetylacetonate ligands are arranged such that there is no net molecular polarity. Furthermore, the

outward facing part of the ligand is a hydrocarbon chain which is very different than the solvent. Thus the solubility of  $V(\text{acac})_3$  might be expected to be low in ACN.

Initial ligand-modification experiments focused on functionalizing the acetylacetonone (Hacac) ligand precursor (cf. Figure 2.3.2-1) by appending hydrocarbon groups in place of terminal H atoms. The Sanford group provided V complexes involving a variety of custom ligands, including 2,2,6,6-tetramethyl-3,5-heptanedionate (Htmhd), 1,5-diphenyl-2,4-pentanedionate (Hdppd), and 3-methyl-2,4-pentanedionate (Hmpd), summarized in Figure 2.3.2-2.

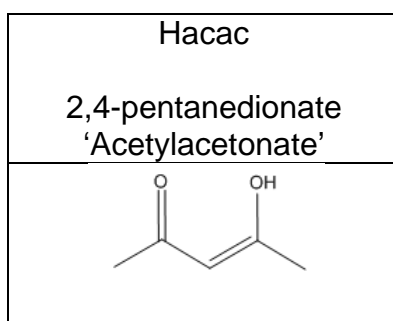


Figure 2.3.2-1 Base ligand structure for modifications

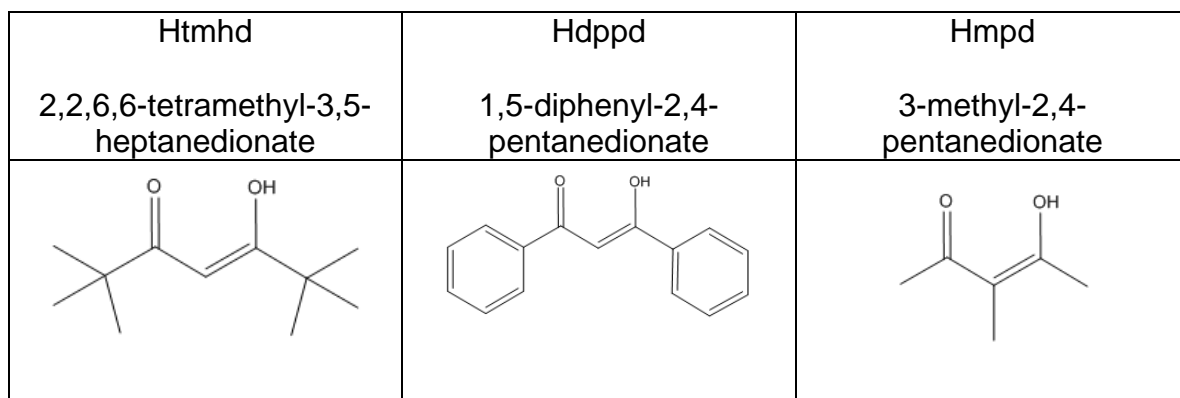


Figure 2.3.2-2 Structures of ligands created by Sanford group in the University of Michigan Chemistry Department.

Htmhd and Hdppd are modifications to the first and fifth carbons of acetylacetonone while Hmpd modifies the third carbon. Literature also suggests that it is possible to functionalize the first or fifth carbon individually [48]. The ligands used could sterically hinder attack of the V center by oxygen, and their different electron-withdrawing properties could shift the redox potentials of the complex. But the ligand structures shown in Figure 2.3.2-2 are not expected to increase the solubility of a V complex in a polar solvent like ACN, because the complexes remain non-polar, and functionalization of the ligands also makes them larger.

### 2.3.3 Results

#### *Acetylacetonate [acac]*

Detailed characterization of  $\text{acac}^-$  complexes is critical to the understanding of cyclic voltammograms associated with functionalized complexes. Examination of the cyclic voltammograms of  $\text{V}(\text{acac})_3$  in Figure 2.2.4-1 and Figure 2.2.4-5 does not reveal any significant peaks associated with the free ligand. Thus, to get a clear picture of how free ligand affects the voltammetric response, a procedure adopted from Richert *et al.* was used [85]. The Hacac is mixed with a strong base (tetraethylammonium hydroxide, TEAOH) to deprotonate it, thus liberating free  $\text{acac}^-$  that can be oxidized. Figure 2.3.3-1 shows the resulting CV when this experiment is performed. Multiple lines on the plot show that the peak current at  $\sim 0.05$  V increases in direct proportion to the TEAOH concentration. This indicates that the peak is associated with the free ligand being created since auxiliary experiments rule out most other options.

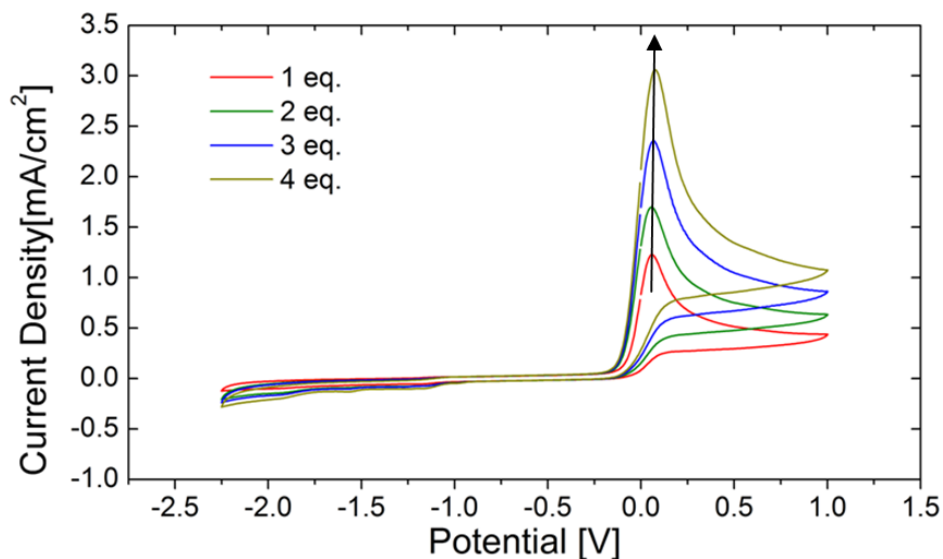


Figure 2.3.3-1 Cyclic voltammogram of 0.1 M TEABF<sub>4</sub> in acetonitrile at 100 mV/s with a glassy carbon working electrode. Sequential additions of 1 equivalent of ~2.6 mM Hacac and ~2.3 mM TEAOH.

Based on the results shown in Figure 2.3.3-1, it is expected that an oxidation peak at ~0.05 V should appear when TEAOH is added to a solution of V(acac)<sub>3</sub>, since the strong base should oxidize the vanadium and remove ligands from the complex just as it did with Hacac. This experiment has been tried by Richert *et al.* in an iron acetylacetonate (Fe(acac)<sub>3</sub>) solution. They observed an intermediate peak at short times which disappeared in favor of a peak at the location observed in the Hacac + TEAOH experiment, as Figure 2.3.3-2 shows.

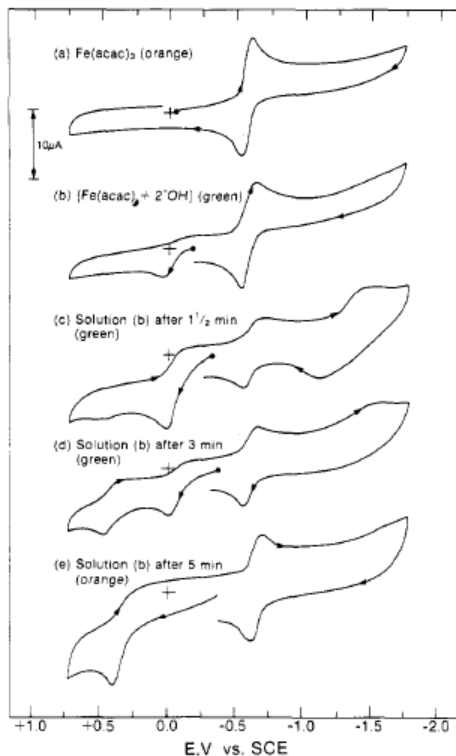


Figure 2.3.3-2 Cyclic voltammograms: (a) 0.5 mM  $\text{Fe}(\text{acac})_3$ ; (b) 0.5 mM  $\text{Fe}(\text{acac})_3 + 2 \text{ equiv of OH}^-$  [ $(\text{Bu}_4\text{N})\text{OH}$ ], initial scan; (c) solution from (b), 1.5 min later; (d) solution from (b), 3 min later; (e) solution from (b), 5 min later. Cold acetonitrile [0.1 M  $(\text{Et}_4\text{Cl})\text{ClO}_4$ ] (dry ice/acetonitrile bath) solutions were used. Conditions: scan rate 0.1 V/s; glassy-carbon working electrode ( $0.09 \text{ cm}^2$ ); SCE vs NHE, +0.242 V. Figure reproduced from [85].

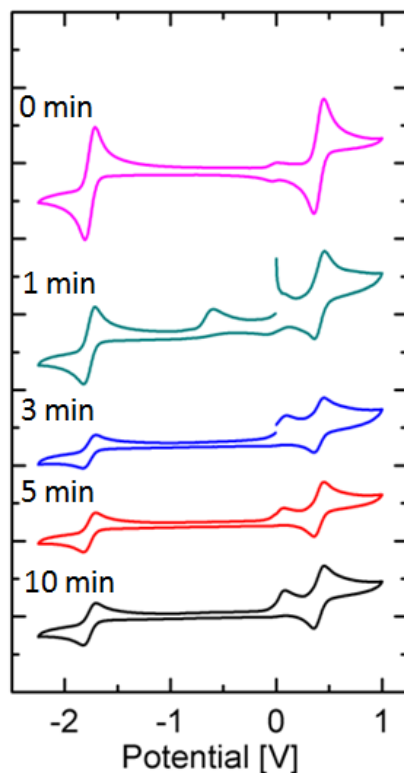


Figure 2.3.3-3 Cyclic voltammogram of 0.01 M  $V(acac)_3$ , 0.01 M TEAOH, and 0.1 M  $TEABF_4$  in acetonitrile. Solution cycled at 100 mV/s; displaying voltammograms from [pink] 0 min, [green] 1 min, [blue] 3 min, [red] 5 min, [black] 10 min after the addition of the TEAOH.

Figure 2.3.3-3 shows the results of a similar experiment to that of Richert *et al.* with the  $V(acac)_3$  active species. As expected, the results are similar, in that an intermediate oxidation is observed at short time at  $-0.5$  V. This peak disappears in favor of an increase in the peak at  $+0.05$  V associated with the free ligand. A similar strategy will be used for the ligands made at the University of Michigan when determining if any peaks in the cyclic voltammogram owe to the free ligand.

#### *2,2,6,6-tetramethyl-3,5-heptanedionate [Htmhd]*

The compounds made by the University of Michigan Chemistry Department were tested under the same window as used for  $acac^-$  [ $-2.25$  V to



1.0 V], unless the window was insufficient for observing the redox couples. Within this potential window, the solutions were subjected to scan rates of 500, 200, 100, 50, 20, and 10 mV/s. After this CV was performed, the window was widened to examine the full stability window afforded by the ACN solvent. Throughout this process, a variety of potential windows were used to determine the source of each peak. If, for example, a first peak only appears when the window being scanned includes a second peak, then the first peak likely corresponds to a half-reaction involving a species produced with the second. Lastly, TEAOH was added to the solution with the intention of observing an increase in the peak current associated with the free ligand.

The first ligand molecule we discuss is Htmhd, which provides an anion,  $\text{tmhd}^-$ , that can coordinate with vanadium. Vanadium tris(2,2,6,6-tetramethyl-3.5-heptanedione) ( $\text{V}(\text{tmhd})_3$ ) was found to have 0.011 M solubility in ACN. Figure 2.3.3-4 shows the cyclic voltammograms for  $\text{V}(\text{tmhd})_3$  in ACN with a 0.5 M  $\text{TEABF}_4$  supporting electrolyte. The solutes were not completely soluble at the 0.1 M concentration prepared, so the concentrations stated in the figure caption are not reflected in the peak currents. Nevertheless, redox couples believed to owe to the disproportionation of the vanadium complex (based on their being the most significant peaks in the voltammogram) were observed at  $-2.05$  V and  $+0.21$  V vs  $\text{Ag}/\text{Ag}^+$ . Thus a 2.26 V formal potential is expected for a RFB made with this active species, which is 0.08 V higher than the disproportionation of  $\text{V}(\text{acac})_3$  yields. The peak-height ratios are near unity for these couples and no appreciable extraneous peaks were observed over this potential range.

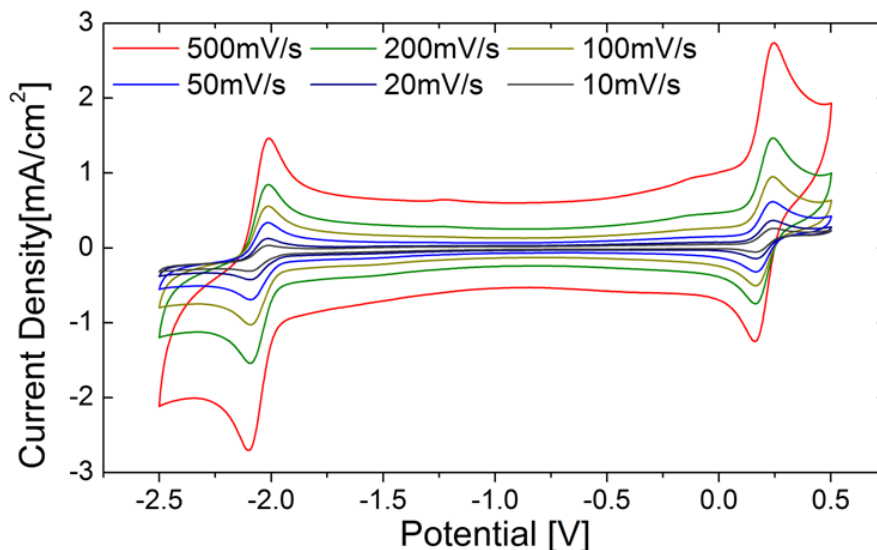


Figure 2.3.3-4 Cyclic voltammograms of 0.01 M  $V(tmhd)_3$ , 0.5 M  $TEABF_4$  in acetonitrile with a glassy carbon electrode. Multiple voltammograms were taken at varying scan rates.

Although no significant unexpected peaks arose in CV of this complex, it is still important to know where the free ligand peak occurs when looking for evidence of long-term degradation of the complex during charge/discharge experiments. Thus TEAOH was added in increments to liberate the ligand anions. This reaction takes time to go to completion, so data was not measured until 15 minutes after the addition of TEAOH. Four different quantities of TEAOH were added so that a trend in peak current arising from the addition could be observed; results are shown in Figure 2.3.3-5. There are three peaks that increase in height with increasing TEAOH concentration, located at: -2.65 V, 0.0 V, and several others in the range of 0.75-0.93 V. To help with assigning these peaks to electrochemical reactions, the ligand was examined by itself.

Figure 2.3.3-6 shows the cyclic voltammogram for a solution containing only the Htmhd molecule and the Htmhd + TEAOH in 0.5 M  $TEABF_4$  and ACN.

This CV was performed using a larger potential window than the one shown in the previous figure to establish the entire stability window. In this case, a reduction peak is observed at  $-2.65$  V, and oxidation peaks appear near  $0$  V and  $+1.8$  V. Unexpectedly, adding TEAOH to the  $\text{Htmhd}$  does not appear to affect the electrochemistry of the complex, suggesting it may already be deprotonated in the solution (this would not be the case in the  $\text{V}(\text{tmhd})_3$ ). Using this information to explain Figure 2.3.3-5 suggests that the  $0$  V and  $-2.65$  V peaks are associated with the free ligand and the peak at higher potentials may be related to the modified active complex that forms upon its liberation.

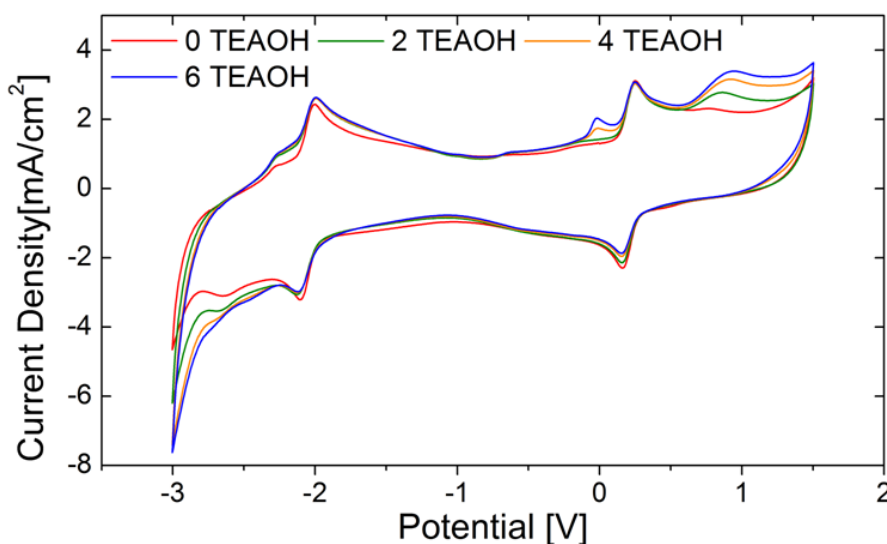


Figure 2.3.3-5 Cyclic voltammograms of  $0.01$  M  $\text{V}(\text{tmhd})_3$ ,  $0.5$  M  $\text{TEABF}_4$  in acetonitrile with a glassy carbon electrode at a scan rate of  $500$  mV/s. Multiple voltammograms were taken at varying amounts of TEAOH added.

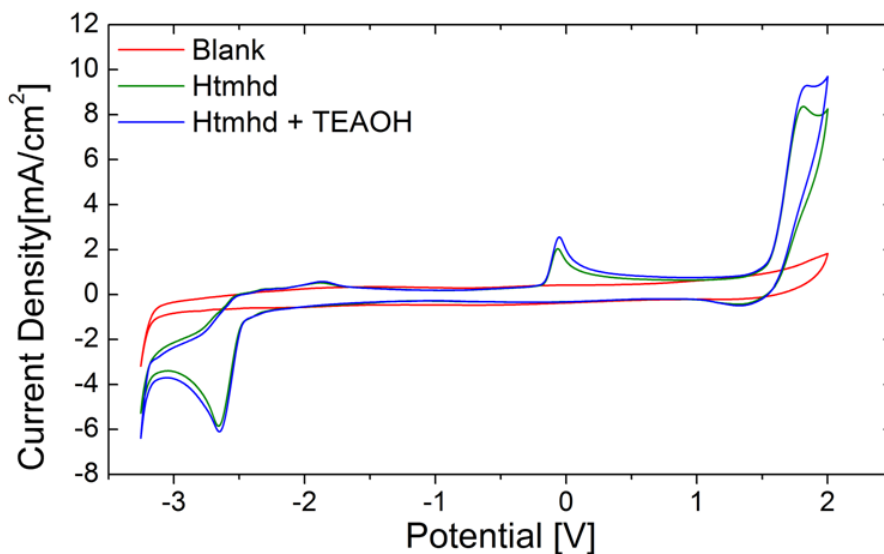


Figure 2.3.3-6 Cyclic voltammograms of [Htmhd] 0.01 M Htmhd and 0.5 M TEABF<sub>4</sub> in acetonitrile, [Htmhd + TEAOH] 0.01 M Htmhd, 0.01 M TEAOH, and 0.5 M TEABF<sub>4</sub> in acetonitrile, [Blank] 0.5 M TEABF<sub>4</sub> in acetonitrile with a glassy carbon electrode at a scan rate of 100 mV/s.

#### *1,5-diphenyl-2,4-pentanedionate [Hdppd]*

The second ligand we examined was Hdppd. The solubility of vanadium tris(1,5-diphenyl-2,4-pentanedione) (V(dppd)<sub>3</sub>) in acetonitrile was 0.002 M. Figure 2.3.3-7 shows the cyclic voltammograms for V(dppd)<sub>3</sub> in ACN. As with Htmhd, the concentration stated in the figure caption is not correct since it was not completely soluble. In fact, the solubility of active species is so low that it is difficult to discern which peaks arise from redox reactions involving the complex, and which arise from impurities in the sample. The voltammogram shows six primary redox couples: -2.1 V, -1.85 V, -1.5 V, 0.1 V, 0.45 V, and 0.7 V. The relative peak heights look comparable for the peaks at -2.1 V, -1.5 V, 0.45 V, and 0.7 V, which is an initial indication that the reactant whose electrochemistry underlies each peak has a similar concentration, and thus may be common to all

of the peaks. Furthermore, when increasing the potential window for the experiment two additional redox couples are observed at  $-2.35$  V and  $-2.65$  V as well as an oxidation peak at  $-0.9$  V (shown in Figure 2.3.3-8). The ligand-freeing experiment is necessary to narrow down the fundamental source of this electrochemical response.

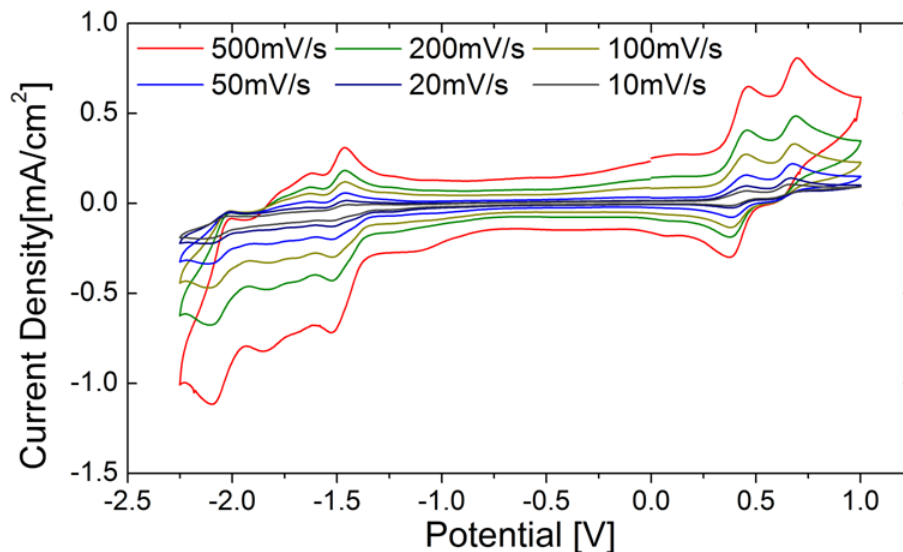


Figure 2.3.3-7 Cyclic voltammograms of  $0.01$  M  $V(dppd)_3$ ,  $0.5$  M  $TEABF_4$  in acetonitrile with a glassy carbon electrode. Multiple voltammograms were taken at varying scan rates.

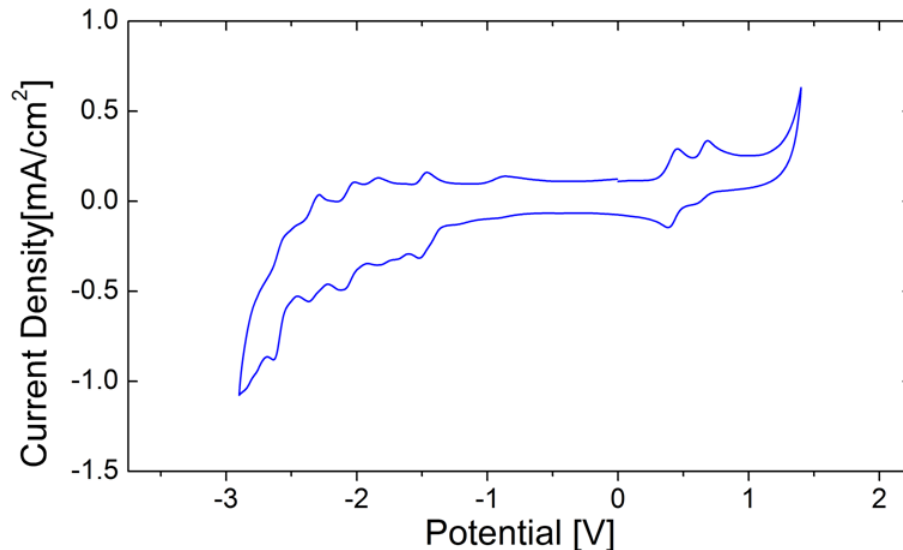


Figure 2.3.3-8 Cyclic voltammograms of 0.01 M  $V(dppd)_3$ , 0.5 M  $TEABF_4$  in acetonitrile with a glassy carbon electrode at 100 mV/s. Voltage window  $-2.9$  V to  $1.4$  V.

Figure 2.3.3-9 shows the cyclic voltammogram for ACN solutions of the Hdppd ligand and Hdppd + TEAOH, which should show evidence of  $dppd^-$ . Peaks are observed at  $-2.1$  V,  $-1.9$  V,  $-0.9$  V,  $+0.14$  V, and  $+1.62$  V. The peak heights of all the redox peaks are decreased by the presence of TEAOH, excepting the peak at  $-0.9$  V, which may be inherent to the solution. Thus, of the eight peaks observed in the original cyclic voltammogram, only the peaks at  $-2.65$  V,  $-2.35$  V,  $-1.5$  V,  $+0.45$  V, and  $+0.7$  V cannot be attributed to redox chemistry involving the ligand.

To confirm what has been observed in the ligand-only and active-species-only experiments, a TEAOH solution was incrementally added, and a cyclic voltammogram was recorded after 15 minutes. Four different amounts of TEAOH were added, yielding the cyclic voltammograms shown in Figure 2.3.3-10. There appears to be some oxygen getting into the CV cell,

confounding the results – as can be observed by the reduction at  $\sim -1.15$  V. This makes it impossible to decipher trends based on the amount of TEAOH added.

It is difficult to make conclusions regarding the electrochemistry of this system since it appears that the ligand is dissolved in the solution at a concentration approximately equal to the active species, and the active species is at a concentration so low that any other impurities will contribute significant peaks. Based solely on its solubility limit, Hdppd is not viable as a ligand for use in ACN solutions.

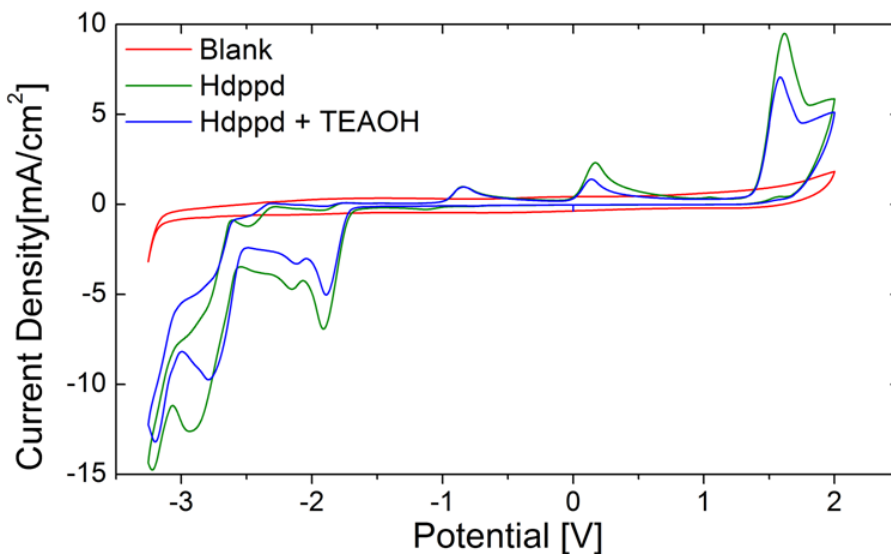


Figure 2.3.3-9 Cyclic voltammograms of [Hdppd] 0.01 M Hdppd and 0.5 M TEABF<sub>4</sub> in acetonitrile, [Hdppd + TEAOH] 0.01 M Hdppd, 0.01 M TEAOH, and 0.5 M TEABF<sub>4</sub> in acetonitrile, [Blank] 0.5 M TEABF<sub>4</sub> in acetonitrile with a glassy carbon electrode at a scan rate of 100 mV/s.

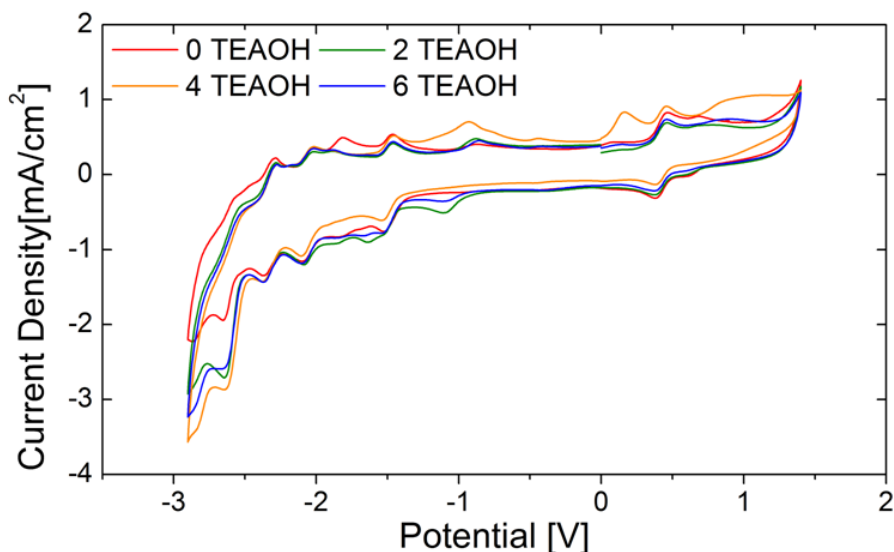


Figure 2.3.3-10 Cyclic voltammograms of 0.01 M  $V(dppd)_3$ , 0.5 M  $TEABF_4$  in acetonitrile with a glassy carbon electrode at a scan rate of 500 mV/s. Multiple voltammograms were taken at varying amounts of TEAOH added.

### *3-methyl-2,4-pentanedionate [Hmpd]*

The last ligand we examined was Hmpd. The solubility of vanadium tris(3-methyl-2,4-pentanedione) ( $V(mpd)_3$ ) in ACN was 0.15 M. Figure 2.3.3-11 shows cyclic voltammograms for  $V(mpd)_3$  in 0.5M  $TEABF_4$  and ACN. The solutes were completely soluble and resulted in redox couples at  $-1.95$  V and  $+0.11$  V vs.  $Ag/Ag^+$ , which were likely caused by the vanadium complex since they are the only significant peaks in the voltammogram. Thus a 2.06 V formal potential is expected for a RFB based on the disproportionation of this active species, a cell voltage 0.12 V lower than  $V(acac)_3$ . The peak height ratios are 0.79 and 0.88 for the peaks at  $-1.95$  V and  $+0.11$  V respectively. It is visually apparent that the peak height ratio is not unity and the reaction kinetics should therefore be examined further if this complex is tested further. Note also that one other large redox couple is visible in the cyclic voltammogram, centered at 0.51 V. I



hypothesize that this couple may correspond to a degrade, vanadyl-centered complex, as is observed with  $V(\text{acac})_3$  system. A minor oxidation peak is also located at  $\sim -0.2$  V and may suggest the presence of free ligand.

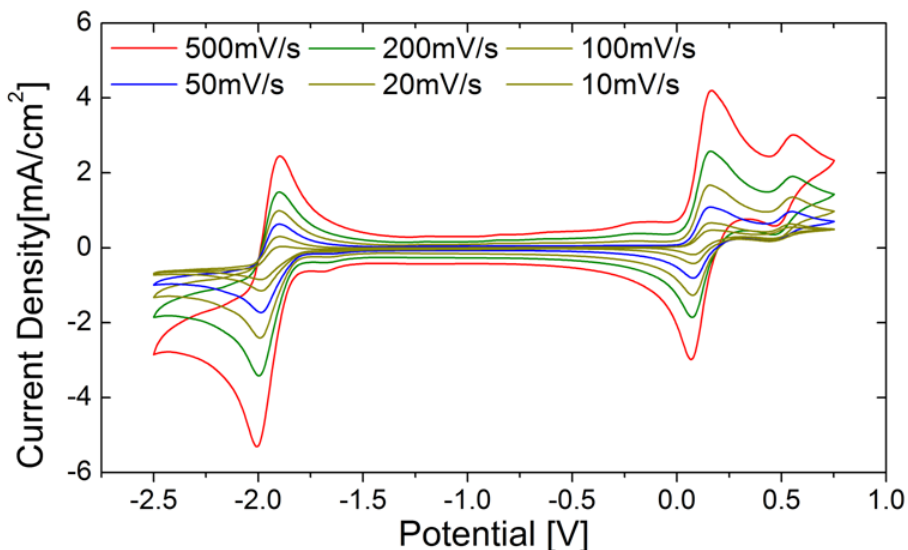


Figure 2.3.3-11 Cyclic voltammograms of 0.01 M  $V(\text{mpd})_3$ , 0.5 M  $\text{TEABF}_4$  in acetonitrile with a glassy carbon electrode. Multiple voltammograms were taken at varying scan rates.

Five different quantities of TEAOH were added, leading to the trend in peak current shown in Figure 2.3.3-12. Two peaks, located at  $-0.2$  V and  $+0.5$  V, change height as the concentration of TEAOH increases; the peak current at  $-0.2$  V increases, while the peak current at  $+0.5$  V decreases. Note that there are peaks located at  $-2.7$  V,  $-2.55$  V,  $-1.25$  V, and  $+1.45$  V as well, which do not scale with the TEAOH concentration. Based on previous CV experiments, it is known that the reduction peak at  $-1.25$  V owes to superoxide [79]. To help with assigning these peaks, the ligand was again examined by itself.

Figure 2.3.3-13 shows the cyclic voltammogram for ACN solutions of the Hmpd ligand and Hmpd + TEAOH with 0.5 M  $\text{TEABF}_4$ . For Hmpd alone,

reduction peaks are observed at  $-2.7$  V and  $-2.55$  V and an oxidation peak occurs at  $+1.45$  V. This accounts for all the peaks that do not scale with TEAOH concentration. An oxidation peak appears at  $-0.2$  V which matches one of the peaks scaling with TEAOH concentration. Using this information to explain Figure 2.3.3-12 suggests that the  $-0.2$  V peak is associated with the free ligand and the peak at higher potentials may be related to the resulting active complex.

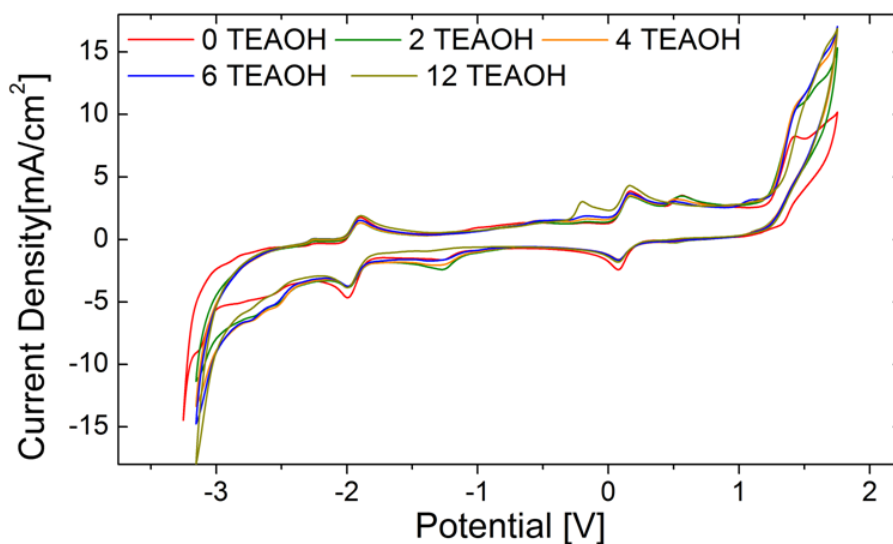


Figure 2.3.3-12 Cyclic voltammograms of  $0.01$  M  $V(\text{mpd})_3$ ,  $0.5$  M  $\text{TEABF}_4$  in acetonitrile with a glassy carbon electrode at a scan rate of  $500$  mV/s. Multiple voltammograms were taken at varying amounts of TEAOH added.

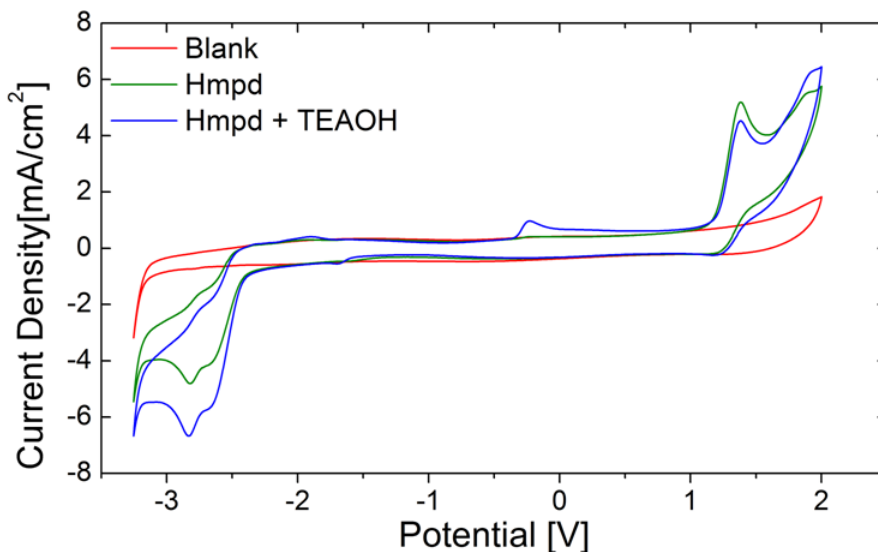


Figure 2.3.3-13 Cyclic voltammograms of [Hmpd] 0.01 M Hmpd and 0.5 M TEABF<sub>4</sub> in acetonitrile, [Hmpd + TEAOH] 0.01 M Hmpd, 0.01 M TEAOH, and 0.5 M TEABF<sub>4</sub> in acetonitrile, [Blank] 0.5 M TEABF<sub>4</sub> in acetonitrile with a glassy carbon electrode at a scan rate of 100 mV/s.

#### 2.3.4 Discussion & Future Ligand Work

The  $\text{acac}^-$  ligand was functionalized to produce  $\text{tmhd}^-$ ,  $\text{dppd}^-$ , and  $\text{mpd}^-$ . It showed that the solubilities of  $\text{VL}_3$  complexes with  $\text{L} = \text{acac}$ ,  $\text{tmhd}$ ,  $\text{dppd}$ , and  $\text{mpd}$  are 0.6 M, 0.011 M, 0.002 M, and 0.15 M respectively. Thus the solubility can be changed by two orders of magnitude by changing ligand structure, an observation similar to what Yamamura *et al.* saw with uranium complexes [48]. However, the solubility decreased, rather than increasing, a trend which does not help to produce RFB electrolytes with higher energy density. This trend likely owes to the fact that the addition of hydrocarbon functional groups in a symmetric fashion makes the active complex larger and fails to change its polarity. In order to increase the solubility of the active species in polar solvents like ACN, the ligand must have polar functionality as well. Thus, a suggested next step for

ligand modification will be the addition of pendant poly-ether groups to the third carbon position.

## 2.4 Solvent and Support Selection

### 2.4.1 Background

The solvent and supporting electrolyte are key components of an RFB solution; the supporting electrolyte provides ionic conductivity and the solvent controls the maximum stable potential window, as well as determining the mechanical properties and basic thermodynamic properties of the solution. Work on solvents and supporting electrolytes must be performed simultaneously, since a solution with no supporting electrolyte is not feasible for electrochemical studies due to low inherent conductivities of pure solvents. Many possible combinations of solvent and supporting electrolyte are available for examination. Although some information is available in the literature, there are few systematic studies that give information directly applicable to non-aqueous RFB research.

Considerable information about non-aqueous solvents is available from the past 30 years of research on lithium-ion batteries. A review by Kang Xu describes different non-aqueous solvents in detail [84]. The review suggests that only polar solvents are feasible for solvating ions to any significant extent. Thus the supporting electrolyte as well as charged species will both require polar solvents. In lithium-ion batteries, it is uncommon to use a single solvent; instead, the properties of electrolytes are tailored to specific applications by using multiple-solvent blends. Since my research is preliminary in this area, I will limit

the number of possible solvent/support combinations by restricting the investigations to pure solvents. My research suggests that mixed solvents may be promising for optimizing the performance of RFB liquids, which could be a possible avenue for future research.

Information about supporting electrolytes can also be adapted from lithium-ion battery literature; however, the information is not directly applicable to non-aqueous RFBs because the supporting cation in these systems is always lithium. Lithium will react with the active species in the non-aqueous RFB systems focused on here, and therefore it must be exchanged for a non-reactive cation. The most common non-reactive cations used for non-aqueous electrochemistry are quaternary ammonium species. Anions including perchlorate ( $\text{ClO}_4^-$ ), tetrafluoroborate ( $\text{BF}_4^-$ ), hexafluorophosphate ( $\text{PF}_6^-$ ), trifluoromethanesulfonate ( $\text{CF}_3\text{SO}_3^-$ , also called “triflate”) and bis(trifluoromethanesulfonyl)imide ( $\text{N}[\text{CF}_3\text{SO}_2]^-$ , also called TFSI<sup>-</sup>) were discussed by Kang Xu [84]. The  $\text{ClO}_4^-$  anion is a very strong oxidizer and can lead to explosive reactions when mixed with organic solvents, and is therefore not viable for large-scale use.  $\text{BF}_4^-$  is not widely used in lithium-ion-battery research, because it provides lower conductivity than  $\text{PF}_6^-$ , while failing to provide many advantages. Triflate and TFSI<sup>-</sup> behave similarly to  $\text{BF}_4^-$  but are corrosive to aluminum substrates, which are used as current collectors in lithium batteries.  $\text{PF}_6^-$  is the most commonly used lithium-ion-battery anion used today, because it is the least expensive and least objectionable of the available options. However, any of the anions mentioned above could be feasible in a non-aqueous

RFB application, and all should be tested again in conjunction with inert cations and  $V(\text{acac})_3$  active species.

Several physical properties are of primary importance when deciding what solvent/support combination to use in a RFB. The most important properties are: high maximum solubility of the supporting electrolyte, high solubility of the active species, and high solution conductivity. Other liquid properties such as viscosity, density, flash point, boiling point, and general safety are also important concerns. Solvents should not impede reaction kinetics or active-species transport; to screen for these characteristics, minimal peak separation and peak height ratios near unity are desired in CV. Since the electrochemistry for  $V(\text{acac})_3$  is very reversible, the choice of solvent and support is expected to have little effect on its electrochemistry (this may not be accurate if the solvent drastically changes the bonds within the active species). Also, it is desirable that no additional peaks appear in CV – these would indicate a propensity for undesired side reactions involving the solvent or supporting electrolyte. If the physical properties and electrochemical characteristics are satisfactory, then it is also desirable to have a solution that is resistant to vanadyl formation (e.g. with low water solubility and oxygen solubility) and low in cost. These characteristics will be examined below for a variety of solvent/supporting electrolyte combinations.

#### 2.4.2 Experimental Design

An initial set of 25 solvent/supporting electrolyte combinations (five solvents and five supporting electrolytes) was chosen for testing. The supporting electrolytes chosen are shown in Table 2.4.2-1. Several anions and cations were

selected and combined to form various supporting electrolytes. The cations are sodium ( $\text{Na}^+$ ), tetraethylammonium ( $\text{TEA}^+$ ), Tetrabutylammonium ( $\text{TBA}^+$ ), and (1-butyl,3-methyl)imidazolium ( $\text{bmim}^+$ ). The anions are  $\text{BF}_4^-$ ,  $\text{PF}_6^-$ , and  $\text{TFSI}^-$ . The first three supporting electrolytes evaluate the effect of cation size by using the same anion, changing between  $\text{Na}^+$ ,  $\text{TEA}^+$  and  $\text{TBA}^+$ . The third and fourth electrolytes employ the same cation while varying the anion. The final supporting electrolyte is an ionic liquid and thus may provide interesting properties when compared to the former solid electrolytes. All of the supporting electrolytes [ $\text{NaBF}_4$  (Oakwood Products, US, 98 %),  $\text{TBABF}_4$  (Oakwood Products, US, 98 %),  $\text{TBAPF}_6$  (Oakwood Products, US, 98 %),  $\text{BmimTFSI}$  (Sigma Aldrich, US, >98 %), and  $\text{TEABF}_4$ ] are known to be stable in non-aqueous media [59].

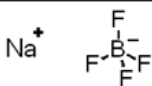
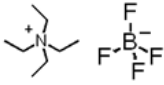
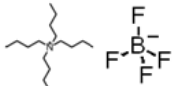
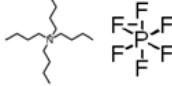
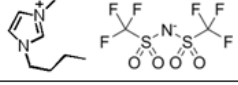
Name	Structure
Sodium Tetrafluoroborate [ $\text{NaBF}_4$ ]	
Tetraethylammonium Tetrafluoroborate [ $\text{TEABF}_4$ ]	
Tetrabutylammonium Tetrafluoroborate [ $\text{TBABF}_4$ ]	
Tetrabutylammonium Hexafluorophosphate [ $\text{TBAPF}_6$ ]	
1-butyl,3-methylimidazolium Bis(trifluoromethylsulfonyl)imide [ $\text{BmimTFSI}$ ]	

Table 2.4.2-1 List of supporting electrolytes examined and their chemical structure.

Table 2.4.2-2 shows the solvents being tested in this study along with their chemical structures [acetonitrile, dimethylformamide (Alfa Aesar, US, anhydrous 99.8 %), tetrahydrofuran (Alfa Aesar, US, anhydrous unstabilized 99.8 %),

dimethylcarbonate (Sigma Aldrich, US, anhydrous 99 %), and hexane (Alfa Aesar, US, anhydrous). They are known to be stable solvents for non-aqueous electrochemistry. Solvents must be aprotic for use in non-aqueous electrochemistry or the proton will react, dramatically reducing the solvent stability window [84]. The solvents were chosen to have a variety of functional groups and wide range of dielectric constants. The dielectric constants for these solvents are: ACN 36.64, DMF 38.25, THF 7.52, DMC 3.1, HEX 1.88 (the dielectric constant for DMC was taken from [86], while all others were from [87]). Many other solution properties vary across the solvents such as boiling point, melting point, viscosity, density, etc. but were not used as primary selection criteria for this list, and may vary inconsistently within the group.

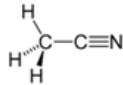
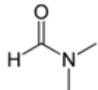

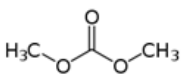
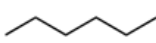
Name	Structure
Acetonitrile [ACN]	
Dimethylformamide [DMF]	
Tetrahydrofuran [THF]	
Dimethylcarbonate [DMC]	
Hexane [HEX]	

Table 2.4.2-2 List of solvents examined and their chemical structure.

To be experimentally efficient while still examining all interesting solvent and supporting electrolyte combinations, a multi-step screening algorithm was



created, schematized in Figure 2.4.2-1. The physical characterization tests were performed at the outset of the screening process, and were followed by electrochemical tests on the most promising systems. First, a 0.1 M solution of supporting electrolyte or active species in solvent was tested for its conductivity and solubility. If the solute was not completely soluble to 0.1 M, then it was deemed not useful for RFB applications and was removed from further testing. After solubility was considered, if the solution conductivity was found to be too low, it was removed from further testing on the basis that the ohmic energy loss during charge/discharge experiments would be prohibitively high. The solvent and supporting electrolyte combinations that remained after these two stages were tested to assess maximum active-species and supporting-electrolyte solubilities, as well as electrochemical performance. The maximum solubility was determined using a densimetric method outlined below. Electrochemical properties were examined using CV, focusing specifically on peak height ratios and shifts in the formal potential. If no obvious problems were observed in CVs, then a charge/discharge test was performed on the electrolyte system.

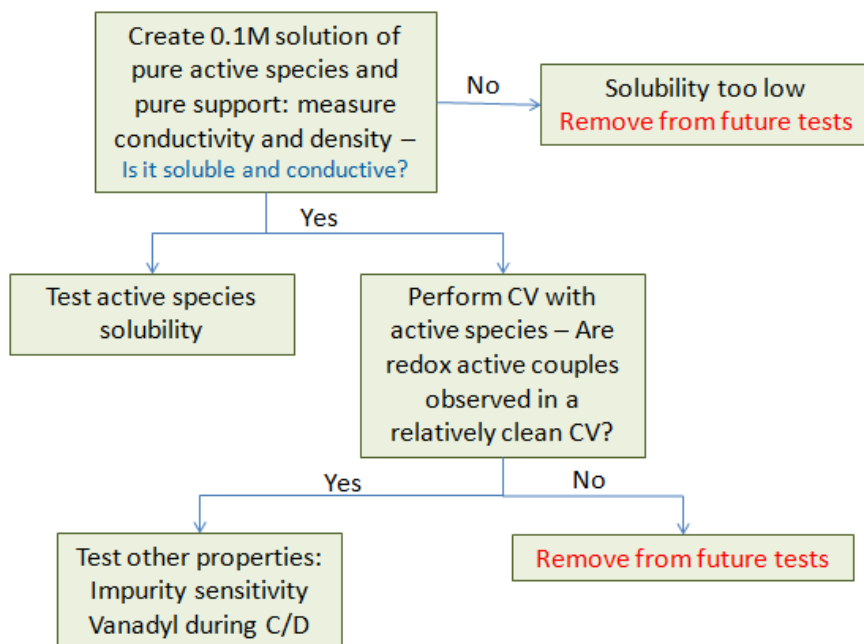


Figure 2.4.2-1 Experimental screening plan for solvent/supports.

### 2.4.3 Results: Physical Properties

The 0.1 M solutions were first screened for the minimal sufficient solubility; the results are shown in Figure 2.4.3-1.  $\text{NaBF}_4$  was not soluble at 0.1 M in any of the solvents tested. Likewise, none of the solutes were soluble in hexane. Thus  $\text{NaBF}_4$  and hexane were not studied further. Also,  $\text{TEABF}_4$  is not completely soluble at 0.1 M in THF and DMC but is soluble in ACN and DMF. The conductivities of all of the solutions were tested and are shown in Figure 2.4.3-2. The row labeled “blank” on the plot indicates the conductivities of the pure solvents, to illustrate that the electrolyte conductivities result from the presence of the supporting electrolytes, and not from the solvents themselves. The data points for hexane and  $\text{NaBF}_4$  were removed from the plot due to their low solubilities, but  $\text{TEABF}_4$  in THF and DMC remain on Figure 2.4.3-2 – although the solubility limits for these systems were less than 0.1 M, the solubility was high

enough to provide a measurable level of conductivity. A clear trend is observed across the solvents studied. Independent of the supporting electrolyte, ACN solutions have the highest conductivity, followed by DMF, THF, and DMC. THF and DMC have too low of conductivity to be feasible for the RFB system and thus were removed from further testing. Examining the supporting electrolytes failed to reveal any significant differences among them. Small differences in the conductivity would suggest that the conductivity follows the trend: TEABF<sub>4</sub> > BmimTFSI > TBABF<sub>4</sub> ~ TBAPF<sub>6</sub>. This trend matches those observed in previous reports [88].

		Solvent				
		ACN	DMF	THF	DMC	HEX
Solute	Na BF <sub>4</sub>	X	X	X	X	X
	TEA BF <sub>4</sub>			X	X	X
	TBA BF <sub>4</sub>					X
	TBA PF <sub>6</sub>					X
	bmimTFSI					X
	V(acac) <sub>3</sub>					X

Figure 2.4.3-1 Indication of solubility at 0.1 M for all solvent/solute combinations.

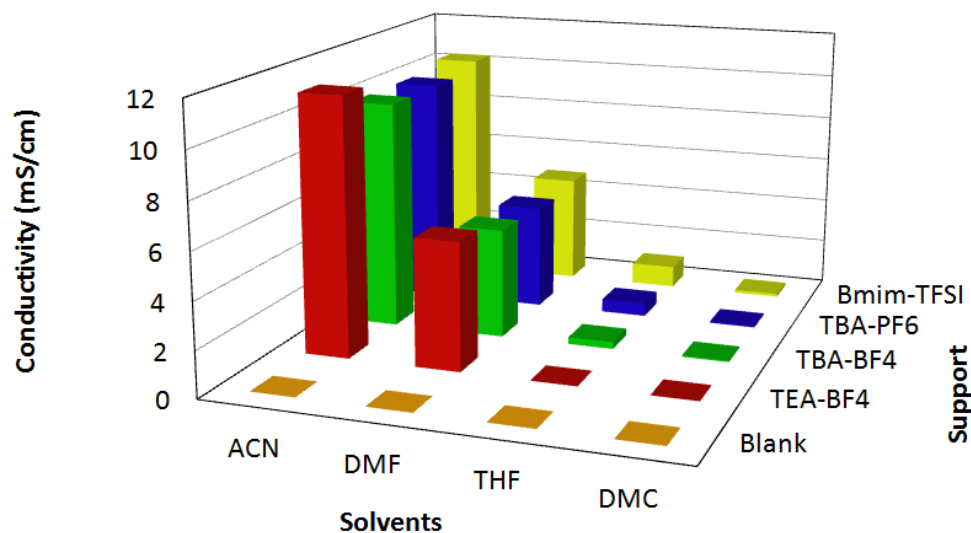


Figure 2.4.3-2 Conductivity of each 0.1 M supporting electrolyte in solvent combination.

The next step in electrolyte screening is to determine the maximum solubility of supporting electrolytes in the remaining viable solvent / supporting electrolyte combinations. This was done via a densiometric method as opposed to the more widespread evaporation method. Densiometry was used for several reasons. First, the solvents are not always volatile, and thus an evaporation method could not always be used. Even if a solvent is volatile, it is difficult to evaporate the solvent without allowing oxygen to affect the system (also, in inert glove-box atmospheres, it is desirable to keep solvent partial pressures low). Secondly, when testing solutes that are opaque it is difficult to determine when a solution is saturated, because precipitates cannot be seen.

For the densiometric method, a solution well past the saturation limit is created. The liquid head is decanted, then a fixed volume is placed in a volumetric flask, where its mass is measured to determine the saturated-solution density.

The density of binary electrolytic solutions varies approximately linearly with solute concentration across the solubility domain. If density  $\rho$  varies linearly with solute concentration  $c$ , then the partial molar volume  $\bar{v}$  of the solute is constant [89] and a plot of solution density vs. solute concentration can be used to compute

$$\bar{v} = \frac{M - (\partial\rho / \partial c)_{T,p}}{\rho_0} \quad (2-21)$$

where  $M$  is the molar mass of solute and  $\rho_0$  is the solvent density. With the electrolyte's partial molar volume known, the concentration of a saturated solution,  $c_{sat}$ , can be estimated from its density  $\rho_{sat}$  through

$$c_{sat} = \frac{\rho_{sat} - \rho_0}{M - \rho_0 \bar{v}} \quad (2-22)$$

Figure 2.4.3-3 illustrates the densities of binary solutions of  $V(acac)_3$  in ACN as a function of the  $V(acac)_3$  molar concentration. Within the 1 % experimental error, the density varied linearly with respect to concentration of the solute. When incorporated into Eq. ( 2-21 ), the slope of the linear fit in Figure 2.4.3-3 yields  $\bar{v} = 256$  mL/mol for  $V(acac)_3$  in ACN.

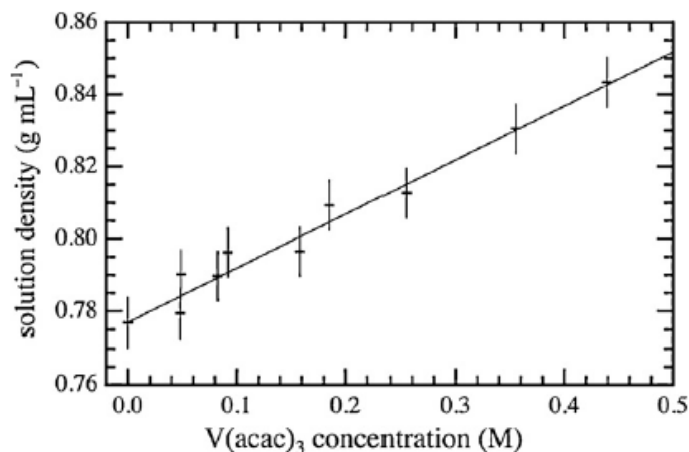


Figure 2.4.3-3 Densities of binary solutions of vanadium acetylacetonate in acetonitrile as a function of solute concentration. The points represent experimental measurements and the line is a linear fit ( $R^2 = 0.97$ ) forced through the density of pure ACN at room temperature.

Figure 2.4.3-4 shows a similar plot for the TEABF<sub>4</sub> supporting electrolyte in acetonitrile. The red dots in Figure 2.4.3-4 show the density of several solutions with varying concentrations below the solubility limit, which are connected with a trend line. The solution density is plotted as a horizontal line on a plot of density vs. concentration shown in Figure 2.4.3-4 (black line) because all solutions which are above the solubility limit will have that density. The point at which the trend line meets the black line is shown with the green circle and marks the maximum solubility for the solvent / supporting electrolyte solution; for TEABF<sub>4</sub> in ACN this limit is 1.60 M.

Using the densimetric solubility measurement method described and literature values, Figure 2.4.3-5 was created to illustrate the effect of solvent on the maximum solubility of the supporting electrolyte. The supporting electrolytes are generally more soluble in ACN than DMF. This could be correlated to the solvent polarity, which is higher for ACN than DMF. Notably, the ionic liquid

BmimTFSI was completely miscible in both solvents of interest. The vanadium acetylacetonate follows the solubility trend ACN > DMF ~ THF > DMC > HEX.

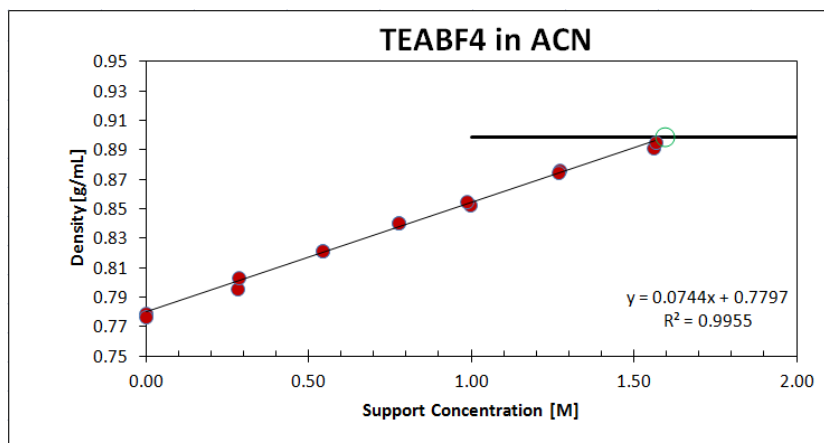


Figure 2.4.3-4 Plot of density vs. support concentration for TEABF<sub>4</sub> in ACN.

Solute	Solvent			
	ACN	DMF	THF	DMC
TEA BF <sub>4</sub>	1.70m <sup>1</sup> 1.60M	1.38m <sup>1</sup>	X <sup>1</sup>	
TBA BF <sub>4</sub>	>3.04m <sup>1</sup>	>3.04m <sup>1</sup>	>3.04m <sup>1</sup>	>3.0M
TBA PF <sub>6</sub>	1.60M	0.56M		
Bmim TFSI	Misc.	Misc.		
V(acac) <sub>3</sub>	0.60M	0.51M	0.52M	0.44M

Figure 2.4.3-5 Maximum solubility of each solute/solvent combination. Data labeled (1) are values taken from [90].

#### 2.4.4 Results: Electrochemical Properties

Although the physical properties of the solutions are very important to energy density, they are not the only factor – electrochemical stability and performance are also both integral to the utility of an RFB supporting liquid.

Cyclic voltammograms were measured for each of the eight solvents and

supporting-electrolyte combinations of interest (solvents DMF and ACN; supporting electrolytes TEABF<sub>4</sub>, TBABF<sub>4</sub>, TBAPF<sub>6</sub>, and BmimTFSI); the results are shown in Figure 2.4.4-1 through Figure 2.4.4-4. Each figure shows how the V(acac)<sub>3</sub> electrochemistry is affected by the solvent for a single supporting electrolyte. The results at low scan rates (less than 50mV/s) suggest that all solvent and supporting electrolyte combinations are essentially reversible. The double layer region, at ~-0.5 V, has comparable shape for all the solvent/supporting electrolyte combinations, suggesting that the supporting electrolytes are fully dissociated in both solvents at the concentrations used; the peak heights yielded by the redox couples are not the same, however showing that mass transfer of the active species differs significantly across the solvents. In general, the ACN based solutions yield higher peak heights with all supporting electrolyte tested, as would be expected because ACN has the lowest viscosity. Furthermore, limiting currents at high and low voltage in the ACN system appear larger, consistent with the assertion that diffusion in ACN is faster.

Another observation is that the formal potentials of active-species redox reactions are shifted to relatively negative potentials in ACN. The V(II) / V(III) couple is shifted ~60 mV while the V(III) / V(IV) couple is shifted ~15 mV. The formal potential of a redox couple depends on interactions with the solvent such as: electrostatic interactions between the solvent dipoles, changes in internal solvent order, and specific solvent effects such as hydrogen bonding and Lewis acid/base interactions [91]. This positive shift suggests the solvent interacts with the solute in a stabilizing manner as is expected due to the differences in the



solvents properties. The formal potentials of the V(II)/ V(III) redox couple are not statistically different for TEABF<sub>4</sub>, TBABF<sub>4</sub>, and TBAPF<sub>6</sub> in ACN, but the potential in BmimTFSI/ACN is 15 mV higher; the same trend holds across the salts in DMF. The formal potentials of the V(III)/V(IV) redox couple are not statistically different for any supporting electrolyte in either solvent. The peak separation and peak height ratio do not show statistically significant changes amongst the supporting electrolytes or solvents. The lone exception being the peak separation for the V(II) / V(III) redox couple, which does show some variation. In DMF the peak separation for the V(II)/V(III) couple is 107 mV ± 5 mV and in ACN it is 95 mV ± 5 mV. This suggests that the kinetics of V(III) reduction are faster in ACN than DMF, but that the supporting electrolyte has minimal effect on reaction rates.

Some qualitative understanding of differences in stability among the supporting electrolyte systems can be seen by examining peaks in CV that are not associated with the V(II/III) or V(III)/(IV) reactions. The main peaks of interest are the oxidation of free ligand at ~0 V and the redox reaction of vanadyl acetylacetonate at ~0.75 V. In Figure 2.4.4-1, using TEABF<sub>4</sub> as the supporting electrolyte, the auxiliary peaks are present in ACN, but are not present in DMF. No observable trends are present to predict which supporting electrolyte will suppress certain electrochemistry based on Figure 2.4.4-2 through Figure 2.4.4-4. However, changing supporting electrolytes could be a useful method to restrict unwanted side reactions, since the choice of support does not appear to

appreciable effect on the physical or electrochemical properties of the solution as a whole.

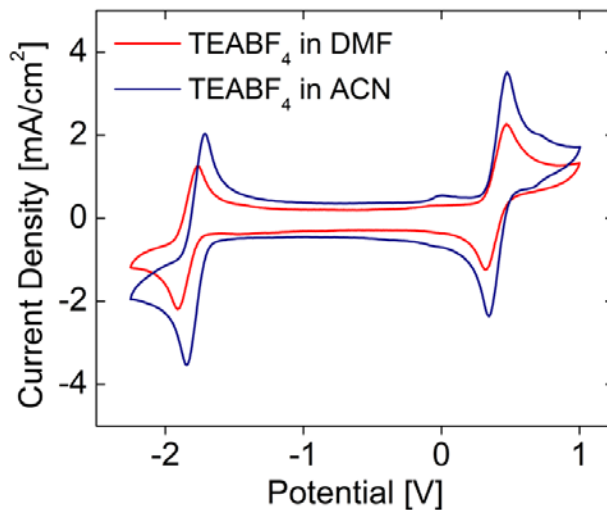


Figure 2.4.4-1 Cyclic voltammogram of 0.01 M V(acac)<sub>3</sub> and 0.05 M TEABF<sub>4</sub> in DMF or ACN. Scan rate 100 mV/s with glassy carbon working electrode and Ag/Ag<sup>+</sup> reference electrode.

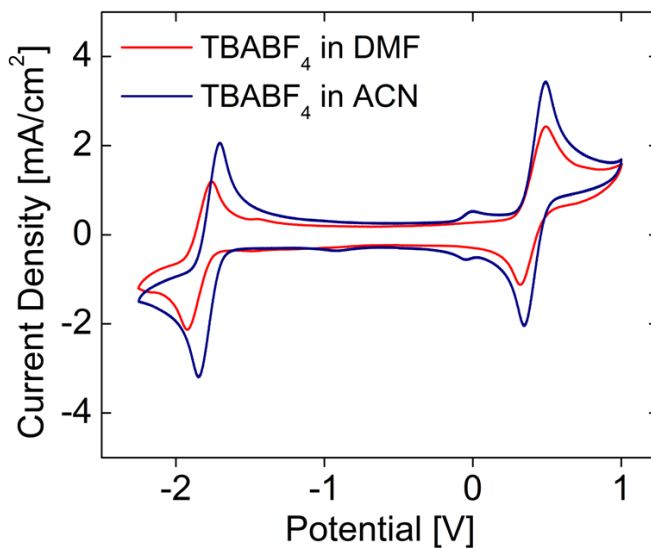


Figure 2.4.4-2 Cyclic voltammogram of 0.01 M V(acac)<sub>3</sub> and 0.05 M TBABF<sub>4</sub> in DMF or ACN. Scan rate 100 mV/s with glassy carbon working electrode and Ag/Ag<sup>+</sup> reference electrode.

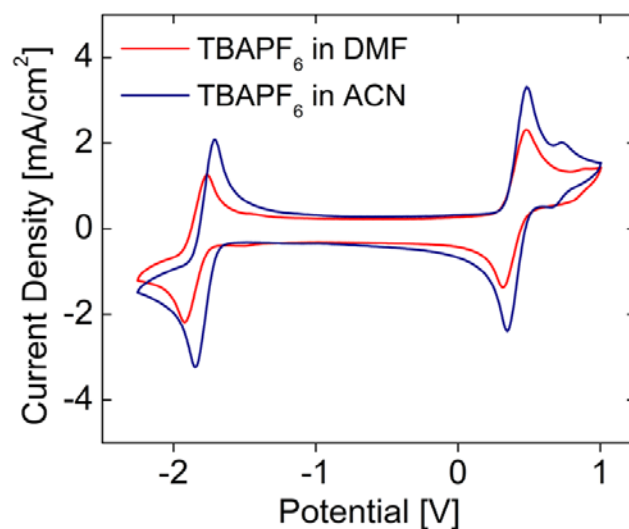


Figure 2.4.4-3 Cyclic voltammogram of 0.01 M  $V(acac)_3$  and 0.05 M  $TBAPF_6$  in DMF or ACN. Scan rate 100 mV/s with glassy carbon working electrode and  $Ag/Ag^+$  reference electrode.

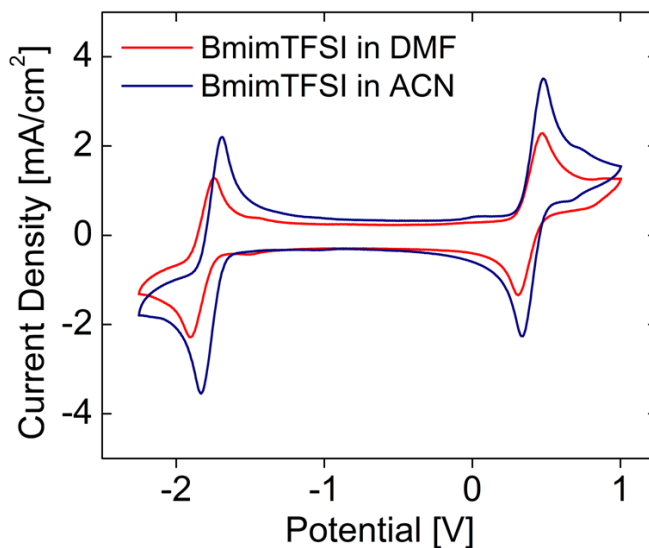


Figure 2.4.4-4 Cyclic voltammogram of 0.01 M  $V(acac)_3$  and 0.05 M  $BmimTFSI$  in DMF or ACN. Scan rate 100 mV/s with glassy carbon working electrode and  $Ag/Ag^+$  reference electrode.

The electrochemical properties screened in CV appear viable for all the solvent and supporting electrolyte combinations tested. The charge/discharge performance of these systems was therefore tested using a 4-electrode cell. The

results are shown in Figure 2.4.4-5 and Figure 2.4.4-6 for  $V(\text{acac})_3$  and  $\text{TEABF}_4$  in ACN and DMF respectively. These are the only charge/discharge shown because their conductivities were sufficiently high. The overall potential (shown in blue) for ACN initially has a charge potential of  $\sim 2.5$  V, which increases slightly over the first few cycles until the cell begins to overcharge. The discharge step is relatively flat at 1.75 V for all cycles. When the %SOC reaches  $\sim 90$  %, the reference potential for the  $V(\text{II})/(\text{III})$  side increases continuously until the charge step has ended, which is the expected Nernstian response. The reference for the  $V(\text{III})/(\text{IV})$  side starts at 120 mV and moves to a new plateau value at 240 mV starting in the 3<sup>rd</sup> and 4<sup>th</sup> cycles. During discharge, both of the reference potentials are steady at 120 mV for all cycles. To avoid side reactions, indicated by a shift in the reference potential, the RFB can be run at a constant potential or the SOC controlled using a cut-off potential for the charge step instead of a time cut-off. The increase in the reference potential at lower SOC is surprising and indicates the likely presence of a secondary unknown reaction.

Figure 2.4.4-6 shows a test similar to the one shown in Figure 2.4.4-5, with the ACN solvent replaced by DMF. The charge voltage begins at 2.7 V in DMF, but by the third cycle a new plateau height of 4 V is reached. There is no discharge at all for the first three cycles and upon the observation of a discharge plateau in cycle 4, the voltage plateau appears extremely close to the 0.5 V cutoff voltage. The reference electrode on the  $V(\text{III})/(\text{IV})$  side has a constant potential of  $\sim 1.3$  V when charging and 0.6 V when discharging. The  $V(\text{II})/(\text{III})$  side has varying potentials from 120 mV to 1 V during charge. These are extremely high

overpotentials, which is disconcerting because on the basis of CV and conductivity measurements, they should theoretically be near zero. It is particularly significant that the reference potential on the 2/3 side does not change signs as the current changes signs; this indicates that a corrosion reaction is occurring in the cell.

Subtraction of the reference potentials from the overall potentials during the first charge cycle of the DMF cell leaves a remainder of  $\sim 1.2$  V. This places an upper limit on the equilibrium cell potential that is significantly lower than the formal potential of the desired vanadium reaction. Thus the bulk, if not all, of the current is being applied to an undesired reaction.

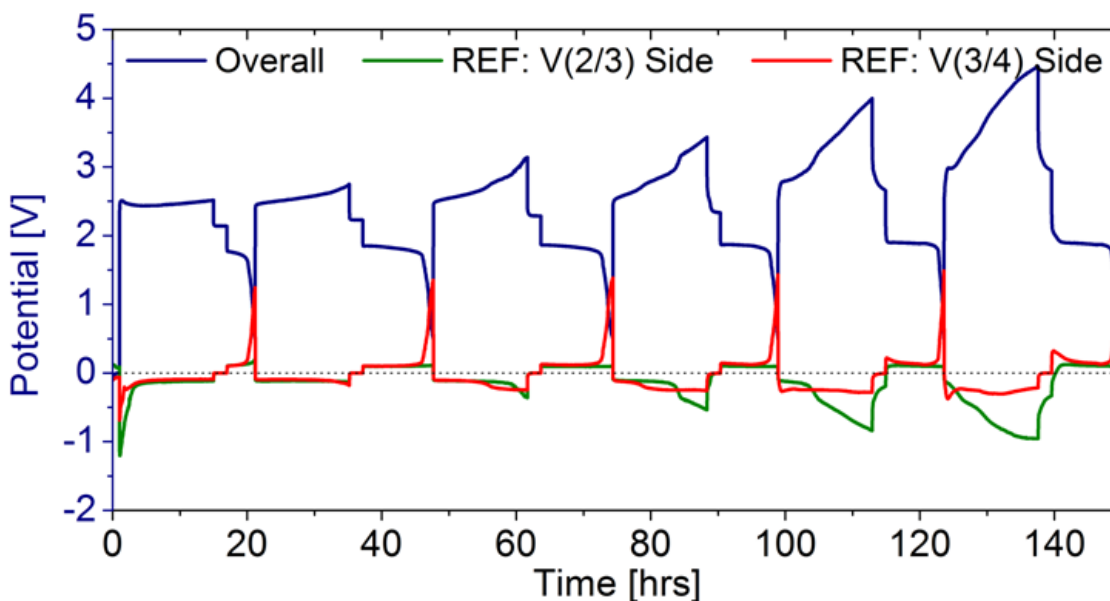


Figure 2.4.4-5 Charge/Discharge plot for 0.1 M  $V(acac)_3$  and 0.5 M  $TEABF_4$  in acetonitrile in a 4-electrode 1-D cell with graphite electrodes and Neosepta AHA membrane. 1mA charge current added until 40 % of the theoretical maximum energy has been added, rest for 2 hours, then discharge at 1 mA until 0.5 V.

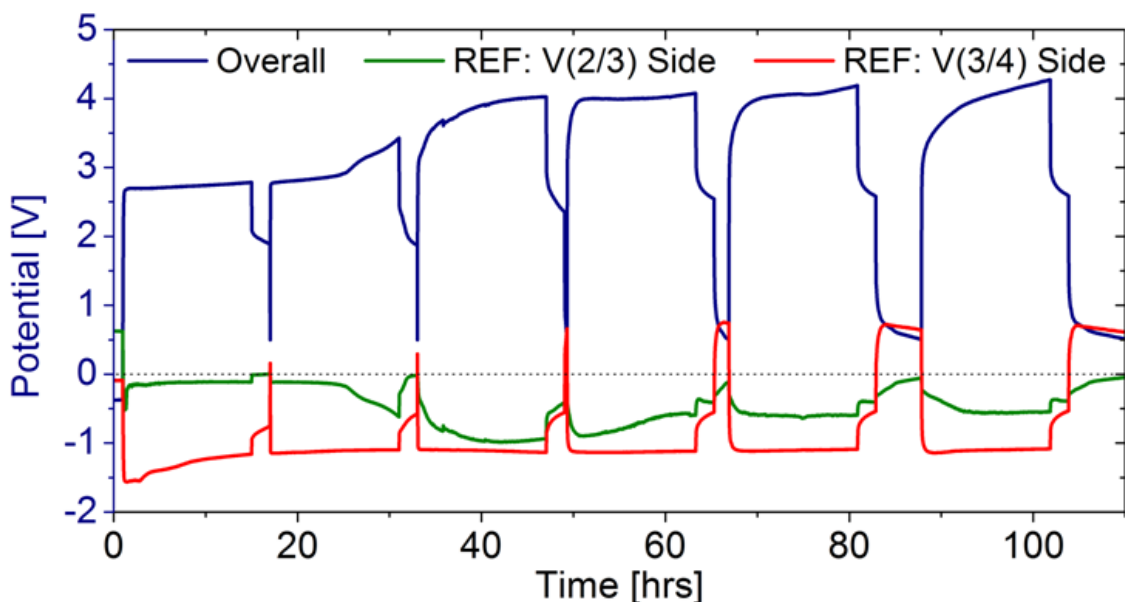


Figure 2.4.4-6 Charge/Discharge plot for 0.1 M  $V(acac)_3$  and 0.5 M  $TEABF_4$  in dimethylformamide in a 4-electrode 1-D cell with graphite electrodes and Neosepta AHA membrane. 1 mA charge current added until 40 % of the theoretical maximum energy has been added, rest for 2 hours, then discharge at 1 mA until 0.5 V.

#### 2.4.5 Discussion: Desired Solution Properties

ACN appears to be the most stable and conductive solvent tested, in combination with almost any supporting electrolyte. It is worthwhile to consider what characteristics of this solvent underpin its performance, because that effort will help to identify other promising solvents. Thus solvent properties were recorded and a regression analysis was performed to correlate properties to  $V(acac)_3$  solubility and solution conductivity. Many solvent parameters have been created to predict solute solubilities. Unfortunately, the different theoretical methods have unreliable predictive capacity, and there is no universal, experimentally validated method that can be generally used. Hansen solubility parameters are a common scheme used to predict solubilities. The Hansen theory uses the “like dissolves like” strategy to characterize the dispersion,

polarity, and hydrogen-bonding energy associated with the solvent. The three parameters essentially work as a coordinate in a three-dimensional space established by these three parameters; a solute which matches the coordinates of the solvent is expected to dissolve readily [92]. Another method of solubility prediction uses the Hildebrand solubility parameter, which is the measure of the cohesive energy density of the solvent (main factors are the solvent molar volume and heat of vaporization). The Hildebrand theory is primarily used to predict the solubility of polymers in solvents [93]. These are just two examples of the many approaches to solubility estimation that exist.

The solvent parameters I examined were the Hildebrand solubility parameter, solvent molar volume, Hansen hydrogen bonding, Hansen polarity, Hansen dispersion,  $\pi^*$  (polarizability),  $\beta$  (hydrogen bond acceptor),  $\alpha$  (hydrogen bond donor),  $E_t(30)$  (empirical polarity), donor number, acceptor number, and dielectric constant. These parameters are based on bulk properties of the solvent, empirical solvent polarity parameters, and molecular properties of the solvent. A similar analysis has been performed for other solutions by multiple groups. For example, Yeagley *et al.* examined the ferrocene Hammett reaction constant against many of the same parameters and saw that the  $E_t(30)$  and Hildebrand solubility parameter had the best correlation [94]. The following table shows the solvent parameter values for each solvent.

Compound	Acetonitrile (ACN)	Dimethyl formamide (DMF)	Tetrahydrofuran (THF)	Dimethyl carbonate (DMC)	Hexane (HEX)
Hildebrand Solubility Parameter (cal <sup>1/2</sup> cm <sup>2/3</sup> )	11.27 [95]	11.57 [95]	9.9 [95]	9.74 [95]	7.27 [95]
Molar Volume (cm <sup>3</sup> /mol)	52.5 [95]*	76.9 [95]*	81.1 [95]*	84.3 [95]*	131.6 [95]*
Hansen H-bonding	6.1 [95]	11.3 [92]	8 [95]	9.7 [92]	0 [95]
Hansen Polarity	18 [95]	13.7 [92]	5.7 [95]	3.9 [92]	0 [95]
Hansen Dispersion	15.3 [95]	17.4 [92]	16.8 [95]	15.5 [92]	14.9 [95]
Pi* [polarizability]	75 [96]	88 [96]	58 [96]		-4 [96]
Beta [hydrogen bond acceptor]	40 [96]	69 [96]	55 [96]		0 [96]
Alpha [hydrogen bond donor]	19 [96]	0 [96]	0 [96]		0 [96]
Et(30) [Empirical Polarity] (kcal/mol)	45.6 [95]	43.2 [95]	37.4 [95]	38.2 [95]	31 [95]
Donor Number (kcal/mol)	14.1 [95]	26.6 [95]	20 [95]	17.2 [95]	0 [95]
Acceptor Number	18.9 [97]	16 [97]	8 [97]		0 [97]
Dielectric Constant	36.64 [86]	38.25 [86]	7.52 [86]	3.1 [87]	1.88 [86]

Table 2.4.5-1 Table of solvent properties for ACN, DMF, THF, DMC, and HEX. The asterisk denotes that the value is calculated by dividing the molar mass by the solvent density found in [95].



In the experiments presented here, a linear fit with the five solvents was performed using Minitab comparing each solvent property to the  $V(\text{acac})_3$  solubility and solution conductivity. The p-value for the fitting parameter compared to the  $V(\text{acac})_3$  solubility was plotted in Figure 2.4.5-1. Lower p-values have better correlation between the solvent parameter and the solubility. The three parameters with the best correlation are: Et(30), Hildebrand Solubility Parameter, and solvent molar volume. However, solvent molar volume shows the strongest correlation along with the Hildebrand solubility parameter, which is not surprising since the Hildebrand solubility parameter is calculated based on the solvent molar volume. The Et(30) is based on an empirical polarity, suggesting the polarity may also have an effect on the solubility. Interactions between several parameters were also examined, however none of them showed statistical significance. The regression plot is shown for  $V(\text{acac})_3$  solubility vs. solvent molar volume in Figure 2.4.5-2. This suggests the ideal solvent would have a small solvent molar volume. To check these results, a 0.01 M solution of  $V(\text{acac})_3$  in BmimTFSI (solvent molar volume =  $292 \text{ cm}^3/\text{mol}$ ) was prepared. The  $V(\text{acac})_3$  did not dissolve in the solution, which was expected based on these results.

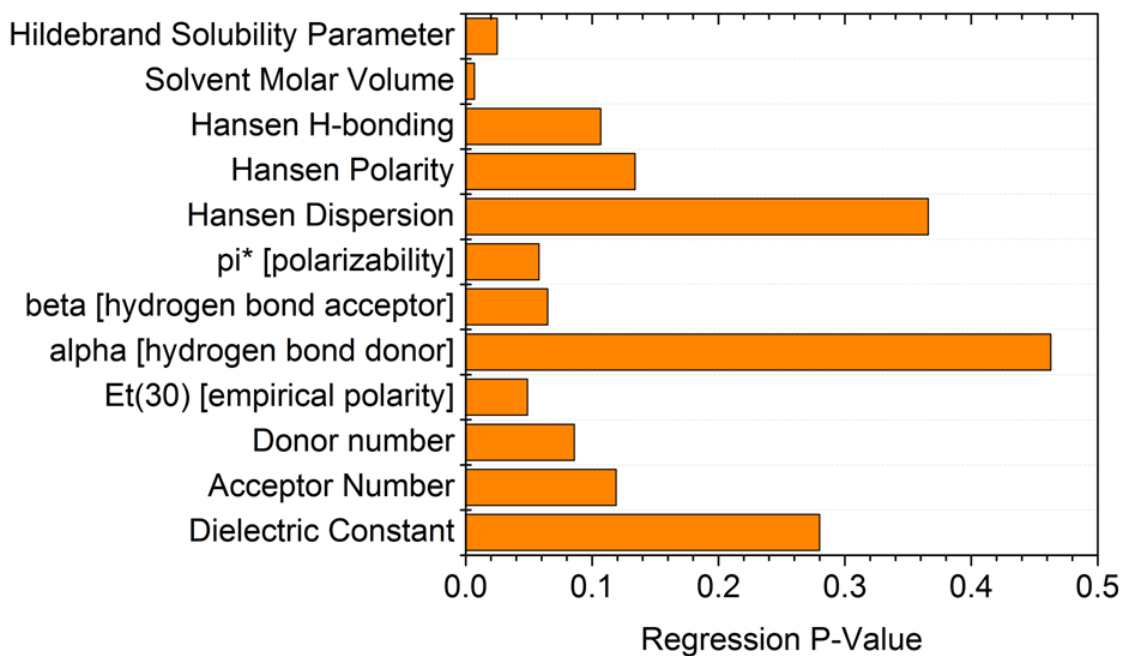


Figure 2.4.5-1 Plot of p-values for the correlation between each solvent property and the  $V(\text{acac})_3$  solubility.

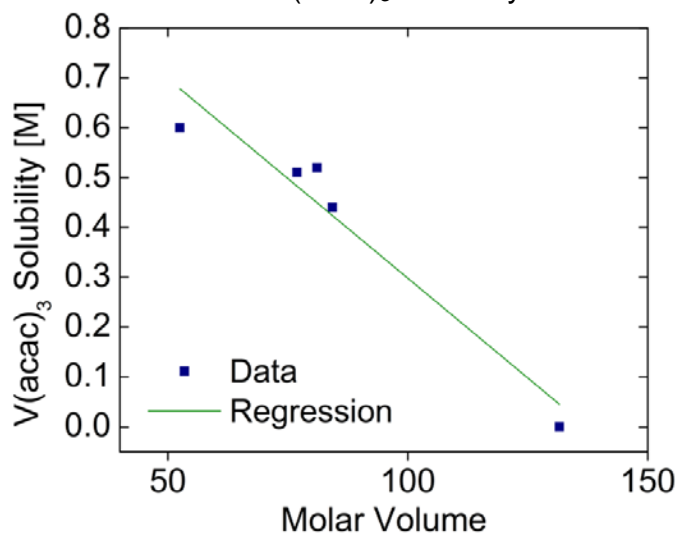


Figure 2.4.5-2 Regression of  $V(\text{acac})_3$  solubility with solvent molar volume.

A similar analysis was performed to correlate the solvent parameters to the solution conductivity. Prior literature on correlations with solvent properties to conductivity are not as forthcoming, as it is generally accepted that the conductivity scales with the viscosity [98]. For instance, a report by Doyle *et al.*

examined the conductivity of a Nafion membrane and found it to be dependent on the solvent viscosity and molar volume (along with membrane properties) [99]. However, when a regression was performed to examine the conductivity as a function of the viscosity in this work, a p-value of 0.718 was observed, indicating no correlation. It might also be expected that the polarity of the solvent will greatly affect the conductivity, on the basis of the Born solvation theory [100]. Thus the same parameters used for solubility were examined in the context of conductivity.

The p-values for fits of solvent properties vs. solution conductivity are shown in Figure 2.4.5-3 when using ACN, DMF, DMC, and THF only, since they provided solutions of 0.1M concentration. The results showed Hansen polarity, solvent molar volume, and the  $E_t(30)$  [empirical polarity] to have the highest correlation. These results follow expected trends as two of them are based on the polarity and the solvent molar volume had been observed to be significant in experiments by Doyle *et al.* When using all five solvents,  $\alpha$  [H-bonding donor number], dielectric constant, and Hansen polarity exhibit the best correlation. The  $\alpha$  values for all solvents are zero except ACN and therefore produces a false trend. As with the results excluding HEX, the polarity appears to be the dominant property since both the dielectric constant and Hansen polarity are based on it. As with the  $V(\text{acac})_3$  solubility, the interactions between several solvent parameters were examined. If the  $\alpha$  value and the dielectric constant are used as fitting parameters, an  $R^2$  value of 99.8 % results. A similar result occurs when using the Gutmann acceptor and donor number. Figure 2.4.5-4

shows the regression fit for Hansen polarity to solution conductivity. In order to obtain high conductivity solutions, the Hansen polarity should be high.

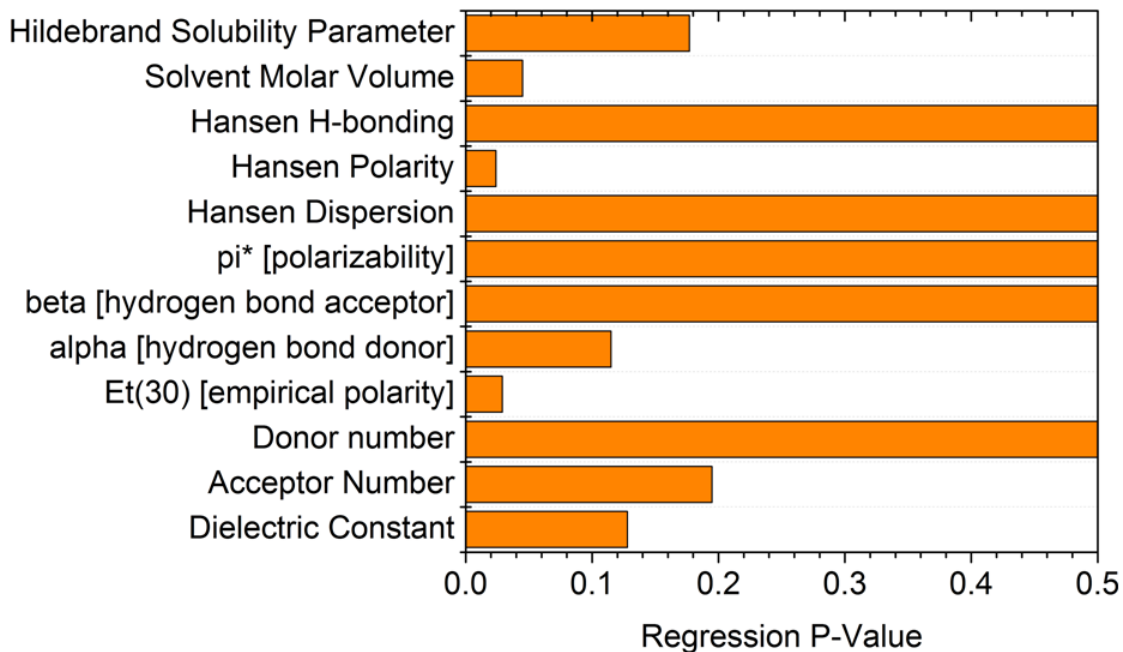


Figure 2.4.5-3 Plot of p-values for the correlation between each solvent property and the solution conductivity.

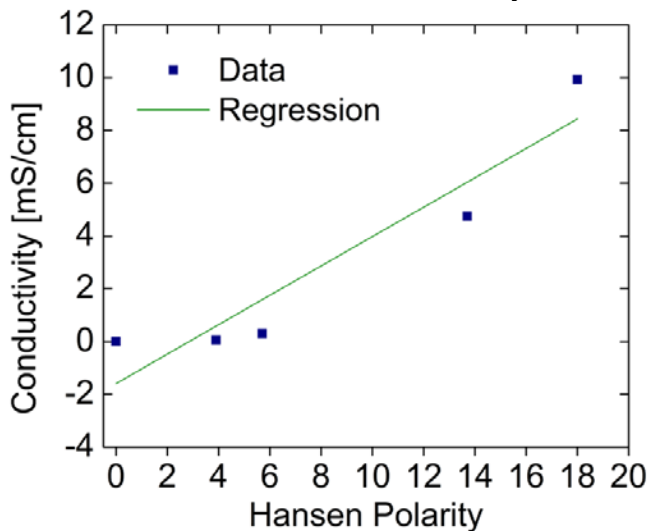


Figure 2.4.5-4 Regression of solution conductivity with Hansen polarity.

The Hansen polarity parameter, shown to correlate well with solution conductivity, is generally related to molecular structure. Hansen created a chart

which shows how chemicals involving different types of functional groups (ketones, alcohols, nitriles, etc.) compare in terms of Hansen polarity parameter [92]. The results are shown in Figure 2.4.5-5 in a plot of Hansen Polarity Parameter vs. Hansen Hydrogen Bonding Parameter. It illustrates that nitriles have the highest Hansen polarity parameter, followed by amides. It is also of note that nitromethane and dimethylsulfoxide have high values for the Hansen polarity parameter. Thus these solvents may be targeted for systems in which higher conductivity is desired.

Table 2.4.5-2 shows the values for several of these compounds. Ethylene carbonate, ACN,  $\gamma$ -butyrolactone, and dimethylsulfoxide have the highest Hansen Polarity Parameter: 21.7, 18, 16.6, and 16.4 respectively. These also have some of the smallest molar volumes of the solvents examined. ACN, dichloromethane, ethylene carbonate, and dimethylsulfoxide have the lowest solvent molar volumes. Considering both the solution conductivity and  $V(\text{acac})_3$  solubility, acetonitrile, ethylene carbonate, and dimethylsulfoxide should be the most promising solvents to use for future experiments.

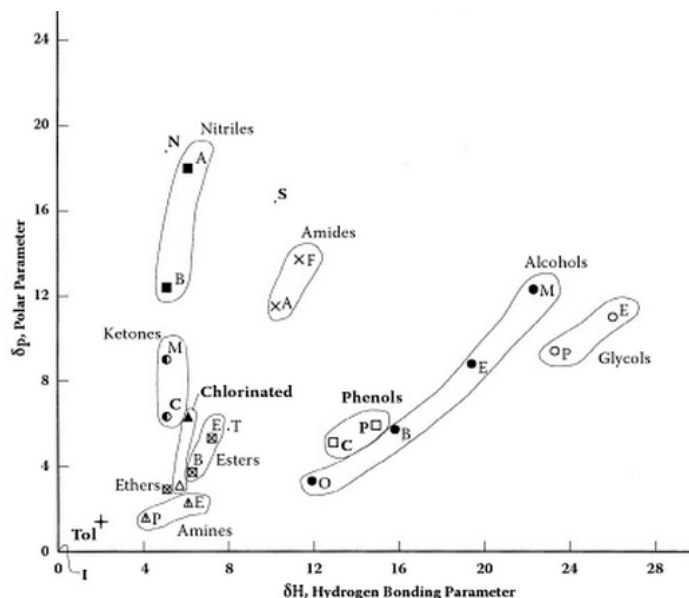


Figure 2.4.5-5 Plot of Hansen Polarity Parameter vs. Hansen Hydrogen Bonding Parameter for several classifications of solvents. [N] is Nitromethane and [S] is Dimethylsulfoxide. Taken from [92].

Compound	Hansen Polarity	Molar Volume (cm <sup>3</sup> /mol)
Acetonitrile (ACN)	18	52.5
Dichloromethane	7.3	64.0
Ethylene carbonate (EC)	21.7	66.7
Dimethylsulfoxide (DMSO)	16.4	71.5
Acetone	10.4	73.9
Gamma butyrolactone	16.6	76.2
Dimethylformamide (DMF)	13.7	76.9
Tetrahydrofuran (THF)	5.7	81.1
Dimethyl carbonate (DMC)	3.9	84.3
Propylene carbonate (PC)	8.8	84.7
1,4-dioxane	1.8	85.2
Dimethylacetamide	5.6	92.5
Ethyl acetate	5.3	98.6
Dimethoxyethane (DME)	4.6	104.7
Hexane	0	131.6
1-butyl,3-methylimidazolium		292.6
Bis(trifluoromethylsulfonyl)imide		292.6

Table 2.4.5-2 Table of aprotic solvents with the corresponding Hansen Polarity Parameter and Solvent molar volume.

#### 2.4.6 Conclusion

The physical and electrochemical properties of a set of combinations of five solvent and five supporting electrolytes (25 total combinations) were examined. The supporting electrolytes did not meet the minimum solubility baseline in HEX while  $\text{NaBF}_4$  did not meet the minimum solubility in any of the solvents tested. The conductivity of the 0.1 M solutions were highest in ACN followed by DMF, while THF and DMC were eliminated from further testing due to comparatively low conductivity. The supporting electrolytes examined in this work did not appreciably change the conductivity of the solution. The maximum solubilities of  $\text{V}(\text{acac})_3$  in the solvents were 0.6 M, 0.51 M, 0.52 M, and 0.44 M for ACN, DMF, THF, and DMC respectively.

The electrochemistry of  $\text{V}(\text{acac})_3$  was very reversible in both ACN and DMF solutions. Different characteristics were observed for the peaks associated with free-ligand oxidation and vanadyl acetylacetonate peaks, suggesting that the solvent / supporting electrolyte combination can be altered to mitigate undesired side reactions in an RFB application. Despite CV results that looked promising, the charge/discharge experiments resulted in severe corrosion of the electrodes in DMF, causing up to 2 V of mixed potential loss.

Solvent parameters were used to predict what type of solvent should be selected to yield high  $\text{V}(\text{acac})_3$  solubility and overall solution conductivity. Trends indicate that the ideal solvent should have a low solvent molar volume to

increase  $V(\text{acac})_3$  solubility, and high Hansen polarity to obtain a high overall solution conductivity. In my experiments the optimal solvent was ACN. Using the experimental trends and considering other polar, aprotic solvents, ACN remains the most promising solvent, followed by ethylene carbonate and dimethylsulfoxide. If the ligand was modified, these relations may change. However, I think the changes will be minor because the solvent must remain a polar solvent in order to solvate and dissociate the supporting electrolyte. Thus polarity will still be the main driver for conductivity. The solubility was driven by the solvent molar volume and should remain relatively unchanged by the ligand modifications.



## Chapter 3 Effects of the Cell Components

### 3.1 Membrane

#### 3.1.1 Background

The separator in a RFB is responsible for keeping electrodes electronically isolated while allowing ion exchange between the two liquid electrolytes. The membrane should have low resistance to support-ion transport, high selectivity against active-species crossover, and be stability to all states of charge. The separator can be as simple as a porous glass frit or as complex as aggregation of several ion-exchange membranes. Most lithium ion batteries (non-aqueous systems) use microporous polyolefin membranes [10]; commercial examples include the microporous membranes by Celgard and Asahi, which are 20-25  $\mu\text{m}$  thick and 30-50 % porous [10]. The ionic resistance of a separator is proportional to its thickness, which is conventionally selected to be as thin as practically possible; high porosity also provides higher conductivity, but can be a large concern in flow batteries, where active-species crossover is more detrimental.

Most redox flow batteries use ion-exchange-membrane separators, although a few researchers used microporous membranes to lower cell cost [4, 9, 101]. Typical ion-exchange membranes for flow-battery applications have a polymer backbone with a branched structure, where pendant charged groups

terminate the branches. Cation-exchange membranes have terminal negative groups, whereas anion-exchange membranes have terminal positive groups. Commonly sulfonate is used to facilitate cation exchange; tetraethylammonium is used to facilitate anion exchange.

Support-ion mobility is usually taken to be the primary concern when selecting an ion-exchange membrane for an RFB, on the basis that high ion mobility corresponds to high power efficiency. The polarity of RFB membranes is typically chosen in the hopes that the smaller of the supporting ions will be more readily transported. Aqueous RFBs with acidic supporting electrolytes thus invariably use cation-exchange membranes [9] to facilitate  $H^+$  transport. This selection yields more losses owing to crossover since all species in the battery are also positively charged. The membrane choices for non-aqueous RFB systems are not as easily pre-determined since all ions are fairly large and the active species is normally both positively and negatively charged (anion-exchange membranes are typically used [46, 61]).

Ion-exchange membrane choice for a given RFB system should also be guided by examining its selectivity against active-species transport, which can also be related to their charge states. Vafiadis *et al.* examined several anion and cation separators and compared their effectiveness to a Hipore microporous separator [44] in an aqueous vanadium RFB. They were unable to cycle the RFB when anion-exchange membranes were used. The microporous separator yielded a lower coulombic efficiency than the cation exchange membrane. As one might expect, the charge time when using a microporous separator was

longer than the theoretical maximum – indicating that solution had recombined via the membrane. Also, the liquid levels became unbalanced much faster in the microporous separator cell, indicating a greater imbalance of osmotic pressure in response to migration. They concluded that the cation-exchange membranes were the most ideal for the aqueous all-vanadium RFB in order to achieve high efficiencies [44]. However, upon examination of the membrane after cycling it was observed that all ion-exchange membranes show some form of degradation in terms of blistering or discoloration. Thus the goals of improving membrane stability and crossover resistance have driven research by Skyllas-Kazacos *et al.* on the aqueous all-vanadium system [9]. Approaches either modify existing Nafion membranes, like the study by Xi *et al.*, who created a sol-gel method to combine Nafion with SiO<sub>2</sub> to reduce crossover [102], or start with a non-perfluorinated polymer backbone and add Nafion-like functionality, as in the studies by Mohammadi *et al* [39-41].

Once a membrane with favorable properties has been chosen for an RFB, the next step is to establish a pretreatment procedure relevant to the particular chemistry. Pretreatment is necessary because ion-exchange membranes are synthesized with counter-ions bound to the pendant charged groups. The pretreatment exchanges these counter-ions for the counter-ion in the supporting electrolyte used for the RFB. Additionally, most membranes swell when wetted, so they must be pre-soaked with the supporting electrolyte and solvent to fit properly in the test chamber. The pretreatment of all commercial membranes for

aqueous systems is well documented by the manufacturers as well as researchers.

For Nafion membranes, the community standard pretreatment involves sequential soaks in: boiling hydrogen peroxide, room temperature water (some researchers use boiling water), boiling sulfuric acid, and lastly boiling water [103]. The pretreated membrane is then stored in water until it is ready to be used to ensure that it stays in a wetted form. In our work, 18M $\Omega$  ultrapure water is used at every step during the pretreatment to decrease the risk of membrane contamination. This pretreatment procedure is used to swell the dry membrane, as well as exchange sodium ions (the counter ion used in most cation exchange membranes) for hydrogen ions. When performing these experiments in non-aqueous solvents, design of pretreatment procedures is left to the researcher as only a small amount of literature reports are available and most manufacturer data is in water. Membranes can be swelled in the solvent experiments will be conducted in, but counter-ion exchange procedures are not as clear-cut.

Another issue when moving to non-aqueous systems is that most commercial membranes are not designed for long-term exposure to non-aqueous solvents. Membranes are sometimes known to be unstable in certain organic solvents; more often, their stability is completely unknown. Stability after solvent exposure has been assessed in many ways: observing visible color change, structural cracks with microscopy, change in resistance. The vanadium (V) in the aqueous all-vanadium RFB system reacts with Nafion membranes to slowly

degrade the battery [44]. Even if a membrane is stable in the organic solvent, they may be unstable in the presence of the charged species.

The issues with ion-exchange membranes have lead some researchers to examine membraneless systems [42]. Chakrabarti *et al.* examined several RFB systems in a microfluidic device that relies on laminar flow in the main cell chamber to minimize mixing of the two electrolytes. This eliminates the challenge of finding stable membranes, as well as eliminating the energy and power losses associated with separator resistance. Unfortunately, the laminar-flow-cell design is not very effective in a redox flow battery setup – especially as the solution gets to a higher state of charge, where active-species recombination (self-discharge) dominates at the interface. The highest energy efficiency Chakrabarti *et al.* obtained was 12 % using a 0.1 M all-vanadium aqueous RFB [42]. Thus use of porous or ion-exchange membranes currently appears to be the most effective route by which to separate RFB electrolytes.

### 3.1.2 Results: Pretreatment

In order to design a pretreatment procedure, a method is needed to measure the fraction of counter-ions that can be removed from a membrane by ion exchange. To determine the fraction of chloride remaining in the membrane after ion exchange, tests can be performed either on the membrane or on the surrounding solution. Tests on the membrane are destructive, so they can be used to evaluate the general effectiveness of ion exchange, but not quantify the amount of remaining  $\text{Cl}^-$  in a given membrane intended for use. Therefore,

analysis of ambient liquid electrolyte was used to determine how much chloride remained in the membrane after ion exchange. The simplest ion-exchange procedure involves soaking the membrane in a solution containing the supporting ion desired in the membrane. In my experiments, the soaking procedure used 0.75M TEABF<sub>4</sub> in ACN solution. The membranes were soaked in the solution over the course of several days then the solution was tested.

Ion-exchange experiments were performed according to the above procedure by an undergraduate researcher, Kurt Kurtzenhauser, who focused on developing preparation schemes for anion-exchange membranes. These are typically delivered from suppliers with chloride counter-ions on pendant tetra-alkylammonium endgroups. The presence of chloride is unacceptable in non-aqueous RFBs based on metal coordination complexes, because chloride readily exchanges with negatively charged ligands. Chloride-substituted active species tend to be non-reactive. Three possible methods by which ion content in a liquid can be measured are inductively coupled plasma (ICP), precipitation, or CV. ICP does not work well with organic solvents, as well as involving very high temperature plasmas. Even with small amounts of organic solvent, initial tests showed that samples would extinguish the ICP torch. The precipitation method involves dissolving a flocculent (such as AgNO<sub>3</sub>), which produces a chloride-containing precipitate (in this case, AgCl) that can be dried and weighed. However, due to the small amounts of chloride removed, this method was found to be extremely error prone. Also, the precipitation event occurred most commonly inside the membrane due to diffusion of the flocculant species –

destroying the membrane. CV is applicable to non-aqueous electrolytes, is able to resolve small concentration differences, and is easier to implement than ICP.

The cyclic voltammogram of a tetraethylammonium chloride (TEACl) (Sigma Aldrich, US, >98 %) and TEABF<sub>4</sub> solution was obtained and is shown in Figure 3.1.2-1. For our purposes, it does not matter what the source electrochemistry underlies each peak in the voltammogram; it is only important that the peak current at a given scan rate depends linearly on the TEACl concentration. Theory suggests such a dependence. For reversible reactions ( 3-1 ) or irreversible reactions ( 3-2 ) the peak current in the forward sweep of a voltammetry scan is directly proportional to the reactant concentration [59].

$$i_p = [(2.69 \times 10^5) n^{3/2} A D^{1/2} \nu^{1/2}] * C \quad ( 3-1 )$$

$$i_p = [(2.99 \times 10^5) \alpha^{1/2} A D^{1/2} \nu^{1/2}] * C \quad ( 3-2 )$$

, where  $A$  is the electrode area,  $D$  is the diffusion coefficient of the reactant in the solution,  $C$  is the bulk reactant concentration,  $n$  is the number of electrons transferred,  $\nu$  is the scan rate, and  $\alpha$  is a constant.

CV experiments were run under the condition that the concentration of TEA<sup>+</sup> was held constant (i.e. with the sum of the concentrations of TEACl and TEABF<sub>4</sub> held constant, often referred to as “constant ionic strength”) to keep the diffuse double-layer capacitance comparable across experiments. A TEA<sup>+</sup> concentration of 0.12 M was used while varying the ratio of Cl<sup>-</sup> to BF<sub>4</sub><sup>-</sup> (TEABF<sub>4</sub> is an inactive species with no redox couples). A calibration curve was created using the peak height from the oxidation at ~0.2 V because it was the most pronounced peak during a forward scan and had clearly discernible baseline at

~0 current density. The resulting calibration curve is shown in Figure 3.1.2-2, where squares present experimental data and the red line represents a linear fit.

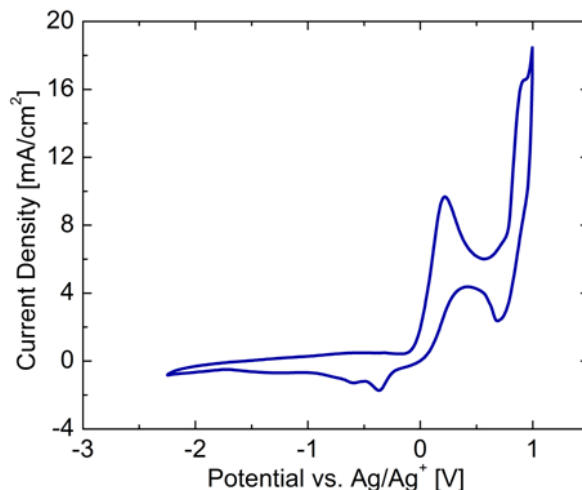


Figure 3.1.2-1 Cyclic voltammogram of 0.06 M TEABF<sub>4</sub> and 0.06 M TEACl in acetonitrile. Gold microelectrode working electrode at 100 mV/s.

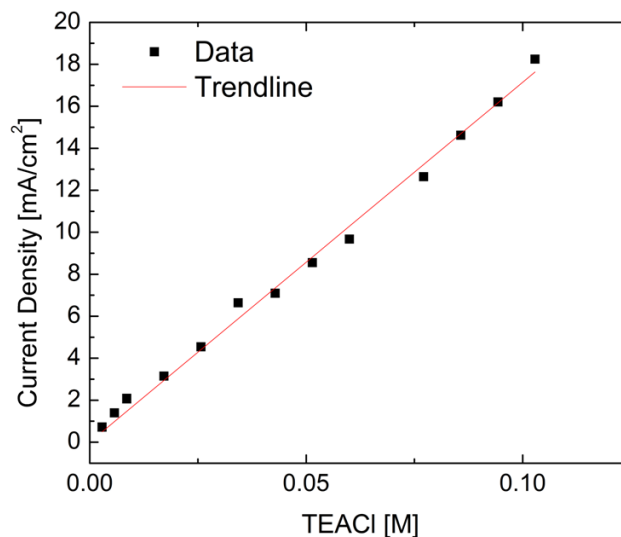


Figure 3.1.2-2 Calibration curve for the peak height of the oxidation at ~0.2 V as a function of the concentration of TEACl in a 0.12 M TEA<sup>+</sup> solution (Balance is TEABF<sub>4</sub>). Gold microelectrode working electrode with scan rate 100 mV/s.

One assumption with this method is that TEACl is the species formed in the solution when Cl<sup>-</sup> diffuses out of the membrane – an assumption that would



not be correct if other reactions chemistry occurs between the membrane and the adjacent non-aqueous electrolytic solution. After examining the cyclic voltammogram for a solution which had a Neosepta AHA membrane soaking in it, we see similar behavior to that expected for a TEACl solution (Figure 3.1.2-3) so this assumption is justified. The blue line represents the voltammetric response of a solution in which a Neosepta AHA membrane was soaked for 10 hours. The red line represents one of the standards created for the calibration experiment. Both curves look extremely similar. The mismatch between the two curves at potentials below -1 V vs. Ag/Ag<sup>+</sup> can be explained by differences in the amounts of dissolved oxygen in the two solutions [56, 80], which do not affect the height of the oxidation peak of interest. Application of the calibration equation allows peak heights to be used to quantify the amount of TEACl in solution, which, along with an independent measurement of the total membrane ion capacity (usually reported by suppliers), allows for the calculation of the percentage of chloride removed from the membrane during one round of ion exchange. After 10 hours, only 6 % of the chloride in the membrane had been exchanged for BF<sub>4</sub><sup>-</sup>.

Solutions in which membranes were soaked for different amounts of time were measured; the percentage of Cl<sup>-</sup> exchanged out of the membrane is shown as a function of time in Figure 3.1.2-4. Although only five different lengths of time were tested, it is fairly clear that after one day equilibrium has been reached and negligible additional Cl<sup>-</sup> can be removed from the membrane. The maximum amount of chloride removed in one soaking of a membrane in a 0.4 M TEABF<sub>4</sub>

solution is approximately 7 %. This leaves a vast majority of the chloride in the membrane. No further work was performed on improving pretreatment, which should be examined in further research.

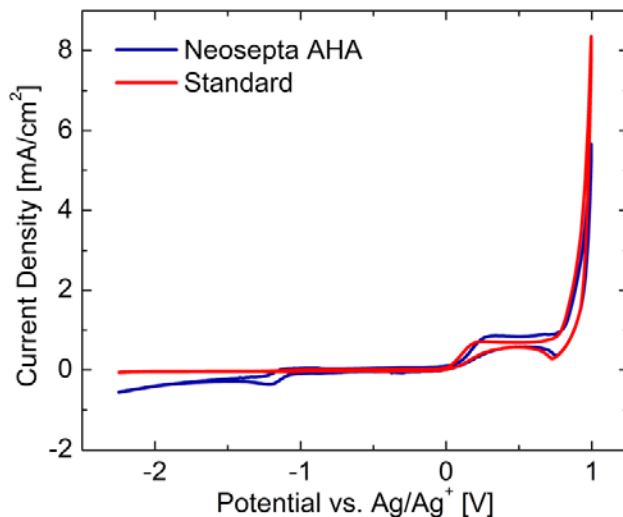


Figure 3.1.2-3 Cyclic voltammogram of [Standard (Red)] 0.0029 M TEACl and 0.1171 M TEABF<sub>4</sub> in acetonitrile, [Neosepta AHA (Blue)] Solution after soaking a Neosepta AHA membrane for 10 hours.

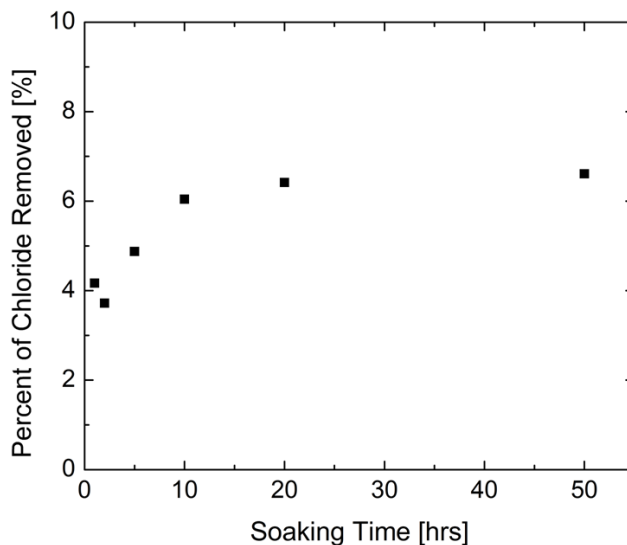


Figure 3.1.2-4 Plot of percentage chloride removed by a single soaking of Neosepta AHA in a 0.4 M solution of TEABF<sub>4</sub> with time.

### 3.1.3 Results: Impedance

The impedance of the membrane directly affects the resistance of the entire cell and thus is the main property of concern for its performance as a battery separator. If the membrane has high resistance, loss of energy is observed during both charge and discharge. Therefore, it is desirable to have a membrane whose impedance is low, without compromising selectivity.

The membrane pretreatment for impedance measurements was to soak in acetonitrile for 24 hours to wet pores within the membrane, and then soak in 0.3 M dibutylammonium tetrafluoroborate in acetonitrile for 1 week. The impedance was performed in a Swagelok cell shown in Figure 3.1.3-1. A PTFE Swagelok union was used as the outer body of the cell. Two aluminum pegs (previously used for SEM) were employed with an EPDM rubber ring around the outside to create a seal against the PTFE casing. The cell was assembled by placing an EPDM washer into the cap of the Swagelok union, which was followed by the electrode. One drop of ACN was then placed on the electrode prior to placing the membrane in the cell. A second drop of ACN was placed on top of the membrane. Then the other electrode was placed on top, followed by another washer. Finally the cap was screwed into the rest of the Swagelok union until finger tight. Alligator clips were attached to the back of the electrode pegs when testing. The impedance experiments were run with a minimal amount of electrolyte because an inductance was observed when using excess electrolyte, which made the results difficult to process.



Figure 3.1.3-1 Picture of impedance cell.

Figure 3.1.3-2 and Figure 3.1.3-3 shows Nyquist impedance plots for a system assembled as described above, with a Selemion DSV and Neosepta AHA membrane, respectively. Impedance measurements were taken about a 0V bias with signal amplitude of 10 mV, over a frequency range of 100 mHz to 100 kHz. The intersection between a circle fit to the data and the real axis yields the series resistance of the cell, which, in this case, is dominated by the liquid-saturated membrane. Data was fitted using the Autolab FRA program, which uses three of the data points from the data set (of the user's choice) to determine the circle. Figure 3.1.3-4 shows a screen capture of this process. The red arrows show the data points used to fit the data set, while the blue dashed line shows the resulting circle.

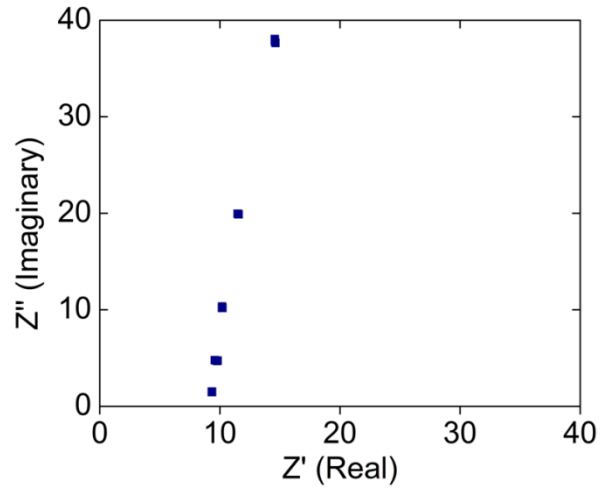


Figure 3.1.3-2 Impedance plot for Selemion DSV anion exchange membrane zoomed in to the high frequency region.

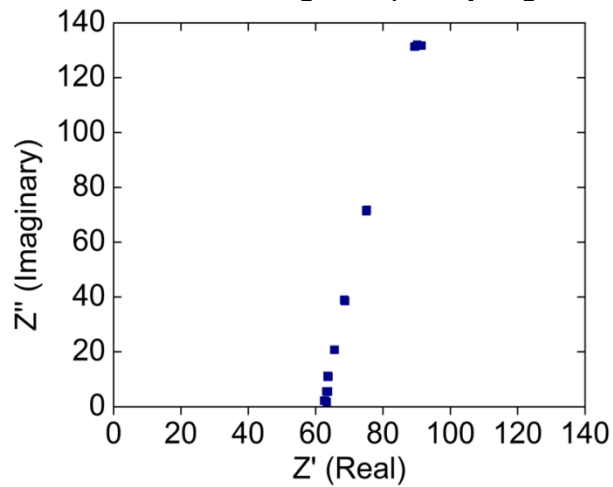


Figure 3.1.3-3 Impedance plot for Neosepta AHA anion exchange membrane zoomed in to the high frequency region.

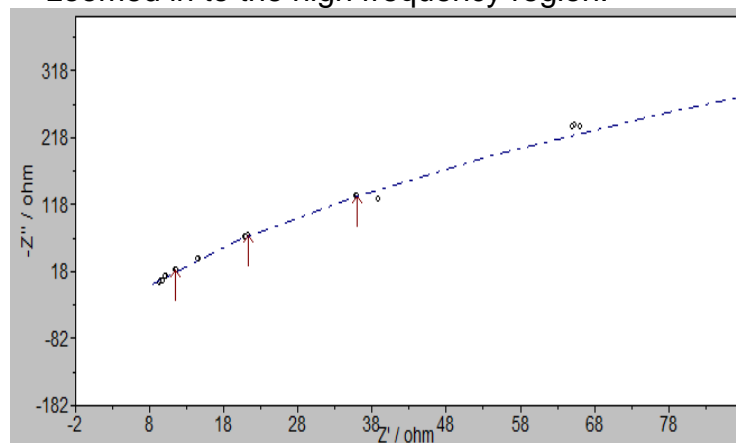


Figure 3.1.3-4 Screen capture of the fitting program used to determine the circle fit to the data for Selemion DSV shown in Figure 3.1.3-2.

Anion Exchange Membrane	Resistance [Ω]	Resistivity [Ω cm]	Capacitance [μF]
Selemion DSV	8.3	477	2.2
Neosepta AHA	53.9	1740	2.7
Selemion APS4	64.3	2550	1.1
Fumasep FTAM	150	1790	1.7
Membranes Int. AMI-7001	341	3760	1.2

Table 3.1.3-1 Table of results detailing the resistance and resistivity of several commercial anion exchange membranes.

Table 3.1.3-1 contains the measured bulk resistance and computed resistivity of each membrane tested. The resistivity calculation normalizes out the thickness of the membrane, according to

$$\text{Resistivity} = \frac{\text{Resistance} * \text{Area}}{\text{Thickness}} \quad (3-3)$$

All the impedance measurements reported were performed by two undergraduate researchers: Kurt Kurtzenhauser and David Thaler.

The Selemion DSV membrane showed the lowest resistance at 8 Ω followed by Neosepta AHA with 54 Ω. The most resistive membrane measured was the Membranes International AMI-7001, which measured 340 Ω. The resistance of this membrane is quite high because it is very thick. In fact the AMI-7001 and FTAM are approximately three times thicker than the Neosepta AHA. Although the resistivity is useful for normalizing out the thickness of the

membrane, it was not possible to synthesize thinner membranes, so my choice focused on commercial membranes with the lowest resistance.

The capacitance is not the deciding factor in choosing a membrane given the wide range of resistances associated with the membranes. But it is worth noticing that cell capacitance could also be extracted from the data fit.

Capacitances were highest in the cell with the lowest resistances. My subsequent research uses Neosepta AHA, but the Selemion DSV appears to have a lower resistance in contact with ACN-based electrolytes. Thus the Selemion APS4 may be a feasible alternative, if it is found to be chemically and electrochemically stable.

#### 3.1.4 Discussion & Future Membrane Work

A significant amount of work is left to address the challenge of separator selections for non-aqueous RFB systems. A pretreatment procedure that completely exchanges the native chloride for alternative anions has not been created. The pretreatment used for my work resulted in up to 7 % chloride exchange based on CV.

Possible methods to fully exchange ions are:

1. Create an analogous procedure to that used for Nafion membranes, which involves several sequential soaking steps in boiling liquid to increase the rate – and possibly the extent of ion exchange. At each step use an initially chloride-free soaking solution to provide the greatest possible chemical driving force for ion exchange

2. Pass current through the membrane, providing a driving force for chloride ions to migrate out of the membrane. This will probably require that a sacrificial solution be used, which will degrade as current can be passed. Steps will have to be taken to transfer the membrane into a chloride free electrolyte without fouling.
3. Place membranes in a solution with two solutes. One has the anion desired to be exchanged into the membrane backbone. The other is a chemical that will react with the chloride to form a molecule that precipitates. This would provide a continuous chemical driving force for chloride to leave the membrane, which would take much less time than the procedure proposed in step 1. A precipitation-driven procedure was attempted, but the precipitate formed inside the membrane, and could not be easily removed.

Note that there is no need to restrict analysis to the anion exchange membranes. It is also possible to use cation-exchange membranes for non-aqueous RFB systems. Thus impedance should be performed for cation-exchange membranes. Porous separators are also less costly, and are worth investigating for comparison. It would be worth evaluating these alternative membranes if anion-exchange membranes are found to be unstable in the particular solvent/supporting electrolyte solution being used. Membrane stability needs further attention as well, as it is one of the main factors that leads to degradation in aqueous RFB systems over time.



## 3.2 Electrodes

### 3.2.1 Background

Ideally, the electrode in a RFB should be inert and participate in the reactions as a reversible source or sink for electrons [104], but such behavior is not always observed in practice. Rychcik *et al.* investigated the aqueous all-vanadium RFB electrochemistry with glassy-carbon, gold, lead, and iridium-oxide-on-titanium electrodes [104]. They observed that the electrode material significantly affected the oxidation kinetics and stability; lead was even shown to inhibit the desired reaction. Hodes *et al.* examined the effects of electrode material on the polysulfide redox half-reaction, which could be used in a bromine-polysulfide RFB [105]. Polarization curves for carbon, platinum black, brass, and various transition-metal sulfides (RuS, PbS, and CoS) revealed that the reaction rates for the polysulfide redox half-reaction were dependent on electrode type. Hollax *et al.* [106] and Lopez-Atalaya *et al.* [107] studied kinetics of an aqueous iron/chromium RFB. Lopez-Atalaya *et al.* examined gold-on-graphite electrodes and observed a change in peak shape upon the addition of gold particles to the graphite surface.

Linear-sweep voltammetry (LSV) at microelectrodes can be used to quantify the effect of electrode material by evaluating the reaction kinetics and liquid-phase transport properties for electrochemical reactions. Aoki *et al.* developed a model to determine the current from a linear-sweep voltammogram based on a single, diffusion-limited elementary half-reaction and compared it to experimental results [108]. A model was created by Baur *et al.* to determine

diffusion coefficients for several systems (aqueous ferrocyanide, aqueous ruthenium hexamine, and non-aqueous ferrocene) which matched literature values with less than 5 % error [109]. Mirkin *et al.* created tables to relate half- and quartile-wave potentials, from LSV data to kinetic and mass-transfer parameters [110]. All of this previous literature examines single half-reactions, and is consequently not immediately applicable to the non-aqueous vanadium RFB system. At equilibrium, the non-aqueous vanadium electrolyte contains small concentrations of  $V(acac)_3^-$  and  $V(acac)_3^+$  associated with the equilibrium of  $V(acac)_3$  in bulk solution. The presence of all three oxidation states of the complex results in a mixed current at each electrode during charge and discharge. For example, if the potential at an electrode is large and positive, then oxidation of  $V(acac)_3$  will dominate, but  $V(acac)_3^-$ , which is present in trace amounts in the bulk, will still oxidize to a minor extent. This coupled behavior makes it difficult to apply previous models to the non-aqueous vanadium chemistry.

It is common for coordination complexes to undergo successive one-electron transfers, where sequentially greater or lesser energies are associated with each electron exchanged [111]; several researchers have modeled these systems. Asselt *et al.* used chronoamperometry and steady-state voltammetry to measure the diffusion coefficients for several palladium complexes at a gold electrode and observed reversible electron-transfer reactions [112]. Norton *et al.* used the steady-state voltammogram, along with a known expression for the equilibrium constant, to determine the reaction rate for comproportionation of

methyl viologen in acetonitrile [113]. Both of these previous investigations treat the successive reactions separately. The electron-transfer mechanism, including the effects of neutral-species concentration changes, will be discussed below for the non-aqueous vanadium chemistry.

This section reports a study of the effect of electrode type on the oxidation and reduction rates of  $V(\text{acac})_3$  in a  $\text{TEABF}_4$  and ACN electrolyte. Three electrode materials (glassy carbon, gold, and platinum) were evaluated using cyclic and LSV to determine the coulombic reversibility, kinetic reversibility, and exchange-current density for  $V(\text{acac})_3$  oxidation and reduction on each material. The  $V(\text{acac})_3$  oxidation and reduction occurs simultaneously, causing a mixed current, which required the derivation of a model to decouple the results. LSV was also used to study active-species transport.

### 3.2.2 Approach

#### *Microelectrodes*

Planar disks of glassy carbon, gold, and platinum were used as working electrodes for the voltammetric experiments. The glassy-carbon microelectrode consisted of a 1 mm glassy-carbon rod embedded in PEEK (ALS, Japan). Gold and platinum microelectrodes were produced by flame-sealing a 100  $\mu\text{m}$  diameter gold or platinum wire (99.998%, Alfa Aesar, US) into soda-lime glass, followed by polishing to expose a disk of the material. All electrodes were polished sequentially with 15  $\mu\text{m}$ , 6  $\mu\text{m}$ , and 0.1  $\mu\text{m}$  silicon carbide paper prior to each experiment.

### *Cyclic and Linear-Sweep Voltammetry*

Every CV and LSV experiment was performed at the same dimensionless scan rate,  $\omega$ , to ensure that electrodes of different sizes were examined under similar conditions. The dimensionless scan rate,  $\omega$ , is defined as [45]

$$\omega = \frac{\dot{v} n F r^2}{RTD} \quad (3-4)$$

where  $\dot{v}$  is the scan rate in V/s,  $n$  is the number of electrons transferred ( $n=1$  in all reactions discussed here),  $F$  is Faraday's constant ( $96485 \text{ C mol}^{-1}$ ),  $r$  is the radius of the disk microelectrode,  $R$  is the gas constant ( $8.314 \text{ J mol}^{-1} \text{ K}^{-1}$ ),  $T$  is the absolute temperature ( $297 \text{ }^\circ\text{K}$ ), and  $D$  is the diffusion coefficient of the neutral active species through the support solution. The temperature and diffusion coefficient were considered constant when determining the dimensionless scan rate. The diffusion coefficient used was  $3.93 \times 10^{-6} \text{ cm}^2/\text{s}$ , which is determined later in this report. Results were measured after the voltammogram stabilized, typically after 20 cycles. Peak potentials and currents were measured using the Autolab software package, GPES.

#### 3.2.3 Results: Experimental

Figure 3.2.3-1 shows cyclic voltammograms of a  $0.01 \text{ M V}(\text{acac})_3$  and  $0.05 \text{ M TEABF}_4$  solution in ACN, with three different working-electrode materials. A low active-species concentration was used to approach ideal solution behavior and does not reflect the maximum solubility of  $\text{V}(\text{acac})_3$  in the system ( $0.6 \text{ M}$  in ACN). The scan rate was selected to be as slow as possible while retaining

definitive redox peaks,  $\omega=500$  (this number is dependent on the diffusion coefficient). To normalize the peak currents with respect to mass-transfer limitations, current densities are multiplied by the electrode radii on the ordinate axes. Isolated peak pairs centered around  $-1.77$  V and  $0.45$  V vs.  $\text{Ag}/\text{Ag}^+$  were observed for all electrode materials. These peak locations are consistent with  $\text{V}(\text{acac})_3$  oxidation and reduction equilibria [76]. It is important to note that the peak at  $+0.75$  V vs  $\text{Ag}/\text{Ag}^+$  which was reported previously [49] is not observed because most of the vanadyl acetylacetonate has been removed from the solution precursor [56].

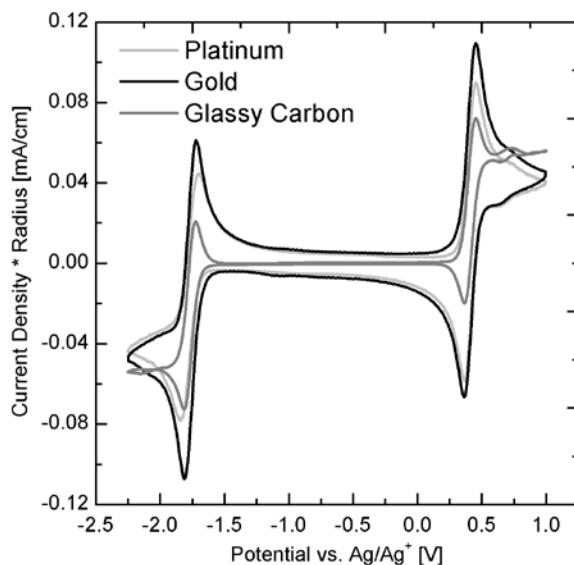


Figure 3.2.3-1 Cyclic voltammograms ( $\omega=500$ ) for glassy carbon, gold, and platinum microelectrodes in  $0.01\text{M V(III)(acac)}_3$ ,  $0.05\text{ M TEABF}_4$  in ACN. Measurements performed at  $23^\circ\text{C}$ .

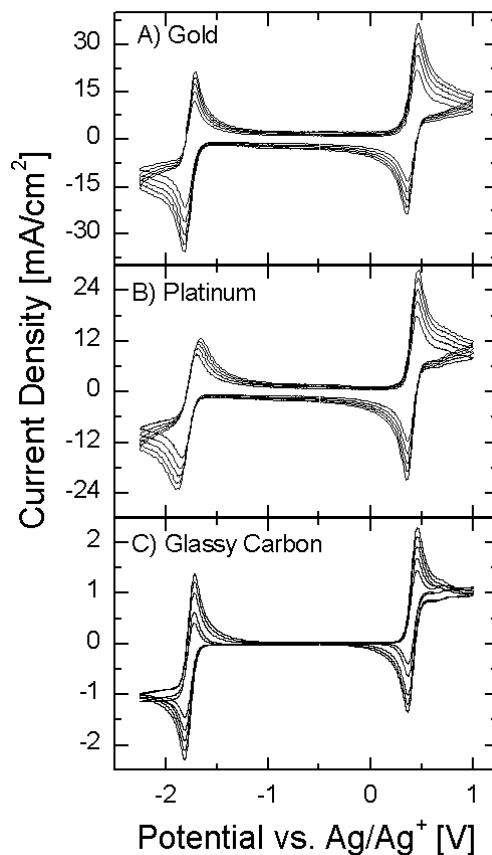


Figure 3.2.3-2 Cyclic voltammograms ( $\omega=500-1490$ ) for (A) gold, (B) platinum, and (C) glassy carbon microelectrodes in 0.01M  $V(III)(acac)_3$ , 0.05 M  $TEABF_4$  in ACN. Measurements performed at 23 °C.

Information about the coulombic and kinetic reversibility can be gained by examining CV results as a function of scan rate, shown in Figure 3.2.3-2. The coulombic reversibility of a redox couple can be determined from its cyclic voltammogram by comparing the anodic and cathodic peak heights at several scan rates [45]. Scan rates for Au and Pt were calculated, according to equation (3-4), by multiplying the glassy-carbon scan rate by 100 to account for the ten-fold decrease in electrode radius. The peak-height ratios for  $V(acac)_3$  reduction are  $1.00 \pm 0.05$ ,  $1.03 \pm 0.05$ , and  $0.99 \pm 0.05$  on glassy carbon, gold, and

platinum, respectively – each unity within experimental error. The peak-height ratios for  $V(\text{acac})_3$  oxidation are  $0.98 \pm 0.05$ ,  $1.05 \pm 0.05$ , and  $0.98 \pm 0.05$  on glassy carbon, gold, and platinum, respectively – again unity within experimental error. Thus, it can be concluded that the redox reactions are coulombically reversible within error for all the electrode materials.

A range of dimensionless scan rates  $\omega$  ranging from 500 to 1490 were used to determine the change in peak separation. The observed change over this range of scan rates on glassy carbon, gold and platinum was approximately 20 mV for the  $V(\text{acac})_3 / V(\text{acac})_3^+$  redox couple (Figure 3.2.3-2). This small change in peak separation suggests the redox couple is kinetically fast. Peak-separation changes of 20 mV, 70 mV, and 30 mV were observed for the  $V(\text{acac})_3 / V(\text{acac})_3^-$  redox couple on glassy carbon, platinum, and gold respectively. Glassy carbon showed the least change in peak separation, however this may owe to the larger electrode area used. The small change in peak separation makes it difficult to determine the exchange current using CV methods, justifying the use of LSV, which accounts for the actual reaction mechanism, to more precisely quantify rates.

#### 3.2.4 Results: Mechanistically-Based Kinetic Model

Figure 3.2.4-1 and Figure 3.2.4-2 show LSV results for the  $V(\text{acac})_3 / V(\text{acac})_3^+$  and  $V(\text{acac})_3^- / V(\text{acac})_3$  redox couples, respectively, on each of the three electrode materials. All currents are normalized by the limiting current of the  $V(\text{acac})_3 / V(\text{acac})_3^+$  redox couple to eliminate electrode-size effects when

comparing different disk electrodes. For Figure 3.2.4-1 and Figure 3.2.4-2, graphs (A) – (C) show data fitted by the model derived below for glassy carbon, gold, and platinum. At least three sets of data are displayed on each plot to illustrate the error associated with the experimental procedure. Graph (D) shows one data set from each electrode material to facilitate comparison among them. A scan rate of 0.3 mV/s was shown to be suitably slow to achieve pseudo-steady mass transfer for all the electrode sizes. An identical dimensionless scan rate was not used in LSV for the largest electrode because bulk concentration changes due to the overall extent of reaction and evaporation of the solvent were found to be significant on that long time scale.



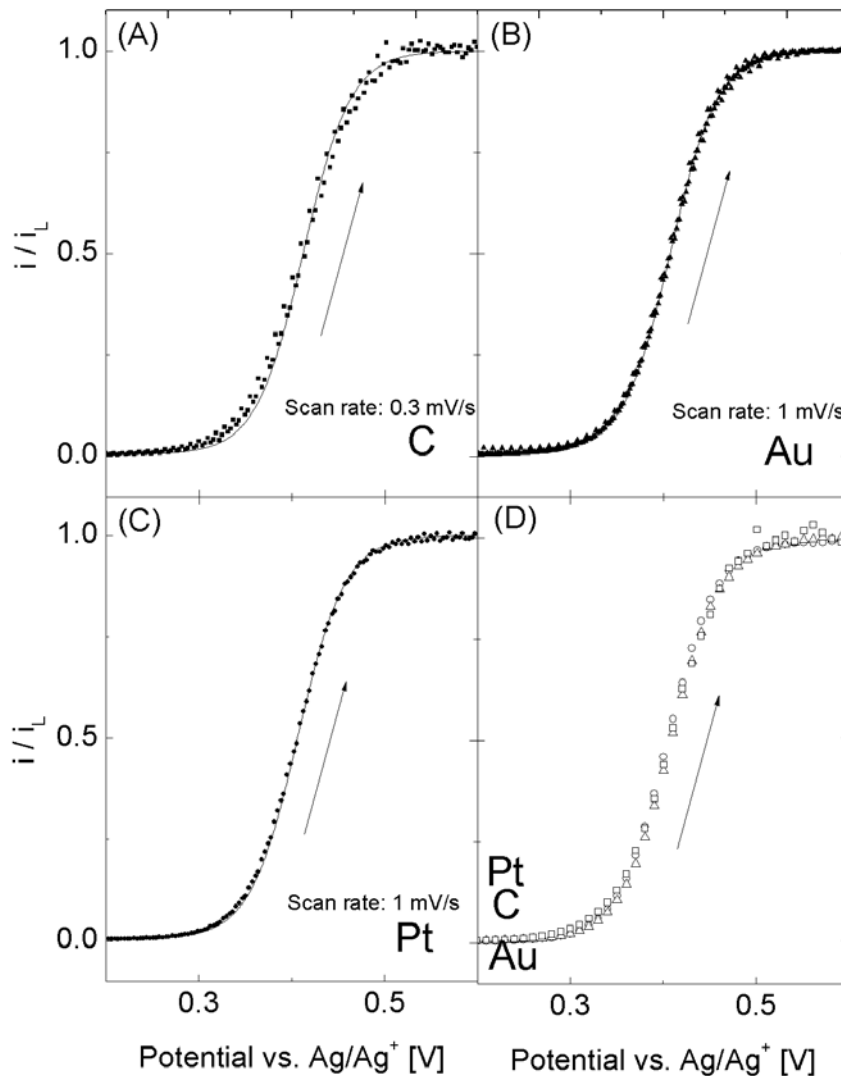


Figure 3.2.4-1 LSV for the V(III) / V(IV) redox couple at (A) glassy carbon [squares] (B) gold [triangles] (C) platinum [circles], and (D) all microelectrodes in 0.01 M V(III)(acac)<sub>3</sub> and 0.05 M TEABF<sub>4</sub> in ACN. Scan rate 0.3 mV/s ( $\omega=7.4$ ) on glassy carbon and 1 mV/s ( $\omega=0.25$ ) on gold and platinum; measurements performed at 23 °C; arrow indicates direction of change in potential.

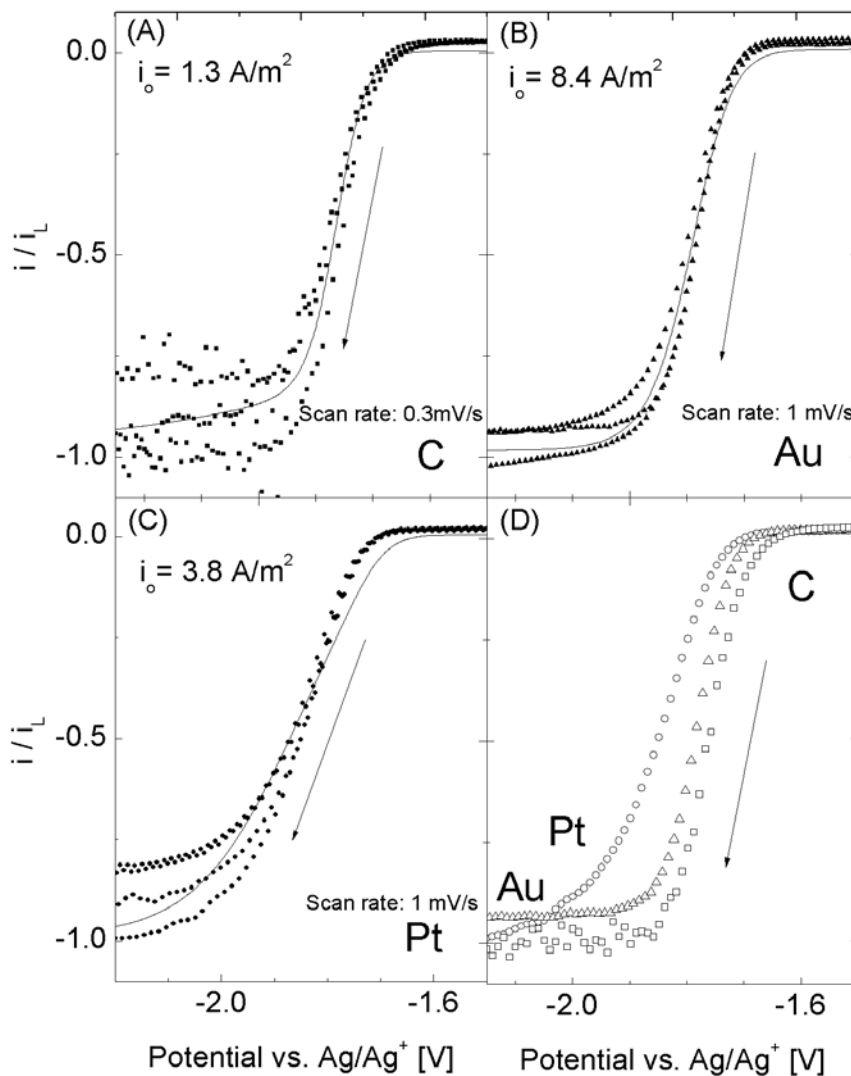


Figure 3.2.4-2 LSV for the V(II) / V(III) redox couple at (A) glassy carbon [squares] (B) gold [triangles] (C) platinum [circles], and (D) all microelectrodes in 0.01 M V(III)(acac)<sub>3</sub> and 0.05 M TEABF<sub>4</sub> in ACN. Scan rate 0.3 mV/s ( $\omega=7.4$ ) on glassy carbon and 1 mV/s ( $\omega=0.25$ ) on gold and platinum; measurements performed at 23 °C; arrow indicates direction of change in potential.

An ideal reversible linear-sweep voltammogram for an elementary half-reaction has a sigmoidal shape centered about zero current at the equilibrium potential [45]. Its anodic and cathodic limiting currents have opposite signs and are proportional to the bulk concentrations of oxidized and reduced species,

respectively. As the exchange-current density decreases, the sigmoid broadens. In the case where one species concentration is small and kinetics is slow, the linear-sweep voltammogram half-wave potential will be significantly shifted from the equilibrium potential and one of the limiting currents will be very small. The linear-sweep voltammograms in Figure 3.2.4-1 have half-wave potentials close to the equilibrium potential, suggesting that the reaction rate is fast, but the current has the same sign across the entire wave. In order to rationalize this observation, it is important to note that the electrolyte contains  $V(acac)_3^-$ ,  $V(acac)_3$ , and  $V(acac)_3^+$  in proportions corresponding to the disproportionation equilibrium constant of  $V(acac)_3$ . Since all three species exist in solution, a mixed current is seen from both the oxidation and reduction half-steps of the disproportionation. Thus, when LSV is performed in the potential domain associated with  $V(acac)_3$  oxidation, the observed currents stem from the oxidation of both  $V(acac)_3$  and  $V(acac)_3^-$ ; when LSV is performed in the  $V(acac)_3$  reduction domain, the current reflects reduction of both  $V(acac)_3$  and  $V(acac)_3^+$ . A second complicating factor is that the  $V(acac)_3 / V(acac)_3^+$  and  $V(acac)_3^- / V(acac)_3$  redox couples both involve  $V(acac)_3$ . Consequently, the currents associated with the two reactions, which both depend on the  $V(acac)_3$  concentration, cannot be decoupled [45]. Therefore, a model was created to account for the mixed current generated by two coupled redox reactions.

Both the  $V(acac)_3 / V(acac)_3^+$  and  $V(acac)_3^- / V(acac)_3$  half-reactions are assumed to be elementary. Thus the current density  $i_n$  induced by an

experimentally controlled potential  $V$  can be described in terms of Butler-Volmer kinetic expressions associated with the two simultaneous redox reactions,

$$i_n = i_{0+}^* \left[ \frac{c_0}{c_0^*} e^{(1-\beta_+)f(V-E_+^*)} - \frac{c_+}{c_+^*} e^{-\beta_+f(V-E_+^*)} \right] + i_{0-}^* \left[ \frac{c_-}{c_-^*} e^{(1-\beta_-)f(V-E_-^*)} - \frac{c_0}{c_0^*} e^{-\beta_-f(V-E_-^*)} \right] \quad (3-5)$$

Here  $c_k$  is the concentration of active species in state  $k$  at the electrode surface and  $c_k^*$ , its bulk concentration; subscripts +, -, and 0 denote properties of the vanadium active complex in its positive (V(IV), V(acac)<sub>3</sub><sup>+</sup>), negative (V(II), V(acac)<sub>3</sub><sup>-</sup>), and neutral (V(III), V(acac)<sub>3</sub>) states, respectively. In the rate expression  $i_{0k}^*$  represents the exchange-current density of the half-reaction that converts neutral vanadium to charged species  $k$ ,  $\beta_k$  is the associated symmetry factor,  $f$  is equal to  $F/RT$ , and  $E_k^*$  is the formal potential for the half-reaction involving species  $k$  measured from CV.

For LSV experiments performed at sufficiently low dimensionless scan rates ( $\omega < 1$  [45]), the concentration distributions of the various redox states of V(acac)<sub>3</sub> can be assumed to be in quasi-steady states within the diffusion layer. Under these circumstances the concentrations of V(acac)<sub>3</sub><sup>-</sup> and V(acac)<sub>3</sub><sup>+</sup> ( $c_-$  and  $c_+$ ) can be substituted in favor of their known bulk concentration using the relation for steady-state flux at a disk electrode [114],

$$N_k = 4D_k (c_k^* - c_k) r \quad (3-6)$$

a material balance at the electrode surface,

$$N_+ + N_- + N_0 = 0 \quad (3-7)$$

and Faraday's law:

$$i_n = F(N_+ - N_-) \quad (3-8)$$

where  $N_k$  is the molar flux of species  $k$  and  $D_k$  is the diffusion coefficient of  $k$  through the supporting solution.

First equations ( 3-5 ) – ( 3-8 ) will be used to describe the  $V(acac)_3 / V(acac)_3^+$  redox couple (oxidation of the active complex). Since the formal potentials are very far apart (2.2 V), it is assumed that the current component associated with the  $V(acac)_3 / V(acac)_3^-$  reaction is constant and at the reaction's limiting current. The resulting equation can be simplified by assuming the equilibrium potential is far away from that of the  $V(acac)_3 / V(acac)_3^-$  reaction, implying  $f(V - E_-^*) \gg 1$  and  $c_- / c_-^* = 0$ . The resulting equation relates the observed current to both dimensionless permeabilities and the exchange-current density of the positive reaction.

$$\frac{i_n}{i_L} = \frac{i_{0+}^* \left[ \phi_+ (1 + 2\phi_-) e^{(1-\beta_+)f(V-E_+^*)} + (\phi_- - \phi_+) e^{-\beta_+f(V-E_+^*)} \right]}{\phi_+ i_L + i_{0+}^* \left[ \phi_+ e^{(1-\beta_+)f(V-E_+^*)} + e^{-\beta_+f(V-E_+^*)} \right]} \quad (3-9)$$

$$\text{where } \phi_+ = \frac{D_+ c_+^*}{D_0 c_0^*} \quad \text{and} \quad \phi_- = \frac{D_- c_-^*}{D_0 c_0^*} \quad (3-10)$$

$$\text{also } i_L = 4nFD_0 c_0^* r \quad (3-11)$$

The anodic and cathodic limiting currents for the  $V(acac)_3$  oxidation reaction can be identified from equation ( 3-9 ) by examining the expression in the limits

$V - E_- \rightarrow \infty$  and  $V - E_- \rightarrow -\infty$  to yield

$$\frac{i_{L,a}^+}{i_L} = \lim_{V-E_+^* \rightarrow \infty} \frac{i_n}{i_L} = (1 + 2\phi_-) \quad \text{and} \quad \frac{i_{L,c}^+}{i_L} = \lim_{V-E_+^* \rightarrow -\infty} \frac{i_n}{i_L} = \frac{\phi_+ + \phi_-}{1 + 2\phi_-} \quad (3-12)$$

During LSV the anodic limiting current is reached when voltages are far positive of the equilibrium potential for V(acac)<sub>3</sub> oxidation.

The dimensionless permeabilities of the oxidized and reduced active species through the liquid phase,  $\phi_+$  and  $\phi_-$ , are defined by equation ( 3-10 ). Qualitatively they can be thought of as mobilities of charged active species relative to the neutral active-species mobility. To determine the values of  $\phi_+$  and  $\phi_-$ , equation ( 3-9 ) can be examined in the limit that the exchange current density  $i_{0+}^*$  is very large compared to  $i_L$ , yielding a mass-transfer-limited expression:

$$\frac{i_n}{i_L} = \frac{(\phi_- - \phi_+) + \phi_+ (1 + 2\phi_-) e^{f(V-E_+^*)}}{1 + \phi_+ e^{f(V-E_+^*)}} \quad ( 3-13 )$$

In terms of the chemistry being studied here, this assumption implies that there is a minimal kinetic overpotential associated with neutral-vanadium oxidation. This approximation is consistent with the CV experiments discussed earlier, which showed near-constant peak separation with respect to scan rate for the V(acac)<sub>3</sub> / V(acac)<sub>3</sub><sup>+</sup> redox couple in CV on all three electrodes (Figure 3.2.3-2). This observation can be rationalized by Marcus theory, which associates low kinetic overpotentials (high electron transfer rates) with correspondingly low reorganization energy of the reactants, products, and the electronic structure of the electrode materials [115, 116]. The data for all electrode materials were fit well by this mass-transfer-limited model and were indistinguishable when overlaid. Therefore, V(acac)<sub>3</sub> oxidation likely occurs by a mass-transfer-limited

elementary electron transfer mechanism on all three electrode materials studied here.

The dimensionless permeabilities in equation ( 3-10 ) can be defined in terms of experimental values, which are easily extracted from the data by adding a single measurement of the current density at the equilibrium potential of the  $V(acac)_3 / V(acac)_3^+$  redox half-reaction,  $i_n(E_+^*)$ , to eliminate  $i_L$ . The relations

$$\phi_+ = \frac{i_n(E_+^*) - i_{L,c}^+}{i_{L,a}^+ - i_n(E_+^*)} \quad \text{and} \quad \phi_- = \frac{i_n(E_+^*)(i_{L,a}^+ - i_{L,c}^+)}{[i_{L,a}^+ - i_n(E_+^*)](i_{L,a}^+ - 2i_{L,c}^+)} \quad (3-14)$$

were determined by evaluating equation ( 3-13 ) at the equilibrium potential and in the limit of large negative voltages. Here  $i_{L,c}^+$  is the cathodic limiting current of the neutral-vanadium reduction half-reaction (the limiting current reached at very negative voltages); and  $i_{L,a}^+$  is the anodic limiting current of the neutral-vanadium reduction half-reaction.

Dimensionless permeabilities  $\phi_+$  and  $\phi_-$  were determined by applying the mass-transfer-limited rate expression for oxidative LSV sweeps, and found to be  $1.25 \pm 0.11$  and  $1.27 \pm 0.12$ , respectively. The accuracy of the permeabilities was checked by predicting the limiting current for  $V(acac)_3$  reduction based on the permeabilities determined using results from the  $V(acac)_3$  oxidation. The reduction limiting currents were predicted within 7 % – less than the inherent measurement error in the permeabilities. The dimensionless permeabilities are expected to be identical across systems with different electrode materials, since they are solution characteristics. However, it is surprising that both  $\phi_+$  and  $\phi_-$  are

of order 1, because the neutral and charged vanadium complexes are expected to have very different concentrations. Deviations from this expected characteristic may owe to large differences in the diffusion coefficients or activities of the charged complex compared to the neutral species. It may also owe to the neglect of ionic migration in the transport model [117].

The dimensionless permeability can be used to evaluate the active-species diffusion coefficient. The diffusion coefficient of  $V(\text{acac})_3$  in the supporting electrolytic solution can be derived from equation ( 3-6 ) and ( 3-9 ) evaluated at the equilibrium potential.

$$D_0 = \frac{|i_{L,a}^+|}{4nFc_0^*r(1+2\phi_-)} \quad (3-15)$$

The limiting current,  $|i_{L,a}^+|$ , and permeability,  $\phi_-$ , are determined from the experiments shown in Figure 3.2.4-1. Error in the microelectrode radius and solution concentration increases the uncertainty of the resulting diffusion coefficient. The diffusion coefficient for  $V(\text{acac})_3$  in  $\text{TEABF}_4$ -supported ACN was found to be  $3.93 \times 10^{-6} \pm 7.2 \times 10^{-7} \text{ cm}^2/\text{s}$  which is approximately 1.5 times the value found by Liu *et al* [49] using the Randles-Sevcik method. This difference could be caused by a deviation in the  $V(\text{acac})_3$  concentration from the expected value due to the neglect of vanadyl acetylacetonate formation [56] in the report by Liu *et al*.

A similar strategy to the one detailed above can be used to describe the neutral-vanadium-complex reduction. When deriving the expression for the reduction current, the assumption of very fast kinetics is no longer valid because the equilibrium potential for the oxidation is close to the onset potential observed



in LSV (Figure 3.2.4-2) and a visible increase of peak separation with scan rate is seen in the CV results (Figure 3.2.3-2). First, equations ( 3-5 ) – ( 3-8 ) were used to describe the  $V(acac)_3 / V(acac)_3^-$  redox couple (reduction of the active complex). Since the formal potentials are very far apart (2.2 V), it is assumed that the current component associated with the  $V(acac)_3 / V(acac)_3^+$  reaction is constant at its limiting current. The resulting equation can be simplified by assuming the potential is far away from that of the  $V(acac)_3 / V(acac)_3^+$  reaction, implying that  $f(E_+^* - V) \gg 1$  and  $c_+ / c_+^* = 0$ . The resulting equation relates the observed current to both dimensionless permeabilities (determined from the positive reaction) and the exchange-current density of the negative reaction.

$$\frac{i_n}{i_L} = \frac{i_{0-}^* \left[ (\phi_- - \phi_+) e^{(1-\beta_-)f(V-E_-^*)} - \phi_- (1+2\phi_+) e^{-\beta_- f(V-E_-^*)} \right]}{\phi_- i_L + i_{0-}^* \left[ e^{(1-\beta_-)f(V-E_-^*)} + \phi_- e^{-\beta_- f(V-E_-^*)} \right]} \quad (3-16)$$

The anodic limiting current of the  $V(acac)_3$  reduction half-reaction can be related to the parameter  $i_L$  by examining equation ( 3-16 ) in the limit  $V - E_- \rightarrow -\infty$  to yield

$$i_L = \frac{1}{(1+2\phi_-)} i_{L,a}^+ \quad (3-17)$$

The kinetics of the  $V(acac)_3^- / V(acac)_3$  redox couple is therefore described by the following equation:

$$\frac{i_n}{|i_{L,a}^+|} = \frac{\frac{i_{0-}^*}{|i_{L,a}^+|} \left[ (\phi_- - \phi_+) e^{(1-\beta_-)f(V-E_-^*)} - \phi_- (1+2\phi_+) e^{-\beta_- f(V-E_-^*)} \right]}{\phi_- + \frac{i_{0-}^*}{|i_{L,a}^+|} (1+2\phi_-) \left[ e^{(1-\beta_-)f(V-E_-^*)} + \phi_- e^{-\beta_- f(V-E_-^*)} \right]} \quad (3-18)$$

The current-density parameter  $i_L$  and mobilities  $\phi_+$  and  $\phi_-$  were determined from the experimental data for the  $V(acac)_3 / V(acac)_3^+$  redox couple (Equation ( 3-14

)). Using transport parameters from the  $V(\text{acac})_3 / V(\text{acac})_3^+$  redox couple to fit the  $V(\text{acac})_3^- / V(\text{acac})_3$  redox couple adds confidence to the validity of the data-fitting strategy.

Graphs (A) – (C) on Figure 4 show model fits line alongside the data, which were used to calculate exchange-current densities for  $V(\text{acac})_3$  reduction. The model current was fit to data by using  $i_{0-}/i_{L,a}^+$  and  $\beta_-$  as fit parameters with a nonlinear curve fitting program (OriginLab OriginPro 8). Exchange currents were normalized by the anodic limiting currents to facilitate convergence during curve fitting. Prior to performing this analysis, the data were shifted such that the anodic limiting current matched the model prediction. This had to be done to subtract out any current associated with residual dissolved oxygen in the acetonitrile at  $-1.25$  V vs  $\text{Ag}/\text{Ag}^+$  [56]. Shifting the curve is reasonable since neither of these reactants is involved in the reactions of interest [45]. All the data are fit well by equation ( 3-18 ), consistent with the assumption that the electron transfers are elementary.

The exchange current for the  $V(\text{acac})_3^- / V(\text{acac})_3$  redox couple is expected to be comparable to or smaller than  $i_L$  since the kinetics is relatively slow. The best-fit values of  $i_{0-}/i_{L,a}^+$  were 1.5, 0.09, and 0.22 for glassy carbon, platinum, and gold, respectively. These results correlate well with the relative rates of reaction, estimated by the slope and onset potential, observed from Figure 3.2.4-2 graph D as well as peak separations from Figure 3.2.3-2. Since the glassy-carbon electrode has a tenfold larger radius, the glassy carbon exchange-current density is smallest. Measured values of exchange-current

density for the three electrode materials are shown in Table 3.2.4-1. The  $V(acac)_3^- / V(acac)_3$  couple exhibits exchange-current densities of 1.3 A/m<sup>2</sup>, 3.8 A/m<sup>2</sup>, and 8.4 A/m<sup>2</sup> for glassy carbon, platinum, and gold, respectively. All of the exchange-current densities are of the same order of magnitude, suggesting that this reaction proceeds through a similar pathway on all of the electrode materials. The peak separation measurements predicted that the exchange-current density would be smallest on platinum. However, the peak shape also affects the reaction rate [110] and may have convoluted the results. Since the electrode materials all yield exchange-current densities of the same order, and gold and platinum cost significantly more than carbon, it would be more practical to use glassy carbon as the electrode material. The exchange current of a carbon electrode can be increased by using high-surface-area carbon.

Electrode Material	Symmetry factor ( $\beta$ )	Exchange-current Density
Glassy Carbon	0.079 $\pm$ 0.007	1.3 A/m <sup>2</sup>
Platinum	0.278 $\pm$ 0.003	3.8 A/m <sup>2</sup>
Gold	0.567 $\pm$ 0.008	8.4 A/m <sup>2</sup>

Table 3.2.4-1 Symmetry factor and exchange-current density for the  $V(II) / V(III)$  redox couple at glassy carbon, gold, and platinum electrodes in 0.01M  $V(III)(acac)_3$ , 0.05M TEABF<sub>4</sub> in ACN. Measurements performed at 23°C.

Despite the differences in active-complex structure and metal valence states between the non-aqueous and aqueous vanadium RFB chemistries, values for the half-reaction exchange-current densities can provide meaningful comparisons of the kinetic overpotential losses between the two systems. In the aqueous system, the largest overpotential comes from the positive electrode: the  $V(IV)/V(V)$  redox couple has the lowest exchange-current density, which indicates the slowest reaction kinetics. Zhong and Skyllas-Kazacos reported that

the exchange-current density (based on geometric surface area) for the V(IV) / V(V) redox couple at a carbon electrode was 2.47 A/m<sup>2</sup> [118]. The largest kinetic overpotential in the non-aqueous system comes from the reaction that takes place at the negative electrode, the V(acac)<sub>3</sub><sup>-</sup> / V(acac)<sub>3</sub> redox couple. On glassy carbon, this reaction has a slightly lower exchange-current density than the aqueous V(IV)/V(V) couple; on gold and platinum, the V(II)/V(III) reaction exchange-current densities are higher. Also, the non-aqueous V(acac)<sub>3</sub>/V(acac)<sub>3</sub><sup>+</sup> redox couple is reversible (immeasurably high exchange-current density) – it is significantly faster than any electrode process in the aqueous all-vanadium flow battery. It is also worth noting that even the lowest exchange-current densities reported by Zhong and Skyllas-Kazacos are relatively high in light of the peak separation shown in CV during the same study [118].

Measurements of exchange-current densities in the aqueous system may be artificially large, owing to differences between the superficial and electrochemical surface areas of the electrodes used.

The exchange current is the key parameter that determines the kinetic overpotential of a RFB. As the exchange current increases, the RFB kinetic overpotential decreases. An expression for linear kinetics (in the limit that applied voltage *V* is near the equilibrium voltage *E*₋) can be used to approximate the kinetic overpotential in a RFB assuming small overpotential [45].

$$\Delta E = \frac{RT}{nF} \frac{i}{i_0} \quad (3-19)$$

I reported a constant current (1.4 A/m<sup>2</sup> charge current) charge/discharge curve in an H-cell configuration with carbon electrodes and observed charge voltages of

up to 2.9 V (0.7 V of overpotential) [49]. Under those conditions, using equation (3-19), the total kinetic overpotential is estimated to be 31 mV. Therefore, even with carbon electrodes, in this case the kinetics was sufficiently fast that it only contributed ~4 % of the total overpotential observed. The main criterion when choosing an electrode material for the non-aqueous vanadium RFB system is the electrode stability because the rates are similar on all electrode materials.

### 3.2.5 Discussion

To determine the effect of electrode material on the electrochemistry of the  $V(\text{acac})_3/\text{TEABF}_4/\text{ACN}$  redox-flow-battery system, a mechanistic model was developed. CV showed peak-height ratios near unity for all redox couples and electrode materials within experimental error. For oxidation of  $V(\text{acac})_3$ , the change in peak separation was approximately 20 mV on all electrode materials; while the change in peak separation for the reduction of  $V(\text{acac})_3$  was up to 70 mV on platinum. This suggests that the oxidation reaction is quasi-equilibrated, whereas reduction of  $V(\text{acac})_3$  exhibits slower rates.

LSV was used to examine the redox kinetics of  $V(\text{acac})_3$  by fitting an elementary mechanism to the data. The electrode material does not apparently affect the  $V(\text{acac})_3 / V(\text{acac})_3^+$  redox reaction, for which the electron transfer is very fast. The  $V(\text{acac})_3^- / V(\text{acac})_3$  couple has exchange-current densities of 1.3  $\text{A}/\text{m}^2$ , 3.8  $\text{A}/\text{m}^2$ , and 8.4  $\text{A}/\text{m}^2$  for glassy carbon, platinum, and gold, respectively. The exchange-current densities have similar magnitude, suggesting a similar electron-transfer mechanism at all three electrode materials. The diffusion coefficient of  $V(\text{acac})_3$  was determined based on model parameters and was

consistent across all electrode materials, supporting the model's validity. The improvement in reaction rates by using gold or platinum is sufficiently small that it can be overcome by the use of high-surface-area carbon electrodes.

## Chapter 4 Redox Flow Battery Performance

### 4.1 Degradation Mechanisms

This discussion emphasizes how the use of non-aqueous RFB chemistries requires consideration of several new engineering aspects. For instance, the exposure of system materials to environmental oxygen and water before and during battery assembly can significantly affect performance. The charge/discharge response over long-term cycling is discussed in light of these environmental effects.

#### 4.1.1 Approach

In all voltammetry experiments, the working electrodes were 3 mm diameter ( $0.07 \text{ cm}^2$  area) glassy-carbon disk electrodes, which were polished sequentially with 15, 6, and  $0.1 \text{ }\mu\text{m}$  silicon carbide polishing paper, washed, and dried for 8 h prior to each experiment. Charge/discharge experiments were performed with positive and negative electrolytes comprised of  $\text{V}(\text{acac})_3$  and  $\text{TEABF}_4$  in anhydrous ACN. All the solutions were deaerated with pre-purified nitrogen (99.998 %) prior to experiments, which were performed under a blanket of flowing nitrogen unless stated otherwise. For experiments involving oxygen, solutions were subsequently oxygenated with oxygen gas (99.993 %). All the presented results were obtained after performing several cycles at  $500 \text{ mV/s}$

(until the voltammogram stabilized – typically 15 cycles) to remove any residual electrochemically active contaminants.

#### 4.1.2 Results: Cyclic Voltammetry

Regardless of the solvent or active species in a RFB, side reactions that consume the active metal can significantly reduce charge-storage capacity. To maintain reproducible, constant charge capacity over many cycles, procedures should be designed to prevent all irreversible reactions involving the active species. It is worth noting that the supporting electrolytes used in these non-aqueous RFBs are light sensitive. Also, oxygen and water may act as environmental impurities that cause degradation of non-aqueous RFB systems. Several experiments were performed to assess whether oxygen or water adversely affect the non-aqueous  $V(\text{acac})_3$  RFB chemistry.



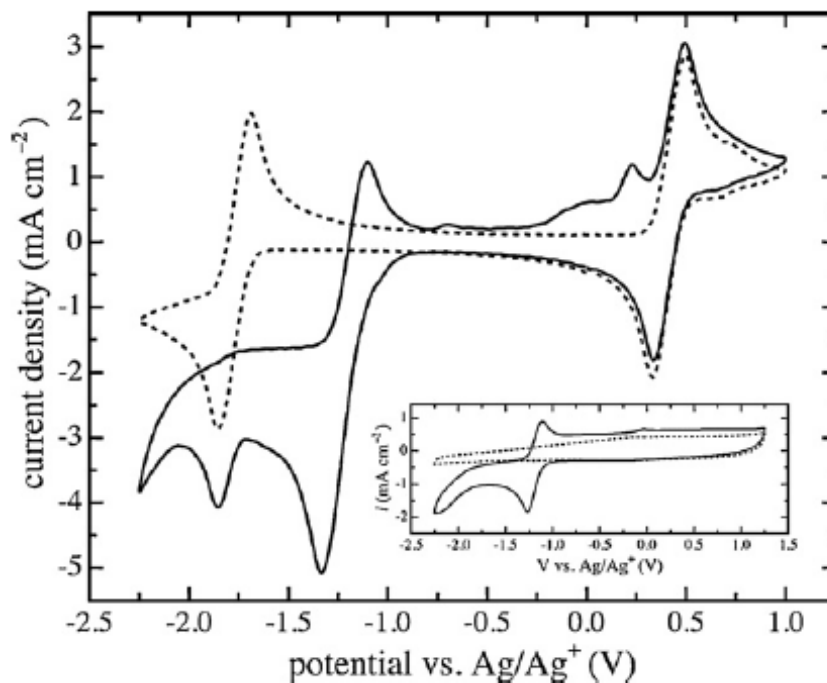


Figure 4.1.2-1 Comparison of cyclic voltammograms with a glassy carbon electrode in deoxygenated (dotted line) and oxygenated (solid line) solutions of 0.01 M  $V(\text{acac})_3$  and 0.05 M  $\text{TEABF}_4$  in ACN. Scan rate 100 mV/s; measurements performed at room temperature. Inset: cyclic voltammograms at 200 mV/s of a similar system without active species present.

Figure 4.1.2-1 compares cyclic voltammograms of deoxygenated and oxygenated solutions of  $V(\text{acac})_3$  in  $\text{TEABF}_4$ -supported ACN. After 2 min of bubbling with oxygen gas, several features appear and persist for many cycles. The presence of dissolved molecular oxygen brings about a step to a very negative limiting current at low voltages, as well as manifesting a reversible redox couple near  $-1.25$  V vs.  $\text{Ag}/\text{Ag}^+$  and several irregular oxidation features over the range between 0.0 and 0.5 V vs.  $\text{Ag}/\text{Ag}^+$ . The oxidation peak associated with the  $V(\text{acac})_3/V(\text{acac})_3^-$  couple appears to be suppressed almost entirely by the addition of oxygen, and the reduction peak is smaller. Note that the formation of oxygen-functionalized groups on carbon electrode surfaces has been shown to

impede aqueous RFB reactions [24]. It is also plausible that the superoxide being formed is reacting (non-electrochemically) with the  $V(II)acac_3$  such that it cannot be converted back to  $V(III)acac_3$ .

Generally the negative limiting current is associated with oxygen reduction. Nawi *et al.* have associated irregular peaks ranging over 0.5 V below the  $V(acac)_3$  oxidation couple to acetylacetonate oxidation [76]. The redox couple at  $-1.25$  V vs.  $Ag/Ag^+$  remains visible when CV is performed using an oxygenated support solution in the absence of  $V(acac)_3$  (see inset in Figure 4.1.2-1), suggesting that the associated reaction does not involve the active species. When the oxygenated solution was purged of oxygen by bubbling with nitrogen for 15 min, the deoxygenated voltammetric signature was reproduced identically. These observations suggest that any irreversible degradation of the active species by oxygen (associated with the peaks between 0 and 0.5 V vs.  $Ag/Ag^+$ ) was minimal, and that the largest voltammetric features brought about by oxygen arise from reactions involving the carbon electrode surface, the solvent, or the supporting electrolyte.

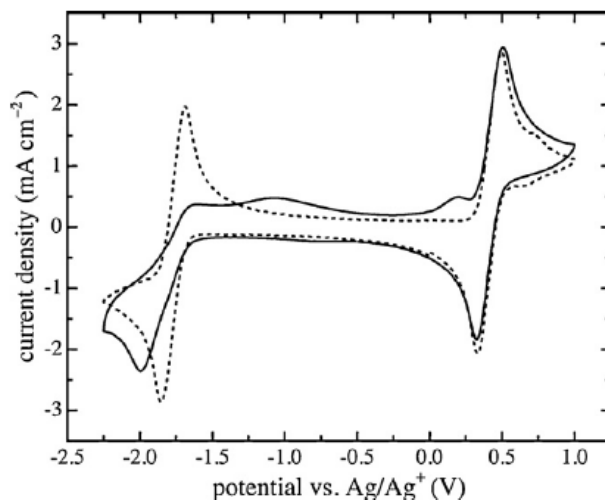


Figure 4.1.2-2 Comparison of cyclic voltammograms with a glassy carbon electrode for water-free (dotted line) and hydrated (solid line) solutions of 0.01 M  $V(acac)_3$  and 0.05 M  $TEABF_4$  in ACN. Scan rate 100 mV/s; measurements performed at room temperature. The hydrated experiment contains 4 vol% water.

Water can have a more pernicious effect than oxygen on vanadium complexes as shown in equation ( 2-19 ). To test sensitivity of the system constituents to environmental water, an experiment was performed in which liquid  $H_2O$  was added to the  $TEABF_4$  supported  $V(acac)_3$  solution in ACN. Figure 4.1.2-2 compares the voltammograms obtained from the water-free solution and the hydrated solution. Note that the voltammetry of the hydrated solution does not stabilize with respect to cycle number. The data reported are for the third cycle after the addition of water; all the observed features shown in Figure 4.1.2-2 continued to increase in magnitude. However, additional features did not appear with continued cycling during the 1 hr timeframe of the experiment.

Upon adding water to the non-aqueous vanadium acetylacetonate RFB electrolyte, small oxidation peaks form near  $-1.0$  and  $0.25$  V vs.  $Ag/Ag^+$ . These features are consistent with oxidation of the vanadium center via reaction( 2-19 ),

which has been hypothesized to proceed by a two-step mechanism [76] consisting of an oxidation reaction ( 2-17 ) followed by an irreversible step:



Since reaction ( 4-1 ) is non-electrochemical, the formal potential of reaction ( 2-19 ) is indistinguishable from that of reaction ( 2-17 ). The peak in the voltammogram at 0.25 V vs. Ag/Ag<sup>+</sup>, can be attributed to the oxidation of free acac<sup>-</sup> anions. The broad oxidation peak near -1.0 V vs. Ag/Ag<sup>+</sup> appears similar to one observed by Nawi *et al.* when Hacac was added to supported non-aqueous V(acac)<sub>3</sub> solutions [76]. Although peaks corresponding to products of reaction ( 4-1 ) were observed, peaks corresponding to redox activity of the VO(acac)<sub>2</sub> complex were not. This could be due to the time-frame of the experiment, which was too short for appreciable VO(acac)<sub>2</sub> formation.

Dissolved water significantly affects the negative vanadium couple (reaction ( 2-16 )). The reduction peak shifts to more negative potential, and the oxidation wave takes on a sigmoidal shape, with the oxidation peak disappearing almost entirely. Water thus appears to impede the kinetics of V(acac)<sub>3</sub> reduction in both the anodic and cathodic directions. During the operation of a RFB the presence of dissolved water could therefore induce significant increases in kinetic overpotential on the negative electrode during charge and discharge steps.

Once formed, VO(acac)<sub>2</sub> must be taken to very negative voltages (below -2.0 V) in an Hacac enriched solution to reform V(acac)<sub>3</sub> [76, 77, 119, 120]. Thus VO(acac)<sub>2</sub> is expected to remain in the RFB system after it is formed. It is unclear whether the conversion of V(acac)<sub>3</sub> to VO(acac)<sub>2</sub> impedes overall function of the

RFB. Figure 4.1.2-3 compares cyclic voltammograms of  $V(acac)_3$  and  $VO(acac)_2$  active species in similar non-aqueous supporting electrolytes. In previous work regarding the non-aqueous vanadium RFB chemistry, a redox couple at  $\sim 0.75$  V vs.  $Ag/Ag^+$  has been observed and attributed to a  $V(IV)/V(V)$  couple [49]. This couple could arise from electrochemically-formed  $VO(acac)_2$  in the presence of dissolved water, which cycles in the battery according to

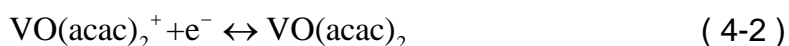


Figure 4.1.2-3 suggests that this reaction is kinetically quasi-reversible. (It is difficult to draw conclusions about coulombic reversibility from peak-height ratios, because the peaks are superimposed on an upward step in current arising from a mass-transfer limitation.) A couple which can be associated with  $VO(acac)_2$  reduction to  $VO(acac)_2^-$ ,



is also visible at  $\sim -2.0$  V vs.  $Ag/Ag^+$ .

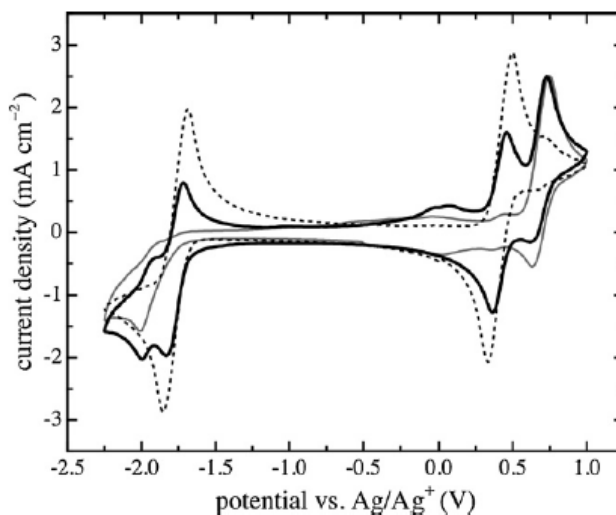


Figure 4.1.2-3 Comparison of cyclic voltammograms with a glassy carbon electrode for 0.01 M  $V(acac)_3$  and 0.05 M  $TEABF_4$  in ACN (dotted line), 'aged' 0.01 M  $V(acac)_3$  and 0.05 M  $TEABF_4$  in ACN (black line), and 0.01 M  $VO(acac)_2$

and 0.05 M TEABF<sub>4</sub> in ACN (grey line). Scan rate 100 mV/s; measurements performed at room temperature.

The formation of VO(acac)<sub>2</sub> during RFB cycling could lead to mixed potentials on the positive and negative electrodes, associated with reactions ( 4-2 ) and ( 4-3 ), respectively. This would make the non-aqueous system operate comparably to the aqueous system, in the sense that the charge/discharge response of the system would reflect the redox behavior of four or more redox-active complexes.

In air one would expect reaction ( 2-19 ) to occur in parallel with the reduction of molecular oxygen, leading to the overall reaction



A free-energy calculation leads to the expectation that reaction ( 2-19 ) will occur on the positive RFB electrode if reaction ( 4-4 ) goes spontaneously to completion in ambient air – i.e., if the reduction potential of Eq. ( 2-19 ) is less than the reduction potential of O<sub>2</sub>.

The progression of reaction ( 4-4 ) was investigated by studying the redox activity of the solid V(acac)<sub>3</sub> precursor as it aged in air over time. Figure 4.1.2-3 shows a voltammogram of a solution prepared using a V(acac)<sub>3</sub> solid precursor that had been aged for several months in ambient air. Peaks corresponding to V(acac)<sub>3</sub> oxidation and reduction (half-reactions ( 2-17 ) and ( 2-16 )) and VO(acac)<sub>2</sub> oxidation and reduction (reactions ( 4-2 ) and ( 4-3 )) are apparent in the voltammogram, providing clear evidence that VO(acac)<sub>2</sub> forms from V(acac)<sub>3</sub> in air. Moreover, the peak currents associated with V(acac)<sub>3</sub> have decreased by almost half, suggesting that reaction ( 4-4 ) has been driven significantly toward

completion. An oxidation peak at 0.25 V vs. Ag/Ag<sup>+</sup> is also visible, suggesting the presence of acetylacetonone derivatives.

To ensure that cell reaction ( 2-18 ) occurs in the non-aqueous V(acac)<sub>3</sub> RFB, it is crucial to eliminate ambient water and air, and to take care that the precursors used to prepare anolyte and catholyte solutions are not exposed to air.

#### 4.1.3 Results: Charge/Discharge – Modest Oxygen Content Glovebox

Charge/discharge characteristics for a 1-D cell containing 0.1 M V(acac)<sub>3</sub> and 0.5 M TEABF<sub>4</sub> in ACN were evaluated. The glove box used for these tests had a continuously flowing nitrogen glove box. No purifier was present in the glove box, so the amount of water/oxygen was >10 ppm (likely less than 100 ppm, based on the rate of phosphoric acid generation on a phosphate indicator). Backflow of air into the glove box was stopped by forcing the outlet stream through a bubbler with a liquid head of mineral oil.

Cycling was performed at very low rates, with a total of 10 cycles performed over approximately a week. The nominal charge and discharge rates were C/14 based on the theoretical maximum SOC, assuming one-electron disproportionation of V(acac)<sub>3</sub>. Charge steps were run from 0 to 40 % of the theoretical maximum SOC, and discharge steps ran until the voltage reached 0.25 V.

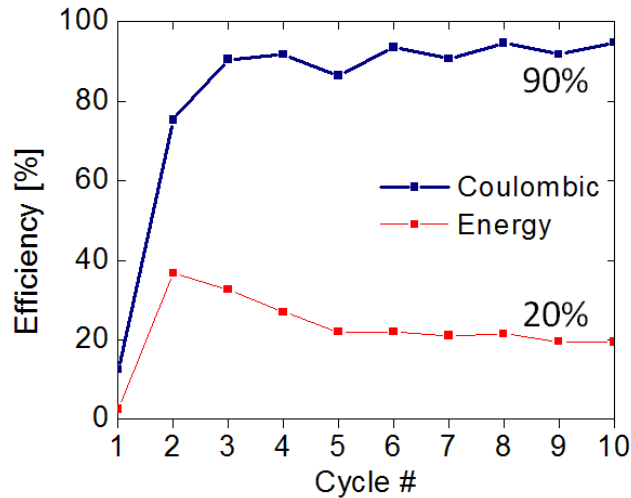


Figure 4.1.3-1 Coulombic and energy efficiency plot associated with the charge / discharge experiment shown in Figure 4.2.2-5.

Figure 4.2.2-5 illustrates the first 10 cycles of the charge / discharge experiment. The % SOC at end-of-charge increases gradually as the RFB is cycled and reaches 100 % of the theoretical state of charge by cycle 6. The first cycle shows no appreciable capacity on discharge; however the subsequent cycle shows a flat discharge plateau near 1.75 V. Over the next three cycles, the 1.75 V plateau fades away in favor of a lower voltage plateau at ~0.7 V. The coulombic efficiency (quantified for a given cycle as charge output divided by charge input) is shown in Figure 4.1.3-1, and is fairly constant over all cycles at 90 %. Since one plateau fades away but the total discharge duration remains constant, this suggests that the active species is being converted into a new species with cycling. The energy efficiency (quantified as energy output divided by energy input) is also shown in Figure 4.1.3-1; it reaches almost 40 % on cycle 2, then falls to ~20 % by cycle 10.



In an attempt to determine the cause of the shift in discharge-plateau position, the electrolyte from each side of the battery was removed and tested using CV. Since this is a reversible battery system, it is expected that the cyclic voltammogram should look the same as voltammograms taken before cycling the battery. Figure 4.1.3-2 shows the cyclic voltammogram before and after cycling for the positive liquid electrolyte. The main redox couples associated with V(II)/(III) and V(III)/(IV) still appear in data gathered from the electrolytes that had experienced prolonged cycling in the RFB cell. Several very prominent differences exist between the voltammograms, however. A redox couple is present at  $\sim 0.75$  V after cycling, which could either be associated with incomplete comproportionation of the charged  $V(acac)^+$  and  $V(acac)^-$  species to  $V(acac)_3$  or with the formation of  $VO(acac)_2$ . Additionally, a reduction peak is observed at  $\sim -1.25$  V, which is associated with the formation of a very reactive superoxide. Peaks associated with oxidation of the  $acac^-$  near  $-0.5$  V vs.  $Ag/Ag^+$  are visible, and are consistent with the ligand-shedding mechanism proposed by Nawi and Riechel [76].

Figure 4.1.3-3 shows the cyclic voltammogram of the solution extracted from the negative side of the same charge/discharge cell Figure 4.1.3-1. The voltammetric signature of the primarily expected redox chemistry is readily apparent. A large oxidation peak is observed near 0 V, which could be associated with the formation of  $acac^-$ . Although ligand is expected to be liberated on the positive side of the cell, it is worth noting that the presence of an

anion-exchange membrane allows migration of negatively charged species across the membrane, justifying the presence of this peak.

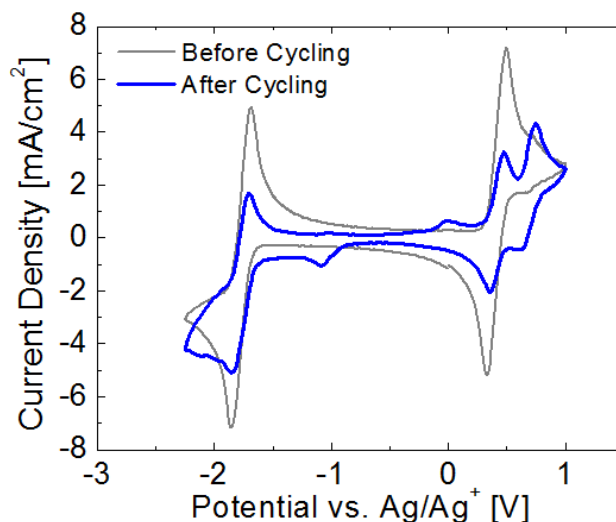


Figure 4.1.3-2 Cyclic voltammograms of the positive electrolyte before (thin gray line) and after (thick blue line) performing the charge/discharge experiment presented in Figure 4.2.2-5. Glassy carbon electrode; scan rate 100 mV/s; room temperature. Pure acetonitrile was used to dilute the V(acac)<sub>3</sub> concentration down to 0.0125 M before voltammetry was performed.

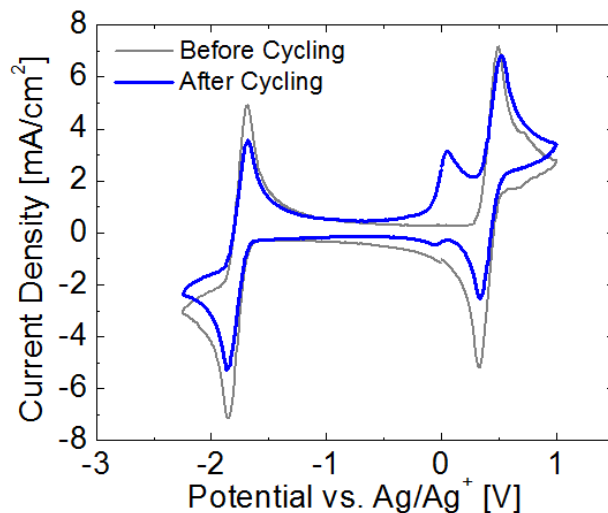


Figure 4.1.3-3 Cyclic voltammograms of the negative electrolyte before (thin gray line) and after (thick blue line) performing the charge/discharge experiment presented in Figure 4.2.2-5. Glassy carbon electrode; scan rate 100 mV/s; room temperature. Pure acetonitrile was used to dilute the V(acac)<sub>3</sub> concentration down to 0.0125 M before voltammetry was performed.

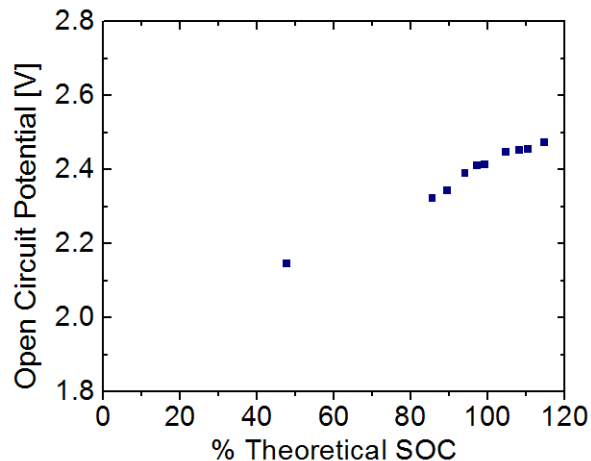


Figure 4.1.3-4 Plot of open circuit potential vs. % theoretical SOC for the charge/discharge experiment shown in Figure 4.2.2-5.

The last piece of information gathered from this charge/discharge (C/D) experiment is the open-circuit potential at end of charge, which generally varies as tests proceed. Figure 4.1.3-4 shows open-circuit potentials gathered at end-of-charge as a function of the % theoretical SOC – similar to Figure 2.1.2-8 from the section on C/D experimental technique. Based on Nernstian analysis, these potentials are expected to be 2.18 V at 50 % SOC and diverge as 100 % SOC is approached. The experimental data clearly shows that a second equilibrium voltage is being reached, and that the transition to this second cell voltage is smooth, suggesting that a mixed potential is being observed. Over time a second cell reaction with a slightly higher equilibrium potential than that of  $V(acac)_3$  disproportionation apparently begins to dominate. The 2.5 V cell voltage is consistent with a cell reaction where  $VO(acac)_2$  oxidizes and reduces at the positive electrode, consistent with the hypothesis that trace amounts of ambient oxygen and water cause  $VO(acac)_2$  to form over time.

#### 4.1.4 Results: Charge/Discharge – Minimal Oxygen Content Glovebox

The results shown in Figure 4.1.3-2 and Figure 4.1.3-3, lead to the conclusion that invasive impurities from the environment can have a significant negative impact on non-aqueous RFB cycle life. After the extent of the problems caused by residual water and oxygen impurities, additional C/D tests were performed using a different glove box with much lower water and oxygen tolerance. The glove box used was a Vacuum Atmospheres static argon glove box oxygen/water sensors and a purifier to guarantee oxygen and water levels below 0.5ppm. It was hypothesized that these lower tolerances on water and oxygen levels are sufficient to inhibit appreciable side reactions during RFB cycling tests.

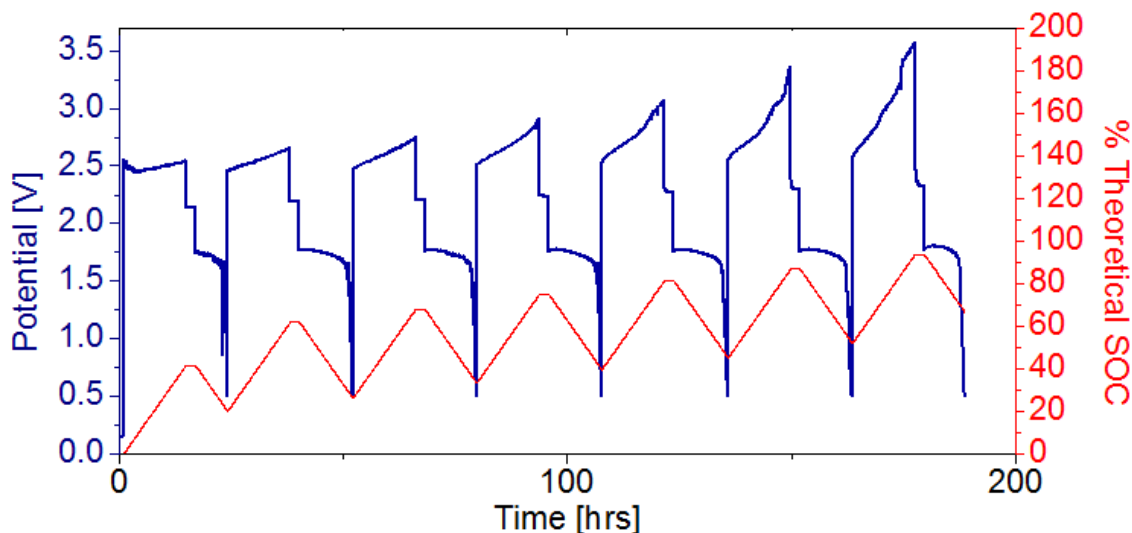


Figure 4.1.4-1 Charge/discharge response for the first 7 cycles of 0.1 M  $V(acac)_3$  and 0.5 M  $TEABF_4$  in ACN in an 1-D cell with graphite electrodes and a Neosepta AHA separator. Measurements performed at room temperature in an Ar-atmosphere glove box.

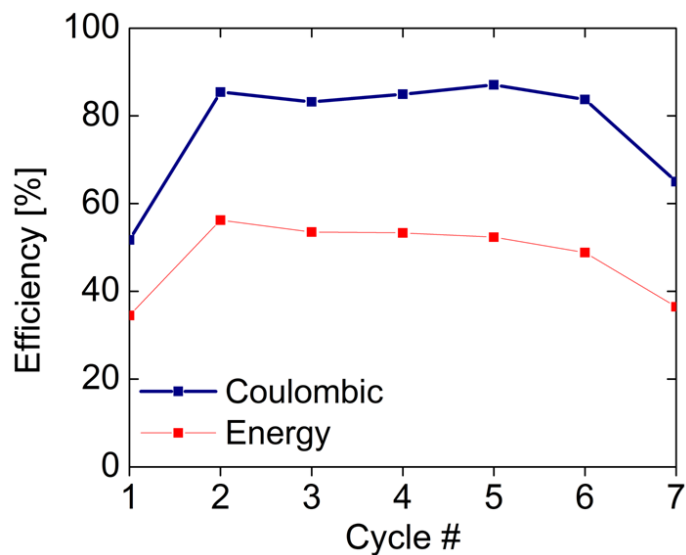


Figure 4.1.4-2 Coulombic and energy efficiency plot associated with the charge/discharge experiment shown in Figure 4.1.4-1.

Figure 4.1.4-1 shows the charge/discharge signature in the new glove box environment. The charge voltage starts at ~2.5 V and overcharging begins at cycle 7. There is a small plateau at ~2.8 V on the charge curve whose origin remains unknown. Unlike previous C/D plots, significant capacity is observed upon the first discharge, and the 1.75V discharge plateau does not fade away in favor of a lower plateau. The exclusion of ambient air resulted in a dramatic improvement in energy efficiency, as Figure 4.1.4-2 shows. Rather than stabilizing at 20 %, energy efficiency reaches ~50 %, where it stabilizes until overcharging begins. The coulombic efficiency was constant at 85 %, indicating that most of the current input went into the active species.

The plot of open circuit potential vs. % theoretical SOC for the C/D performed in the Ar glove box is shown in Figure 4.1.4-3. The blue dots are experimental open-circuit potentials at end-of-charge, and the green line shows

the result predicted by the Nernst equation, with a formal potential of 2.18 V.

This Nernstian model fits the experimental data very well across the entire range of charge states probed.

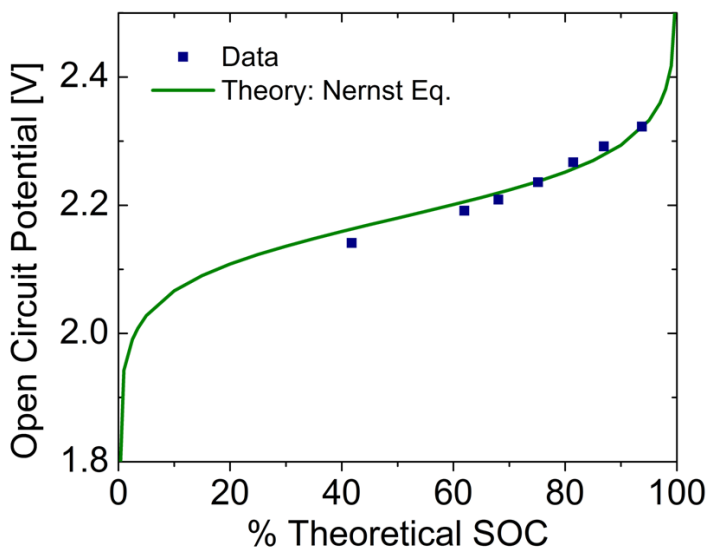


Figure 4.1.4-3 Plot of open circuit potential vs. % theoretical SOC for the charge/discharge experiment shown in Figure 4.1.4-1.

#### 4.1.5 Discussion

Based on the results obtained in the two glove boxes, I hypothesize that reaction ( 4-4 ) occurs in cells cycled in the flowing-nitrogen glove box, but that it does not occur in the argon glove box with the purifier. The undesired side reaction involves constituents of ambient air, which react with  $V(acac)_3$  (or  $V(acac)_3^+$ ) to form  $VO(acac)_2$  (or  $VO(acac)_2^+$ ). This hypothesis is supported by CV results at end-of-service, which show evidence of free ligand in solution, as well as dissolved oxygen (in the form of superoxide). Air is the only potential source of oxygen, suggesting that water is present as well as oxygen.

Deviations from Nernstian behavior, shown in Figure 4.1.3-4, likely owe to the presence of environmental contaminants. To support this hypothesis, CV was performed on  $\text{VO}(\text{acac})_2$  to observe its redox activity; the resulting cyclic voltammogram is shown in Figure 4.1.5-1. The hypothesis suggests that on the positive side,  $\text{VO}(\text{acac})_2$  is formed and reacts electrochemically, while  $\text{V}(\text{acac})_3$  remains in its native state on the negative side of the cell. If this was the case, then the cell potential is expected to be  $\sim 2.5$  V instead of 2.18 V. This is close to the potential the data are drifting towards in Figure 4.1.3-4. All the evidence gathered supports the hypothesis that the amounts of oxygen and water in the flowing-nitrogen glove box are high enough to affect the long-term performance of the RFB.

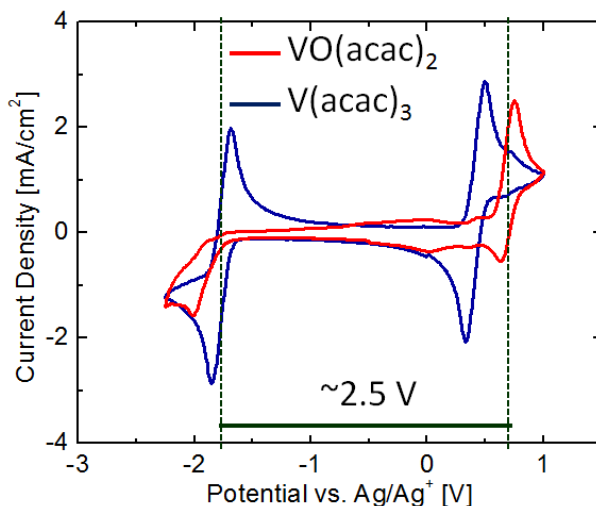


Figure 4.1.5-1 Cyclic voltammogram of [blue] 0.01 M  $\text{V}(\text{acac})_3$ , 0.05 M  $\text{TEABF}_4$  in acetonitrile and [red] 0.01 M  $\text{VO}(\text{acac})_2$ , 0.05 M  $\text{TEABF}_4$  in acetonitrile. Glassy carbon working electrode; 100 mV/s scan rate;  $\text{Ag}/\text{Ag}^+$  reference electrode.

A cursory examination of the rate of  $\text{VO}(\text{acac})_2$  formation in Figure 4.2.2-5 was performed based on the coulombs observed in the discharge for each

plateau. For cycles 2 through 4, 25-30 % of the coulombs are associated with the formation of new  $\text{VO}(\text{acac})_2$ . After that, the formation rate dramatically slows down and reaches a plateau when the vanadyl concentration is expected to be 0.028 M. Using  $\text{VO}(\text{acac})_2$ ,  $\text{V}(\text{acac})_3$ , and  $\text{TEABF}_4$  concentrations normalized by solubility limit, this would suggest that 90% of the solution's solute capacity is utilized (assuming the concentration of charged  $\text{V}(\text{acac})_3$  is the same as the neutral species). The reduction in vanadyl formation rate may be due to the solution approaching its solubility limit.

#### 4.1.6 Summary

Performance characteristics of the non-aqueous vanadium acetylacetonate RFB were evaluated. The impact of oxygen and water on the electrochemistry of the system were studied. Oxygen was shown to block the reduction of  $\text{V}(\text{acac})_3$  on carbon, and may degrade the solvent and supporting electrolyte. Vanadyl acetylacetonate formed in the presence of water, either spontaneously in ambient air or electrochemically at the positive electrode. Water was also shown to impede kinetics of the negative  $\text{V}(\text{acac})_3$  redox couple. The  $\text{VO}(\text{acac})_2$  species was associated with positive and negative redox couples centered at  $\sim 0.75$  and  $-2.0$  V vs.  $\text{Ag}/\text{Ag}^+$ .

Charge/discharge characteristics of the system were assessed using a 1-D cell with an anion-exchange membrane separator. In ambient nitrogen gas with oxygen and water at levels between 10 and 100ppm, two discharge plateaus were observed at approximately 1.75 V and 0.7 V. The plateau at 1.75 V is



associated with the single-electron disproportionation of  $V(\text{acac})_3$ , whereas the plateau at 0.7 V may owe to side products – most likely, vanadyl complexes. Coulombic and energy efficiencies of 90 % and 20 %, respectively, were calculated.

When using an argon-atmosphere glove box with ambient water and oxygen levels below 0.5 ppm of water/oxygen, only one discharge plateau is observed at 1.75 V, corresponding to the single-electron disproportionation of  $V(\text{acac})_3$ . Coulombic and energy efficiencies of 85 % and 50 %, respectively, were observed. Auxiliary cyclic voltammograms and open-circuit potential measurements support the conclusion that  $VO(\text{acac})_2$  does not form during cycling in the Ar glove box, but does form in the flowing- $N_2$  glove box. Very stringent controls on oxygen and water must be applied when assembling high-voltage non-aqueous RFB systems (controls which are already established for lithium-ion batteries).

## 4.2 Concentration tests

### 4.2.1 Background and Approach

The energy density of an RFB electrolyte is dictated by the concentration of active species, the voltage at which the active species react, and the number of electrons transferred in the cell reaction. The theoretical maximum energy density can be assessed using equilibrium measurements such as the voltammetry discussed in chapter 2.1. In practice the energy density of an RFB is lower because of limitations in the cell. Power must be expended on any

dynamic process (kinetics, transport, etc.) within the cell, and can cause significant efficiency losses. Kinetic overpotentials and ohmic losses in membranes are discussed extensively in chapters 3.2 and 3.1; this section focuses on the effect of active-species concentration on performance.

Active-species concentration has a marked effect on the rate of active-species crossover in the reactor chamber. Crossover will occur at higher rate if the active-species concentration is higher, thus reducing the efficiency of the RFB. This phenomenon was observed and discussed by Matsuda *et al.* with a non-aqueous RFB based on Ru [46]. They looked at several concentrations and measured the efficiency of a stagnant RFB cell similar to the cells used for our experiments. A plot of efficiency vs. active species concentration went through a maximum. Efficiency decrease at higher concentrations was attributed to higher active-species crossover, while the source of lower efficiency at lower concentrations was left undetermined. They concluded the active species concentration in the Ru RFB should be between 0.02 M and 0.05 M for optimal efficiency.

Efficiency and energy density are not the only factors to consider; neither the active species nor the supporting electrolyte can precipitate. It is straightforward to determine the solubility limit of the neutral active species; however, determining the solubility limits of the charged species (both positive and negative) is more challenging. Furthermore, the active-species solubility limit for a non-aqueous RFB electrolyte is a function of the supporting electrolyte used (and its concentration), as well as the non-aqueous solvent chosen.

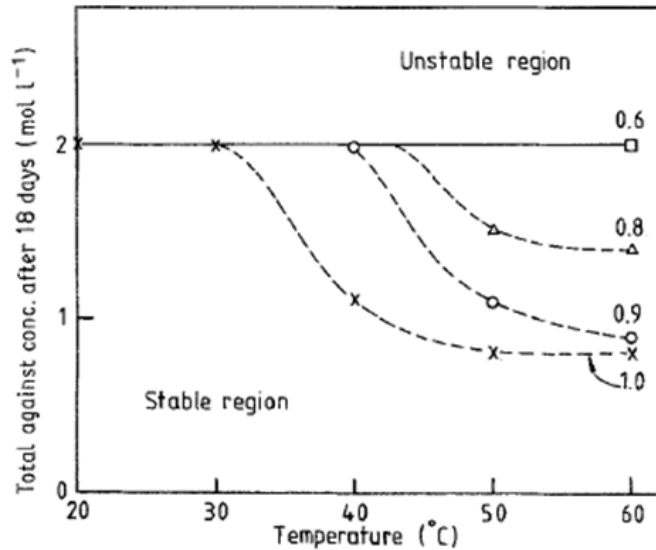


Figure 4.2.1-1 Plot of active species concentration remaining in solution after waiting 18 days for precipitation to occur as a function of solution temperature. Numbers on the right side are the fraction of V(V) in a V(IV) solution. Figure taken from [121].

Figure 4.2.1-1 shows how the presence of charged species affects the precipitation limit for an aqueous RFB electrolyte. The figure can be read similarly to a phase diagram, with the state variables being the maximum running temperature and %SOC of the battery. According to the data shown, if an aqueous all-vanadium RFB is run at 50 °C up to 80 %SOC, then the maximum active-species concentration on the positive side of the battery that does not precipitate to any visible extent after 18 days is 1.5 M; if instead the RFB is run at 40 °C, then solutions up to 2 M will remain free of precipitates. Similar data exists for the negative species in the aqueous RFB, and additional data could be developed to test the effect of supporting electrolyte concentration. Our work aimed to perform similar studies for the non-aqueous vanadium RFB chemistries.

In the next section, the effect of active-species concentration on the charge/discharge performance will be shown. Based on the solubilities

measured in section 2.4, charge/discharge experiments were performed with a variety of active-species concentrations in a fixed background supporting-electrolyte concentration in ACN. Qualitative features of the charge and discharge curves were examined, and the cells were inspected after many cycles for signs of precipitation.

#### 4.2.2 Results

Charge/Discharge experiments were performed with 0.5 M TEABF<sub>4</sub> (31 % of the maximum pure species solubility, established in section 2.4). The active-species concentration was varied across its pure species solubility range: 0.05 M, 0.075 M, 0.1 M, 0.25 M, and 0.4 M which are 8.3 %, 12.5 %, 16.6 %, 41.6 %, and 66.7 % of the maximum solubility respectively.

Since two solutes are being added to the solvent, it is important to know how the presence of one impacts the other. To determine this, the solubility envelope was elucidated by making solutions of varying concentration TEABF<sub>4</sub> and V(acac)<sub>3</sub> in ACN, shown in Figure 4.2.2-1. The plot axis are the concentrations of V(acac)<sub>3</sub> and TEABF<sub>4</sub> normalized by the maximum concentration for the pure solute in ACN (0.60M for V(acac)<sub>3</sub> and 1.60M for TEABF<sub>4</sub>). Blue dots represent solutions which were prepared and solubility determined by an undergraduate researcher (Colleen Wang). Figure 4.2.2-2 shows a similar experimental setup for Cr(acac)<sub>3</sub> instead of V(acac)<sub>3</sub> performed by undergraduate researcher Tim Pomaville. The red line on both figures show how the solubility envelop is expected to trend assuming the solute molecules act as filler in the solvent interstitial sites. It is proposed that the solubility limit

follows the red line trend in both cases and the points above the solubility limit in Figure 4.2.2-1 are associated with human error in the undergraduate's measurements. These experiments allow for the selection of active species and supporting electrolyte compositions in charge discharge which will not precipitate (when in an uncharged state). The highest concentration discussed in this section is 0.4M  $V(acac)_3$  and 0.5M  $TEABF_4$  (a point associated with the coordinates (0.31, 0.67) on Figure 4.2.2-1) in ACN, which is on the cusp of the neutral species solubility envelope.

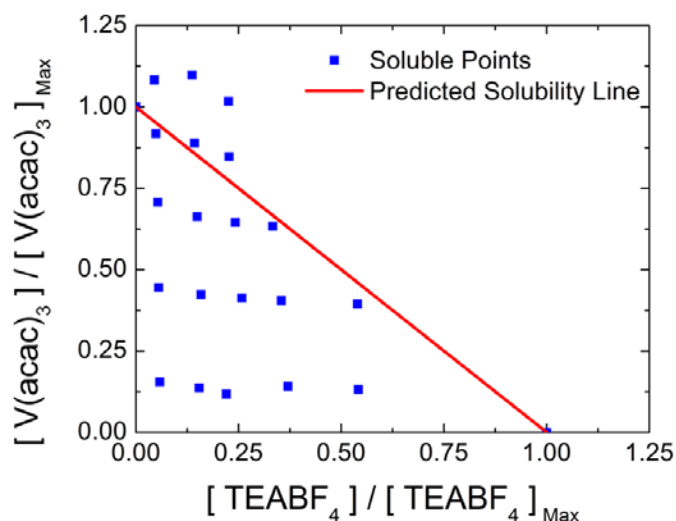


Figure 4.2.2-1 Solubility plot for  $V(acac)_3$  and  $TEABF_4$  in ACN. [Blue dots] Miscible solutions [Red line] Predicted solubility limit.

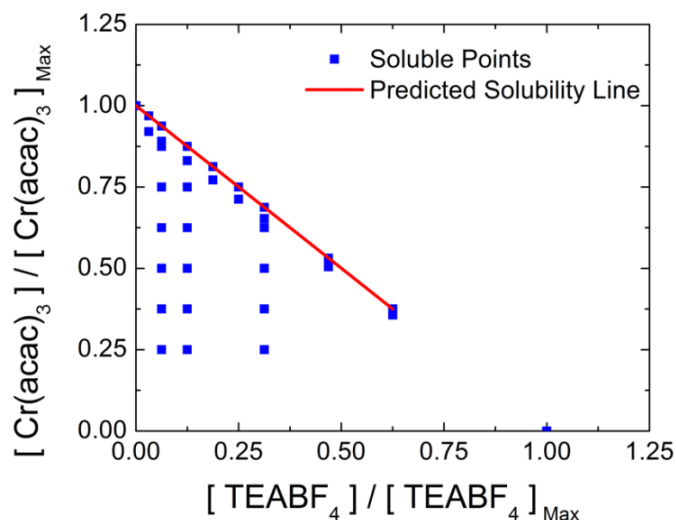


Figure 4.2.2-2 Solubility plot for  $\text{Cr}(\text{acac})_3$  and  $\text{TEABF}_4$  in ACN. [Blue dots] Miscible solutions [Red line] Predicted solubility limit.

The results of charge/discharge tests are shown in Figure 4.2.2-3 to Figure 4.2.2-7. First and foremost, the 0.25 M and 0.4 M cells had precipitation in the positive electrolyte after/during cycling, which indicates the charged species has a lower solubility limit than the neutral species. The resulting charge/discharge plot character can be segregated into two categories: cells which had precipitation and those which did not precipitate.

The cells that show no visible precipitation after 10 cycles (0.05, 0.075, and 0.1 M, Figure 4.2.2-3 to Figure 4.2.2-5) started with charge voltages of approximately 2.5 V in the first cycle. Typically, no significant discharge plateau was evident on the first discharge, a phenomenon whose cause is unknown. The open circuit potential measured at end of charge suggests, however, that the vanadium remains in a relatively uncharged state, suggesting that on first charge current goes into some reaction besides the desired  $\text{V}(\text{acac})_3$  disproportionation reaction. In the second cycle, an additional plateau manifests during charging, at

~2.75 V. During the second discharge, two discharge plateaus are observed, at 1.75 V and at 0.5 V; approximately 15-40 % of the charge extracted is with the lower voltage plateau. Discharge curves over subsequent cycles show a gradual fade of the 1.75 V plateau in favor of the lower voltage plateau (0.5 V). The exact cause of this plateau shift will be discussed further in the section on degradation mechanisms, but for present discussion, we hypothesize that the plateau shift can be attributed to the conversion of  $V(\text{acac})_3$  active species into a  $VO(\text{acac})_2$  species. In the remainder of the cycles, the charge curve retains similar features to the second cycle, save that the potential begins to rise dramatically at the end of charge. This large potential increase is consistent with the Nernst equation, and can be associated with overcharging, as the % theoretical SOC curve approaches or exceeds 100%.

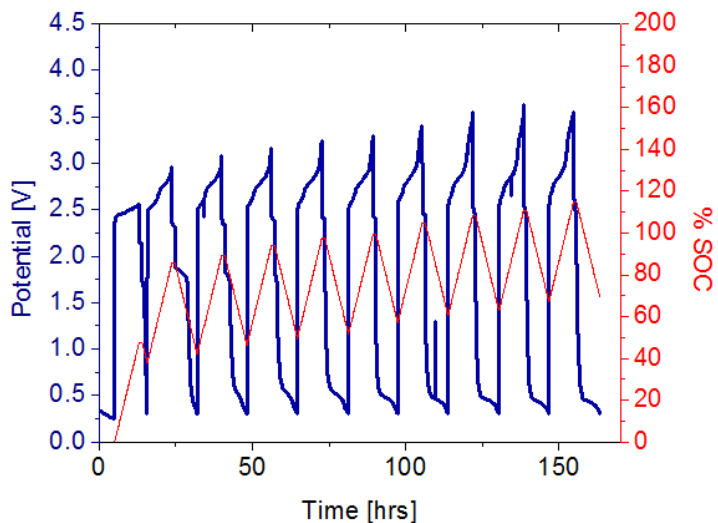


Figure 4.2.2-3 Charge/discharge response for the first 10 cycles of 0.05 M  $V(\text{acac})_3$  and 0.5 M  $\text{TEABF}_4$  in ACN in a 1-D cell with graphite electrodes and a Neosepta AHA separator. Measurements performed at room temperature in a  $\text{N}_2$ -atmosphere glove box.

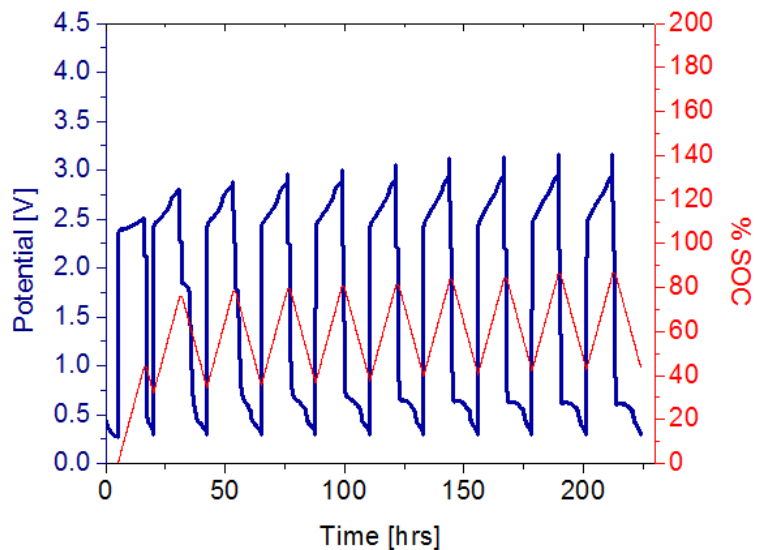


Figure 4.2.2-4 Charge/discharge response for the first 10 cycles of 0.075 M  $V(acac)_3$  and 0.5 M  $TEABF_4$  in ACN in a 1-D cell with graphite electrodes and a Neosepta AHA separator. Measurements performed at room temperature in a  $N_2$ -atmosphere glove box.

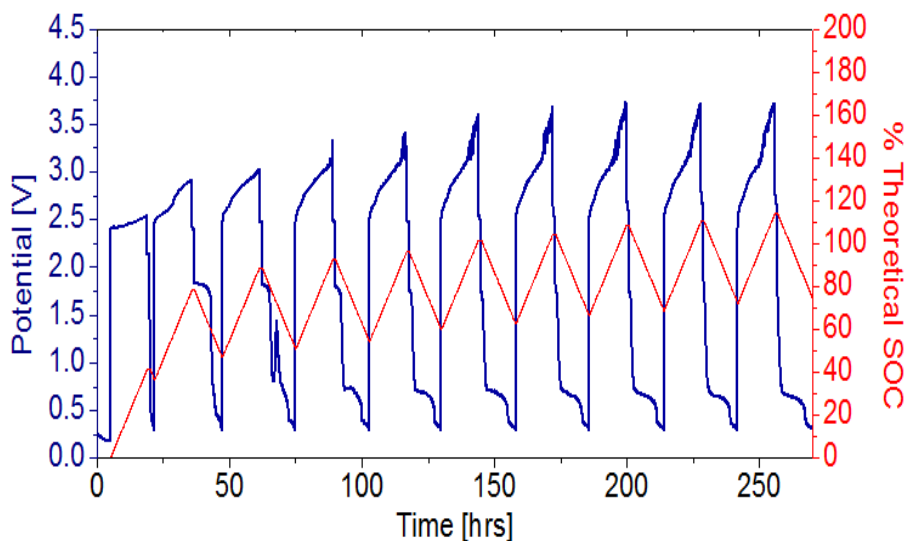


Figure 4.2.2-5 Charge/discharge response for the first 10 cycles of 0.1 M  $V(acac)_3$  and 0.5 M  $TEABF_4$  in ACN in a 1-D cell with graphite electrodes and a Neosepta AHA separator. Measurements performed at room temperature in a  $N_2$ -atmosphere glove box.

Although the first charge/discharge cycles look similar at all active-species concentrations, the cells in which precipitation was observed (0.25 M and 0.4 M  $V(acac)_3$ , Figure 4.2.2-6 and Figure 4.2.2-7) have very different character at later



cycles. The source of precipitation at higher active-species concentrations is not known, but is suspected to be the charged species, as a brown precipitate is observed in the positive chamber after repeated cycling, even in environments where residual oxygen and water are strictly controlled below 1ppm levels. The first noticeable difference in the charge/discharge response comes in the discharge step of the first cycle, when discharge occurs for an appreciable amount of time, with a plateau at 1.75 V. The most startling aspect of the curve is that the discharge plateau at 1.75 V remains for all the cycles measured, and does not fade in favor of a lower voltage plateau.

Since the concentration study discussed here was performed in a glovebox without a purifier (oxygen and water 10ppm+), it is more likely that precipitation in these experiments owes to parasitic side reactions caused by ambient water and oxygen impurities, which cause formation of  $\text{VO}(\text{acac})_2$  (discussed in section 2.2.4). The solubility limit of  $\text{VO}(\text{acac})_2$  is 0.06 M in ACN – far lower than  $\text{V}(\text{acac})_3$  – precipitation would also be expected if the amount of residual water and oxygen suffices to convert enough  $\text{V}(\text{acac})_3$  to exceed the  $\text{VO}(\text{acac})_2$  solubility limit. As  $\text{V}(\text{acac})_3$  continues to be converted to  $\text{VO}(\text{acac})_2$ , the cell loses capacity, consistent with the observation that the %SOC continues to creep upward with continued cycling.

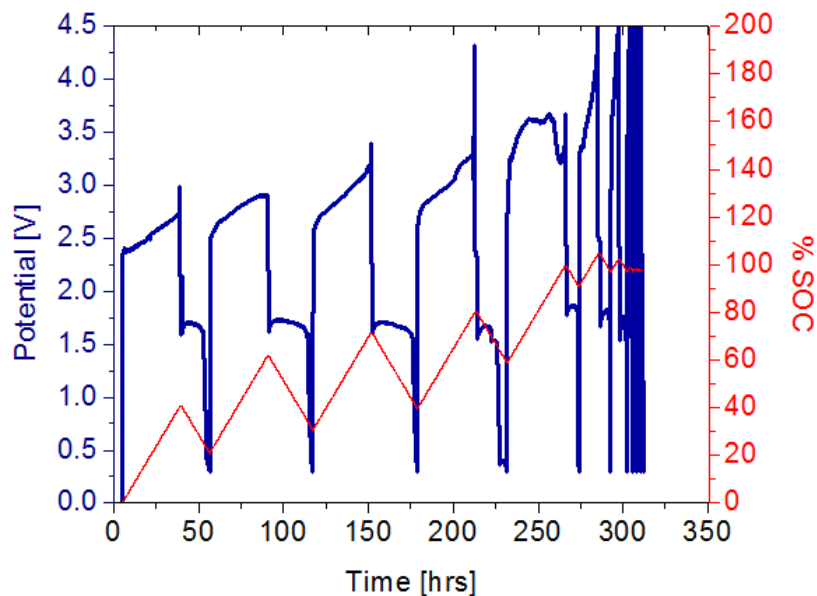


Figure 4.2.2-6 Charge/discharge response for the first 10 cycles of 0.25 M  $V(acac)_3$  and 0.5 M  $TEABF_4$  in ACN in a 1-D cell with graphite electrodes and a Neosepta AHA separator. Measurements performed at room temperature in a  $N_2$ -atmosphere glove box.

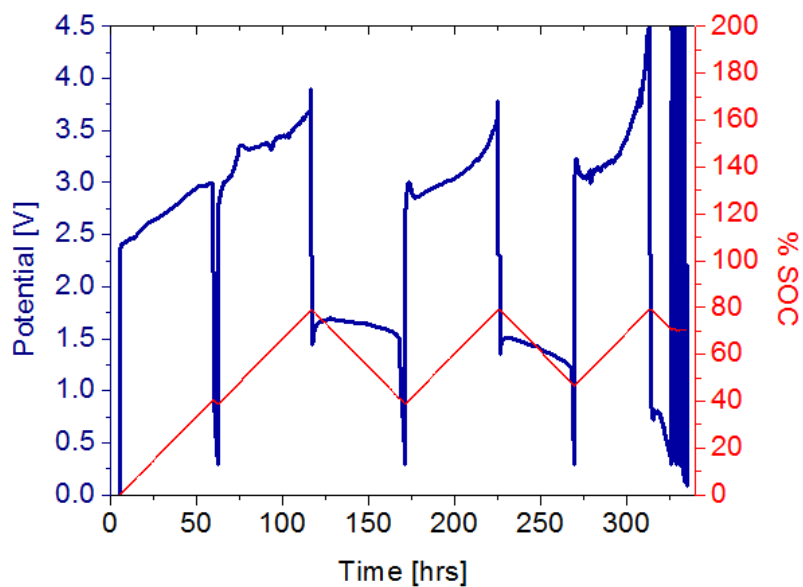


Figure 4.2.2-7 Charge/discharge response for the first 10 cycles of 0.4 M  $V(acac)_3$  and 0.5 M  $TEABF_4$  in ACN in a 1-D cell with graphite electrodes and a Neosepta AHA separator. Measurements performed at room temperature in a  $N_2$ -atmosphere glove box.

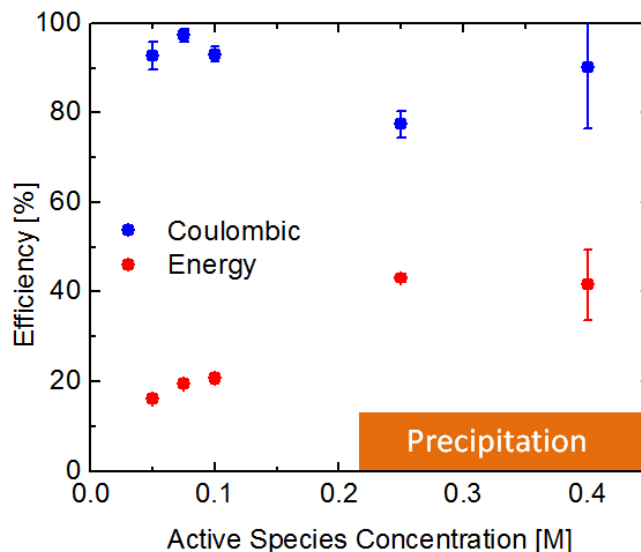


Figure 4.2.2-8 Plot of efficiency as a function of active species concentration based on the C/D shown in Figure 4.2.2-3 through Figure 4.2.2-7.

The coulombic and energy efficiencies of the cells used for the concentration study are shown in Figure 4.2.2-8. The coulombic efficiencies of all the precipitate-free cells (below 0.25M) are 90 % or higher; although  $\text{VO}(\text{acac})_2$  is likely formed, it still remains possible to charge and discharge the  $\text{VO}(\text{acac})_2$  species that remains in solution. The coulombic efficiency for the cells with precipitation is lower (~75 %) because the energy put into the precipitated species cannot be recovered from it on discharge. Energy efficiency has the opposite trend. The soluble cells have energy efficiencies near 20 % because the mixed potential observed with  $\text{VO}(\text{acac})_2$  and  $\text{V}(\text{acac})_3$  is lower than that of just  $\text{V}(\text{acac})_3$  indicating that the kinetics of  $\text{VO}(\text{acac})_2$  oxidation and reduction are slow.

### 4.2.3 Discussion

One of the goals of my research is to examine how the choices of RFB chemistry, composition, and cell components affect the practical energy density in working cells. To show the effect of active-species content, Figure 4.2.3-1 shows energy density as a function of active-species concentration for the charge/discharge experiments discussed in section 4.1.2. The blue dots show the data from the experimental cells; the theoretically expected energy density predicted by equation ( 1-4 ) is shown with a red line. As well as providing high energy density, it is also desirable that a RFB electrolyte be stable. Figure 4.2.3-2 presents a qualitative expectation for how the maximum concentrations of active species and supporting electrolyte are coupled in a traditional solvent. The plot shows active-species concentration, normalized by its maximum concentration, on one axis; the normalized supporting electrolyte concentration is shown on the other axis. The figure is presented as a phase diagram: the diagonal line shows the approximate solubility limit for a solution in which both solutes are present. If the neutral active species and support concentrations combine to produce a point above the line, a precipitate will eventually form in the neutral, fully discharged solution; if the concentrations combine to produce a point below the line, the neutral solution will be completely soluble.

The red dots on the vertical red line shows the points tested in this section which were soluble and the green X shows solutions which precipitated. It is clear that the charged species has a lower solubility limit than the neutral species, similar to what was observed by Kazacos *et al.* [121]. Based on these

results, the optimal concentration for the  $V(acac)_3$  RFB is between 0.1 M and 0.25 M, which is the highest active species concentration that can be used without precipitation on the positive side during charging. Note that our conclusions differ from those of Matsuda *et al.*, in that we do not observe a parabolic efficiency curve, which may suggest that active-species crossover is less significant than it was in Matsuda's system.

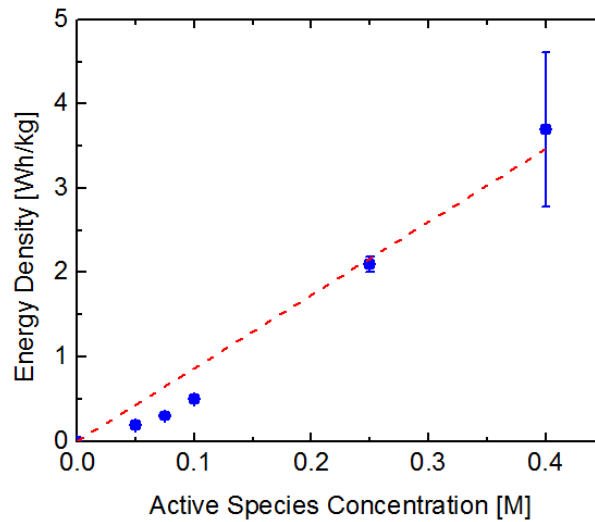


Figure 4.2.3-1 Plot of energy density as a function of active-species concentration based on the C/D shown in Figure 4.2.2-3 through Figure 4.2.2-7.

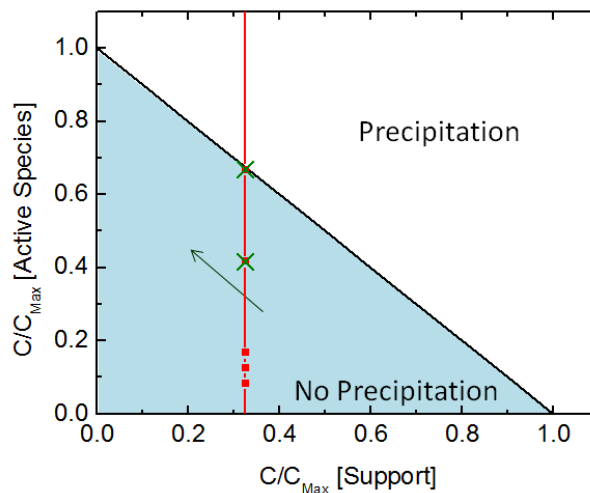


Figure 4.2.3-2 Plot of active species concentration as a function of support concentration, based on the C/D shown in Figure 4.2.2-3 through Figure 4.2.2-7, showing the regions of precipitation.

## 4.3 Capacity

### 4.3.1 Background and Approach

Based on equation ( 2-4 ), a 12.5mL RFB cell containing 0.1M V(acac)<sub>3</sub> should discharge for 33.5 hrs at 1 mA. Realistic battery systems do not achieve the theoretical maximum capacity due to internal rate limitations, and are often subject to additional capacity fade with cycling as materials within the battery degrade[98]. An understanding of the sources of capacity fade is critical to the development of longer-lived RFB cells.

### 4.3.2 Results: Electrochemistry

The charge/discharge test procedure we used throughout this work involves constant applied currents during the charge and discharge steps, as described earlier in section 2.1; a relatively exemplary output result is shown in Figure 4.1.4-1. Experiments run according to our established protocol are not representative of typical modes of battery control. Since side reactions led to unpredictable results, our tests proceeded with fixed charge and discharge times, rather than relying in cutoff voltages, which is a more typical control approach. Since the charge time is always fixed, any coulombic inefficiency propagates from cycle to cycle, causing the % theoretical SOC to increase gradually with cycle number. With our control procedure, eventual overcharging is inevitable. Overcharged cells will invariably fail, because once the %SOC rises above 100 %, other side reactions are driven.

When cells can be fabricated to yield a reproducible potential response, a voltage-control mode can be used to prevent overcharging side reactions from occurring. Instead of charging the cell for a constant time (inputting a fixed amount of charge), charge cycles can be stopped when the cell reaches a chosen cutoff potential. Results from a cell fabricated in the Ar glove box and tested according to a voltage-cutoff control scheme are shown in Figure 4.3.2-1. The biggest effect of this procedural change is that it allows the SOC at end of charge to be controlled. In the experiments shown, the SOC oscillates about 60 %, instead of drifting upwards with sequential cycling. On the other hand, the charge capacity does not remain constant; a large fade is observed, which is quantified in Figure 4.3.2-2. The volumetric discharge capacity obtained on the first cycle is 0.5 Ah/L, which fades to 0.2 Ah/L by cycle 7. This 60 % capacity fade is unexpected based on the reversible electrochemistry seen in CV.

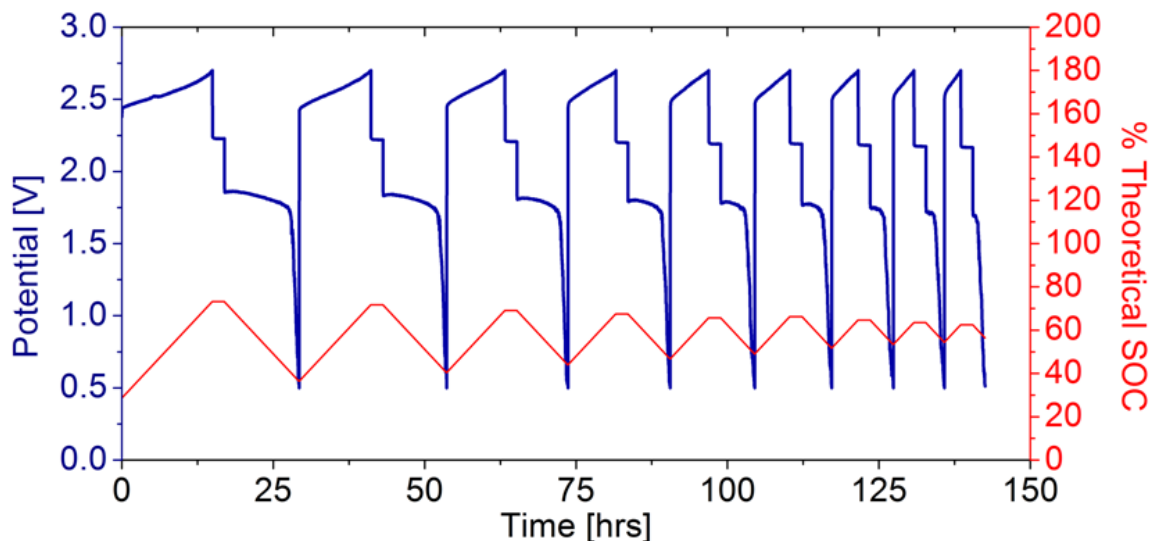


Figure 4.3.2-1 Charge/discharge response for the first 9 cycles of 0.1 M  $V(acac)_3$  and 0.5 M  $TEABF_4$  in ACN in a 1-D cell with graphite electrodes and a Neosepta AHA separator. Measurements performed at room temperature in an Ar-atmosphere glove box.

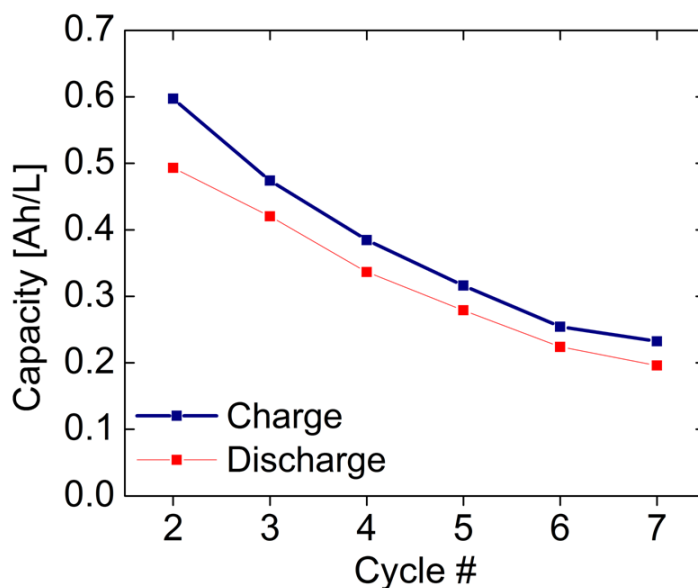


Figure 4.3.2-2 Plot of capacity vs. cycle number associated with Figure 4.3.2-1.

To elucidate the cause of the capacity fade, the experiments shown in Figure 2.4.4-5 and Figure 2.4.4-6 were repeated along with additional tests in 4-electrode cells (cf. section 2.1). Data from 4-electrode cells was analyzed to show how overpotentials associated with the membrane, solution, and electrodes varied as the cell cycled. Also, the electrodes were weighed before and after performing the charge/discharge experiment to quantify any changes in mass associated with deposition of precipitates or bulk erosion.

Figure 4.3.2-3 shows the results of a charge/discharge experiment with ACN as the solvent, run at fixed charge capacity (a condition that was relaxed in later cycles, when a 4.5 V safety voltage cutoff was reached). The results in early cycles are similar to those obtained previously, illustrating the reproducibility of the RFB under an Ar atmosphere. The 4.5 V safety cutoff is reached in cycle 8.



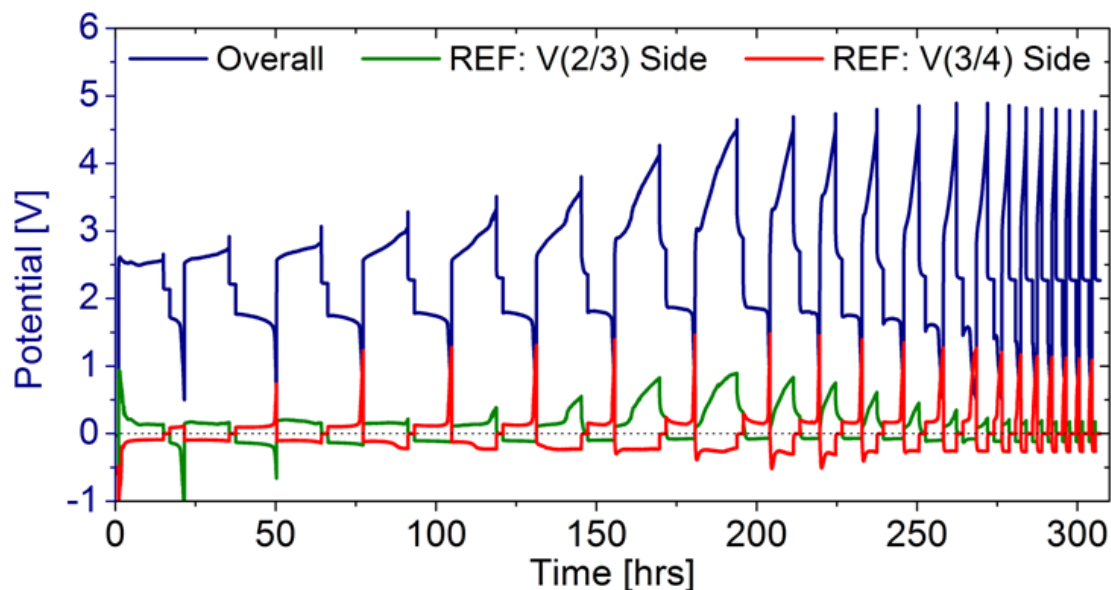


Figure 4.3.2-3 Charge/discharge response for a 0.1 M  $V(acac)_3$  and 0.5 M  $TEABF_4$  in ACN 1-D cell with graphite electrodes and a Neosepta AHA separator. Measurements performed at room temperature in an Ar-atmosphere glove box.

Data from reference electrodes can be used in tandem with the overall cell potential data and Nernstian equilibrium calculations to determine what fractional contribution each component of the RFB makes to the total overpotential. This analysis uses a predetermined solution resistance based on the geometry of the cell and the electrolyte conductivity. In previous charge/discharge experiments, the solution conductivity was observed to be relatively constant before and after cycling, and thus will be assumed constant for this analysis.

The portion of total overpotential loss attributed to the membrane was calculated by subtracting all the other known overpotentials between the electrodes and reference electrodes,

$$\eta_{\text{Membrane}} = V_{\text{Total}} - E_{\text{Nernst}} - \eta_{\text{Electrode}} - \eta_{\text{Solution}} \quad (4-5)$$

Here  $\eta_i$  terms are the overpotential associated with components  $i$  (solution, membrane, positive electrode, and negative electrode)  $V_{\text{Total}}$  is the total potential

measured between the positive and negative terminals of the battery, and  $E_{\text{Nernst}}$  is the Nernst potential at the instantaneous SOC calculated using the current history of the battery cell.

The breakdown of overpotentials in cycles 2-13 is shown in Figure 4.3.2-4. The first cycle gives unreliable numerical results because components of the cell are undergoing the typical “burn-in” discussed previously. The overpotentials observed in the cell appear to depend on whether or not the safety cutoff has been reached. During cycle 2, the membrane, solution, and electrode account for 16 %, 48 %, and 36 % of the total overpotential respectively; at cycle 8, this has changed to 21 %, 38 %, and 41 % respectively. During these cycles, it appears as though the overpotential at the electrode is increasing more than that of the membrane. However, once the cell begins charging up to 4.5 V, the membrane overpotential increases dramatically while the electrode overpotential remains constant or even decreases. By cycle 13, 50 % of the total overpotential can be associated with the membrane. The most likely causes are that the membrane becomes unstable at high potential, or that new species form at higher potentials, which subsequently react with the membrane.

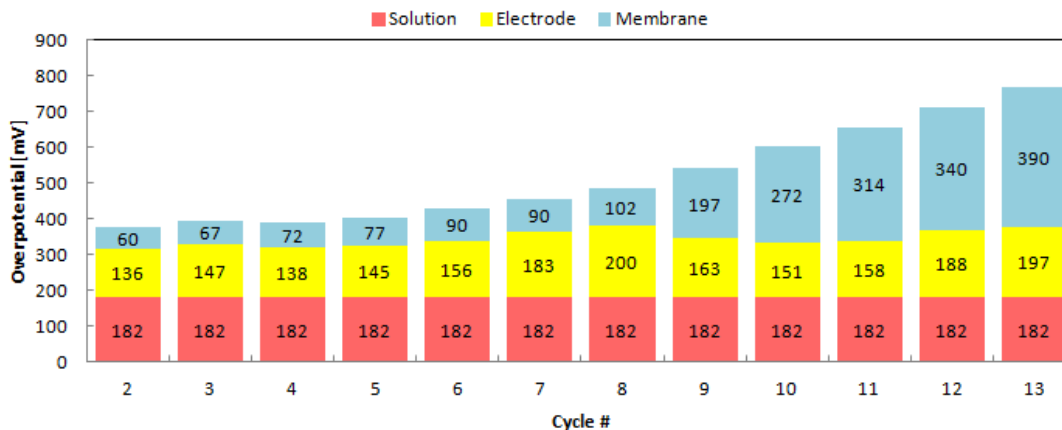


Figure 4.3.2-4 Plot of discharge overpotential as a function of cycle number for the data shown in Figure 4.3.2-3.

To assess whether the electrodes appreciably corrode or incorporate precipitates during cycling, their masses were measured before and after cycling. A baseline for electrode masses was first established by soaking them in the test solution for 300hrs, without cycling. After soaking, the electrodes were removed and dried; they were not rinsed. Although the lack of rinsing potentially contributed to some mass gain, it helped to determine whether any species that are soluble in pure solvent precipitated on the electrode surface during cycling. The ACN control electrode increased in mass by 1.0 %, likely due to the presence of dried electrolyte. The positive cycled electrode saw a 1.4 % increase in electrode mass; it is difficult to say if this is statistically significant since there is only one sample and is near the tolerance of the scale. The negative cycled electrode increased in mass by 3.9 %, which is a statistically significant increase at three times the accuracy of the scale. These results suggest that precipitation occurs on the negative electrode; it is unclear whether precipitation occurs on the positive electrode.

Although electrode mass measurements do not show precipitation on the positive electrode, a brown precipitate was observed at the bottom of the chamber containing the positive electrolyte. Since the cell was run under Ar, it was hypothesized that the precipitate was not simply  $\text{VO}(\text{acac})_2$ . To investigate the precipitate composition further, it was analyzed for carbon, hydrogen, and nitrogen content by Atlantic Microlab. The results showed 38.01 % by mass carbon, 5.21 % by mass hydrogen, and 4.78 % by mass nitrogen. The balance (52.00 % mass) could theoretically owe to any other elements in the periodic table; we primarily expect boron and fluorine from the  $\text{BF}_4^-$ , vanadium from the active species, and oxygen from the  $\text{acac}^-$ . To get further clarity of the species produced, the sample was analyzed using ICP to determine the weight % vanadium in the precipitate. Two aliquots of the precipitate were extracted from the total sample and each of those was split into two tests for a total of three replicates. Based on the ICP,  $13.15 \pm 0.18$  % vanadium by mass is in the sample.

Microsoft Excel was used to determine the resulting mass fractions for C, H, N, and V given input compounds. The input compounds were based on the expected composition of the precipitate and several permutations of that to rationalize the analysis results. If we examine the expected result of a positively charged  $\text{V}(\text{acac})_3^+$  species precipitates as a salt with a  $\text{BF}_4^-$  counter ion, the expected results are 41.41 % carbon, 4.78 % hydrogen, 0 % nitrogen, and 11.71 % vanadium. This is incorrect since there is a significant amount of nitrogen in the actual result. Nitrogen can only come from ACN or  $\text{TEABF}_4$ , since ACN

evaporates readily it is more likely that residual TEABF<sub>4</sub> remains on the precipitate from the solvent evaporating. Adding enough TEABF<sub>4</sub> to the V(acac)<sub>3</sub>BF<sub>4</sub> species to obtain the correct nitrogen mass % (5.7 TEABF<sub>4</sub>: 1 V(acac)<sub>3</sub>BF<sub>4</sub>) results in predicted values of 43.52 % carbon, 8.14 % hydrogen, 4.78 % nitrogen, and 3.05 % vanadium. As compared to the previous scenario, the carbon, hydrogen, and vanadium have all changed in the wrong direction to obtain the experimental results. The vanadium mass % has dropped dramatically and would also be the case if ACN was added instead of TEABF<sub>4</sub> as the nitrogen additive. The only other method to get nitrogen is if the ACN or the TEA<sup>+</sup> react on the electrode to form a new compound, however, this is unlikely because no extra peaks occur in CV.

None of the predicted compounds involving expected starting materials have a low enough mass % carbon to achieve 38 % carbon as seen in the experimental result. Based on this and the low vanadium mass %, it is clear that ligand shedding must occur. A report by Endo *et al.* discusses the electrochemistry of Ru(acac)<sub>3</sub> in several solvents and isolate a precipitate observed in ACN which they identify to be Ru(acac)<sub>2</sub>(CH<sub>3</sub>CN)<sub>2</sub>BF<sub>4</sub> using CHN analysis, UV-visible spectroscopy, and IR spectroscopy [122]. This complex is formed by shedding one of the acac ligands and bonding with the ACN solvent when in the positively charged state. This is a very plausible mechanism occurring in the C/D with vanadium active species. If a 1 to 0.4 mixture of V(acac)<sub>2</sub>(CH<sub>3</sub>CN)<sub>2</sub>BF<sub>4</sub> to V(acac)<sub>3</sub>BF<sub>4</sub> is formed in the precipitate, the expected elemental analysis results would be 40.57 % carbon, 4.83 % hydrogen, 4.73 %

nitrogen, and 12.05 % vanadium. The hydrogen and nitrogen mass fractions match fairly well with the experimental values. The vanadium content is still lower than the experimental value and could be increased by adding  $\text{VO}(\text{acac})_2$ , but this is at the expense of the carbon balance which increases (diverging from the experimental value). Based on these elemental analysis, the precipitate contains a significant amount of vanadium which must be incorporated in a complex which has shed at least one ligand and is suggested to be  $\text{V}(\text{acac})_2(\text{CH}_3\text{CN})_2\text{BF}_4$ .

To investigate the effect of solvent on charge/discharge, similar experiments were performed using DMF in place of ACN, with all other control parameters and composition variables kept the same. The C/D response is shown in Figure 4.3.2-5.

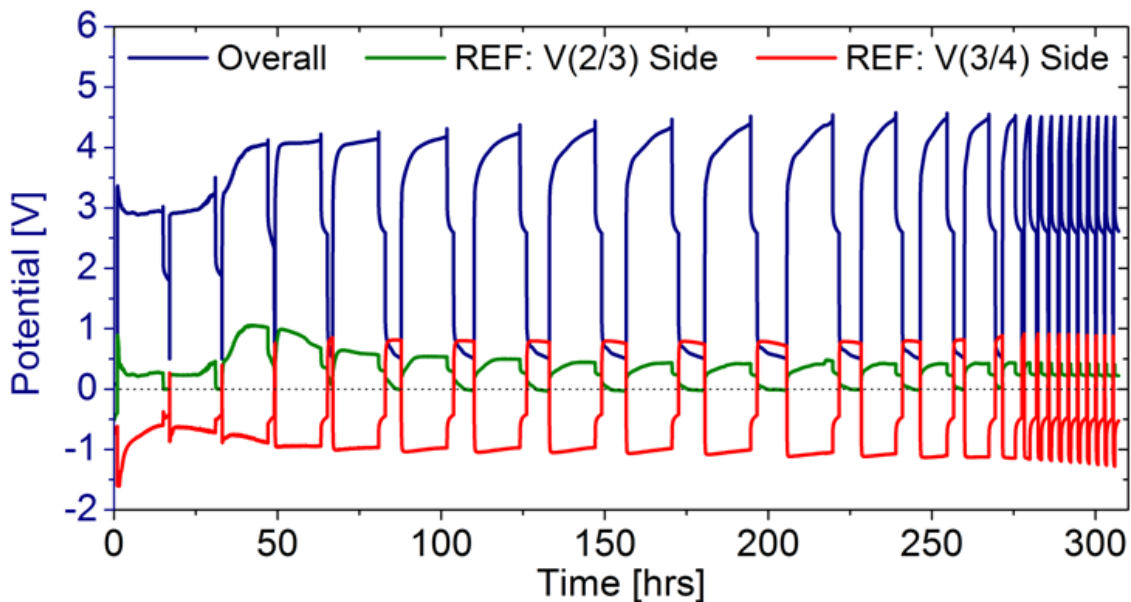


Figure 4.3.2-5 Charge/discharge response for a 0.1 M  $\text{V}(\text{acac})_3$  and 0.5 M  $\text{TEABF}_4$  in DMF 1-D cell with graphite electrodes and a Neosepta AHA separator. Measurements performed at room temperature in an Ar-atmosphere glove box.

The overpotential decomposition for this system is shown in Figure 4.3.2-6. The overpotentials are shown starting at cycle 4 instead of 2, because no appreciable energy was obtained during discharge until cycle 4. In general, the overpotentials are higher in DMF than ACN. In ACN the overpotentials started at 400 mV and reached almost 800 mV by cycle 13; overpotentials in DMF are constant at ~1200 mV. Although the total overpotential remains relatively constant, the fraction associated with each component of the cell changes. In cycle 4, the membrane and electrode account for 7.5 % and 76 % of the total overpotential, respectively. By cycle 13, the membrane contribution has increased to 24 %, while the electrode has reduced to 61 %. This suggests that membrane fouling occurs in DMF as well as ACN. The electrode overpotential is higher during cycles 3 and 4 then decrease and level off by the later cycles.

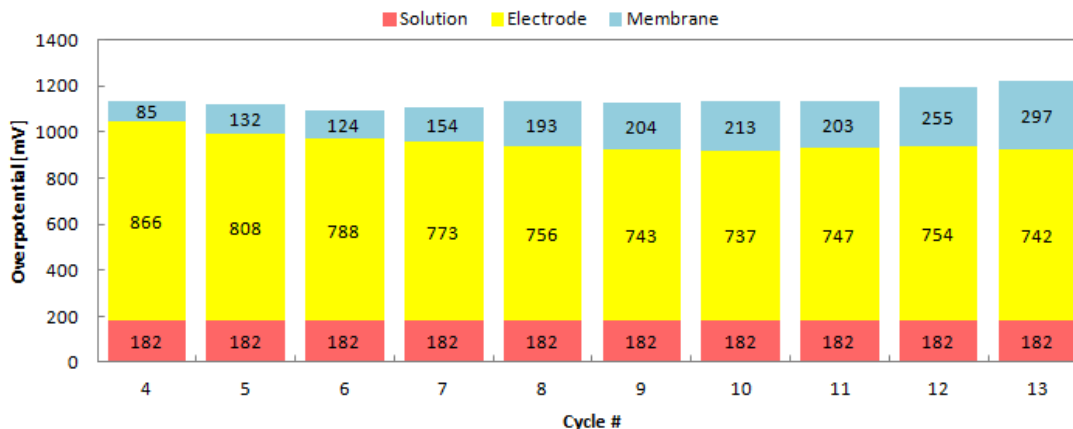


Figure 4.3.2-6 Plot of discharge overpotential as a function of cycle number for the data shown in Figure 4.3.2-5.

As with the experiments using an ACN solvent, the changes in electrode masses were measured for cells cycled with DMF. An increase of 3.3 % was observed in the control electrode. This is approximately 3 times higher than the ACN control, which is unexpected, since the active-species and supporting-

electrolyte concentrations were identical in both experiments. One possible explanation of these results is that the solution is corrosive to the graphite electrode, even when not cycling. While cycling, the positive electrode mass also increased by 3.3 %, indicating that no extra processes occur due to the current passed. No mass was measurable for the negative electrode, because it produced flakes that detached from the electrode in the cell chamber; upon removing the electrode, the remainder of the electrode fractured into pieces. This loss of structural stability suggests erosion of the internal electrode structure increasing the resistance of the electrode.

To further elucidate the cause of negative-electrode degradation in DMF, flakes that accumulated at the bottom of the negative-electrode chamber were analyzed for their carbon, hydrogen, and nitrogen content by Atlantic Microlab. The results showed 84.51 % mass carbon, 2.83 % mass hydrogen, and 1.91 % mass nitrogen. The balance (10.75%) is expected to owe to boron and fluorine from the  $\text{BF}_4^-$ , and vanadium and oxygen from the active species. The results clearly suggest that the bulk of the flakes is carbon; the high carbon ratio can only be achieved if the flakes contain a significant fraction of pure graphite. The minor components of hydrogen and nitrogen are not surprising, considering that the electrode was immersed in the test solution. Using Microsoft excel, the ratio of precipitated supporting electrolyte on the electrode was determined to be 1 part  $\text{TEABF}_4$  to 47 parts carbon (84.51 % C, 2.58 % H, 1.79 % N). A second sample of the flakes, which was soaked in pure DMF to remove residual electrolyte, was also sent for micro analysis. This resulted in 93.29 % C, 1.67 %



H, and 1.30 % N which follows the expected trend, given that electrolyte has been washed away. The optimal ratio of TEABF<sub>4</sub> to carbon changed to 1:132 (93.29 % C, 1.12 % H, and 0.78 % N). It is worth noting that if it is expected that TEABF<sub>4</sub> is present on the electrode, then so should be V(acac)<sub>3</sub>; however, it did not improve the fit to add it.

#### 4.3.3 Results: Scanning Electron Microscopy

Scanning electron microscopy (SEM) images were taken of both electrodes and the membrane from the charge/discharge cells at end-of-service to look for deposition or erosion/corrosion of the electrode and degradation of the membrane. First, SEM images were taken of the as-received membrane and electrode. These were compared to samples that were soaked in the test solution for 300 hrs. While the samples were soaking, identical electrodes were cycled in the test solution. The electrodes were removed and dried without rinsing the electrolyte from the surface. This kept any precipitations that were sparingly soluble in the solvent on the surface. The membranes, however, were soaked in pure solvent for 1 day to completely remove any residual electrolyte or soluble byproducts.

##### *Electrode*

An SEM micrograph of the as-received graphite plate is shown in Figure 4.3.3-1. The surface is very non-uniform. Some sections of the surface are flat and thus have a darker color to them. The lighter regions highlight areas where surface features exist. Most surface features in the as-received samples appear

to be pits of varying size, normally around 10  $\mu\text{m}$ . When comparing the as-received electrode to a cycled electrode, it should be kept in mind that the charge/discharge response indicates a slight increase in the overpotential of the electrodes with cycling. Precipitation on the electrode, corrosive reactions with the electrode, or delamination of the electrode are potential causes that can be observed by microscopy.

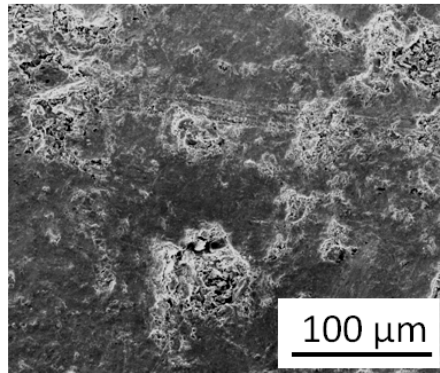


Figure 4.3.3-1 SEM of the as-received electrode.

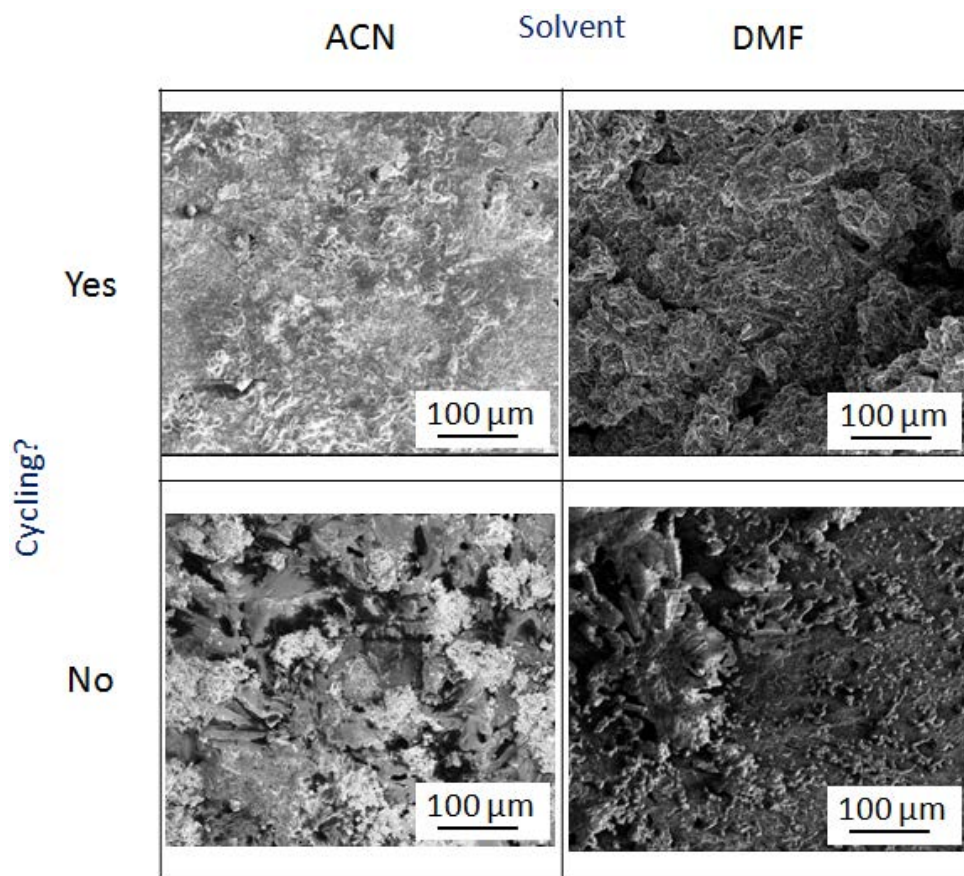


Figure 4.3.3-2 SEM images of the negative electrode in 0.1 M  $V(acac)_3$  and 0.5 M  $TEABF_4$  in solvent. [Top] After cycling for 300 hours with graphite electrodes, [Bottom] After soaking for 300 hours, [Left] Solvent: acetonitrile, [Right] Solvent: dimethylformamide.

The as-received electrode shown in Figure 4.3.3-1 can be compared to electrodes soaked in test solutions, both uncycled and cycled, in the bottom two pictures of Figure 4.3.3-2. The uncycled, soaked electrode from a DMF-based solution shows some evidence of precipitation, with some larger growths and many smaller crystallites present. Between these features the surface looks the same as the as-received electrode. It is unknown whether surface precipitates formed during soaking, or during the process of evaporating liquid off. The uncycled electrode soaked in ACN, shown in the bottom left of Figure 4.3.3-2, is completely covered by a precipitate. Despite the use of identical solutes in both

DMF and ACN solutions, the precipitates do not have the same appearance. It is difficult to determine the status of the underlying electrode because the entire surface is covered; the results of the cycled ACN cell can be used to elucidate the state of the underlying electrode surface.

The negative electrode from the cycled ACN cell has very similar structure to that of the as-received electrode, with a small amount of precipitation seen on the surface. Interestingly, the cycled sample shows less precipitation than the un-cycled sample. The bottom right image in Figure 4.3.3-2 shows the electrode that was cycled in DMF. The image shows no features of the as-received electrode, instead showing significant precipitation. Although it is not visible in the SEM image, the electrode is approximately 75 % thicker than the initial thickness in some places; as mentioned before, flakes from the electrode had fallen off and were sitting at the base of the chamber in the test cell, and the electrode was extremely brittle and broke into several pieces. Several other battery systems use graphite electrodes, such as Li-air batteries. Veith *et al.* saw similar flaking behavior of their Li-air battery electrodes after cycling and suggested that it was due to the large  $\text{PF}_6^-$  anions intercalating between planes of the graphite lattice, causing mechanical fatigue [123]. This flaking behavior leads to a separation of the graphite layers and increases the resistance of the electrode because of this. To try to get a deeper understanding of the cause of this flaking, a greater magnification was used, as shown in Figure 4.3.3-3. The electrode has several rods of unknown origin scattered on the surface, shown in

the left picture. Also, several places show areas of a layered surface, which suggests some erosion, corrosion, or delamination of the electrode has occurred.

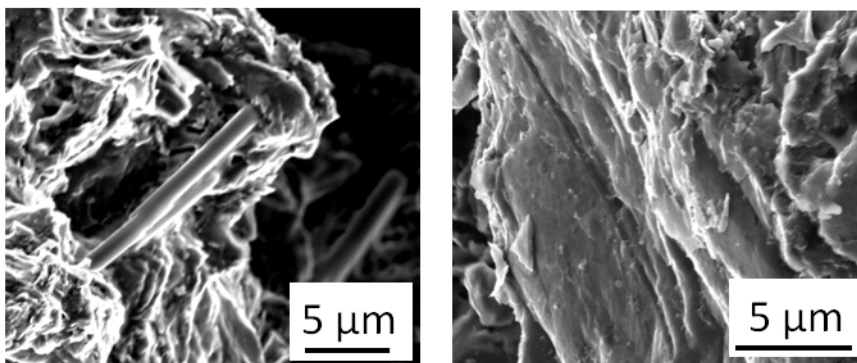


Figure 4.3.3-3 Zoom in of the SEM in the top right of Figure 4.3.3-2 (an electrode cycled in DMF electrolyte).

The positive electrodes from a cycled cell are shown in Figure 4.3.3-4.

These images were taken from the same sample at a different magnification from those in Figure 4.3.3-2. The SEM images of uncycled samples show precipitation on the electrode with retention of the base electrode structure. Electrodes cycled in both ACN and DMF show islands of precipitation with some clean areas in between; however, it is difficult to see if the underlying electrode remains intact at this magnification. Higher magnification images using both solvents are shown in Figure 4.3.3-5. In DMF, the precipitate appears very crystalline, and individual crystallites appear to have aggregated. In areas without precipitation, the surface of the electrode is very clear and looks qualitatively similar to how it did before being placed in the solution. The ACN image shows a large amount of precipitate. In the central dark region, which is the electrode surface, a 50 μm crack is observed. Several other cracks can be seen on the surface of this electrode. This would indicate that mechanical fatigue is occurring on the positive electrode when cycled in ACN.

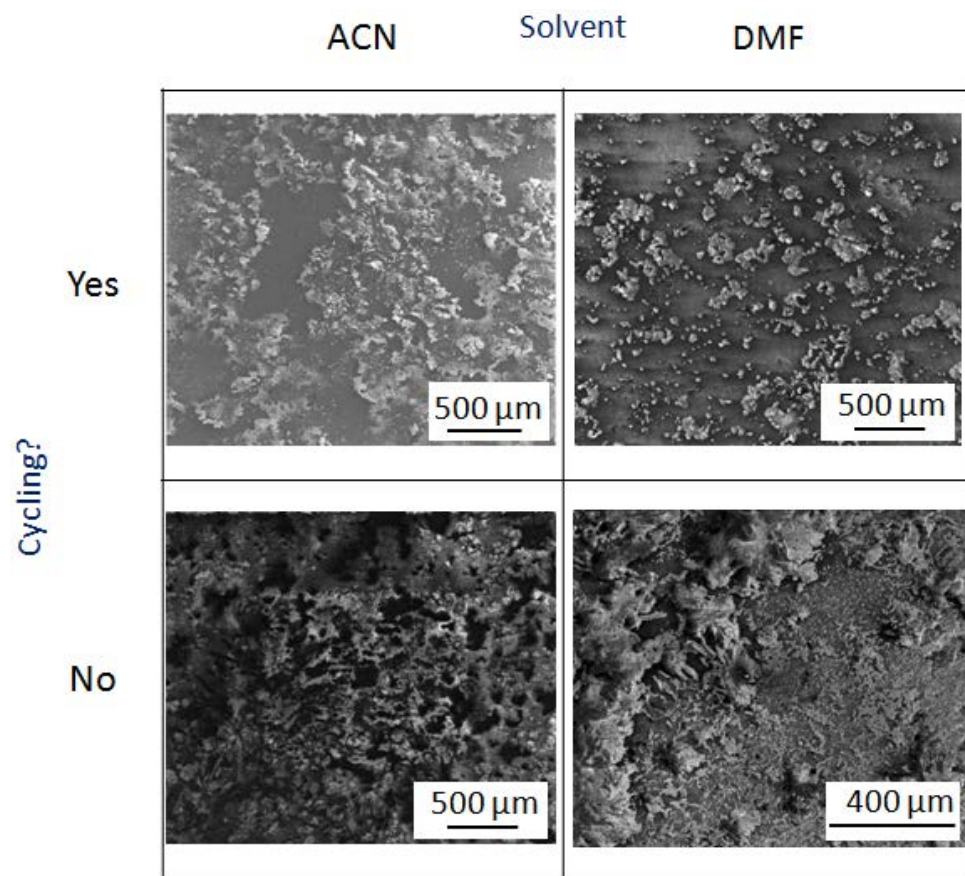


Figure 4.3.3-4 SEM images of the positive electrode in 0.1 M  $V(acac)_3$  and 0.5 M  $TEABF_4$  in solvent. [Top] After cycling for 300 hours with graphite electrodes, [Bottom] After soaking for 300 hours, [Left] Solvent: acetonitrile, [Right] Solvent: dimethylformamide.

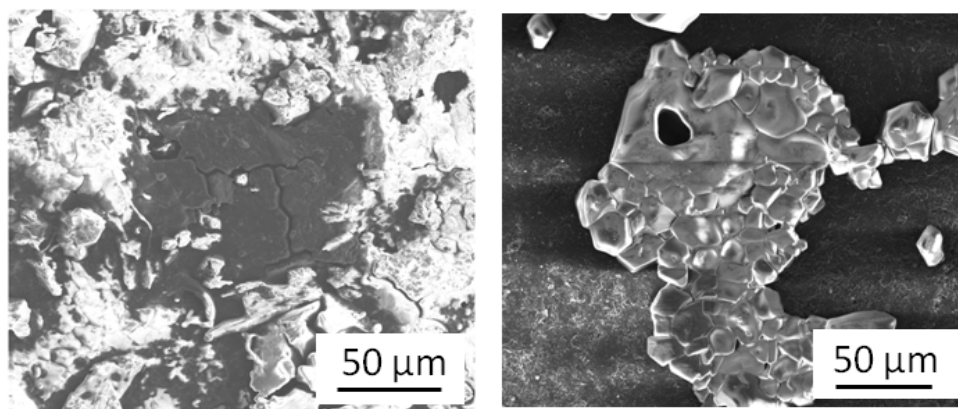


Figure 4.3.3-5 Zoom in of the SEM in the top of Figure 4.3.3-4. [Left] Solvent: ACN, [Right] Solvent: DMF.

*Membrane*

The membranes showed large increases in overpotential during cycling, particularly in ACN solvent. Figure 4.3.3-6 shows an SEM image of the as-received Neosepta AHA membrane at two different magnifications. Unlike Nafion, Neosepta AHA is a reinforced membrane; the ion exchange resin is adhered onto a woven fabric. The individual fabric strands can be clearly seen in the lower-magnification image and has a pattern like diamond plate steel. From the higher-magnification micrograph, it can be seen that cracks have formed around the membrane fibers, suggesting imperfect structural integrity of the membrane. In the as-received samples, these cracks are confined to the raised/threaded areas. Thus the relative number of cracks in flat regions of resin between supporting fibers will be used to assess the mechanical degradation of the membrane structure.

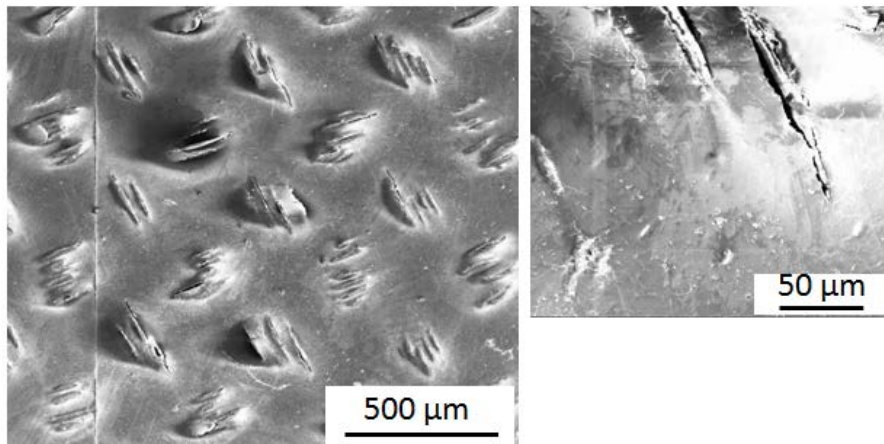


Figure 4.3.3-6 SEM of the as-received Neosepta AHA membrane.

The as-received Neosepta AHA is first compared to the uncycled membranes soaked in the test solution for 300 hrs in Figure 4.3.3-7. Unlike the electrodes, the membranes were soaked in pure solvent for a day after testing. The SEM of the membrane in ACN based solutions is shown on the left at two

different magnifications. First, the cracks still appear localized to the threaded areas of the membrane, and thus mechanical degradation does not seem to be a problem. There are some lighter-colored dots on the membrane, which likely reflect a precipitate, since they are not observed on the as-received sample. The lighter spots arise from surface charging of the samples, which have a relatively low surface conductivity. This is commonly observed on raised portions of low-conductivity samples and is known as 'edge charging' [124]. When soaked in DMF solutions, the membrane appears to show signs of physical degradation – many of the threaded areas have joined together, as seen in the images on the right in Figure 4.3.3-7. There are also very small, lighter-colored dots on this sample, which are not clarified at higher magnification. It is worth mentioning that in several of the images, a rectangle can be seen arising from damage done by the SEM beam during previous data collection at higher magnification.

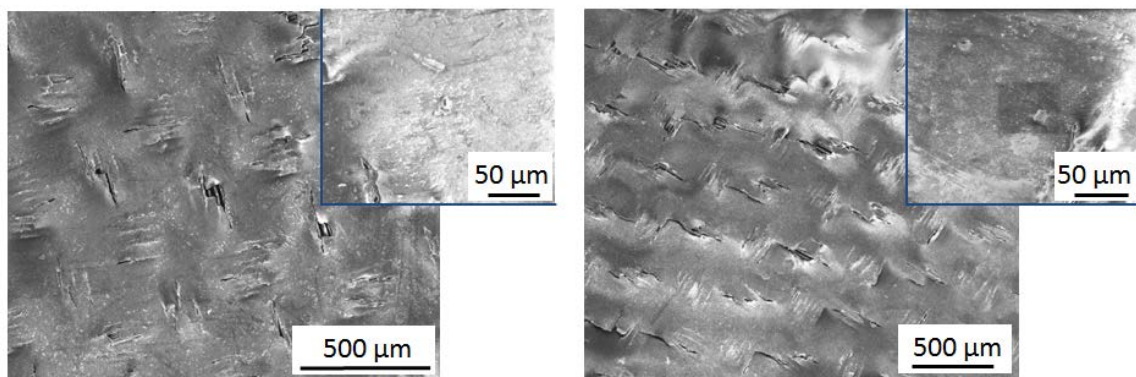


Figure 4.3.3-7 SEM images of the membrane after soaking for 300 hours in 0.1 M  $V(acac)_3$  and 0.5 M  $TEABF_4$  in solvent. [Left] Solvent: ACN, [Right] Solvent: DMF.

Next, the membranes that were cycled for 300 hrs in ACN (Figure 4.3.3-8) or DMF (Figure 4.3.3-9) solutions are shown. The low magnification ACN based SEM image shows several cracks between threaded regions, indicating some



mechanical degradation. The cause of the mechanical fatigue is unknown. Two plausible causes are: physical liquid agitation and ion transport. The cells are magnetically stirred and since the membranes start out with cracks in the ion exchange resin, it is possible that the fluid motion causes the cracks to grow. Ion transport is also a possible cause because  $\text{BF}_4^-$  anions are constantly being shuttled through the ion exchange resin and may fatigue the material. Future researchers may want to determine the cause by varying the amount of current passed in a cell from zero to a large number and examine the membrane fatigue. The lighter-colored dots seen previously in the uncycled control membrane surface are observed; there are several regions where the density of lighter coloration is higher, however. One of these areas is shown at a greater magnification in the image on the right of Figure 4.3.3-8. The light color appears to arise from the presence of crystalline material on the surface of the membrane; the crystals have various sizes, ranging up to approximately 25  $\mu\text{m}$  in diameter. The membrane from the DMF cycled cell is shown in Figure 4.3.3-9. A large amount of cracking has occurred in this sample, providing evidence of extensive mechanical fatigue. Much like the ACN sample, light-colored dots appear on the membrane, with pockets of more lightly-colored particles. The higher-magnification image on the right shows some of the formations observed in several locations on the membrane surface. They resemble dendrites, which may be just under the surface or on the surface.

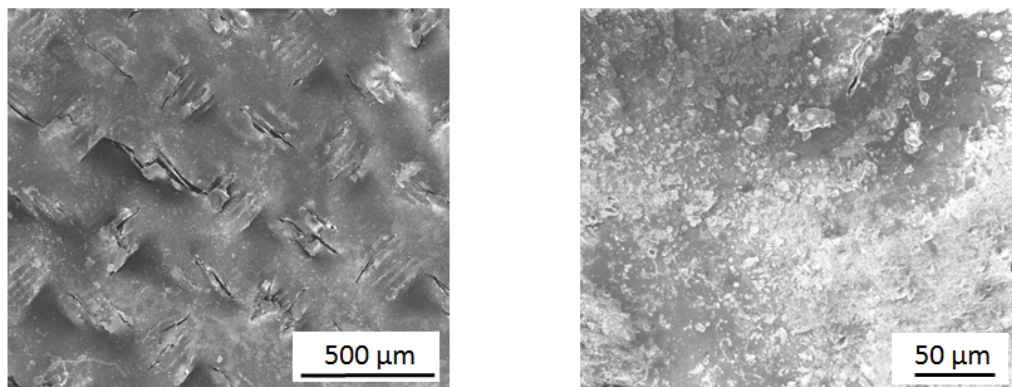


Figure 4.3.3-8 SEM images of the membrane after cycling for 300 hours in 0.1 M  $V(acac)_3$  and 0.5 M  $TEABF_4$  in ACN.

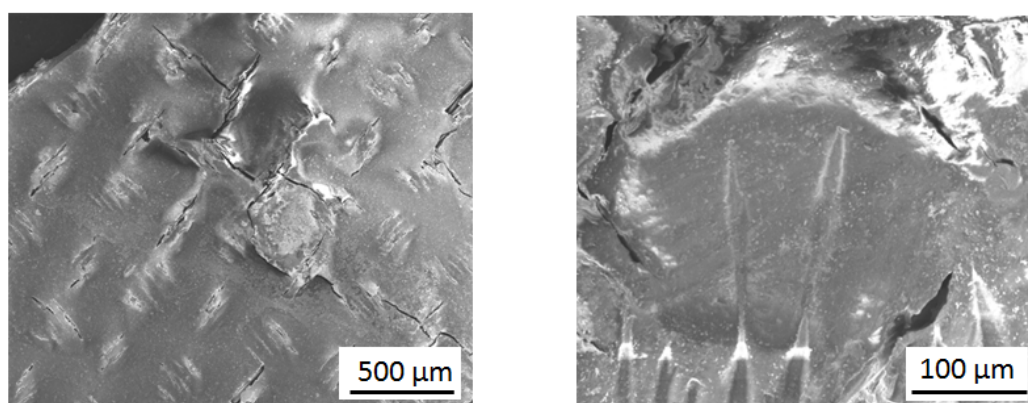


Figure 4.3.3-9 SEM images of the membrane after cycling for 300 hours in 0.1 M  $V(acac)_3$  and 0.5 M  $TEABF_4$  in DMF.

#### 4.3.4 Discussion

In the SEM images of the positive electrodes, very crystalline precipitation is observed in DMF, while a more amorphous precipitate is observed on the ACN electrode. The electrode itself is structurally unchanged when cycling in DMF, while cracks were formed and signs of mechanical degradation were seen in ACN.

The negative electrode shows almost opposite results. The electrode cycled in ACN has a small amount of precipitation on its surface, and is relatively

unchanged relative to the uncycled control. Conversely, the DMF solution completely destroys the negative electrode during cycling. Flakes of the electrode are observed in the liquid electrolyte; the electrode has almost twice its original thickness in some areas after cycling. Furthermore, cracks are observed that propagate completely through the electrode, indicating that not only did precipitation/deposition events occur, delamination and corrosion of the electrode were also significant. Interpretation of the data is somewhat inconclusive owing to uncertainty whether precipitation is caused by cycling, or just by drying after electrodes are removed from soaking solutions. The electrodes need to be additionally soaked in pure solvent to help resolve this question.

Under magnification, the Neosepta AHA membranes show regions where the woven thread is visible with flat areas of resin in between. When cracked, the as-is ion exchange resin is, most often cracked at points of contact with the threads. After soaking the membranes in the test solution for 300 hrs, the appearance of the cracks remains relatively unchanged, although it is possible that they grew in contact with the DMF solution. Both samples have small, light-colored dots on the membrane surface, which are not distinct, even when observed at much higher magnification. Upon cycling the membranes, the density of lightly colored dots increases; at high magnification, small crystals are observed on the surface of the membrane in both ACN and DMF. In terms of mechanical degradation, DMF has a large number of cracks after cycling, while ACN somewhat more crack formation.

The data showing capacity fade, 4-electrode charge/discharge experiments, and the SEM images can be put together to form a clearer picture of what is happening in the cell when cycling. The capacity fade for ACN-solvated systems is mostly caused by an increase in overpotential associated with the membrane. This owes primarily to two different effects. First, SEM images show that an insoluble species precipitates on the membrane during cycling. These crystallites cause the membrane resistance to increase, because they block the pores that electrolyte passes through, increasing the membrane resistance. Surface precipitation causes a dramatic loss of battery capacity as the membrane is cycled. The source of these products is still unknown and should be examined in further research. A second source of rising membrane overpotential is fouling, as described by Assink *et al.* in the context of an aqueous iron/chromium RFB [20]. He observed that the negatively charged iron active species enters the membrane and gets trapped by steric effects, even without applied current. His impedance experiments show the membrane resistance increasing as the adjacent solution concentration is increased. A similar effect may occur in the non-aqueous vanadium RFB, caused by the V(II) oxidation state. To assess which of these two effects causes membrane overpotential to rise during cycling, similar impedance spectroscopy experiments should be performed.

While membranes are the main concern for ACN-based RFB chemistries, overpotentials in DMF-based V(acac)<sub>3</sub> RFBs are dominated by electrode processes on both the positive and negative terminals (based on the 4-electrode

experiments). The SEM images for the positive electrode in DMF showed surface precipitates on the electrode, but no significant change to the underlying morphology was observed. It is not clear whether the precipitate is soluble in the pure solvent or not. For high overpotentials to be observed on both electrodes, the reaction kinetics for both half-reactions involved in  $V(acac)_3$  disproportionation must be slow or the precipitate observed must be insoluble and blocking electrode activity. No kinetic limitations were indicated by CV, so precipitation is likely the source of rising overpotential on the positive electrode. In DMF the negative electrode yielded overpotentials that varied greatly, especially during the third and fourth cycles in 4-electrode experiments. The resulting electrode appeared to be completely destroyed by delamination/corrosion and precipitation. After 300 hrs, the electrode had almost fallen apart from stresses in the electrode. The 4-electrode experiments and SEM images complement each other in describing the key drivers for stability in these two RFB electrolytes.

## Chapter 5 Conclusion and Future Work

### 5.1 Conclusion

Non-aqueous single-metal RFBs were examined by isolating the different components (when possible) in the system and testing the performance of the cell as a whole. The areas examined were: active species metal, active species ligand, solvent/supporting electrolyte, separator, and electrodes. Alongside investigations of the different components, several performance challenges were also addressed. The effect of active-species concentration on cell performance was probed. The sensitivity of the RFB chemistry to ambient water and air during long-term cycling was examined. Lastly, the sources of capacity fade were investigated using 4-electrode charge/discharge tests in combination with SEM and elemental analysis.

Mn, Cr, and V-centered acetylacetonate active species ( $\text{metal}(\text{acac})_3$  complexes) were evaluated for non-aqueous RFB applications, using a tetraethylammonium tetrafluoroborate/acetonitrile electrolyte. Acetylacetonate complexes of V and Mn showed two reversible redox couples separated by 2.2 V and 1.1 V respectively. Disproportionation of  $\text{Cr}(\text{acac})_3$  led to redox couples separated by 3.4 V, which appeared to be kinetically sluggish. The charge/discharge characteristics for single-metal RFB electrolytes containing 0.05 M  $\text{metal}(\text{acac})_3$  and 0.5 M  $\text{TEABF}_4$  in ACN were evaluated in an H-type cell using a Neosepta AHA separator, where the metal are V, Cr, or Mn. For

Mn(acac)<sub>3</sub>, one discharge plateau was observed at 0.3 V with increasing coulombic efficiencies, suggesting that side reactions occur while cycling. Plateau voltages of 2.2 V and 1.25 V were seen for Cr(acac)<sub>3</sub>, the higher of which likely owes to the desired reaction, while the lower must be associated with a side reaction – a conclusion supported by the low observed coulombic efficiencies (53-58 %). V(acac)<sub>3</sub> C/D showed two plateaus at 2.25 V and 1.0 V, which were shown to be caused by formation of VO(acac)<sub>2</sub> in the cell. V(acac)<sub>3</sub> cell run under a high-purity, air-free atmosphere yielded a single discharge plateau at 1.75 V – one of the highest discharge voltages yet observed in a RFB. Vanadium was selected as the active metal for further experiments because of its high maximum energy density and reversibility.

The acetylacetonate ligand was functionalized to produce complexes with tmhd, dppd, and mpd ligands by the UM Chemistry Department; I tested the solubility and electrochemistry. The solubility of V(acac)<sub>3</sub>, V(tmhd)<sub>3</sub>, V(dppd)<sub>3</sub>, and V(mpd)<sub>3</sub> are 0.6 M, 0.011 M, 0.002 M, and 0.15 M, respectively. Each of the functionalizations decreased the solubility in ACN, suggesting that more polar functional groups should be used to modify Hacac to produce complexes more soluble in ACN. The electrochemistry of V(tmhd)<sub>3</sub> and V(dppd)<sub>3</sub> complexes retained peak-height ratios of unity, while that of V(mpd)<sub>3</sub> did not. Due to its low solubility, the electrochemistry of V(dppd)<sub>3</sub> was extremely difficult to discern from that of residual impurities.

Twenty-five solvent and supporting electrolyte combinations were examined for solubility, conductivity, ability to support the cell potential for

$V(\text{acac})_3$  disproportionation, and ability to support stable charge/discharge in a  $V(\text{acac})_3$  RFB cell. Hexane and sodium tetrafluoroborate did not meet solubility requirements, while dimethylcarbonate and tetrahydrofuran did not meet conductivity requirements.  $V(\text{acac})_3$  solubility was highest in ACN, and ranged between 0.44 M and 0.6 M in ACN, DMF, THF, and DMC. The supporting electrolyte choice did not appreciably change solution conductivity, nor did it affect the equilibrium electrochemistry of the active species as quantified by CV. The solvent plays a major role in the cell performance; charge/discharge experiments using DMF show ~2 V more overpotential than those run in ACN. Solvent physical properties were used to predict an ideal solvent for high  $V(\text{acac})_3$  solubility and overall solution conductivity. Acetonitrile is the ideal candidate presently known. Based on observed trends, ethylene carbonate and dimethylsulfoxide are promising solvents for future study.

The performance of an RFB depends not only on the liquid electrolyte, but also on the membrane and electrodes within the RFB reactor. Pretreatment of membranes was briefly examined, and determined that soaking the membrane in the non-aqueous solvent/supporting electrolyte solution removes only 7 % of the residual chloride ions initially present in the membrane. A series of methods to achieve more complete ion exchange was proposed for future testing. Using the soaking pretreatment, the resistance of several commercial membranes was tested using impedance spectroscopy. The results show that Selemion DSV has the lowest resistance of the membranes tested, followed by Neosepta AHA, which was used for charge/discharge studies.



If RFB reactions are fast, outer-sphere electron transfers, the choice of electrode material should have minimal impact on kinetic rates. To examine kinetics further, CV and LSV were performed using gold, platinum, and glassy carbon microelectrodes. All three electrode materials showed fairly reversible kinetics in CV. The LSV data was fit with a theoretical elementary mechanism to determine redox reaction rate constants. The electrode material was not found to affect the  $V(acac)_3 / V(acac)_3^+$  half-reaction rate, for which the electron transfer was immeasurably fast. The  $V(acac)_3^- / V(acac)_3$  couple was found to have exchange-current densities of 1.3 A/m<sup>2</sup>, 3.8 A/m<sup>2</sup>, and 8.4 A/m<sup>2</sup> on glassy-carbon, platinum, and gold surfaces, respectively. Although the rates differed for the different electrode materials investigated, it was found that the difference was sufficiently small that it could be overcome by using high surface-area carbon electrodes.

The performance characteristics of the non-aqueous  $V(acac)_3$  RFB were examined in several different ways, starting with investigations of how active-species concentration affects charge/discharge performance. Based on observations of cycling cells where precipitates formed at concentrations lower than the solubility limits observed in ex-situ tests of neutral electrolytes, the solubility of the positively-charged active species was concluded to be lower than the neutral species in ACN. The maximum solution concentration for complete soluble is 0.1-0.25 M  $V(acac)_3$  with 0.5 M TEABF<sub>4</sub> in ACN. Solutions in which precipitates formed yielded charge/discharge curves with one discharge plateau, while those in which precipitates did not had two. This was concluded to owe to

the conversion of  $V(\text{acac})_3$  to  $VO(\text{acac})_2$  by dissolved constituents of ambient air, a side reaction that can convert almost all of the  $V(\text{acac})_3$  at low concentrations.

The effects of the environment (specifically oxygen and water) on the RFB was examined in more detail using CV and C/D. Both oxygen and water had little effect on the V(III)/V(IV) couple in voltammetry but had a dramatic effect on the V(II)/V(III) couple, almost eliminating the voltammetric signature of V(II) oxidation. Charge/discharge was performed on RFBs in glove boxes with <1 ppm or 10-100 ppm water and oxygen. In the glove box with higher contaminant concentration, two discharge plateaus were observed. These were concluded to derive from the formation of a vanadyl species during cycling. The glove box with a higher-purity atmosphere yielded charge/discharge responses with single discharge plateaus and ~30 % higher energy efficiencies.

Lastly, overpotentials were attributed to different locations in the RFB cell while cycling in ACN and DMF solvents. The ACN system was found to have an initial ~450 mV of overpotential during discharge, which increased to 770 mV after 13 cycles. Over that period, the overpotentials associated with the electrodes increased slightly, but most of the increase could be attributed to the membrane. In DMF, the overpotentials were constant at approximately 1200 mV over the first 13 cycles. Overpotentials could be mostly attributed to electrode processes. To elucidate underlying causes of overpotential increase, scanning electron microscopy images were taken of the electrodes and membrane before and after cycling, and after soaking in uncycled cells. Most of the electrodes showed signs of precipitate formation on the electrode surface; extreme

corrosion accompanied by an delamination process occur on the negative electrode in DMF. After cycling, the membrane shows crystalline deposits of a species that is insoluble in either ACN or DMF.

## 5.2 Future Work

There are many opportunities for further research into non-aqueous single-metal RFBs. The three biggest are in the areas of: active-species ligands, membranes, and cell design.

The active-species concentration must be increased to improve RFB energy density. This can be done by modifying the active species ligand or the solvent to have more chemical affinity. Since the supporting electrolyte is ionic, and the solvent cannot be changed to be less polar without sacrificing the solubility of the supporting electrolyte, the ligand must be changed. Active-species ligands were examined in this thesis, but the ligand modifications attempted did not improve the solubility. Further work in this area needs to be done to determine which ligands will improve the solubility. Current work would suggest that the ligand needs to contain pendant groups with more affinity for polar solvents.

Membranes are an area of significant concern moving forward, since they have proven to be the main driver for capacity fade with cycling. Several factors must be considered when selecting membranes for non-aqueous RFB systems and these differ from those pertinent to aqueous chemistries. The aqueous all-vanadium RFB reaction, for instance, involves  $H^+$  ions and uses an acidic

supporting electrolyte, making proton-exchange membranes a logical choice. Non-aqueous solvents tend to be aprotic, and either degrade or inhibit the ion conduction of many standard proton-exchange membranes. Detailed further study should focus on determining what membranes are stable in, and wet by, non-aqueous solvents; what membranes resist active-species crossover; and which supporting ions provide the highest mobilities. It will also be important to create methods for pretreating membranes that are more effective than those used in this work.

The hardware used for charge/discharge is the third main area in which improvements could be made. Experimental results shown thus far involve a static cell with a stir bar to simulate flow. However, this cell has a large separation between the electrodes, which is a significant source of overpotential. Liquid-phase overpotentials can be eliminated almost entirely in practice by employing a flow-through reactor with high-surface area electrodes. Calculations based on independent measurements of the solution, membrane, and electrode suggests that the removal of the solution resistances would lead to an energy-efficiency increase of ~25 % along with a reduction of crossover.

In the long run, I believe it may be beneficial to look at a different system altogether. The state of current research reveals 5x lower energy density than commercial chemistries, with no ability to improve the potential or number of electrons transferred once choosing vanadium acetylacetonate and its derivatives. Although probably possible, it is difficult to get a 5-fold increase in the system concentration; I suggest revisiting the active metals.  $\text{Cr}(\text{acac})_3$

provided a cell potential of 3.4 V for one electron transfer and 4.1 V for a second electron transfer. This system would be ideal for the first examination of using two-electron transfers if a stable ligand can be identified. The solvent and supporting electrolytes will likely need to be revisited for Cr since it is desirable to use the solvent to improve the reversibility of the peak heights. Use of different metals (or solvents) in either electrolyte would allow for more efficient selection of ligands that stabilize the complex when exposed to relatively positive and negative voltages. One of the challenges with two-metal systems is that the membrane is much more important; active-species crossover may lead to a requirement of purification or separation over time. A chemistry with multiple electron transfers could also be used to bridge the solubility gap between non-aqueous and aqueous RFB chemistries.

Of course, these suggestions require many further experiments to identify plausible chemistries. Further study of non-aqueous RFB chemistry and performance can be guided by the results provided here.



## Bibliography

1. Energy\_Information\_Administration, *Renewable Energy Annual 2007*, U.D.o. Energy, Editor. 2009.
2. Tester, J.W., et al., *Sustainable Energy: Choosing Among Options*. 2005: MIT Press.
3. Lewis, N., *Powering the Planet*. MRS Bulletin, 2007. **32**(10): p. 808-820.
4. Ponce de Leon, C., et al., *Redox flow cells for energy conversion*. J. Power Sources, 2006. **160**(1): p. 716-732.
5. *Ashlawn Energy*. 2012 Dec 20, 2012]; Available from: <http://www.ashlawnenergy.com/index.php>.
6. Lex, P. and B. Jonshagen, *The Zinc/Bromine Battery System for Utility and Remote Area Applications*. Power Engineering Journal, 1999. **13**(3): p. 142-148.
7. Lipman, T.E., R. Ramos, and D.M. Kammen, *An Assessment of Battery and Hydrogen Energy Storage Systems Integrated with Wind Energy Resources in California*, P.F.P. Report, Editor. 2005.
8. Holzman, D.C., *The Vanadium Advantage: Flow Batteries Put Wind Energy in the Bank*. Environ Health Perspect, 2007. **115**(7).
9. Skyllas-Kazacos, M., et al., *Progress in Flow Battery Research and Development*. J. Electrochem. Soc., 2011. **158**(8): p. R55-R79.
10. Arora, P. and Z. Zhang, *Battery Separators*. Chemical Reviews, 2004. **104**(10): p. 4419-4462.
11. Thaller, L.H., *Electrically Rechargeable Redox Flow Cells*, in *Ninth Intersociety Energy Conversion Engineering Conference*. 1974: San Francisco, CA.
12. Lim, H.S., A.M. Lackner, and R.C. Knechtli, *Zinc-Bromine Secondary Battery*. J. Electrochem. Soc., 1977. **124**(8): p. 1154-1157.
13. Barnartt, S. and D.A. Forejt, *Bromine-Zinc Secondary Cells*. J. Electrochem. Soc., 1964. **111**(11): p. 1201-1204.
14. Ge, S.H., B.L. Yi, and H.M. Zhang, *Study of a high power density sodium polysulfide/bromine energy storage cell*. J. Appl. Electrochem., 2004. **34**(2): p. 181-185.
15. Price, A., et al., *A novel approach to utility scale energy storage [regenerative fuel cells]*. Power Engineering Journal, 1999. **13**(3): p. 122-129.
16. O'Donnell, P.M., R.F. Gahn, and J.L. Pfeiffer, *The Redox Flow System for Solar Photovoltaic Energy Storage*, N.T. 73562, Editor. 1976: Lewis Research Center.

17. Savinell, R.F., et al., *Discharge Characteristics of a Soluble Iron-Titanium Battery System*. J. Electrochem. Soc., 1979. **126**(3): p. 357-360.
18. Zhao, P., et al., *Nickel foam and carbon felt applications for sodium polysulfide/bromine redox flow battery electrodes*. Electrochim. Acta, 2005. **51**(6): p. 1091-1098.
19. Besenhard, J.O. and R. Schoellhorn, *The discharge reaction mechanism of the molybdenum(VI) oxide electrode in organic electrolytes*. J. Power Sources, 1977. **1**(3): p. 267-76.
20. Assink, R.A., *Fouling mechanism of separator membranes for the iron/chromium redox battery*. J. Membr. Sci., 1984. **17**(2): p. 205-217.
21. Wiedemann, E., A. Heintz, and R.N. Lichtenthaler, *Transport properties of vanadium ions in cation exchange membranes:: Determination of diffusion coefficients using a dialysis cell*. J. Membr. Sci., 1998. **141**(2): p. 215-221.
22. Pelligri, A. and P.M. Spaziante, *Process and accumulator for storing and releasing electrical energy*. 1980: UK.
23. Skyllas-Kazacos, M., et al., *New all-vanadium redox flow cell J*. Electrochem. Soc., 1986. **133**(5): p. 1057-1058.
24. Sum, E., M. Rychcik, and M. Skyllas-Kazacos, *Investigation of the vanadium(V)/vanadium(IV) system for use in the positive half-cell of a redox battery*. J. Power Sources, 1985. **16**(2): p. 85-95.
25. Sum, E. and M. Skyllas-Kazacos, *A study of the vanadium(II)/vanadium(III) redox couple for redox flow cell applications*. J. Power Sources, 1985. **15**(2-3): p. 179-90.
26. Oriji, G., Y. Katayama, and T. Miura, *Investigation on V(IV)/V(V) species in a vanadium redox flow battery*. Electrochim. Acta, 2004. **49**(19): p. 3091-3095.
27. Oriji, G., Y. Katayama, and T. Miura, *Investigations on V(IV)/V(V) and V(II)/V(III) redox reactions by various electrochemical methods*. J. Power Sources, 2005. **139**(1-2): p. 321-324.
28. Hill, J.O., I.G. Worsley, and L.G. Hepler, *Thermochemistry and oxidation potentials of vanadium, niobium, and tantalum*. Chemical Reviews, 1971. **71**(1): p. 127-137.
29. Kazacos, M. and M. Skyllas-kazacos, *Performance-Characteristics of Carbon Plastic Electrodes in the All-Vanadium Redox Cell J*. Electrochem. Soc., 1989. **136**(9): p. 2759-2760.
30. Skyllas-Kazacos, M., et al., *Recent advances with UNSW vanadium-based redox flow batteries*. International Journal of Energy Research, 2010. **34**(2): p. 182-189.
31. Xue, F.Q., et al., *Investigation on the electrode process of the Mn(II)/Mn(III) couple in redox flow battery*. Electrochim. Acta, 2008. **53**(22): p. 6636-6642.
32. Paulenova, A., et al., *Redox potentials and kinetics of the Ce<sup>+3</sup>/Ce<sup>+4</sup> redox reaction and solubility of cerium sulfates in sulfuric acid solutions*. J. Power Sources, 2002. **109**(2): p. 431-438.
33. Fang, B., et al., *A study of the Ce(III)/Ce(IV) redox couple for redox flow battery application*. Electrochim. Acta, 2002. **47**(24): p. 3971-3976.



34. Xia, X., H.T. Liu, and Y. Liu, *Studies of the feasibility of a  $Ce^{+4}/Ce^{+3}-V^{+2}/V^{+3}$  redox cell*. J. Electrochem. Soc., 2002. **149**(4): p. A426-A430.
35. Rahman, F. and M. Skyllas-Kazacos, *Solubility of vanadyl sulfate in concentrated sulfuric acid solutions*. J. Power Sources, 1998. **72**(2): p. 105-110.
36. Hall, P.J. and E.J. Bain, *Energy-storage technologies and electricity generation*. Energy Policy, 2008. **36**(12): p. 4352-4355.
37. Tsuda, I., et al., *Improvement of performance in redox flow batteries for PV systems*. Solar Energy Materials and Solar Cells, 1997. **47**(1-4): p. 101-107.
38. Sukkar, T. and M. Skyllas-Kazacos, *Water transfer behaviour across cation exchange membranes in the vanadium redox battery*. J. Membr. Sci., 2003. **222**(1-2): p. 235-247.
39. Mohammadi, T. and M. Skyllas-Kazacos, *Use of Polyelectrolyte for Incorporation of Ion-exchange Groups in Composite Membranes for Vanadium Redox Flow Battery Applications* J. Power Sources, 1995. **56**(1): p. 91-96.
40. Mohammadi, T. and M. Skyllas-Kazacos, *Preparation of Sulfonated Composite Membrane for Vanadium Redox Flow Battery Applications* J. Membr. Sci., 1995. **107**(1-2): p. 35-45.
41. Mohammadi, T. and M. Skyllas-Kazacos, *Characterization of Novel Composite Membrane For Redox Flow Battery Applications*. J. Membr. Sci., 1995. **98**(1-2): p. 77-87.
42. Chakrabarti, M.H., E.P.L. Roberts, and M. Saleem, *Charge-Discharge Performance of a Novel Undivided Redox Flow Battery for Renewable Energy Storage*. International Journal of Green Energy, 2010. **7**(4): p. 445-460.
43. Skyllas-Kazacos, M., *Novel vanadium chloride/polyhalide redox flow battery*. J. Power Sources, 2003. **124**(1): p. 299-302.
44. Vafiadis, H. and M. Skyllas-Kazacos, *Evaluation of membranes for the novel vanadium bromine redox flow cell*. J. Membr. Sci., 2006. **279**(1-2): p. 394-402.
45. Bard, A.J. and L.R. Faulkner, *Electrochemical Methods: Fundamentals and Applications*. 2000: Wiley.
46. Matsuda, Y., et al., *A rechargeable redox battery utilizing ruthenium complexes with nonaqueous organic electrolyte*. J. Appl. Electrochem., 1988. **18**(6): p. 909-14.
47. Chakrabarti, M.H., R.A.W. Dryfe, and E.P.L. Roberts, *Evaluation of electrolytes for redox flow battery applications*. Electrochim. Acta, 2007. **52**(5): p. 2189-2195.
48. Yamamura, T., et al., *Electrochemical investigation of uranium beta-diketonates for all-uranium redox flow battery*. Electrochim. Acta, 2002. **48**(1): p. 43-50.
49. Liu, Q.H., et al., *Non-aqueous vanadium acetylacetonate electrolyte for redox flow batteries*. Electrochemistry Communications, 2009. **11**(12): p. 2312-2315.

50. Liu, Q.H., et al., *Non-aqueous chromium acetylacetonate electrolyte for redox flow batteries*. *Electrochemistry Communications*, 2010. **12**(11): p. 1634-1637.
51. Sleightholme, A.E.S., et al., *Non-aqueous manganese acetylacetonate electrolyte for redox flow batteries*. *J. Power Sources*, 2011. **196**(13): p. 5742-5745.
52. Chakrabarti, M.H., R.A.W. Dryfe, and E.P.L. Roberts, *Evaluation of electrolytes for redox flow battery applications*. *Electrochim. Acta*, 2006. **52**(5): p. 2189-2195.
53. Chakrabarti, M.H., et al., *Ruthenium based redox flow battery for solar energy storage*. *Energy Conversion and Management*, 2011. **52**(7): p. 2501-2508.
54. Mun, J., et al., *Non-Aqueous Redox Flow Batteries with Nickel and Iron Tris(2,2'-bipyridine) Complex Electrolyte*. *Electrochemical and Solid State Letters*, 2012. **15**(6): p. A80-A82.
55. Compton, R.G. and C.E. Banks, *Understanding Voltammetry*. 2007: World Scientific.
56. Shinkle, A.A., et al., *Degradation mechanisms in the non-aqueous vanadium acetylacetonate redox flow battery*. *J. Power Sources*, 2012(SI).
57. Nicholson, R.S. and I. Shain, *Theory of Stationary Electrode Polarography - Single Scan + Cyclic Methods Applied to Reversible Irreversible + Kinetic Systems*. *Analytical Chemistry*, 1964. **36**(4): p. 706-&.
58. Nicholson, R.S., *Theory and Application of Cyclic Voltammetry for Measurement of Electrode Reaction Kinetics*. *Analytical Chemistry*, 1965. **37**(11): p. 1351-1355.
59. Bard, A.J., Faulkner, Larry R., *Electrochemical Methods - Fundamentals and Applications*. Second Edition: Wiley.
60. Pourbaix, M., *Atlas of Electrochemical Equilibria in Aqueous Solutions*. 2 ed. 1974.
61. Chakrabarti, M.H., R.A.W. Dryfe, and E.P.L. Roberts, *Organic electrolytes for redox flow batteries*. *J. Chem. Soc. Pak.*, 2007. **29**(4): p. 294-300.
62. Tocher, J.H. and J.P. Fackler, *Electrochemical Investigations of Several Transition-Metal Tris-(Acetylacetonate) Complexes*. *Inorganica Chimica Acta-Articles and Letters*, 1985. **102**(2): p. 211-215.
63. Gritzner, G., H. Murauer, and V. Gutmann, *The polarographic and voltammetric behavior of acetylacetonato and hexafluoroacetylacetonato complexes in acetonitrile*. *Journal of Electroanalytical Chemistry and Interfacial Electrochemistry*, 1979. **101**(2): p. 177-83.
64. Gritzner, G., H. Murauer, and V. Gutmann, *Solvent and salt effects on the redox behavior of trisacetylacetonato manganese(III)*. *Journal of Electroanalytical Chemistry and Interfacial Electrochemistry*, 1979. **101**(2): p. 185-200.
65. Sock, O., P. Lemoine, and M. Gross, *Mechanisms of electrochemical reduction of transition metal acetylacetonate complexes*. *Electrochimica Acta*, 1981. **26**(1): p. 99-109.

66. Yamaguchi, K. and D.T. Sawyer, *Redox chemistry for the mononuclear tris(picolinato)- tris(acetylacetonata)-, and tris(8-quinolinata)manganese(III) complexes: reaction mimics for the water-oxidation cofactor in photosystem II*. Inorganic Chemistry, 1985. **24**(6): p. 971-6.
67. Ponce de Leon, C., et al., *Redox flow cells for energy conversion*. Journal of Power Sources, 2006. **160**(1): p. 716-732.
68. Liu, Q., et al., *Non-aqueous vanadium acetylacetonate electrolyte for redox flow batteries*. Electrochemistry Communications, 2009. **11**(12): p. 2312-2315.
69. Liu, Q., Shinkle, A., Li, Y., Monroe, C., Thompson, L., Sleightholme, A.E.S., *Non-aqueous chromium acetylacetonate electrolyte for redox flow batteries*. Submitted to Electrochemistry Communications, 2010.
70. Anderson, C.W., K.R. Lung, and T.A. Nile, *Electrochemistry of homogeneous catalysts: correlation of the electrochemistry and the Ziegler-Natta catalytic activity of metal acetylacetonate complexes*. Inorganica Chimica Acta, 1984. **85**(1): p. 33-6.
71. Landsberg, R., P. Janietz, and M. Pruegel, *Ligand exchange reactions of some chromium(III) complexes investigated by cyclic voltammetry*. Monatshefte fuer Chemie, 1978. **109**(6): p. 1287-94.
72. Landsberg, R., P. Janietz, and M. Pruegel, *On the electrochemical reduction of some chromium(III) complexes in DMSO investigated by cyclic voltammetry*. Monatshefte fuer Chemie, 1979. **110**(4): p. 831-40.
73. Beaver, B.D., et al., *Reactions of coordinated molecules. XXVIII. Cyclic voltammetry of several transition metal metalla-acetylacetonate complexes*. Inorganica Chimica Acta, 1981. **47**(1): p. 25-30.
74. Carano, M., et al., *Synthesis of heteroleptic anthryl-substituted beta-ketoenolates of rhodium(III) and iridium(III): Photophysical, electrochemical, and EPR study of the fluorophore-metal interaction*. Inorganic Chemistry, 2002. **41**(13): p. 3396-3409.
75. Anderson, C.W., K.R. Lung, and T.A. Nile, *Electrochemistry of Homogeneous Catalysts - Correlation of the Electrochemistry and the Ziegler-Natta Catalytic Activity of Metal Acetylacetonate Complexes*. Inorganica Chimica Acta-Articles and Letters, 1984. **85**(1): p. 33-36.
76. Nawi, M.A. and T.L. Riechel, *Electrochemical Studies of Vanadium(III) and Vanadium(IV) Acetylacetonate Complexes in Dimethylsulfoxide*. Inorganic Chemistry, 1981. **20**(7): p. 1974-1978.
77. Nawi, M.A. and T.L. Riechel, *Electrochemical studies of vanadium (V) acetylacetonate complexes in dimethyl sulfoxide*. Inorganic Chemistry, 1982. **21**(6): p. 2268-2271.
78. Vlckova, B., B. Strauch, and M. Horak, *Measurement and Interpretation of Infrared and Raman Spectra of Vanadyl Acetylacetonate*. Collection of Czechoslovak Chem. Commun., 1987. **52**: p. 686-695.
79. Lorenzola, T.A., B.A. Lopez, and M.C. Giordano, *Molecular-Oxygen Electroreduction at Pt and Au Electrodes in Acetonitrile Solutions*. J. Electrochem. Soc., 1983. **130**(6): p. 1359-1365.

80. Sawyer, D.T., et al., *Effects of Media and Electrode Materials on the Electrochemical Reduction of Dioxygen*. Analytical Chemistry, 1982. **54**(11): p. 1720-1724.
81. Zoski, C.G., *Handbook of Electrochemistry*. 2007, Amsterdam, Netherlands: Elsevier.
82. Gritzner, G., H. Murauer, and V. Gutmann, *Polarographic and Voltammetric Behavior of Acetylacetonato and Hexafluoroacetylacetonato Complexes in Acetonitrile*. J. Electroanal. Chem., 1979. **101**(2): p. 177-183.
83. Patterson, G.S. and R.H. Holm, *Effects of chelate ring substituents on the polarographic redox potentials of tris(beta-diketonato)ruthenium(II,III) complexes*. Inorganic Chemistry, 1972. **11**(9): p. 2285-2288.
84. Xu, K., *Nonaqueous liquid electrolytes for lithium-based rechargeable batteries*. Chemical Reviews, 2004. **104**(10): p. 4303-4417.
85. Richert, S.A., P.K.S. Tsang, and D.T. Sawyer, *Ligand-Centered Redox Processes for MnL<sub>3</sub>, FeL<sub>3</sub>, and CoL<sub>3</sub> Complexes (L = Acetylacetonate, 8-Quinolate, Picolinate, 2,2'-Bipyridyl, 1,10-Phenanthroline) and for Their Tetrakis(2,6-Dichlorophenyl)Porphinato Complexes [M(Por)]*. Inorganic Chemistry, 1989. **28**(12): p. 2471-2475.
86. *CRC Handbook of Chemistry and Physics*, W.M. Haynes, Editor. 2011.
87. *Dimethylcarbonate Product Data Sheet*. 2012 Aug 2012]; Available from: [www.novolyte.com](http://www.novolyte.com).
88. Ue, M., K. Ida, and S. Mori, *Electrochemical Properties of Organic Liquid Electrolytes Based on Quaternary Onium Salts for Electrical Double-Layer Capacitors*. J. Electrochem. Soc., 1994. **141**(11): p. 2989-2996.
89. Newman, J. and K.E. Thomas-Alyea, *Electrochemical Systems*. 2004: John Wiley & Sons.
90. Riddick, J.A. and W.B. Bunger, *Organic solvents*. Journal of Pharmaceutical Sciences, 1971. **60**(7): p. 1112-1112.
91. Noviandri, I., et al., *The decamethylferrocenium/decamethylferrocene redox couple: A superior redox standard to the ferrocenium/ferrocene redox couple for studying solvent effects on the thermodynamics of electron transfer*. Journal of Physical Chemistry B, 1999. **103**(32): p. 6713-6722.
92. Hansen, C.M., *Hansen Solubility Parameters: A User's Handbook, Second Edition*. 2007: Taylor & Francis.
93. Hildebrand, J.H. and R.L. Scott, *The Solubility of Nonelectrolytes*. 1964: Dover Publications.
94. Yeagley, A., et al., *Substituent and solvent dependence of the one-electron reduction of 5-substituted-N-methylisatins in aprotic solvents*. J. Electroanal. Chem., 2011. **651**(2): p. 228-232.
95. *Knovel Critical Tables*. 2008.
96. *Kamlet-Taft Solvent Parameters*. 2011; Available from: <http://www.stenutz.eu/chem/solv26.php>.

97. Mayer, U., V. Gutmann, and W. Gerger, *Acceptor Number - Quantitative Empirical Parameter for Electrophilic Properties of Solvents*. Monatshefte Fur Chemie, 1975. **106**: p. 1235-1257.
98. Zhang, S., et al., *Physical Properties of Ionic Liquids: Database and Evaluation*. Journal of Physical and Chemical Reference Data, 2006. **35**(4): p. 1475-1517.
99. Doyle, M., et al., *Relationship between ionic conductivity of perfluorinated ionomeric membranes and nonaqueous solvent properties*. J. Membr. Sci., 2001. **184**(2): p. 257-273.
100. Born, M., *Volumen und Hydratationswärme der Ionen*. Zeits. f. Physik, 1920. **1**: p. 45.
101. Bartolozzi, M., *Development of Redox Flow Batteries - a Historical Bibliography*. J. Power Sources, 1989. **27**(3): p. 219-234.
102. Xi, J., et al., *Nafion/SiO<sub>2</sub> hybrid membrane for vanadium redox flow battery*. J. Power Sources, 2007. **166**(2): p. 531-536.
103. Zawodzinski, T.A., et al., *Water Uptake by and Transport Through Nafion 117 Membranes*. J. Electrochem. Soc., 1993. **140**(4): p. 1041-1047.
104. Rychcik, M. and M. Skyllas-kazacos, *Evaluation of Electrode Materials for Vanadium Redox Cell*. J. Power Sources, 1987. **19**(1): p. 45-54.
105. Hodes, G., J. Manassen, and D. Cahen, *Electrocatalytic Electrodes for the Polysulfide Redox System*. J. Electrochem. Soc., 1980. **127**(3): p. 544-549.
106. Hollax, E. and D.S. Cheng, *The Influence of Oxidative Pretreatment of Graphite-Electrodes on the Catalysis of the Cr<sup>+3</sup>/Cr<sup>+2</sup> and Fe<sup>+3</sup>/Fe<sup>+2</sup> Redox Reactions*. Carbon, 1985. **23**(6): p. 655-664.
107. Lopezatalaya, M., et al., *Behavior of the Cr(III)/Cr(II) Reaction on Gold Graphite-Electrodes - Application to Redox Flow Storage Cell*. J. Power Sources, 1991. **35**(3): p. 225-234.
108. Aoki, K., et al., *Linear sweep voltammetry at very small stationary disk electrodes*. Journal of Electroanalytical Chemistry and Interfacial Electrochemistry, 1984. **171**(1-2): p. 219-230.
109. Baur, J.E. and R.M. Wightman, *Diffusion coefficients determined with microelectrodes*. Journal of Electroanalytical Chemistry and Interfacial Electrochemistry, 1991. **305**(1): p. 73-81.
110. Mirkin, M.V. and A.J. Bard, *Simple analysis of quasi-reversible steady-state voltammograms*. Analytical Chemistry, 1992. **64**(19): p. 2293-2302.
111. Evans, D. and M. Lehmann, *Two-Electron Reactions in Organic and Organometallic Electrochemistry*. Acta Chem Scandinavica, 1999. **53**: p. 765.
112. van Asselt, R., et al., *Divalent Palladium and Platinum Complexes Containing Rigid Bidentate Nitrogen Ligands and Electrochemistry of the Palladium Complexes*. Organometallics, 1997. **16**(3): p. 317-328.
113. Norton, J.D. and H.S. White, *Effect of comproportionation on the voltammetric reduction of methyl viologen in low ionic strength solutions*. J. Electroanal. Chem., 1992. **325**(1-2): p. 341-350.

114. Newman, J., *Frequency Dispersion in Capacity Measurements at a Disk Electrode*. J. Electrochem. Soc., 1970. **117**(2): p. 198-203.
115. Marcus, R.A., *The Theory of Oxidation Reduction Reactions Involving Electron Transfer V. Comparison and Properties of Electrochemical and Chemical Rate Constants*. The Journal of Physical Chemistry, 1963. **67**(4): p. 853-857.
116. Fisher, A.C., *Electrode Dynamics*. 1996: Oxford University Press, USA.
117. Thomas-Alyea, K.E., et al., *Modeling the behavior of electroactive polymers for overcharge protection of lithium batteries*. J. Electrochem. Soc., 2004. **151**(4): p. A509-A521.
118. Zhong, S. and M. Skyllas-Kazacos, *Electrochemical behaviour of vanadium(V)/vanadium(IV) redox couple at graphite electrodes*. J. Power Sources, 1992. **39**(1): p. 1-9.
119. Cotton, F.A., *Advanced Inorganic Chemistry*. 1999: Wiley.
120. Kitamura, M., K. Yamashita, and H. Imai, *Studies on Electrode Processes of Oxovanadium (IV) .2. Electrolytic Reduction of Vanadyl Acetylacetonate in Acetonitrile Solution at Mercury-Electrode*. Bulletin of the Chemical Society of Japan, 1976. **49**(1): p. 97-100.
121. Kazacos, M., M. Cheng, and M. Skyllas-Kazacos, *Vanadium redox cell electrolyte optimization studies*. J. Appl. Electrochem., 1990. **20**(3): p. 463-7.
122. Endo, A., et al., *Electrochemistry of Tris(beta-diketonato) Ruthenium(III) Complexes at Platinum-electrodes in Nonaqueous Solutions and Substituent Effects on their Reversible Half-wave Potentials* Bulletin of the Chemical Society of Japan, 1989. **62**(3): p. 709-716.
123. Veith, G.M. and N.J. Dudney, *Current Collectors for Rechargeable Li-Air Batteries*. J. Electrochem. Soc. **158**(6): p. A658-A663.
124. Rice, P. *Charging Effects on SEM Images*.  
<http://ncf.colorado.edu/instdocs/quickguides/SEM-ChargingEffects.pdf>.